UNIVERSITY OF BELGRADE

FACULTY OF MECHANICAL ENGINEERING

Bashir S. Younise

MICROMECHANICAL FRACTURE ANALYSIS OF HIGH STRENGTH STEEL WELDMENTS

Doctoral Dissertation

Belgrade, 2013

UNIVERZITET U BEOGRADU

MAŠINSKI FAKULTET

Bashir S. Younise

MIKROMEHANIČKA ANALIZA LOMA ZAVARENIH SPOJEVA ČELIKA POVIŠENE ČVRSTOĆE

doktorska disertacija

Beograd, 2013

Dedicated to my parents, wife and teachers

SUPERVISOR:

Dr Aleksandar Sedmak, full professor
Faculty of Mechanical Engineering, Belgrade

BOARD OF COMMISSION:

Dr Radica Prokić-Cvetković , full professor
Faculty of Mechanical Engineering, Belgrade

Dr Marko Rakin, associate professor
Faculty of Technology and Metallurgy, Belgrade

Dr Dražan Kozak, full professor
Faculty of Mechanical Engineering, Osijek

Dr Zoran Radaković, associate professor
Faculty of Mechanical Engineering, Belgrade

Date of defense:

Acknowledgement

My deepest gratitude goes to my advisor Prof. Dr. Aleksander Sedmak for his encouragements, advice and consistent help, and, most of all, his invaluable instructions in the academic area. I truly appreciate all the time he took in guiding me. I also thank him for all the care he has taken of me outside research field over the years I stay in Serbia.

I would like to thank Prof. Dr. M. Rakin and Dr. B. Medjo for his sincere help. Their expertise in structural integrity assessment using continuum damage mechanics, finite element analysis and ABAQUS benefits me a lot in my research.

The author appreciates the help offered by Prof. Dr. N. Gubeljak , Prof. Dr. M. Zrilić and Prof. Dr. M. Burzić in finishing the carried out experimental work.

A special thank is given to the staffs of Mechanical Engineering Faculty. I appreciate their help and their kindness.

Finally, it is a pleasure to acknowledge the continuous support and help received from my family members.

Author

MICROMECHANICAL FRACTURE ANALYSIS OF HIGH STRENGTH STEEL WELDMENTS

Abstract:

The industrial application of high strength steel in structural welded components has increased the demand for understanding the ductile failure behavior of this type of welded materials. Therefore, integrity assessment of those welded structures is required in order to ensure a certain level of safety and reliability, having in mind the effects of constraints and heterogeneity on fracture behavior of crucial regions such as: heat affected zone (HAZ) and weld metal (WM) which usually have low toughness and higher transition temperature. It is also essential that the assessment is done in a realistic and not too conservative way in order not to increase the mass of the structure or impair the economic efficiency too much.

In this thesis, micromechanical approach has been used to study the effect of mechanical heterogeneity and constraints on ductile fracture of high strength steel weldments. This approach has been used as a solution for the transferability problem of conventional fracture mechanics parameters. It has also been used on basis of that fracture mechanics parameters recommended by standard, such as: stress intensity factor, crack opening displacement and contour *J*-integral, cannot reliably describe the reaction of a pre-cracked material to the effects of external loading under all conditions such as: large scale yielding, various effects of heterogeneity, shape and geometry of real welded structures. The fracture mechanics parameters, determined from laboratory scale experiments are not also directly transferable to components and hence additional considerations (like constraint effects etc.) need to be taken care of. In addition, the aim of the thesis was to estimate precise mechanical properties using a combined experimental and numerical procedure for various welded joint regions, especially for narrow HAZ regions, when they are subjected to transversally applied load.

The study was carried out using finite element method and experiments. Experimental analysis was carried out on: welded smooth tensile specimen with ARAMIS measuring system for estimation mechanical properties, welded single-edge notched bend and flat tensile specimens with pre-cracks in weld metal (WM) and heat-affected zone (HAZ) for studying the ductile fracture behavior. *J-R* curves and crack growth initiation

values of fracture mechanics parameter were experimentally and numerically obtained for specimens with a pre-crack in HAZ and WM. Numerical analysis of elastic-plastic finite element models (2D and 3D) was performed in software package Abaqus, with micromechanical complete Gurson model (CGM) applied through user subroutine, UMAT (author: Z.L. Zhang). The crack tip constraint and variation of stress triaxiality in ligament were numerically analyzed on single-edge notched bend and tensile specimens to analyze the transferability of micromechanical damage parameters from one specimen to another. In addition, the geometry effects were also studied by the micromechanical approach and the results were compared with those of the experiments. Most of numerical results obtained with CGM model are in good agreement with the experimental results.

Analysis of results shows that micromechanical approach is reliable technique to describe ductile fracture behavior in high strength steel weldments, including the effect of constraints and heterogeneity. It was also observed that the initiation toughness and the crack growth resistance are greatly affected by the mechanical heterogeneity of the weldment and the crack tip constraint. Additionally, the numerical values of the initiation toughness and the crack growth resistance are also affected greatly by the size of finite element. Moreover, micromechanical damage parameters could be transferred from one component to another without depending on constraint effect etc. The results also show that estimation of mechanical properties for various welded regions, especially for narrow HAZ regions, could be considered as alternative technique to the standard one, which may not be applied to estimate their mechanical properties when welded joint is transversally subjected to applied load.

Keywords: weldments, micromechanical approach, ductile fracture, mechanical heterogeneity, finite element method, constraint effect, initiation toughness, transferability.

Scientific field:

Technical science, Mechanical engineering

Narrow scientific field:

Material science, fracture mechanics

UDC number:

621.791.052:539.42(043.3)

669.14:620.172.24(043.3)

MIKROMEHANIČKA ANALIZA LOMA ZAVARENIH SPOJEVA ČELIKA POVIŠENE ČVRSTOĆE

Rezime:

Industrijska primena čelika povišene čvrstoće u elementima zavarenih konstrukcija čini neophodnim poznavanje ponašanja spojeva ovih materijala pri žilavom lomu. Stoga, procena integriteta zavarenih struktura je potrebna da bi se obezbedio potrebni nivo sigurnsti i pouzdanosti, imajući u vidu uticaj ograničenog deformisanja i heterogenosti na ponašanje pri lomu kritičnih zona spoja: zone uticaja toplote (ZUT) i metala šava (MŠ), koji često imaju nižu žilavost i višu prelaznu temperaturu. Takođe, veoma je važno da procena integriteta bude urađena realno i da ne bude previše konzervativna, kako bi se sprečilo povećanje mase strukture i obezbedilo ekonomično korišćenje materijala.

U ovoj disertaciji, mikromehanički pristup je korišćen za analizu uticaja mehaničke heterogenosti i ograničenog deformisanja na žilav lom zavarenih spojeva čelika povišene čvrstoće. Ovaj pristup je korišćen kao rešenje za problem prenosivosti parametara klasične mehanike loma. Takođe, motiv za njegovu primenu je i to što standardni parametri mehanike loma: faktor intenziteta napona, otvaranje prsline i konturni *J*-integral, ne mogu na odgovarajući način opisati odgovor materijala sa prslinom na dejstvo spoljnog opterećenja u svim uslovima, kao što su izraženo plastično tečenje (*large scale yielding*), različiti uticaji heterogenosti, obika i geometrije zavarenih konstrukcija u eksploataciji. Parametri mehanike loma, određeni laboratorijskim ispitivanjem epruveta, nisu direktno prenosivi na komponente i stoga se moraju uzeti u obzir dodatni faktori (kao što je uticaj ograničenog deformisanja). Takođe, cilj ove disertacije je određivanje mehaničkih osobina zona zavarenog spoja korišćenjem kombinovanog eksperimentalno-numeričkog postupka, što je naročito važno kod zona male širine u okviru ZUT koje su izložene opterećenju u transverzalnom pravcu.

Rad na disertaciji je podrazumevao primenu metode konačnih elemenata i eksperimentalna ispitivanja. Eksperimentalna ispitivanja su urađena na zavarenim glatkim epruvetama (uz korišćenje ARAMIS stereometrijskog mernog sistema) za određivanje mehaničkih osobina, kao i epruvetama za savijanje u tri tačke i epruvetama za zatezanje sa početnom prslinom u metalu šava i zoni uticaja toplote za analizu ponašanja pri lomu. *J-R* krive i vrednosti parametra mehanike loma koje odgovaraju početku rasta prsline

određene su eksperimentalno i numerički na epruvetama sa početnom prslinom u ZUT i MŠ. Numerička analiza elasto-plastičnih modela konačnih elemenata (2D i 3D) je urađena u programskom paketu Abaqus, a mikromehanički kompletni Gursonov model (CGM) je primenjen preko korisničkog potprograma UMAT (autor Z.L. Zhang). Ograničeno deformisanje oko vrha prsline i promena troosnosti u ligamentu su numerički analizirani na epruvetama za savijanje u tri tačke i onim za zatezanje, da bi se analizirala prenosivost mikromehaničkih parametara oštećenja sa jedne epruvete na drugu. Takođe, mikromehaničkim pristupom je određen uticaj geometrije i rezultati su upoređeni sa eksperimentalnim podacima. Najveći deo numeričkih rezultata dobijenih korišćenjem CGM modela pokazuje dobro slaganje sa eksperimentalnim rezultatima.

Analiza rezultata je pokazala da je mikromehanički pristup pouzdana tehnika za predviđanje žilavog loma u zavarenim spojevima čelika povišene čvrstoće, uključujući određivanje uticaja ograničenog deformisanja i heterogenosti. Pokazano je da mehanička heterogenost spoja i ograničeno deformisanje oko vrha prsline imaju veliki uticaj na otpornost prema nastanku i rastu prsline. Takođe, numerički određena otpornost prema nastanku i rastu prsline zavise od veličine konačnih elemenata. Štaviše, mikromehanički parametri oštećenja preneti su sa jedne na drugu komponentu, bez obzira na uticaj ograničenog deformisanja. Pokazano je da se određivanje mehaničkih osobina zona zavarenog spoja, naročito za delove ZUT male debljine, može koristiti kao alternativna tehnika standardnoj, koja se ne može primeniti za određivanje osobina zona spoja u slučaju dejstva opterećenja u transverzalnom pravcu (u odnosu na zavareni spoj).

Ključne reči: zavareni spojevi, mikromehanički pristup, žilav lom, mehanička heterogenost, metoda konačnih elemenata, uticaj ograničenog deformisanja, otpornost prema nastanku loma, prenosivost.

Naučna oblast:

Tehničke nauke, mašinstvo

Uža naučna oblast:

Inženjerstvo materijala, mehanika loma

UDK broj:

621.791.052:539.42(043.3)

669.14:620.172.24(043.3)

Contents

Nomenclature

a	crack length
a_{eff}	effective crack length
a_0	initial crack length
A	strain controlled nucleation rate
A_{A}	area fraction of inclusions
A_{i}	area of detected inclusions
A_{T}	measurement field area
B	specimen thickness
B_{e}	net thickness for a side-grooved specimen
E	Young's modulus
E'	effective Young's modulus
f	current void volume fraction
f^*	modified void volume fraction (damage function)
f_0	initial void volume fraction
f_{c}	critical void volume fraction
f_{F}	void volume fraction at final failure
f_{N}	volume fraction of void nucleating particles
f_{u}^*	ultimate void volume fraction
f_v	volume fraction of non-metallic inclusions
$\dot{f}_{\text{growth}}$	void volume fraction growth rate
$\dot{f}_{\text{nucleation}}$	void volume fraction nucleation rate
F	applied force
F_{Y}	yield load
J	J-integral
J_{i}	J-integral at crack initiation
J_{Ic}	fracture toughness based on J
$J_{0.2/\text{BL}}$	J-integral at 0.2 mm crack growth offset to the blunting line
K	stress intensity factor
K_{I}	mode-I stress intensity factor
K_{eff}	effective stress intensity factor
K_{Ic}	plane strain linear elastic fracture toughness
m	constant relating J and CTOD
M	strength mis-matching factor

n	strain hardening exponent
q_1, q_2	fitting parameters of the Gurson Tvergaard Needleman yield criterion
r	void space ratio
R	actual mean void radius
R_0	initial mean void radius
R_m	ultimate tensile strength
$R_{p0.2}$	yield strength at 0.2 % plastic strain
S	distance between the support cylinders
S_{ij}	deviatoric components of the Cauchy stress tensor
S_N	standard deviation in the Gaussian distribution of nucleation rate
t	tensile specimen thickness
T	stress triaxiality
V_V	volume fraction of detected inclusions
V_{voids}	volume of all voids in material
$\overline{V_V}$	mean value of the volume fraction
W	specimen width
W_{dc}	critical damage work

Greek symbols

ε_e	elastic strain
ε_f	fracture strain
ε_p	plastic strain
$\dot{\varepsilon}_{ij}^{p}$	component of the plastic strain rate tensor
ε_{eq}^{p}	equivalent plastic strain
$\dot{\varepsilon}_{eq}^{p}$	equivalent plastic strain rate
ε_1, ε_2, ε_3	principal strains
ε_N	mean nucleating strain
ϕ	yield function of the Gurson-Tvergaard-Needleman model
λ	mean free path between non-metallic inclusions
ν	Poisson's ratio
σ_1, σ_2, σ_3	principle stresses
σ	current flow stress of the matrix material
σ_e	effective stress
σ_{eq}	von Mises equivalent stress
σ_f	fracture stress

σ_m	mean stress
σ_{YS}	yield strength
σ_T	true stress
δ_{Ic}	crack tip opening displacement near the onset of crack extension
δ_5	crack tip opening displacement defined for a gauge length of 5 mm
Δa	crack length increment
ΔL	remote displacement
$\Delta t_{8/5}$	cooling time from 800° to 500° C

Subscripts

BM	referring to base metal
WM	referring to weld metal

Abbreviations

ASTM	American society for testing and materials
BM	base metal
CCT	center cracked tension
CGHAZ	coarse grain heat-affected zone
CGM	complete Gurson model
CMOD	crack mouth opening displacement
CT	compact tension
CTOD	crack tip opening displacement
$CTOD_i$	crack tip opening displacement at crack initiation
CTOD-δ_5	crack tip opening displacement defined for a gauge length of 5 mm
FE	finite element
FEM	finite element method
FGHAZ	fine grain heat-affected zone
GTN	Gurson-Tvergaard-Needleman
HSLA	high strength low alloyed
J-R	*J*-resistance (fracture resistance)
LEFM	linear elastic fracture mechanics
OM	over-matching
R-curve	fracture material resistance curve
SENB	single edge notched bend
SENB-HAZ	single edge notched bend specimen with pre-crack in heat-affected zone
SENB-WM	single edge notched bend specimen with pre-crack in weld metal

SSY	small scale yielding
SZD	stretch zone depth
SZW	stretch zone width
SZW_c	critical stretch zone width
TP-HAZ	tensile panel with pre-crack in heat-affected zone
TP-WM	tensile panel with pre-crack in weld metal
UM	under-matching
WM	weld metal

Chapter 1

Introduction

1.1 Introduction

The welded joint as a structural solution for joining components and assemblies is the most frequently used form in producing structures and installations, and welded joints are performed massively in pressurized equipment, railway and road vehicles, kilometers of weldments in pipelines, ships, etc. The safe operation under loading is required for these welded structures in service. Very strict safety requirements must be met when the failure of a welded structure can affect human lives. Anyhow, despite these strict requirements and high level of quality assurance, catastrophic failures of welded structures cannot be completely avoided. In many cases the crack of critical size was responsible for a failure. It has been generally recognized that crack occurrence in welded structures cannot be completely excluded and the effect of crack existence and growth has to be analyzed when structure safety is considered. Therefore, evaluation of the residual strength of cracked welded structure data for crack growth behavior in structural material and its weldments are required.

The assessment of structures without a fracture mechanics is insufficient, when considering the safety is important or over-design carries heavy weight penalties. Also, welded joints are widely used in important engineering constructions. They are often the strength of the joints controls the strength of a structure. Joints between dissimilar materials and regions of heat affected zones present particular problems due to heterogeneity of the material, lack of material fusion or weld penetration which is apt to promote the development of cracks and crack-like defects. Crack growth in welded joints is also influenced by differences in the fracture toughness and yield strength of the constituent materials. The ability to understand the interactions of these effects is therefore important for an analysis of the continued fitness-for-service of any structure.

The low fracture toughness and high defect probability of welded joints explain why standard codes require use of weld metal with strength exceeding the base metal strength, so that strength overmatching forces plastic deformation into the base metal. Undermatched weldments are recommended for high-strength low-alloy steels in order to avoid cold cracks [1]. Even in this case, the occurrence of defects or short cracks can not be completely avoided in reality and therefore adequate crack resistance properties of each part of the weld joint are required in addition to tensile strength properties for safety analysis.

The most dangerous failure mechanism is a cleavage fracture where linear elastic fracture mechanics applies. Anyhow, a sudden failure occurred by fast unstable crack propagation, is a rare event. Ductile fracture is more typical failure type with a plastic deformation and slow crack extension accompanying it. Structures such as pressure vessels and pipelines with cracks should operate under conditions in which crack propagates in a stable manner through the thickness, allowing leakage before break and minimizing the danger of brittle fracture or unstable crack propagation. Once leakage occurs, the inner pressure is reduced and catastrophic failure probably avoided.

Welded structures made of high strength low-alloyed steel are usually designed to fail in ductile manner when they are overloaded or fail by any reason. Integrity assessment of those components such as; pressure vessels and pipelines is required in order to have safe and reliable components. Therefore, several engineering procedures have been recently developed to assess their integrity. Using continuum damage mechanics in analyzing structure safety is one of these procedures. The advent of faster computers and the associated computational algorithms have greatly extended the scope of continuum damage mechanics. Accurate numerical analyses can nowadays be performed for arbitrary geometries and loading conditions. Furthermore, the ability to numerically solve complex mathematical problems has inspired extensions of the classical, linear theory with nonlinear material behavior. Under the influence of these developments, a fundamentally different type of modeling has emerged, in which fracture is considered as the ultimate consequence of a material degradation process. Instead of separately defining constitutive relations and a fracture criterion, the loss of mechanical integrity is accounted for in the material constitutive model. Crack initiation and growth then follow naturally from the standard continuum mechanics theory. This theory (called continuum damage mechanics) introduces a set of field or internal variables (damage

variables), which describe the local loss of material integrity or material stress carrying capability. A crack is represented by that part of the material domain in which the damage has become critical, i.e., where the material cannot sustain stress anymore. Redistribution of stresses results in growth of plastic deformation and damage zones in front of the crack tip or the initial critical damage zone.

Unlike fracture mechanics, one does not need to have an initial crack in the model in order to describe the crack initiation and growth processes using continuum mechanics. The ductile damage models such as those of Rousselier [2],Gurson-Tvergaard-Neeedleman (GTN) [3,4] and recently developed complete Gurson model (CGM) have been widely used for predicting load-deformation and fracture resistance behavior of different specimens and components (of widely different materials) in literature. Using these micro-mechanically based damage models to investigate fracture behavior in ductile materials has received a great deal of attention in the past few decades. These models can simulate the physical processes of void nucleation, growth and coalescence using continuum mechanics. They include the micro-mechanical effects of void nucleation, growth and coalescence of micro-voids in the constitutive equation used for description of the mechanical continuum. The advantages of a micro-mechanical damage model, compared with conventional fracture mechanics, is that the model parameters are only material not geometry-dependent. They also include the effect of large-scale deformation and plastic straining on material failure. A disadvantage is that they are computationally expensive, so it is important to develop efficient procedures.

Crack initiation and stable crack growth in ductile materials are conventionally characterized by fracture resistance curves, obtained from the standard fracture mechanics tests. However, testing of the different specimens often reveals considerable differences in these curves, due to the constraint effects [5-9]. These effects are very important even in homogeneous structures, where the fracture resistance is dependent on geometry of the structure and crack, as well as on the loading type. In welded joints (e.g. specimens notched and pre-cracked in different zones), they are much more pronounced than in homogeneous structures, having in mind the material heterogeneity in addition to the geometry constraints. Therefore, it is a known fact that the macroscopic parameters for ductile fracture, such as ductility and crack resistance curve cannot be directly transferred from one geometry to another. Thus, it is important to separate transferable parameters for ductile fracture from the parameters which describe geometry effect. For most

engineering alloys, ductile fracture often comes after the nucleation, growth and coalescence of microvoids. It is therefore natural to link materials fracture behavior to the parameters that describe the evolution of microvoids rather than the conventional global fracture parameters.

The service safety of highly loaded welded structures is strongly dependent on the integrity and fracture resistance of their welded joints. Therefore, mechanical heterogeneity of the joint is a key factor for understanding the fracture and failure of such structures under various exploitation conditions [5,6,10,11]. Above-mentioned constraints are the reason why transferring the fracture parameters from specimens to components is especially questionable in case of welded joints. One of the ways to take into account both constraints due to material mismatching and due to geometry is J-Q-M formulation [12-14], derived by extending the J-Q theory [15] of the two-parameter fracture mechanics.

Recently produced high-strength low-alloyed (HSLA) steel, examined in this study as the base metal (BM), typically exhibits large-scale deformation and plastic straining during tearing, which helps to prevent rapid unstable fracture. Such strain state (large scale yielding) is another reason why traditional J integral approach of classical fracture mechanics cannot give adequate results [16]. Having in mind all the mentioned issues, micromechanical analysis is used in this work to eliminate or decrease the dependence of fracture parameters on geometry of the structure and material heterogeneity. This approach is chosen as appropriate for fracture assessment, since it correlates the local stresses and strains with resistance to crack initiation and growth. Therefore, the constraint effects are inherent in the analysis, which is not the case in the two-parameter fracture mechanics. In case the crack is located in the middle of the weld metal (WM), not in the vicinity of the heat affected zone (HAZ), the joint can be analyzed as bimaterial, as shown through several studies [5,17-20]. However, there are situations when it is also very important to understand the behavior of HAZ during the fracture process [21-25], bearing in mind that it is often susceptible to cracks and its toughness may influence the overall fracture behavior of a welded joint. In [21], experimental tests and FEM analyses have been performed on high strength steel weldments produced using two different consumables for different mismatch levels. Almost all fracture initiation points were in the HAZ, and the probability for initiation in the base material and the weld metal was found to be rather small. Welded HSLA steel specimens with a pre-crack in the heat

affected zone were examined in [22], and it is shown that the strength mismatching of the homogeneous and heterogeneous joints caused a redirection of the crack propagation towards the low-strength region of the joint. In [23], two HSLA steels of different strength level were welded using the same consumables. Fracture deviation from HAZ into weld or base metal occurred: for the BM with higher strength, the crack propagated from HAZ to WM, while for the BM with lower strength the crack propagated from HAZ to BM. Numerical and experimental investigation of ductile tearing of the welded joint with a pre-crack in HAZ using local approach to fracture is conducted in [24]. The fracture assessment has been done using uncoupled and coupled approach, and special attention has been given to modeling of the crack growth direction (the crack deviated towards the BM). Besides the cracks initiated in HAZ (e.g. around some initial defect), it is important to take into account the possibility that the fracture path can run through HAZ even if the crack was initiated in WM or BM. Therefore, there are many cases when a welded joint should not be considered as bimaterial.

In this study, micromechanical fracture analysis of weldments made of high strength low-alloyed steel (NIOMOL 490K) has been done in order to study ductile fracture behavior of these weldments including the effect of constraints and material heterogeneity. In order to apply micromechanical models, material properties were determined for different regions in welded joint. The determination of these material properties are difficult especially for regions such as: heat affected sub-zones and weld metal due to the presence of micro- and macro-heterogeneities of the welded joint, caused by different microstructures and mechanical properties of base metal, weld metal and heat affected zone. In addition, mechanical properties should be determined in the direction of applied load for good structural integrity assessment. Thus, mechanical properties of very narrow regions such as HAZ and weld metal may not be determined by conventional methods when the welded joint is transversally subjected to applied load due to that the specimens could not be cut transversally from welded joint. Therefore, attempts were performed to determine material properties of various regions of welded joint using combination of experimental and numerical procedure, which compares experimental and numerical stress-strain distributions of tested uncracked tensile panel up to obtaining good agreement between them. The advantage of this method in comparison with conventional one is that the mechanical properties of very narrow regions such as HAZ and weld metal can be estimated in the direction of load when it is transversally applied on a welded joint.

Determined material properties were used to analyze the fracture behavior of specimens with pre-cracks in weld metal and heat affected zone. In addition, constraint effect on fracture behavior has been studied to analyze the transferability of micromechanical parameters.

Numerical work, using very detailed elastic-plastic finite element models (2D, plane strain and 3D) have been performed for welded specimens with pre-cracks in weld metal (WM) and heat affected zone (HAZ). Local damage analysis has numerically been performed also to study fracture behavior of welded specimens using recently developed micromechanical models (complete Gurson model, CGM). The CGM has been implemented into the finite element code ABAQUS through the material user subroutine UMAT, which has been developed by Z. L. Zhang [26]. Crack initiation and propagation have been determined using experiments and finite element method.

1.2 Aims and scope of the work

The main objective of this thesis is to study ductile fracture behavior of welded components made of high strength low-alloyed steel (NIOMOL 490K) using recently developed micromechanical model (CGM). Crack initiation and propagation are considered on welded specimens in order to get closer insight in complex behavior of cracked welded joints and study the effect of constraints and material heterogeneity. The following tasks are addressed in this thesis:

1- Estimation of mechanical properties transversally on welded joint for various regions using experimental-numerical procedure.
2- Heterogeneity effect on fracture behavior of welded structure.
3- Study the effect of crack position and configuration (in weld metal and heat affected zone) on crack initiation and propagation.
4- The constraint effect on the crack initiation and ductile crack growth resistance of cracked welded specimens.
5- Micromechanical modeling of crack initiation and propagation of used material (NIOMOL 490K).
6- To develop 2D and 3D finite element models of welded specimens to simulate ductile crack initiation and propagation using micromechanical model (CGM).
7- Transferability study of micromechanical damage parameters using different specimens with various crack positions.

8- Effect of material Gurson parameters on fracture behavior.
9- Verify the ability of recent micromechanical model CGM to describe the ductile fracture behavior in presence of weldment heterogeneity.

1.3 Organization of the thesis

The thesis entitled *"Micromechanical Fracture Analysis of High Strength Steel Weldments"*. The thesis is divided into introduction, covering the scope, aims and tasks of the work, theoretical chapters providing information and achievement, research chapters and conclusions. The following are the chapters of the thesis:

Chapter 1: presents the importance of local damage approach for assessment of flawed structures with the effect of heterogeneity and geometry constraints. Also, it sets the aims and the scope of work.
Chapter 2: introduction to the welding influence on microstructures and mechanical properties of weldment regions.
Chapter 3: covers information and achievement on elastic-plastic fracture mechanics, related topics for assessment of flawed weldments and the effects of constraints on fracture behavior.
Chapter 4: provides local damage analysis in structural integrity assessment in details, used micromechanical models and the effect of damage parameters on ductile fracture behavior.
Chapter 5: provides considerations that are required for elastic-plastic finite element method in fracture mechanics. This also covers the singularity of crack tip elements and applications of finite element method in local damage approach.
Chapter 6: covers experimental researches, which investigate ductile fracture behavior of weldments and their structural integrity using both conventional fracture mechanics and micromechanical approach. Moreover it consists of mechanical properties determination of welded joint regions using experimental-numerical procedure.
Chapter 7: consists of 3-D and 2-D, plane strain finite element models obtained by finite element code ABAQUS with implemented micromechanical model CGM.
Chapter 8: Analysis and discussion of numerical and experimental results.
Chapter 9: draws conclusions of carried works and recommendation for further investigation.

Chapter 2

Weldment Heterogeneity

2.1 Introduction

Fusion welding is a process that involves an input of intensive heat in short time, and this leads to melting of a filler metal and partly of a base metal. The result is a weldment that consists of a mixture obtained from base metal and filler metal (consumable). Significantly different strength and ductility levels often exist in different parts of weldments as the result of this welding process. Therefore, this mechanical heterogeneity directly affects not only the joint performance of welds but also the evaluation of the fracture toughness requirement for cracked welded structures. The overall fracture behavior of a welded joint may depend on the toughness of its most brittle part, which is generally the coarse-grained heat affected zone. However, the fracture toughness behavior of coarse-grained heat affected zone can be strongly influenced by the strength level of the neighboring weld and base metal. It has been reported that the presence of an abrupt strength gradient in the vicinity of the crack tip of commonly used Charpy-V or COD coarse grained HAZ specimens influences the deformation behavior of the crack tip [27].

In this chapter, the aim is to present literature review about weldment heterogeneity with its effect on fracture behavior.

2.2 Weldments thermal cycle

The flow of heat from the source depends on the thickness of the plate. While the flow of heat for a thin plate is two-dimensional, it is three-dimensional for a thick plate, Figure 2.1. Heat losses through the surfaces are usually negligible.

The temperature distribution field is illustrated in Figure 2.2. Note that the intense heat source and very effective heat sink of the plate being welded results in an extremely steep temperature profile.

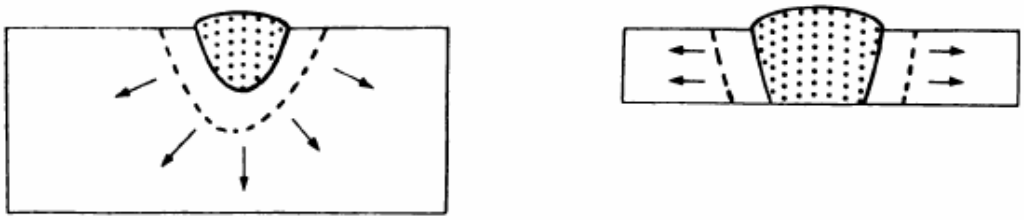

Figure 2.1 *Three and two-dimensional heat flow welding [28].*

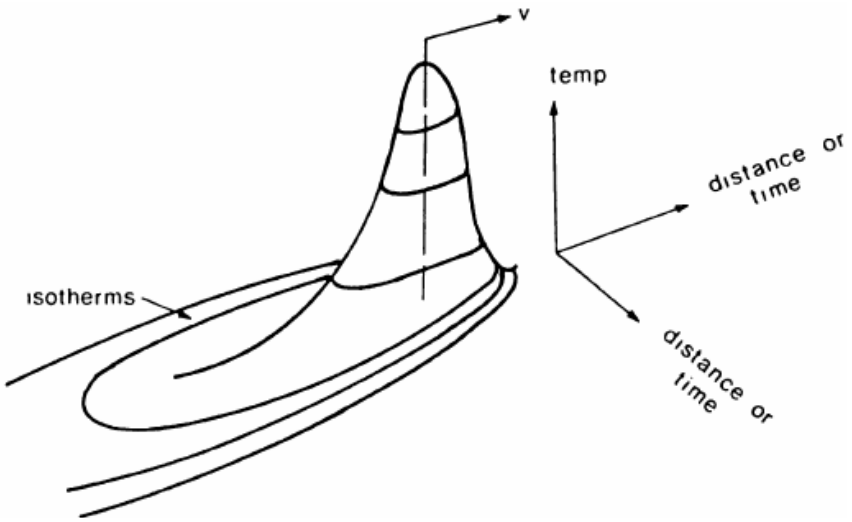

Figure 2.2 *Three-dimensional temperature distribution in arc-welding [28].*

A comparison between the welding of thick and thin plates is illustrated in Figure 2.3. The curve n-n in this figure represents the boundary between rising and falling temperature in the solid. Thus, all points to the left of n-n are in the cooling cycle, and the points to the right are in the heating cycle. Also, note the thick plates are more efficient heat sinks than thin plates. The weld thermal cycle affects the microstructure of the base metal; this is an important result having in mind that the microstructure affects the weldment strength.

It has been found experimentally that the cooling time through the range 800-500°C is constant for a given welding process, weld geometry and material $\Delta t_{8-5} = \text{const}$. The use of Δt_{8-5} as descriptive of a given weld has been adopted widely. Inagaki and Sekiguchi [30] have derived the following form of equation to predict Δt_{8-5}:

$$\Delta t_{8-5} = \frac{\left(\frac{q}{v}\right)^{1.7}}{1.11 \cdot 10^{6} \cdot \beta \cdot \left[1 + \frac{2}{\pi} \tan^{-1}\left(\frac{d-13}{3.5}\right)\right]} \tag{2.1}$$

where

$$q = \eta \cdot V \cdot I \tag{2.2}$$

β is a constant, equal 1 to 1.7

d is a plate thickness

q is a heat flux, in terms of welding voltage and current (V and I)

η is the arc efficiency, equal 0.7 to 0.85 for manual metal arc

v is welding travel speed.

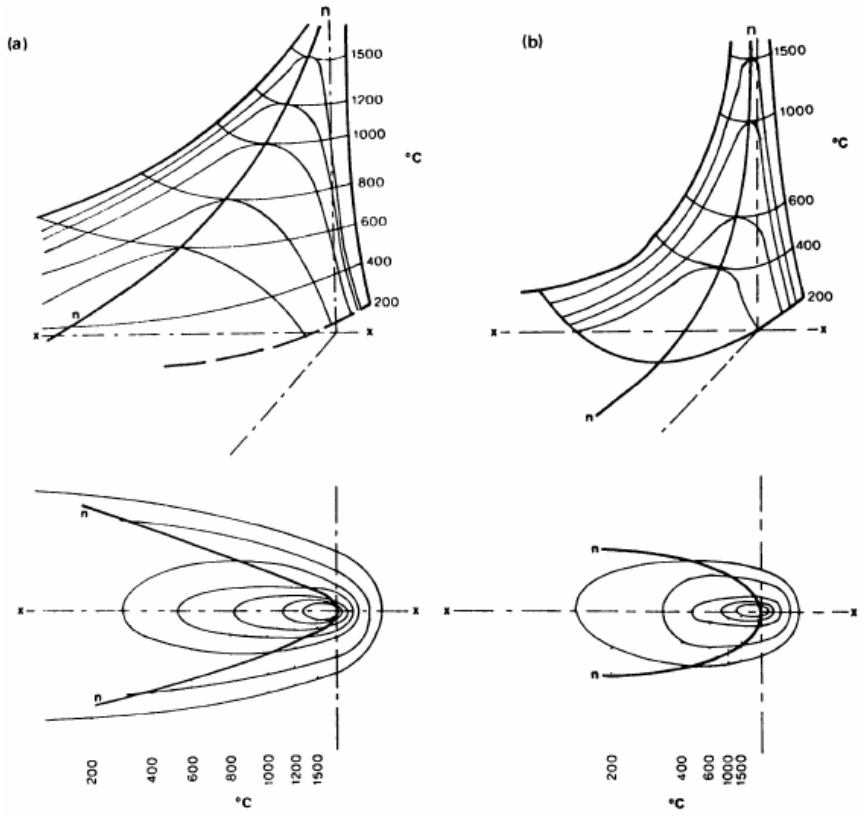

Figure 2.3 *Temperature distribution: (a) thin plates and (b) thick plates [29].*

2.3 The weld metal

Considering the welding pool and the way in which liquid metal solidifies, the shape of the melt depends on the materials thermal conductivity, welding speed and the plate

thickness. The crystal growth occurs in a direction perpendicular to the isotherms. A vector R, Figure 2.4, defines the speed of crystal growth:

$$R = v\cos\theta \tag{2.3}$$

Since the welding speed v and R have to vary depending on the position at liquids. The crystal grows fastest behind the moving heat source (θ=0°), and slowest at edge of the weld (θ=90°). In practice, since the crystal growth tends to grow along certain preferred crystallographic directions, the crystal growth vector has to be modified to the actual crystal growth speed (R'):

$$R' = R\cos\theta^{d} \tag{2.4}$$

where θ^{d} is the angle between the appreciate growth direction to the steepest temperature gradient, Figure 2.5. It is often necessary for crystal to change orientation during growth in order to continue to follow the steepest temperature gradient of the weld pool. One should notice that this occurs irrespective of welding speed.

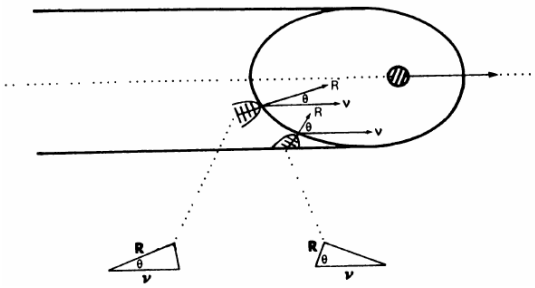

Figure 2.4 *The relation of crystal growth speed [28].*

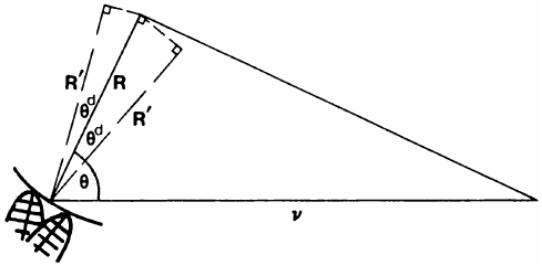

Figure 2.5 *The actual crystal growth speed [28].*

This implies that crystals growing in a certain direction are unable to maintain this direction, because the heat source is moving away, the direction of the steepest temperature gradient is effectively changing, and the solidifying crystals have to change their orientation, Figure 2.6.

Since the base metal adjacent to welding pool is locally heated up to its melting point, the grain growth occurs also in the base metal and it will the most intensive at region where temperature is highest, i.e. closest to the fusion line. The initial solidification of a weld occurs epitaxially, the weld crystal have derived from grains of the base metal. During cooling of the weld metal from its solidification temperature to the ambient temperature, phase transformations occur. Following solidification in low carbon

steel welds, the steel has the characteristic cellular-dendritic (column austentic) cast structure. As it cools below A_3 temperature, ferrite is expected to form between austentic grains. However, the continuous transformation products are a function of cooling rate. For slow cooling rate, a final structure of mixed ferrite and pearlite is obtained. For medium-slow cooling rate, the resulting microstructure is described as Widmanstätten side plates and pearlite or acicular ferrite. For medium-high cooling rate, the final structure is a periodic pearlite. For high cooling rate, the final structure is an upper bainite plus cementite or an upper bainite and retained austenite. Finally, for ultra-high cooling rate, the final microstructure is a lower bainite or lath martensite.

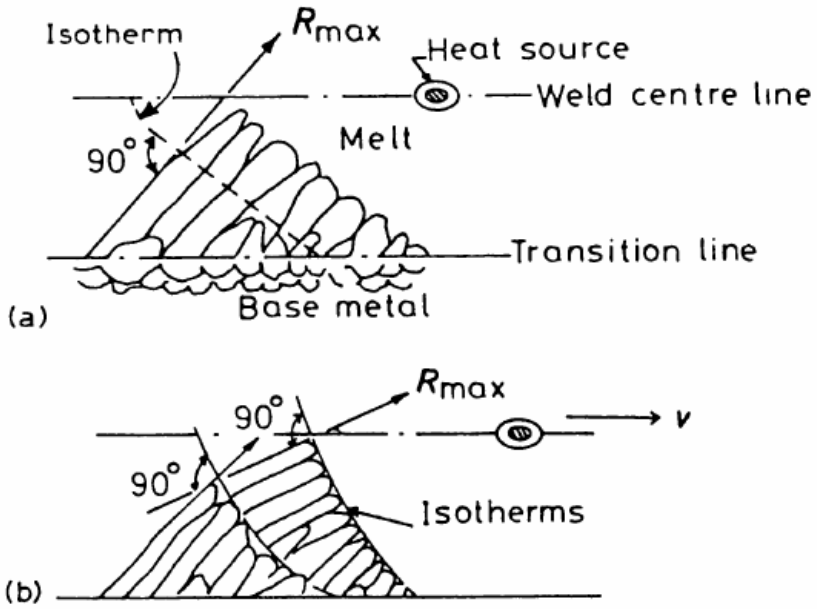

***Figure 2.6**: (a) crystal growth and (b) change crystal growth direction [28].*

2.4 The heat-affected zone

The material close to the weld is heated to its melting point and then cooled rapidly under a restraint imposed by the joint geometry. A zone from the fusion line to the unchanged base material is referred to as the heat affected zone (HAZ). This zone can be divided into number of sub–zones, each sub–zone having different microstructure and thus, different mechanical properties, Figure 2.7. Metallographic examination of C-Mn steel weldments reveals significant differences in HAZ microstructures. In single pass welds, there are four characteristic regions in the HAZ depending on the peak temperature

that the region was exposed to during the weld thermal cycle. These regions and the approximate peak temperature ranges are as follows: coarse grain (1100-1400 ºC), fine grain (900-1100 ºC), intercritical (700-900 ºC) and subcritical (< 700 ºC).

At fusion line, a narrow zone exists, usually characterized by a decrease in grain size, regardless the higher temperature due to $\gamma \rightarrow \delta$ transformation. In the grain growth zone (CGHAZ), the grain growth occurs and it will be most intensive where the temperature is highest, Figure 2.8. In the grain refined zone, the reduction of the peak temperature will limit the time for $\alpha \rightarrow \gamma$ transformation during heat and grain size remains very small.

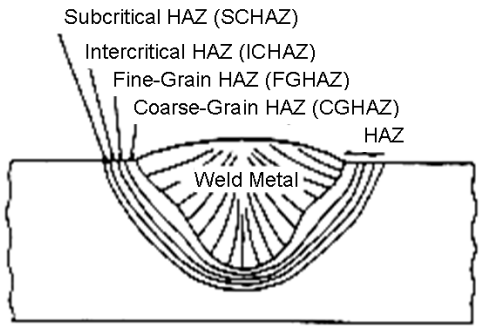

Figure 2.7 *Various sub-zones of heat affected zone [28].*

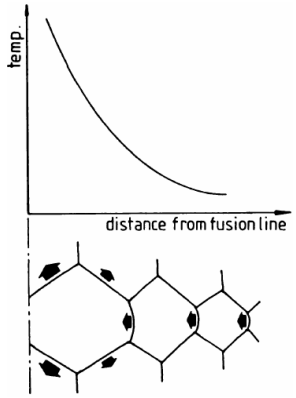

Figure 2.8 *Grain size in HAZ as a function of peak temperature and distance from the fusion line [28].*

In the partially transferred zone, the temperature range 750-900°C, pearlite in the base metal quickly austenitizes because of lower $\alpha \rightarrow \gamma$ transformation temperature and austenite is enriched in C. Thus, different microstructure may develop, depending on cooling rate Δt_{8-5}, e.g. pearlite (dark phase, upper bainite or martensite). In the zone of spheroidized carbides, the temperature range 700-750°C, lamellar pearlite degrades to spheroid particles of Fe_3C. The unchanged base material; temperatures in the range up to 650°C, is characterized by moving dislocations sweeping up interstitial such as C and N, Figure 2.9.

In general, the coarse grained region (CGHAZ), and sometimes the intercritical HAZ (ICHAZ) have the lowest toughness. In a multipass weld, parts of the CGHAZ are subjected to the same range of peak temperatures, i.e., part is melted, part reforms as CGHAZ, part is refined, and part is modified by exposures to lower temperatures. The later parts, which retain the coarse grain structure, are identified as the intercritical

CGHAZ (ICCGHAZ) and the subcritical CGHAZ (SCCGHAZ). The entire coarse grain region, which includes the unaltered plus the ICCGHAZ and the SCCGHAZ, is potentially in local brittle zone (LBZ). The potential LBZ is discontinuous and surrounded by tougher material.

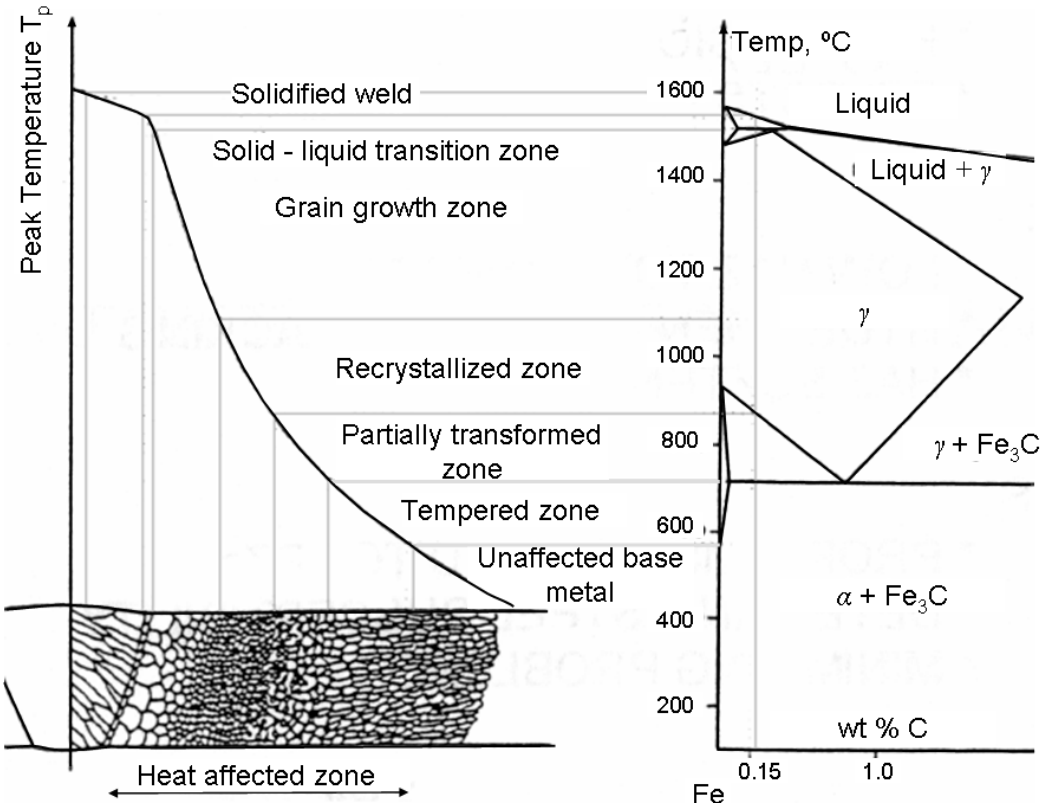

Figure 2.9 *Various sub–zones of HAZ developed during the solidification of the weld metal [28].*

2.4.1 The local brittle zones

In the weld, the occurrence of mechanical and metallurgical heterogeneity is inevitable. For high strength steels, the occurrence of the local brittle zones (LBZs) and local hard/soft zones is often observed. The formation of an LBZ depends on the microstructure in the coarse grain region. Brittle microstructures include large prior austenite grain size, upper bainite, high-carbon martensite islands, and microalloy-carbide precipitates [31]. This heterogeneity has remarkable effects in toughness and strength mismatch [32], Figure 2.10.

The existence of local brittle zones (LBZs) is one of the most important fractures controlling parameters in respect to metallurgical effects observed in HAZ. The general tendency in HAZ is:

(a) The coarse grained HAZ (CGHAZ) generally deteriorates toughness.

(b) For high strength structural steels, the content of Martensite-Austenite (M–A) constituent can be large in CGHAZ.

(c) Microcracks initiate in M–A structures or between M–A and the matrix structure.

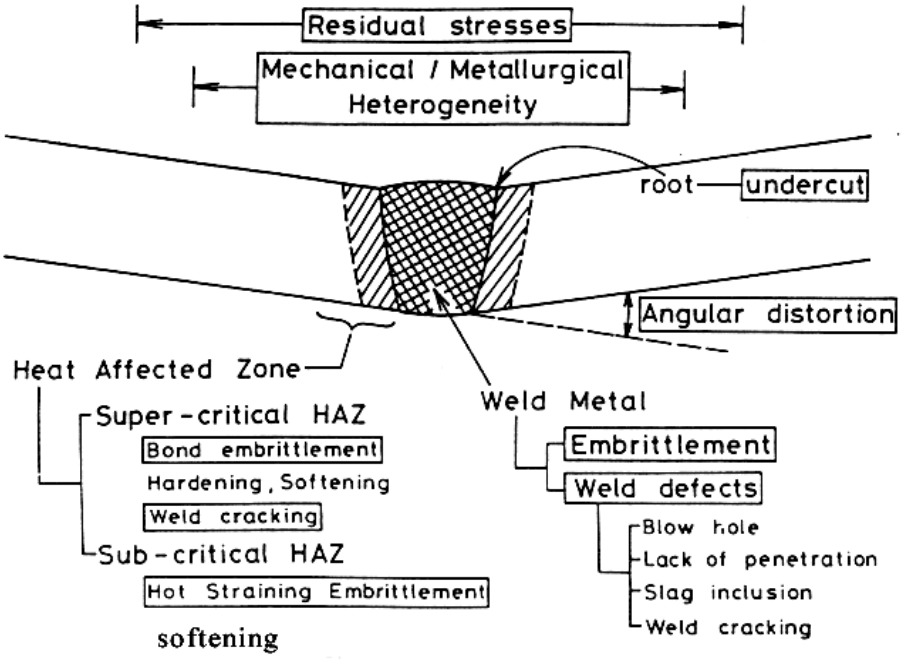

Figure 2.10 *Characteristics of welded joint [32].*

2.5 Multi-run welds

Refinements in microstructure, improvements in toughness and reductions in residual stress can all result from multi-run welding as compared to a single weld run of the same cross-section. The reasons for this are as follows [28]:

(a) The total input energy per weld run is decreased so that the amount of grain growth is accordingly reduced.

(b) That each subsequent weld thermal cycle effectively grain refines or normalizes part of the previous weld metal.

(c) Previous weld runs can provide certain preheat which tends to extend the $\Delta t_{8\text{-}5}$ cooling rate.

(d) Subsequent weld runs tend to anneal out residual stresses caused by previous runs.

The effect of a second weld run is illustrated schematically in Figure 2.11. It is seen that subsequent runs cause parts of earlier welds. i.e. weld metal and HAZ to be reheated.

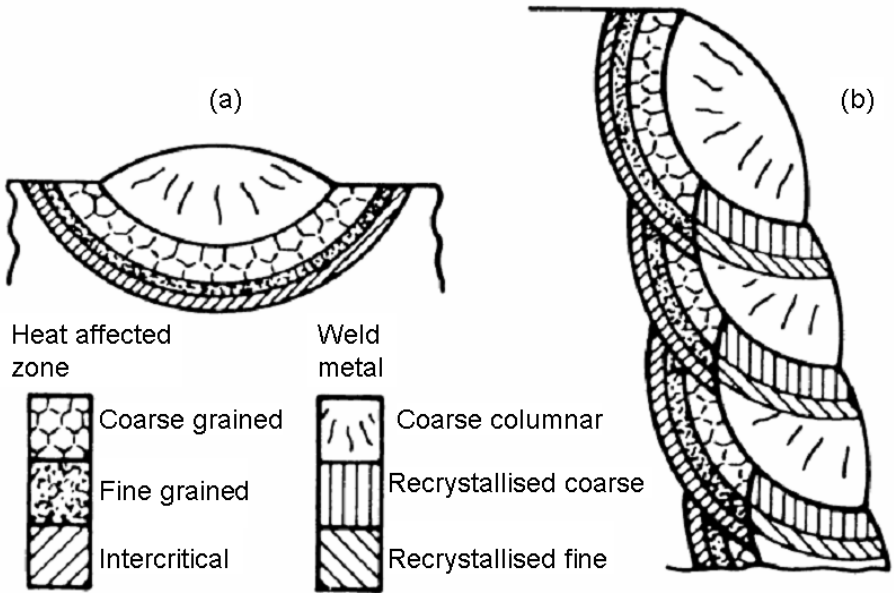

Figure 2.11 *Schematic comparison of the microstructure: (a) single run and (b) multi-run welds [28].*

2.6 Effect of welded joint mis-matching on deformation patterns

Heterogeneity has an important role in the behavior of welded joint, particularly should high stresses causing local plastic strain. The weld metal is commonly produced with the yield strength (σ_{YW}) higher than that of the base metal (σ_{YB}); this is designated as overmatched (OM) welded joint with the mismatch factor M > 1. The mis-match factor is defined as follows:

$$M = \frac{\sigma_{YW}}{\sigma_{YB}} \tag{2.5}$$

with σ_{YW} being the yield strength of the weld metal and that σ_{YB} of the base material, the strain hardening exponents of the two materials, the component and weld geometry and dimensions and the crack size, shape and location with respect to the weld, various deformation patterns may develop such as illustrated in Figure 2.12 [33]. Sometimes an

existing crack is shielded and a new crack initiates away from the tip, e.g., at the fusion line.

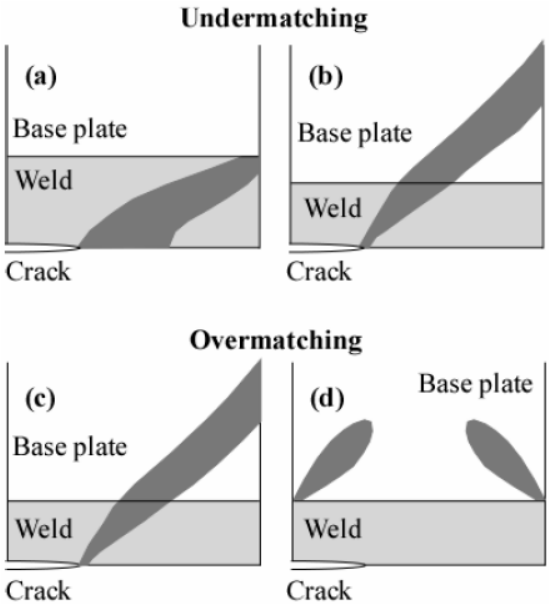

Figure 2.12 *Yield patterns for strength mismatched plates [33]: (a) undermatching, deformation confined to weld metal, (b) undermatching, deformation penetrating to the base plate, (c) overmatching, deformation penetrating to the base plate, and (d) overmatching, base plate deformation.*

The mismatch yield pattern affects the overall deformation behavior of the component which is different from both the base material and the weld material components.

Even in the case of generally accepted approach to design with overmatched weldments, a heat-affected zone (HAZ) of heterogeneous microstructure with possible regions prone to brittle fracture and non-uniform properties can be a weak point because its deformation can be constrained and the plane strain conditions can prevail [34]. However, overmatching reduces the strain in the weld metal as compared to the base plate, thus leading to a shielding effect. On the other hand, a lower strength of weld metal, i.e. the undermatching ($M < 1$), concentrates strains in the weld metal. However, the increase use of high strength steels causes a tendency towards undermatching (UM), Figure 2.13, because the increase in weld metal strength may cause concern with respect to weld metal toughness. Besides that, undermatching weldments may occur unintentionally. In addition, the situation becomes more complex when an undermatching effect is used to prevent cold cracking occurrence in weld joints of high strength steels of yield strength above 700 MPa. In that case plastic strains are localized in the weld metal

until its strain hardening capacity is partly or fully exhausted, and only then the base metal can start to yield.

According to the investigation on different mismatching values and a variety of crack locations, the even–matched welded joint is the most desirable for optimum welded joint performance. Because, the undermatching decrease the fracture resistance of the weld due to the increase of constraint and the overmatching reduces the fracture resistance initiation of the HAZ [35].

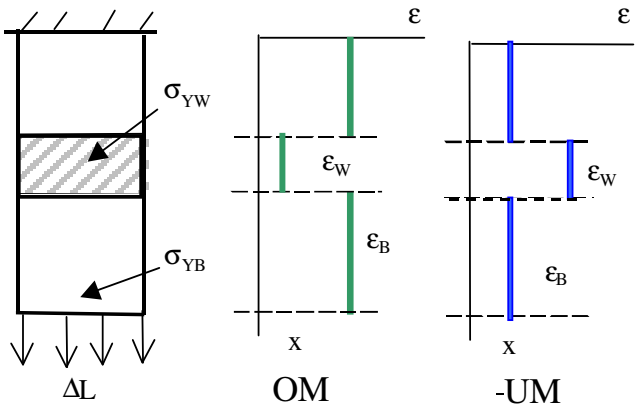

Figure 2.13 *Effect of strength mis-match on the welded joint strain distribution [36].*

2.7 The effect of mechanical heterogeneity on fracture behavior

The effect of mechanical heterogeneity of a weldment on fracture toughness features and crack growth resistance was studied in [27,37,38]. J. Zhang et al. [37] were investigated this effect on fracture toughness features and crack growth resistance of a base metal using various types of welded notched SENB specimens at different positions shown in Figure 2.14. The material tested was 8 mm thick pipe line steel plate of API-X52. They are concluded that the crack initiation toughness and crack growth resistance of base metal near the weld metal zone are greatly affected by the mechanical heterogeneity of the weldment. It is also found that the initiation toughness (δ_{Ic}) and crack growth resistance ($d\delta/da$) decreased as the distance from the fusion boundary to the crack tip increases as shown in Figure 2.15 and Figure 2.16. It is obvious that the tendency of the effect of mechanical heterogeneity is the same on both the initiation toughness and crack growth resistance, but the extent of effect is larger on crack growth resistance than on the initiation toughness.

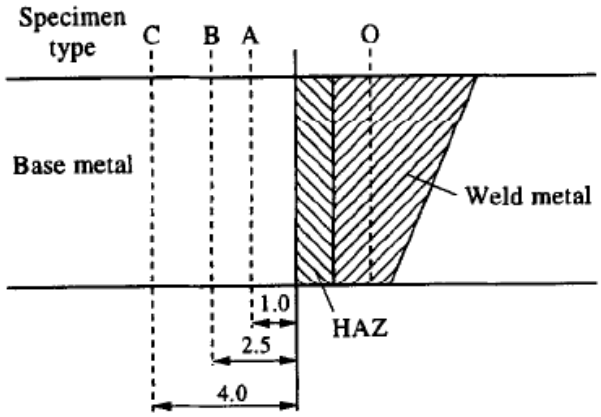

Figure 2.14 *Crack location in specimens [37].*

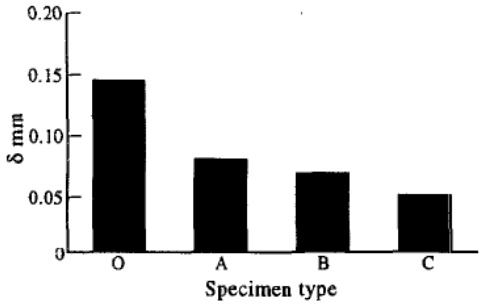

Figure 2.15 *The initiation toughness and specimen type [37].*

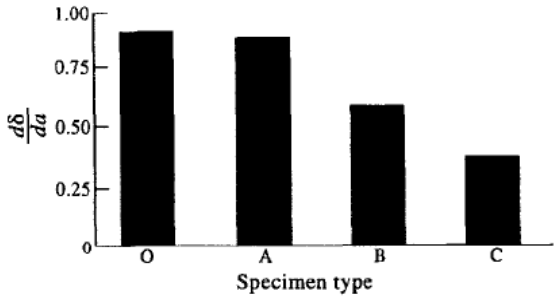

Figure 2.16 *The crack growth and specimen type [37].*

Chapter 3

Elastic – Plastic Fracture Mechanics

3.1 Introduction

Linear elastic fracture mechanics (LEFM) is valid only as long as nonlinear material deformation in confined to a small region surrounding the crack tip. When the fracture response is ductile and the material capable of considerable plastic deformation, the LEFM provides conservative fracture analysis, with net result that designs are penalized by not taking advantage of the material full load carrying capabilities.

Elastic-plastic fracture mechanics applies to materials that exhibit time-independent, nonlinear behavior (i.e., plastic deformation). Two elastic-plastic parameters are introduced as fracture criteria: the crack-tip-opening displacement (CTOD) and the *J* contour integral. Both parameters describe crack-tip conditions in elastic-plastic materials. Critical values of CTOD or *J* give nearly size-independent measures of fracture toughness, even for relatively large amounts of crack-tip plasticity.

Fracture analysis in the elastic-plastic regime involves a number of complications not present in the elastic regime. Foremost are the inherent non-linearity in the material deformation and large geometry changes. A further complication is a significant amount of crack tip blunting prior to initiation and stable crack extension prior to final fracture.

Most of existing fracture mechanics assessment procedures are strictly applicable to cracks in homogeneous structures, not taking into account heterogeneity of any kind, including weldment heterogeneity. On the other hand, it is recognized that welded structures are always prone to cracking in welded joints due to inherent metallurgical or geometrical defects.

In this chapter, literature review about elastic-plastic fracture mechanics parameters, achievement on elastic-plastic fracture mechanics, related topics for assessment of flawed weldments and the effects of constraints on fracture behavior are presented.

3.2 State of stress at a crack tip

A stress concentration causes a change in the state of stress; even if the stress is uniaxial throughout the reminder of the body, the state of stress in the area of the notch will be at least biaxial, Figure 3.1. At the free surface where no external loads are acting the state of stress will be plane (there are no stress on a free surface). Since the free surface carries no shear either, it is a principal plane with a principal stress equal to zero, Figure 3.2.

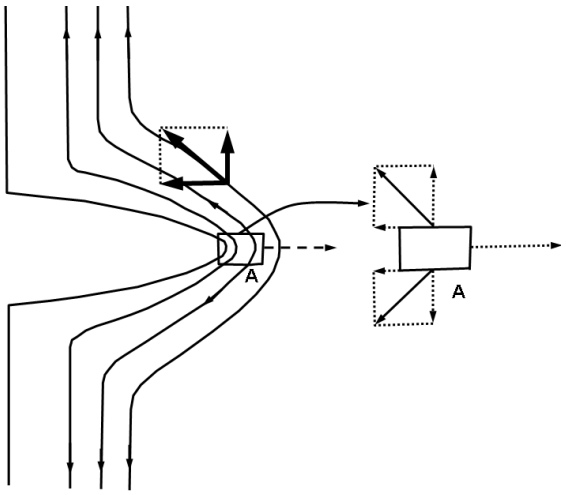

Figure 3.1 *State of stress in the area of the notch (load flow lines) [39].*

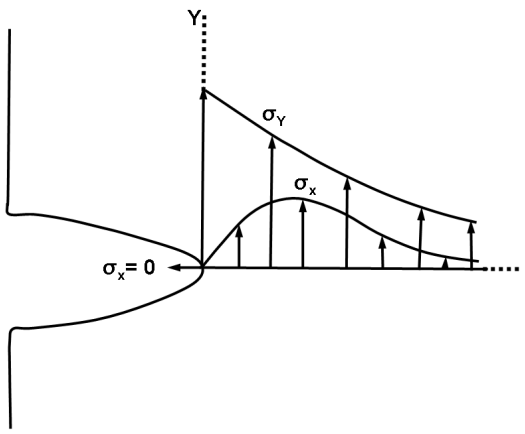

Figure 3.2 *Stress free notch surfaces [39].*

Since the surface is a principal plane, it follows that the stresses σ_x, σ_y ($\sigma_z = 0$) at the notch root in the plane of the notch are the principal stresses σ_1 and σ_2. Due to the stress concentration the local values of σ_1 and σ_2 are very high and so are the strains ε_1 and ε_2. According to Hooke's law, this will cause a strain in z direction, given by (assuming that the stress $\sigma_z = 0$):

$$\varepsilon_z = -\nu\frac{\sigma_x}{E} - \nu\frac{\sigma_y}{E} \tag{3.1}$$

This negative strain indicates a thinning of the plate. However, the stress is high only in the vicinity of the notch. Further away σ_x vanishes and σ_y is much lower, and ε_z would become very small, so $\varepsilon_z = 0$ along the notched face, Figure 3.2. It appears that only a small amount of material at the notch root is under influence of large ε_z. Assuming this material is a cylinder, as shown in Figure 3.3, it can not let large ε_z to take place, because the surrounding material will let not contraction to occur, except at the plate face. The prevented contraction developed a tensile stress in the cylinder. Assume this contraction is prevented completely, then $\varepsilon_z = 0$ (plane strain).

$$\varepsilon_z = \frac{\sigma_z}{E} - \nu\frac{\sigma_x}{E} - \nu\frac{\sigma_y}{E} = 0 \tag{3.2}$$

$$\sigma_z = \nu(\sigma_x + \sigma_y) \approx 0.3(\sigma_x + \sigma_y) \tag{3.3}$$

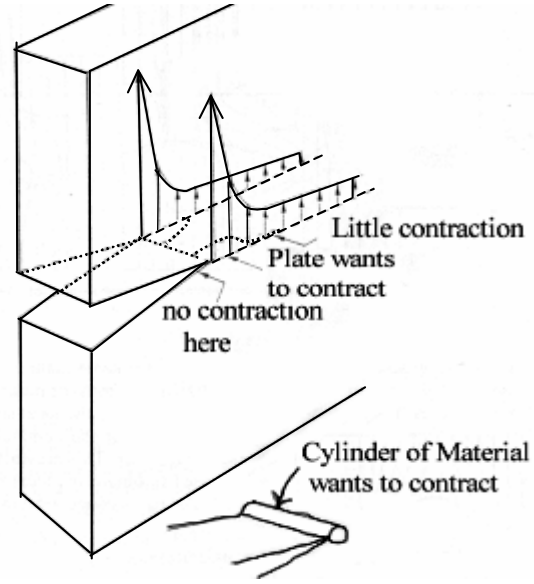

Figure 3.3 *Contraction at notch [39].*

At the free surface this stress can not exist, but it builds rapidly, going inward. Due to the absence of σ_z at the surface, ε_z occurs there, so that a small dimple develops at the surface. For a thin plate, the material wanting to undergo contraction is short and relatively thick. Contraction can occur freely in accordance with Equation (3.1). The stress in the thickness direction will be zero $\sigma_z = 0$ (plane stress). In cases between plane strain and plane stress, there will be some, but not the complete constraint.

The stress required for plastic deformation depends strongly upon the state of stress. In plane stress, yielding occurs when the highest principal stress is approximately equal to yield strength, but much higher stresses are required in the case of triaxial state of stress (for plane strain is approximately equal to 3 times yield strength). Thus a plane strain condition is more severe and can easily lead to brittle fracture. If the notch is blunt, the stress $\sigma_x (\sigma_2)$ can not exist at the notch root. Although there could exist $\sigma_z (\sigma_3)$, the state of stress would still be plane stress. Hence, at the root of notch the stress would be limited to yield strength. Furthermore, σ_x will exist inward the crack tip, Figure 3.2; in thick plate with the constraint, the state of stress will be then triaxial and possibly plane strain. Further inward therefore the stress might reach as high as 3 times yield strength, Figure 3.4. Away from the notch there is again a uniaxial state of stress, so that the stress again will be limited to the yield strength. Whether there is a plane stress or a plane strain at the notch, the final stress distribution will be about the same, apart from a small area where the stress might reach 3 times the yield strength.

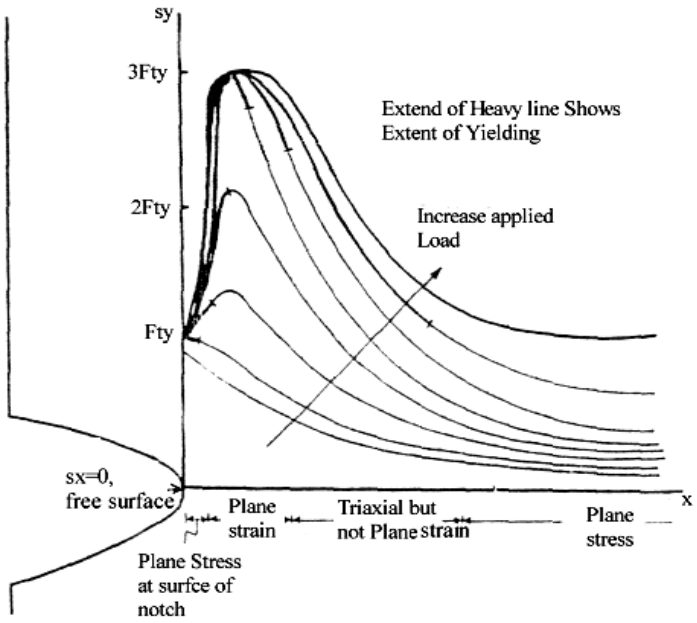

Figure 3.4 *Progress of yield at blunt notch [39].*

At the high stress, failure can occur by plastic collapse, which is always followed by ductile fracture. However, there are cases where fracture will occur before the plastic collapse has taken a place. Such a case is when the stress at the crack tip becomes too high for material to bear, or when the stress intensity factor *K* becomes too high. How

high this stress intensity factor should be depends upon the material; it must be determined by testing.

3.3 Path independence of the *J*–integral

Rice [40] originally has developed *J* as a path independent contour integral:

$$J = \oint_{\Gamma} W dy - \sigma_{ij} n_i \frac{\partial u_i}{\partial x_1} ds \tag{3.4}$$

Where,

W	is strain energy density.
σ_{ij}	is components of stress tensor.
u_i	is displacement vector components.
x_1	is the direction parallel to the crack

Path independence of *J* permits evaluation over a contour remote from the crack tip. Thus, path independence enables easy evaluation of *J* both numerically and experimentally, along the suitable path, Figure 3.5.

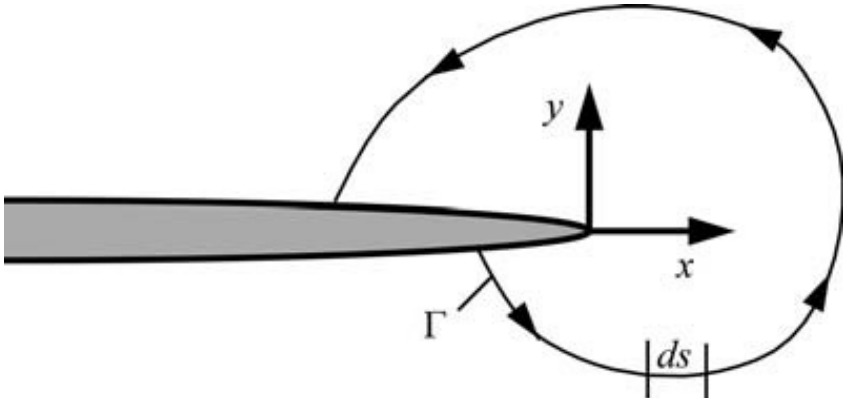

Figure 3.5 *Arbitrary contour around the tip of a crack.*

Rice has shown that *J*-integral is path independent if necessary conditions are fulfilled. This is required for its calculation, because its value is the same for the conditions close to the crack tip, for contours outside plastic zone as well as for path along specimen sides.

3.3.1 3-D *J*-integral

J(s) is a 3-D *J*-integral, J_C is a line integral over remote contour and J_A is an area integral evaluated over the planar surface enclosed by the contour, Figure 3.6.

$$J(s) = J_C + J_A \tag{3.5}$$

$$J_C = \int_r \left(W^{ep} n_1 - \sigma_{ij} n_i \frac{\partial u_i}{\partial x_1} \right) dr \tag{3.6}$$

$$J_A = -\int_A \left[\frac{\partial W^{ep}}{\partial x_1} - \sigma_{ij} \frac{\partial E_{ij}^{ep}}{\partial x_1} + \frac{\partial}{\partial x_3} \left(\sigma_{i3} \frac{\partial u_i}{\partial x_1} \right) \right] dA \tag{3.7}$$

Where *W* is the stress-work density through elastic and plastic strain, superscript *e* and *p* denote elastic and plastic strains, respectively.

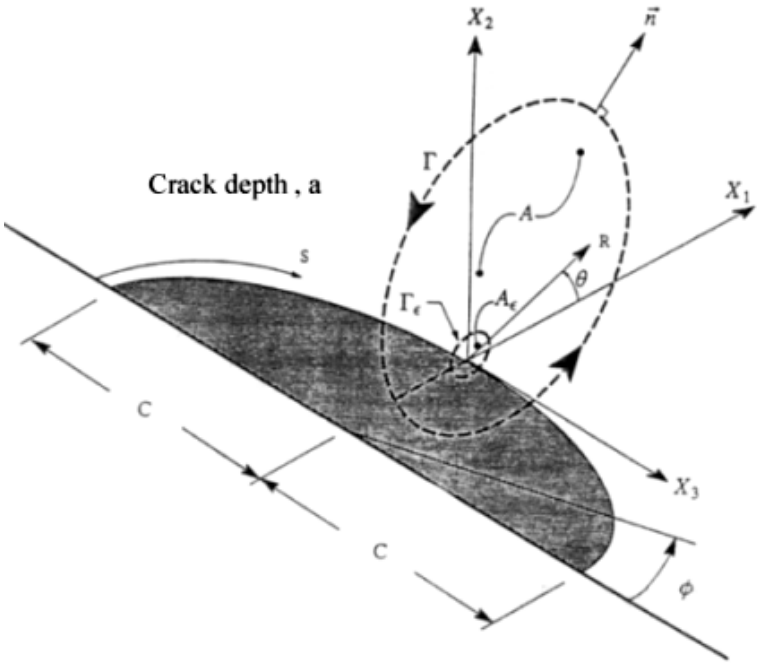

Figure 3.6 *Crack front coordinate system and contour-area J evaluation [41].*

3.3.2 *J*-integral for bi-material

A simple solution based on the homogeneous solutions and a degree of mismatch characterizes the stress and strain field around the crack tip by *J*-integral, Figure 3.7. The

different intensity parameters govern the local field in each material. Soft material experiences higher deformation than the homogeneous material, while hard material experiences lower deformation. Since the interface is parallel to the crack plane, the two contour integral are related to J by:

$$J = I_H + I_S \tag{3.8}$$

$$I_H(r) = \int_{-\pi}^{0} r\left(W\left[\varepsilon\ (r,\theta)\right]\cos\theta - t_i(r,\theta)\frac{\partial u_i}{\partial x_1}\right) d\theta \tag{3.9}$$

$$I_S(r) = \int_{0}^{\pi} r\left(W\left[\varepsilon\ (r,\theta)\right]\cos\theta - t_i(r,\theta)\frac{\partial u_i}{\partial x_1}\right) d\theta \tag{3.10}$$

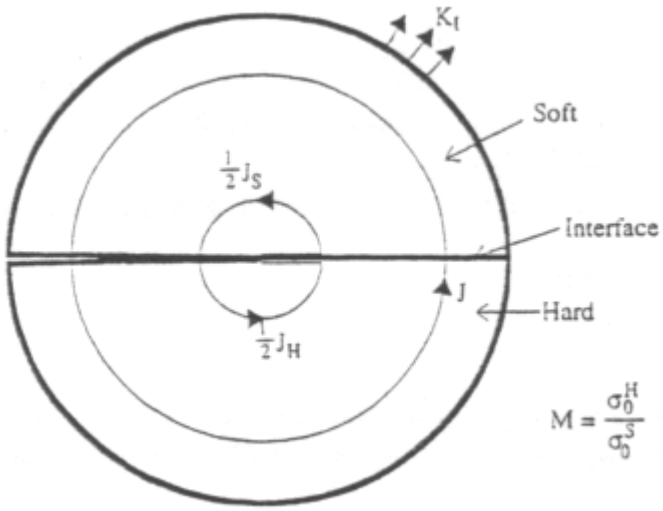

Figure 3.7 *Definition of contour integral for mismatched specimen [42].*

3.3.3 *J*-controlled fracture

J-controlled fracture corresponds to situations where J completely characterizes crack-tip conditions. In such cases, there is a unique relationship between J and crack tip opening displacement (CTOD); thus *J*-controlled fracture implies CTOD-controlled fracture, and vice versa. Just as there are limits to LEFM, fracture mechanics analyses based on J and CTOD become suspect when there is excessive plasticity or significant crack growth. In such cases, fracture toughness and the *J*-CTOD relationship depend on the size and geometry of the structure or test specimen [43].

The required conditions for *J*-controlled fracture are discussed below for fracture initiation from a stationary crack and stable crack growth.

3.3.3.1 Stationary cracks

The effect of plasticity on the crack tip stresses is shown in Figure 3.8; (σ_{yy}) is plotted against the normalized distance from the crack tip. The characteristic length scale *L* corresponds to the size of the structure; *L* could represent the uncracked ligament length. Three cases are shown in Figure 3.8 [43]:

(a) The small-scale yielding

The small-scale yielding, where both *K* and *J* characterize crack-tip condition, is shown in Figure 3.8(a). At a short distance from the crack tip, relative to *L*, the stress is proportional to $1/\sqrt{r}$; this area called the *K-dominated region*. In small-scale yielding, *K* uniquely characterizes crack-tip conditions, despite the fact that the $1/\sqrt{r}$ singularity does not exist all the way to the crack tip. Similarly, *J* uniquely characterizes crack-tip conditions even though the deformation plasticity and small strain assumptions are invalid within the finite strain region.

(b) Elastic-plastic conditions

The elastic-plastic conditions, where *J* is still approximately valid, but there is no longer a *K* field, is illustrated in Figure 3.8(b). As the plastic zone increases in size (relative to *L*), the *K*-dominated zone disappears, but the *J*-dominated zone persists in some geometries. Thus although *K* has no meaning in this case, the *J* integral is still an appropriate fracture criterion.

(c) Large-scale yielding

Large-scale yielding (Figure 3.8(c)), the size of the finite strain becomes significant relative to *L*, and there is no longer a region uniquely characterized by *J*. Single-parameter fracture mechanics is invalid in large-scale yielding, and critical *J* values exhibit a size and geometry dependence.

3.3.3.2 J-controlled crack growth

J-controlled conditions exist at the tip of a stationary crack provided the large strain region is small compared to the in-plane dimensions of the cracked body. Stable crack

growth, however, introduces another length dimension, i.e, the change in the crack length from its original value. Thus *J* may not characterize crack-tip conditions when the crack growth is significant compared to the in-plane dimensions.

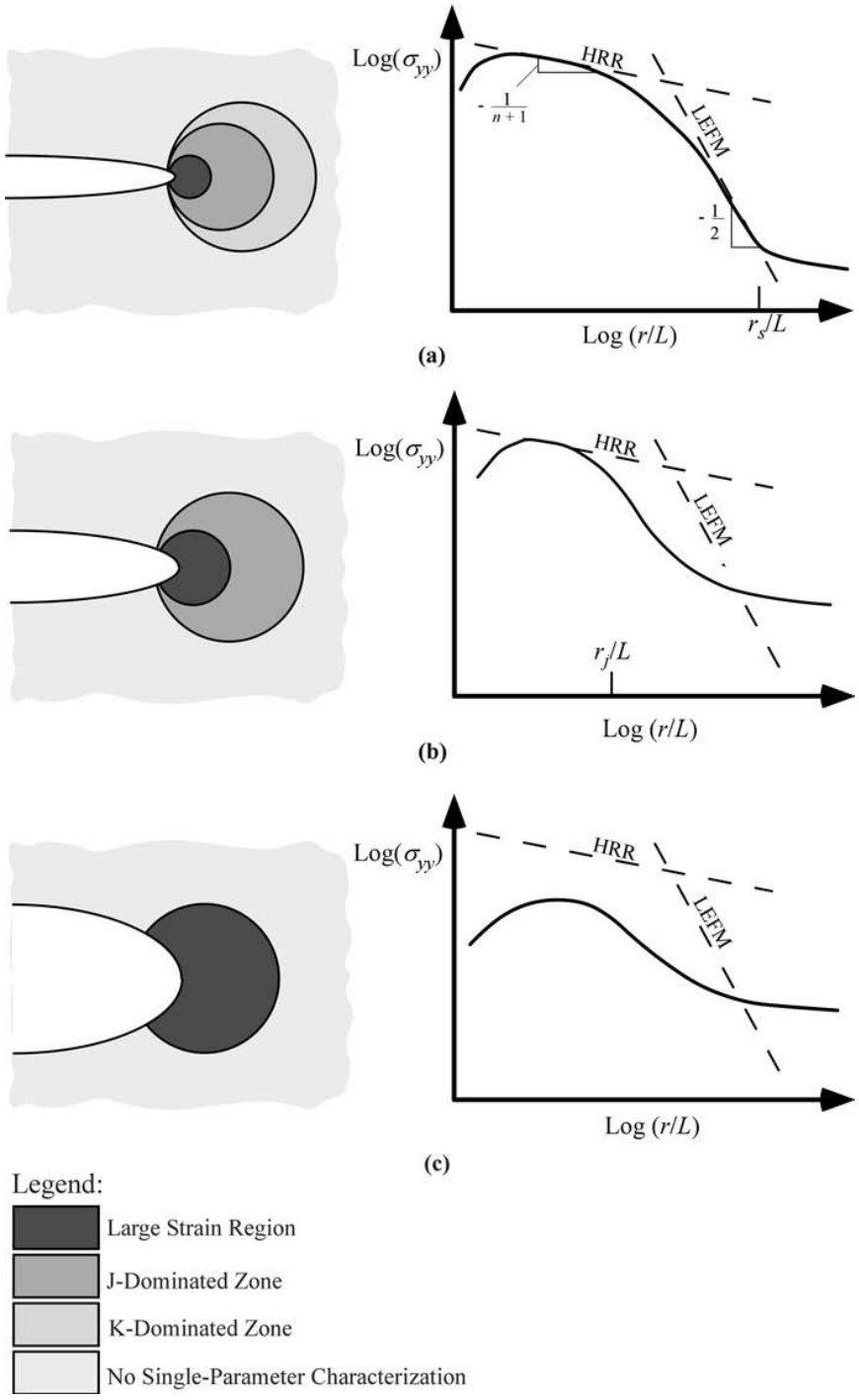

Figure 3.8 *Effect of plasticity on the crack-tip stress fields: (a) small-scale yielding, (b) elastic-plastic conditions, and (c) large-scale yielding [43].*

Crack growth under *J*-controlled conditions is illustrated in Figure 3.9. The material behind the growing crack tip has unloaded elastically. The material in the unloading region of Figure 3.9 obviously violates the assumptions of deformation plasticity. The material directly in front of the crack also violates the single-parameter assumption because the loading is highly nonproportional, i.e., the various stress components increase at different rates and some components actually decrease. In order for the crack growth to be *J* controlled, the elastic unloading and nonproportional plastic loading regions must be embedded within a zone of *J* dominance. The crack never grows out of the *J*-dominated zone as long as all the specimen boundaries are remote from the crack tip and plastic zone [43].

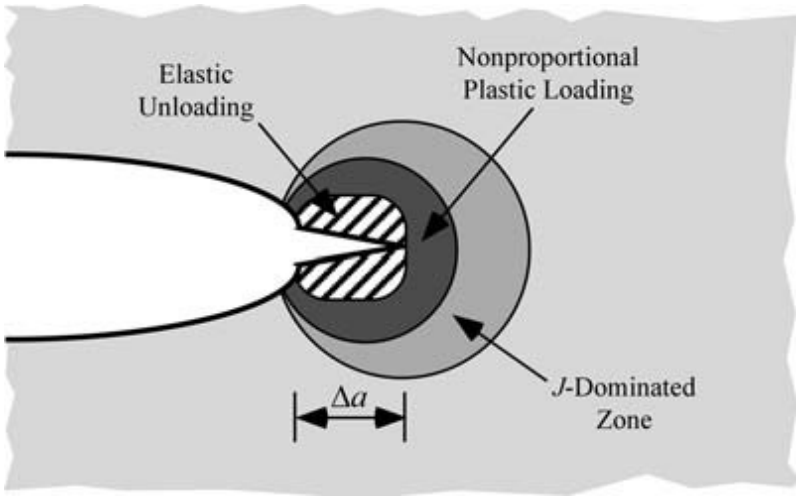

Figure 3.9 *J-controlled crack growth [43].*

3.4 Crack-tip-opening displacement (CTOD or δ)

While examining fractured test specimens, Wells noticed that the crack faces had moved apart prior to fracture; plastic deformation had blunted an initially sharp crack, as illustrated in Figure 3.10. The degree of crack blunting increased in proportion to the toughness of the material. This observation led wells to propose the opening at the crack tip as a measure of fracture toughness [43].

The strip-yield model provides definition for CTOD. In this model, the plastic zone was modeled by yield magnitude closure stresses. The size of the strip-yield zone was defined by the requirement of finite stresses at the crack tip. The CTOD can be defined as the crack-opening displacement at the end of the strip-yield zone, as Figure 3.11

illustrates. According to this definition, CTOD in a through crack in an infinite plate subject to a remote tensile stress (Figure 3.12) is given by [43]:

$$\delta = \frac{8\sigma_y a}{\pi E} \ln \sec\left(\frac{\pi}{2}\frac{\sigma}{\sigma_y}\right) \tag{3.11}$$

Therefore, as $\sigma/\sigma_y \to 0$,

$$\delta = \frac{K_I^2}{\sigma_y E} = \frac{J}{\sigma_y} \tag{3.12}$$

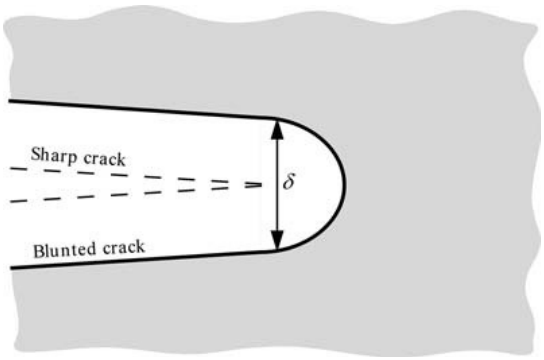

Figure 3.10 *Crack tip opening displacement (CTOD). An initially sharp crack blunts with plastic deformation, resulting in a finite displacement (δ) at the crack tip [43].*

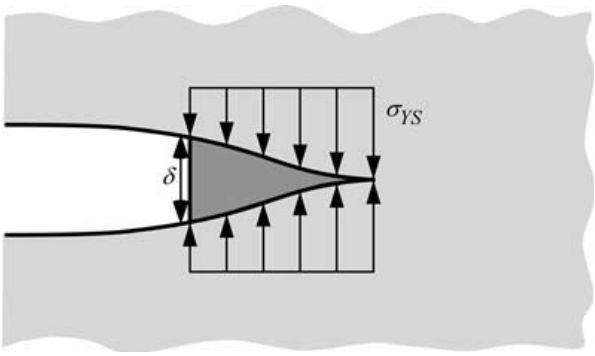

Figure 3.11 *Estimation of CTOD from the strip-yield model [43].*

The strip-yield model assumes plane stress conditions and a nonhardening material. The actual relationship between CTOD and K_I and J depends on stress state and strain hardening. The more general form of this relationship can be expressed as follows:

$$\delta = \frac{K_I^2}{m\sigma_y E'} = \frac{J}{m\sigma_y} \tag{3.13}$$

where m is a dimensionless constant that is approximately 1.0 for plane stress and 2.6 for plane strain [34], and E' is the effective Young's modulus which is defined as follows:

$$E' = E \qquad \text{for plane stress} \tag{3.14a}$$

$$E' = \frac{E}{1-\nu^2} \qquad \text{for plane strain} \tag{3.14b}$$

There are a number of alternative definitions for CTOD. The two most common definitions, which are illustrated in Figure 3.13, are the displacement at the original crack

tip and the 90º intercept. The latter definition was suggested by Rice [40] and in commonly used to infer CTOD in finite element measurements. These two definitions are equivalent if the crack blunts in a semicircle.

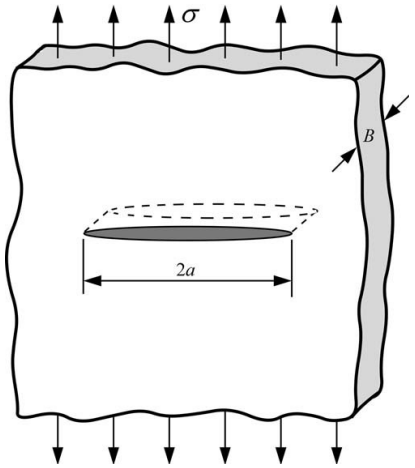

Figure 3.12 *A through-thickness crack in an infinitely wide plate subjected to a remote tensile stress [43].*

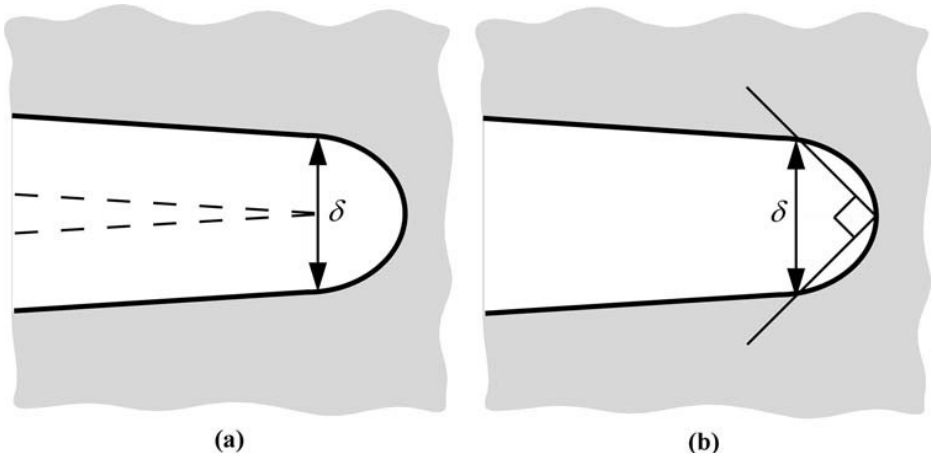

Figure 3.13 *Alternative definitions of CTOD: (a) displacement at the original crack tip and (b) displacement at the intersection of a 90º vertex with the crack flanks [40].*

GKSS has developed a method to measure directly CTOD [44]. The measured value is designated as CTOD-δ_5 or δ_5. Unlike the *J*-integral, δ_5 offers the possibility for determining the crack driving force (CDF) in a direct way by measuring the relative displacement of two gauge points which are located 5 mm apart on a straight line going through the original precrack tip as shown in Figure 3.14. The parameter is determined at the plate surface(s) which might be a problem for heavy structures but not for thin sheets since plane stress conditions usually prevail across the thickness. In addition, due to the location of the gauge points, each 2.5 mm apart from the original crack tip, the δ_5

effectively averages the displacement through the wall thickness [45]. The δ_5 parameter has been shown to be adequate for large amounts of crack extension [46] which makes it particularly suited for thin-walled geometries.

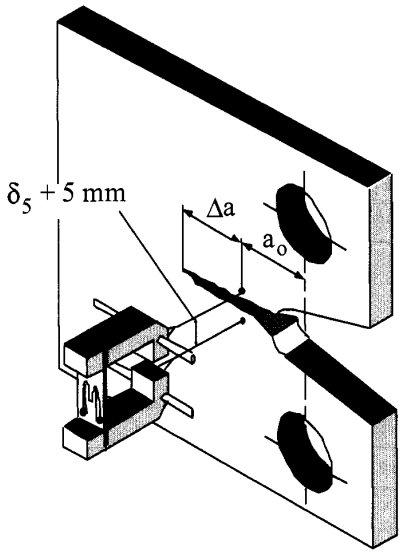

Figure 3.14 *Definition of CTOD- δ_5 [45].*

3.5 Evaluation of initiation fracture toughness J_i

Initiation fracture toughness is defined as a property which describes the ability of a material containing a crack to resist fracture. Several definitions are available to evaluate crack initiation fracture toughness. Among these J_i based on critical stretch zone width SZW_c is getting considered as geometry independent material property [47]. Stretch zone would have two components: stretch zone width (SZW) and stretch zone depth (SZD) (Figure 3.15). Both SZW and SZD are closely related to fracture toughness. However, there is no agreement on which of these stretch zone dimensions should be used for determining initiation fracture toughness. Conventionally, 45° line methods is most commonly used for determining CTOD and ½ CTOD is numerically taken as SZW with the assumption of semicircular blunting of the crack tip (Figure 3.15). The J_i can be determined either using SZW_c with J material resistance curve as shown in Figure 3.16 or using Equation (3.13).

3.6 Crack-growth resistance

Many materials with high toughness do not fail catastrophically at a particular value of J or CTOD. Rather, these materials display a rising R curve, where J and CTOD

increase with crack growth. In metals, a rising *R* curve is normally associated with the growth and coalescence of microvoids. Figure 3.16 schematically illustrates a typical *J* resistance curve for a ductile material [43].

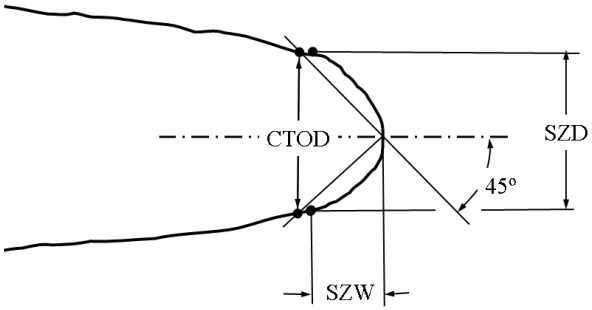

Figure 3.15 *Blunting of initial crack with stretch zones.*

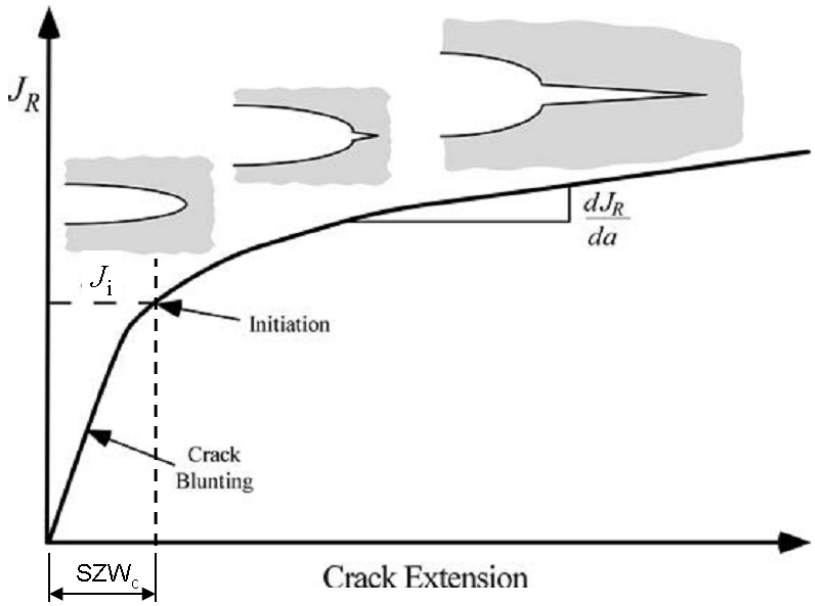

Figure 3.16 *Schematic J resistance curve for a ductile material [43].*

3.7 Crack-tip plasticity

Linear elastic fracture mechanics is related to the condition that the size of the plastic zone around the crack tip is small compared to *K*-dominant region. For the ideally elastic mode I opening stress distribution in the crack plane (θ=0) and in the *K*-dominant region is:

$$\sigma_{yy} = \frac{K_I}{\sqrt{2\pi r}} \tag{3.15}$$

The elastic-plastic stress distributions are shown in Figure 3.17. Identifying the point where $\sigma_{yy} = \sigma_{YS}$ (yielding), this yielding causes the elastic load over the region $0 < r < r_y$ in the crack plane to be uniformly distributed over the length r_p:

$$r_y = \frac{1}{2\pi}\left(\frac{K_I}{\sigma_{YS}}\right)^2 \tag{3.16}$$

$$\int_0^{r_y} \sigma_{yy} dr = \sigma_{YS} r_p \tag{3.17}$$

$$r_p = 2r_y = \frac{1}{\pi}\left(\frac{K_I}{\sigma_{YS}}\right)^2 \quad \text{(plane stress)} \tag{3.18}$$

$$r_p = 2r_y = \frac{1}{3\pi}\left(\frac{K_I}{\sigma_{YS}}\right)^2 \quad \text{(plane strain)} \tag{3.19}$$

The Equation (3.18) defines the state of a plane stress. For a plane strain, the stress required to produce yielding elevates by a factor of $\sqrt{3}$, so Equation (3.19) is the equivalent for a state of plane strain, Figure 3.18.

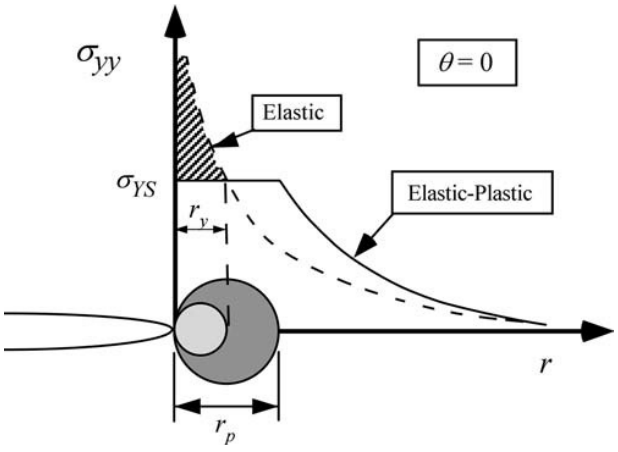

Figure 3.17 *Elastic and inelastic crack plane stress distribution [43].*

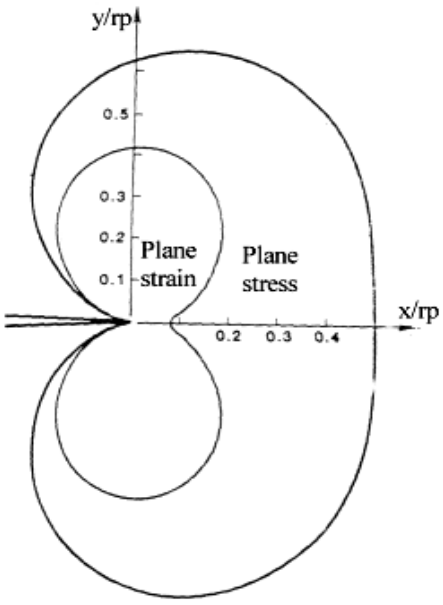

Figure 3.18 *Plane stress and plane strain plastic zone boundaries[48].*

The size of the plastic zone relative to thickness of the body defines whether the plane stress or plane strain is dominant. If the size of plastic zone is of the order of thickness or greater, the plane stress state is dominant. At the other extreme, if the plastic zone is small compared to the thickness, the plane strain dominates. For intermediate sizes of the plastic zones, there is a gradual transition from a plane stress at the free surface to a plane strain at the mid-section, Figure 3.19.

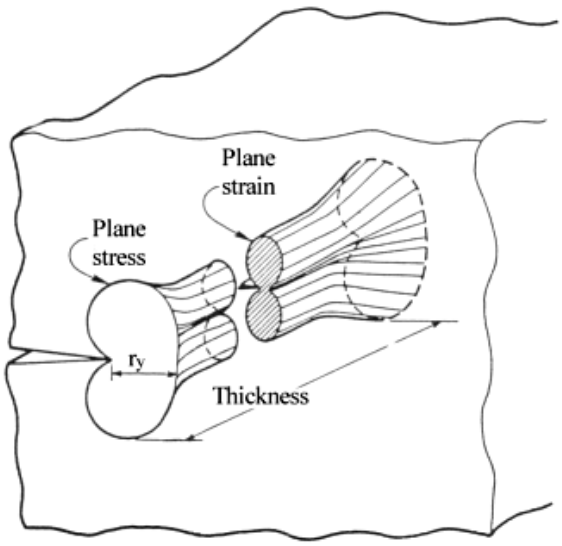

Figure 3.19 *Mode I plastic zone varying from plane stress to plane strain [48].*

Irwin accounted for the softer material in the plastic zone by defining an effective crack length that is slightly longer than the actual crack size [43]:

$$a_{eff} = a + r_y \tag{3.20}$$

The effective stress intensity K is given by:

$$K_{eff} = Y(a_{eff})\sigma\sqrt{\pi a_{eff}} \tag{3.21}$$

Since the effective crack size is taken into account in the geometry correction factor Y. Semielliptical flaw (Figure 3.20) also has an approximate closed-form zone correction. In case of elliptical and semielliptical surface flaw, K_{eff} is given by:

$$K_{eff} = \lambda_s \sigma \sqrt{\frac{\pi a}{Q_{eff}}} \left[\sin^2(\phi) + \left(\frac{a}{c}\right)^2 \cos^2(\phi) \right]^{1/4} \tag{3.22}$$

where Q_{eff} is the effective flaw shape parameter defined as:

$$Q_{eff} = 1 + 1.464\left(\frac{a}{c}\right)^{1.65} \tag{3.23}$$

and λ_s is a surface correction factor defined as:

$$\lambda_s = \left[1.13 - 0.09\left(\frac{a}{c}\right)\right]\left[1 + 0.1(1 - \sin\phi)^2\right] \tag{3.24}$$

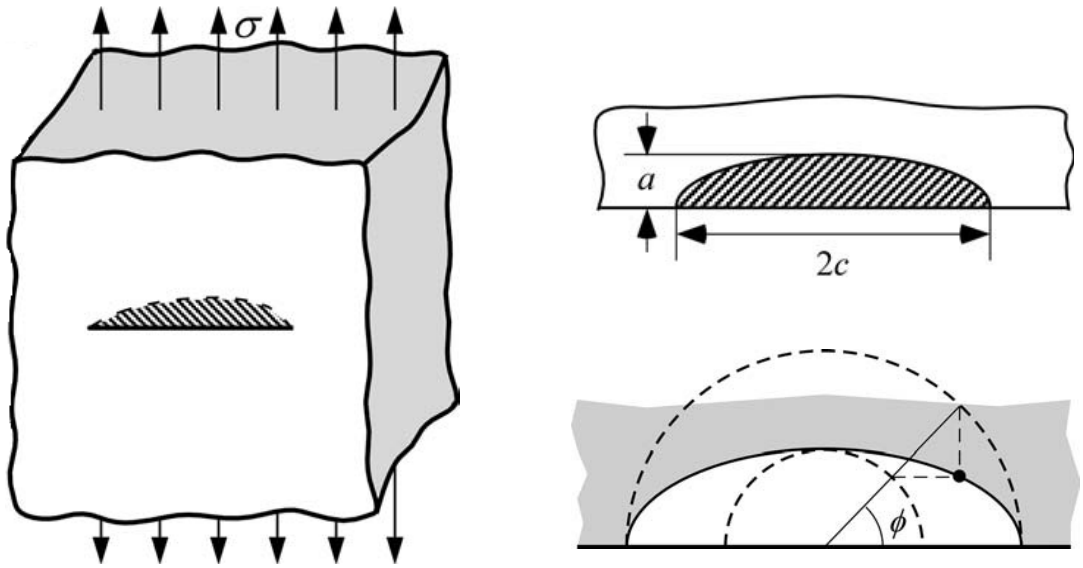

*Figure **3.20** Mode I stress intensity factor for semielliptical surface crack [43].*

Limitations due to the plasticity around the crack for the evaluation of fracture mechanics parameters are getting even more complicated by the yielding condition in the volume close to the section with the crack. Different regimes of yielding are shown in Figure 3.21. In the first one, the yielding is limited to the crack tip and contained in the surrounding volume, enabling this case to be managed by LEFM, and contribution of the plasticity in macro-scale is negligible. Further load increase, the plasticity area extends apart from the crack tip in both dimensions. This will lead to the ligament yielding in one direction, like in thin wall structures. For the limitation in two directions, the net section yielding occurs. In this case, if the crack tip stress reaches the specimen borders, no single fracture mechanics parameter will characterize the crack tip stress, because it must be also geometry dependent. Finally, if the crack is small and the material very ductile, the crack may be neutralized and the conditions of the gross volume or full section yielding will appear. In this case, the remote stress becomes more important.

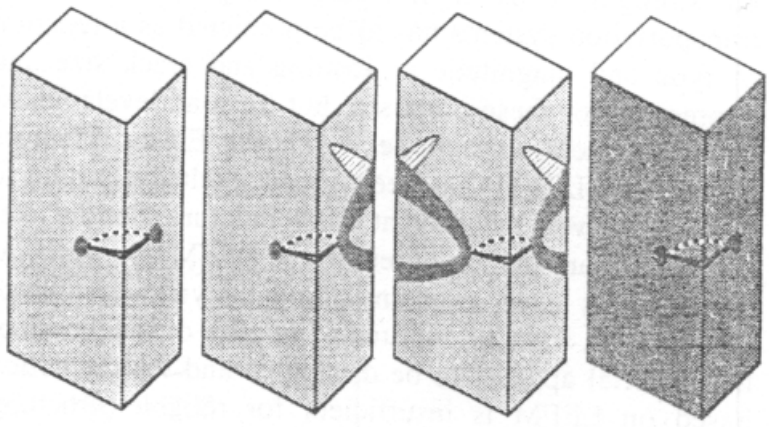

Figure 3.21 *Different regimes of yielding [49].*

3.8 Crack-tip constraint under large-scale yielding

Under small-scale yielding conditions, a single parameter (e.g., K, J, or CTOD) characterize crack-tip conditions and can be used as a geometry-independent fracture criterion. Single-parameter fracture mechanics breaks down in the presence of excessive plasticity, and the fracture toughness depends on the size and geometry of the test specimen.

The effect of specimen size and geometry on cleavage fracture toughness is illustrated in Figure 3.22 and Figure 3.23. Specimen configuration can affect the resistance curve of ductile materials. The crack growth resistance behavior can also be influenced by the crack depth as shown in Figure 3.24. Joyce and Link [43] measured J-R curves for several geometries and found that the initiation toughness J_{Ic} is relatively insensitive to geometry (Figure 3.25).

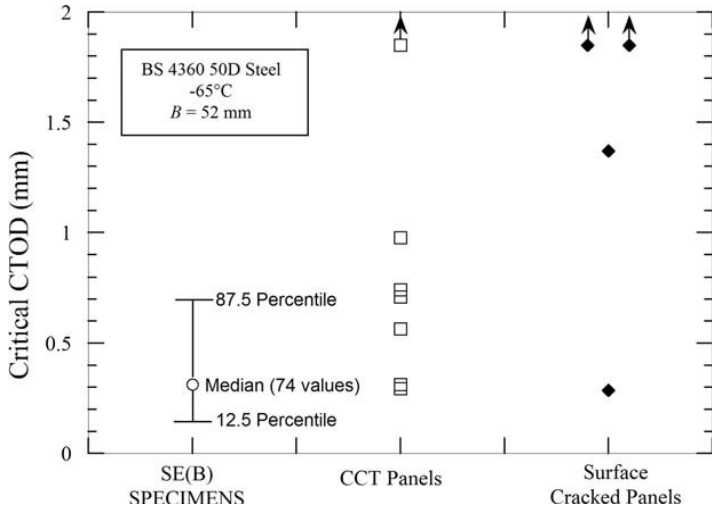

Figure 3.22 *Critical CTOD values for cleavage fracture in bending and tensile loading for a low-alloy structural steel [43].*

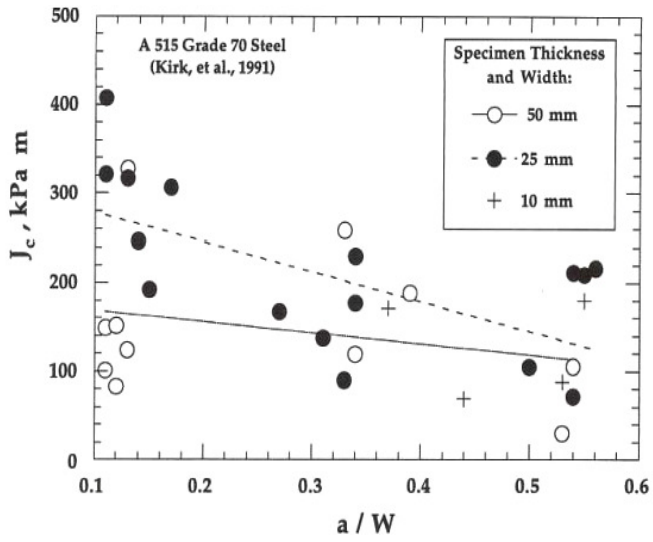

Figure 3.23 *Critical J values for cleavage as a function of crack depth and specimen size of single-edge-notched bend (SENB) specimens [43].*

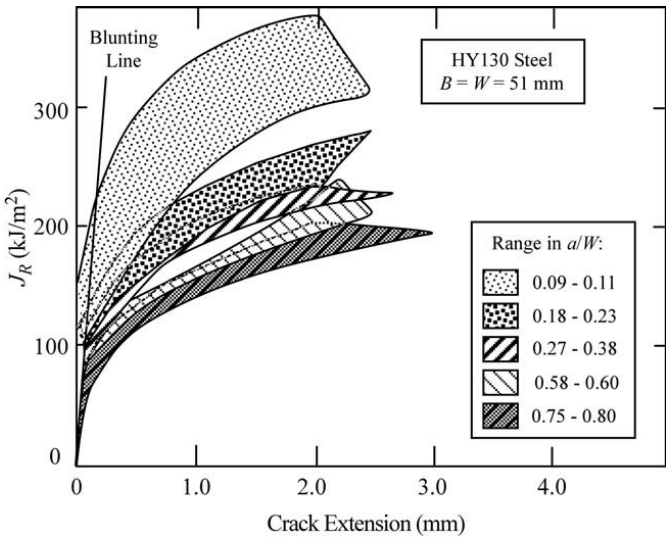

Figure 3.24 *Effect of crack length/specimen width ratio on J-R curves for HY130 steel single-edge-notched bend (SENB) specimens [43].*

3.9 Crack-tip triaxiality effects on fracture behavior

The effect of triaxiality can be illustrated using cracked plate with thickness B subjected to in-plane loading, as shown in Figure 3.26. Material near the crack tip is loaded to higher stresses than the surrounding material causing a triaxial state of stress near the crack tip. The variation of triaxiality near and parallel to the crack front can be seen in Figure 3.27.

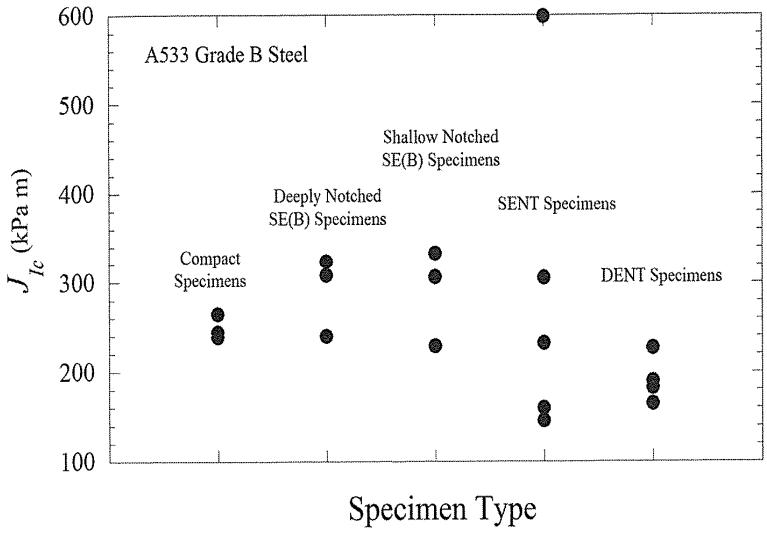

Figure 3.25 *Effect of specimen geometry on critical J value for initiation of ductile tearing [43].*

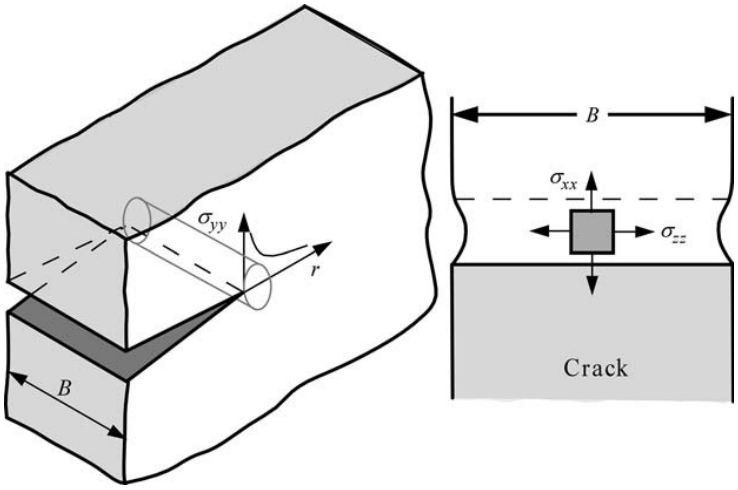

Figure 3.26 *Deformation at the tip of crack [43].*

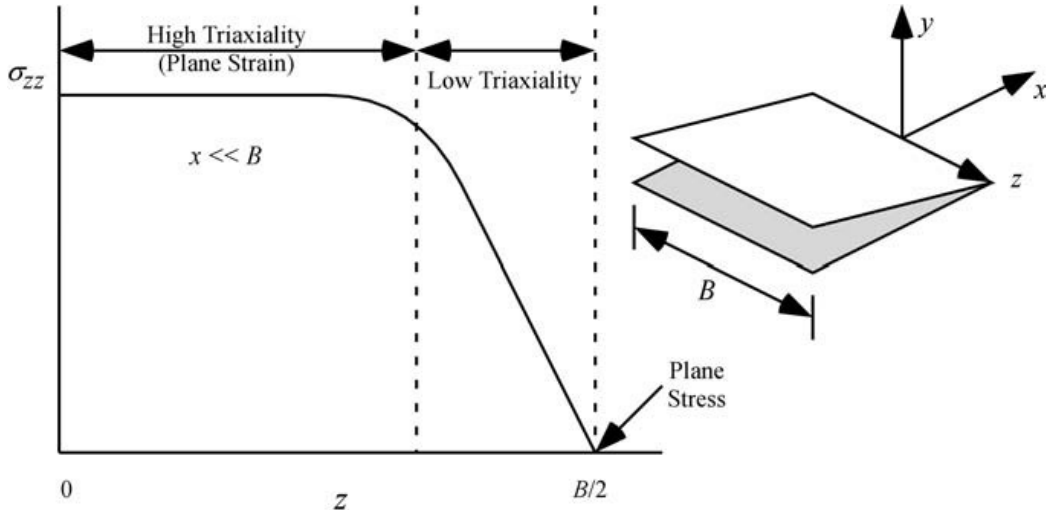

Figure 3.27 *Variation of triaxiality through the thickness near the crack front [43].*

The stress triaxiality T is given by an expression:

$$T = \frac{\sigma_m}{\sigma_{eq}} \tag{3.25}$$

where, σ_{eq} is von Mises equivalent stress, and σ_m is hydrostatic stress given by:

$$\sigma_m = \frac{\sigma_1 + \sigma_2 + \sigma_3}{3} \tag{3.26}$$

σ_1, σ_2, and σ_3 are the three principle stresses.

Fracture processes are highly dependent on constraint (stress triaxiality); this is true for fracture due to void extension and coalescence as well as cleavage fracture. Traditionally, the geometry of a specimen or component (which includes its size) is regarded as the main source of constraint variations. However, as Figure 3.28 demonstrates, there are a range of parameters affecting constraint and hence fracture. A particular point of interest is the observation that constraint tends to fall rapidly when the yield force, F_Y, of a cracked structure is approached. This is of importance in so far as fracture properties are determined on specimens which are frequently much smaller than the component to be assessed. Since for a given fracture event, such as initiation of a crack extension, the degree of plasticity is higher and constraint is lower in smaller bodies, the resistance to crack extension in the larger component may be overestimated [50].

The effect of constraint on the material resistance curve (R-curve), together with some parameters affecting constraint can be seen in Figure 3.29. It is obvious that tensile loading and thin walls promote high resistance to crack extension. Bearing in mind the parameters depicted in Figure 3.28, it is obvious that the resistance to crack extension is a complicated function of several parameters. This makes it impossible to predict the crack extension properties in an actual component in a general way within the framework of classical single parameter fracture mechanics. This is highlighted by Figure 3.30, which shows tests on two types of specimens each of which was made of two different materials. It is clearly seen that the specimen geometry alone is not sufficient to describe the constraint conditions and hence the resistance to crack extension; it seems that in the low strength material 2024-FC, conditions of high constraint cannot be achieved even in

compact tension specimens, which is due to the high degree of plasticity during crack extension, see bottom right diagram in Figure 3.28.

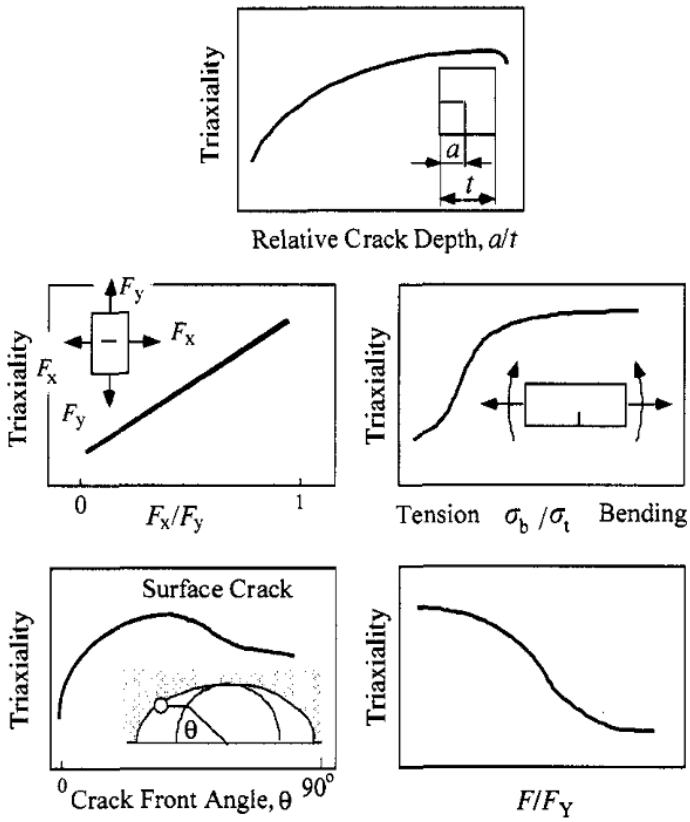

Figure 3.28 *Effect of various parameters on triaxiality (the ratio of mean stress to equivalent stress close to the crack tip) [50].*

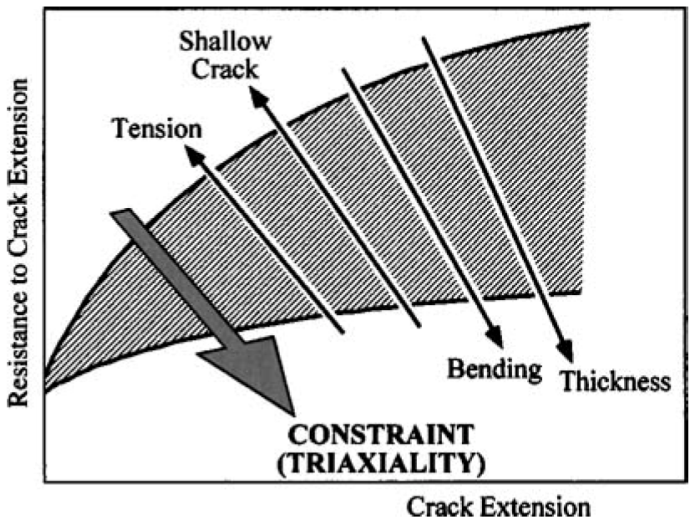

Figure 3.29 *Schematic illustration of constraint effects on crack extension (R-curve) in structural components, indicating the factors affecting the R-curve [50].*

These effects demonstrate the *transferability problem* in fracture mechanics. Figure 3.31 depicts the dilemma: the hatched area is supposed to cover the whole range of crack extension resistance for a given material. An actual structural configuration may be located anywhere within this area. However, standard test methods are designed such that they provide lower bound values of crack extension resistance. The use of data from such specimens usually leads to conservative assessments of structural behavior, which is satisfactory in numerous applications of fracture mechanics. However, there are cases where such an assessment is unduly conservative, and it may be beneficial to reduce existing large safety margins. This problem can be partly overcome by testing specimens modeling the component's stress triaxiality more closely.

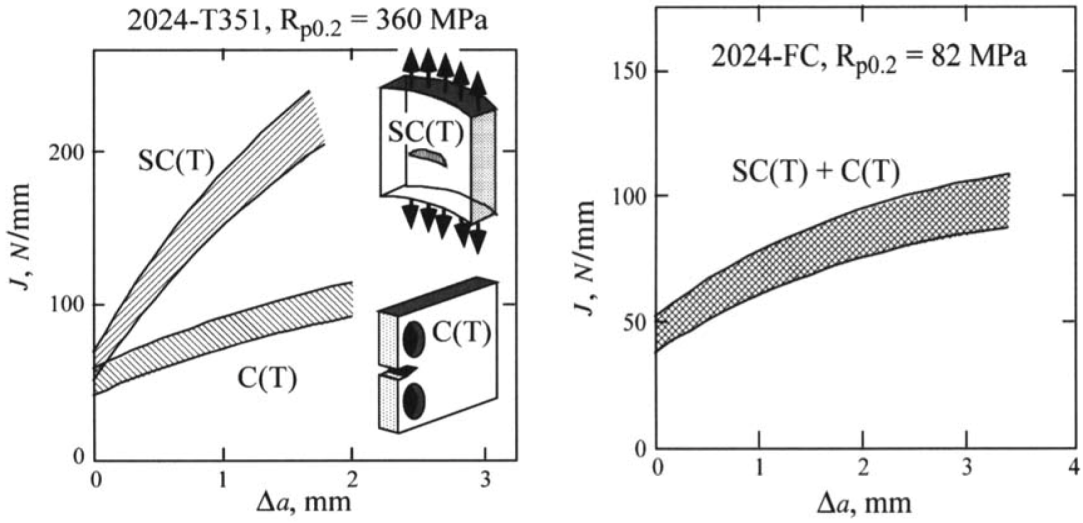

Figure 3.30 *Ductile tearing data obtained on compact tension, C(T), and surface cracked tension, SC(T), specimens for two different materials [50].*

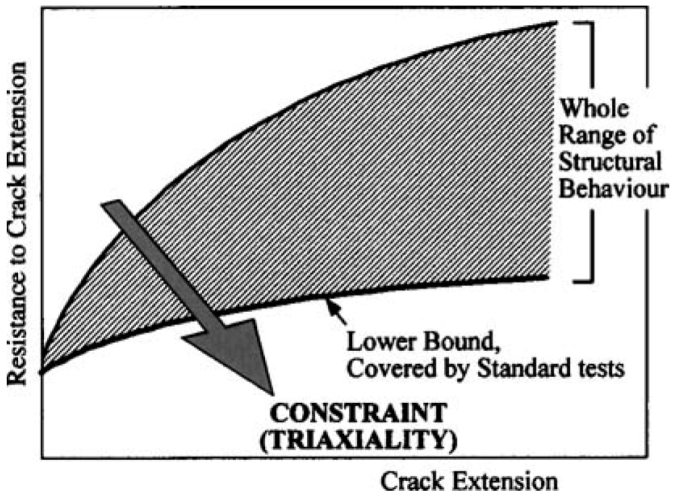

Figure 3.31 *Range of resistance to crack extension (R-curve) in structural components, as compared with lower bound behavior determined in standard tests [50].*

The transferability problem, where a result obtained by a test on a laboratory test piece cannot, in general, simply be transferred to a structural configuration, is the price to be paid for using 2D analyses and single parameter characterizations of cracked bodies. However, this simple concept works satisfactorily for the vast majority of practical applications.

A more rigorous way of analyzing the effects of cracks on the mechanical behavior of structural components is given by the *local approach* whereby the loading conditions local to the crack tip are not given by a single parameter but by the complete 3D stress and strain fields. A number of models have been developed which describe cleavage fracture in steels as well as tearing mechanisms based on the formation, extension, and coalescence of voids as explained in the following chapters. The various material parameters in the models can be determined by simple tests on smooth and/or notched tensile bars or on precracked specimens. Thus, the local approach requires more effort on the computational side than classical single parameter fracture mechanics.

3.10 Deformation patterns in mismatched weldments

The matched weld shows a net section yielding pattern characteristic of deep edge crack in a finite width plate. For a high work hardening material a change to gross yielding for shallow crack might be expected. In overmatched welds, the whole plate outside the weld has gone into gross yielding. A net section yielding pattern exists between the crack tip and the gross yield region. For large cracks in overmatched welds, the stress is concentrated at the crack tip. Plasticity is contained and the parent material has no influence on the welded structure. However, for medium or shorter cracks in overmatched welds, another plastic zone appears at the fusion line in the base metal due to the different strength of the material involved, Figure 3.32. Shallow cracks in extremely overmatched welds devolve the plasticity in the softer base metal.

For undermatched welds, plasticity is concentrated in the weld metal. The intense strain bands follow the weld profile. The weld metal toughness is lower than that measured on a homogeneous specimen entirely made of weld metal, due to extreme concentration of plasticity in the weld metal. Short cracks in welds of great mismatch may generate a strain singularity at the interface between base and weld metals due to the difference of strain carrying capacities, Figure 3.33.

The extent of plastic zone of overmatched joint is larger than that of the undermatched joint for the same CTOD value. The main reason that the plastic zone of an overmatched joint extends to HAZ and BM, but for an undermatched joint restricted with the weld metal.

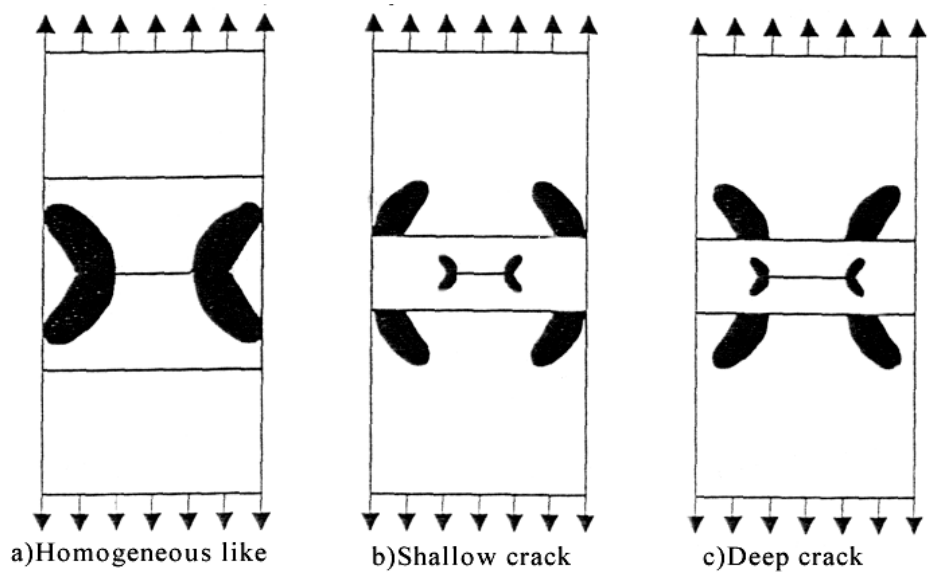

Figure 3.32 *Plasticity development for overmatched CCT specimens [51].*

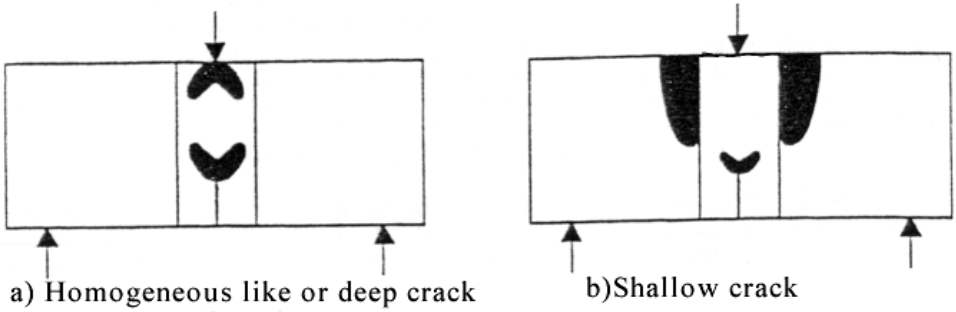

Figure 3.33 *Plasticity development for under matched SENB specimen [51].*

3.11 Welded joint fracture

Fracture behavior of welded component is influenced by mechanical heterogeneity of various regions: HAZ and weld metal as follows:

3.11.1 Weldment fracture

Estimation of fracture toughness values (J and CTOD) using standard experimental procedures are well established for homogeneous material. However, similar standard

experimental procedures do not exist for structures containing mismatched weldments. Different studies addressed the effects of strength mismatch for *J* and *CTOD* values. In these studies, the weld was modeled as regions of material having different strength.

Sedmak et al. [52] investigated the crack growth in the pressure vessel, with attention being paid to the weldment behavior due to mismatching, residual stresses and crack location is carried out on tensile tests. A combination of welded joint of HSLA steel tensile panels was investigated, with a part–through crack positioned in the middle of the specimen. Relation between average stress–strain curves, has defined the effect of the crack. The most expressed crack effect is found in undermatched joint. The loading capacity was found to be lower than load corresponding to the residual ligament area. Welded joint has exhibited exaggerated lower WM yield strength, so the final fracture occurred in the WM. The overmatched joint has produced minimal reduction in strength and a significant reduction in ductility. A welded joint has exhibited a slightly lower BM strength, and the final fracture occurred in the BM. Even in the overmatched welded joint, WM has started to yield before BM. The strain behavior of the various constituent part of weldment is shown in Figure 3.34.

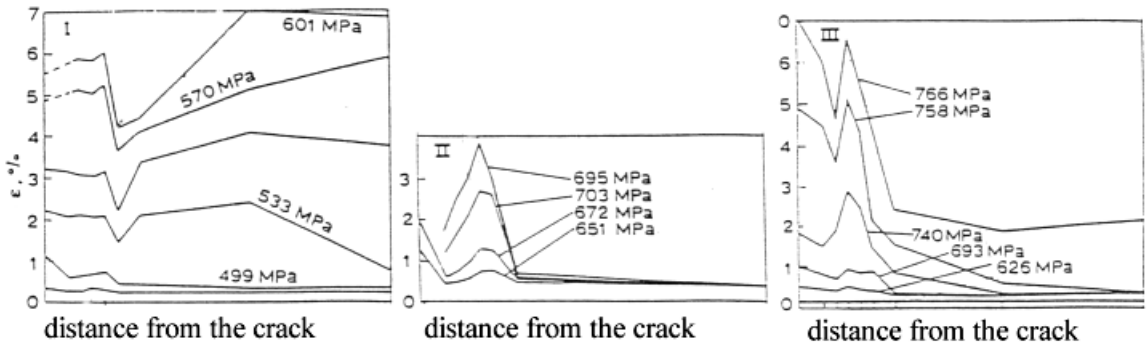

Figure 3.34 *Strain distribution in welded joint: (I) overmatched (II) undermatched and (III) normal-matched joint [52].*

3.11.2 HAZ fracture

The behavior of the heat–affected zone (HAZ) is related to its small volume and structural heterogeneity, as well as to the different mechanical properties of the HAZ' regions. A large overmatching drastically reduces the resistance to the cleavage fracture for HAZ because the plastic deformation in HAZ is constrained, Figure 3.35.

The undermatched tensile panel with crack in HAZ indicates short surface crack causes an unsymmetrical strain distribution at the crack tip vicinity, Figure 3.36.

To evaluate the HAZ toughness, attention should be paid on the crack position in HAZ, especially if the crack tip is in local brittle zone, LBZ (i.e. coarse-grained HAZ, CGHAZ) which is the most brittle and often isolated zone of the HAZ. Kocak and co-workers [55] carried out an investigation for various geometrical configurations (CT, CCT, SENB) with various crack sizes. The results demonstrate that all tensile panels showed fully ductile failure, while all SENB exhibited pop-ins, and toughness of LBZs increased with the decreasing *a*/*W* ratios. Results of the study show that the fundamental difference is in outcome of tensile panels concerning the structural significance of LBZs.

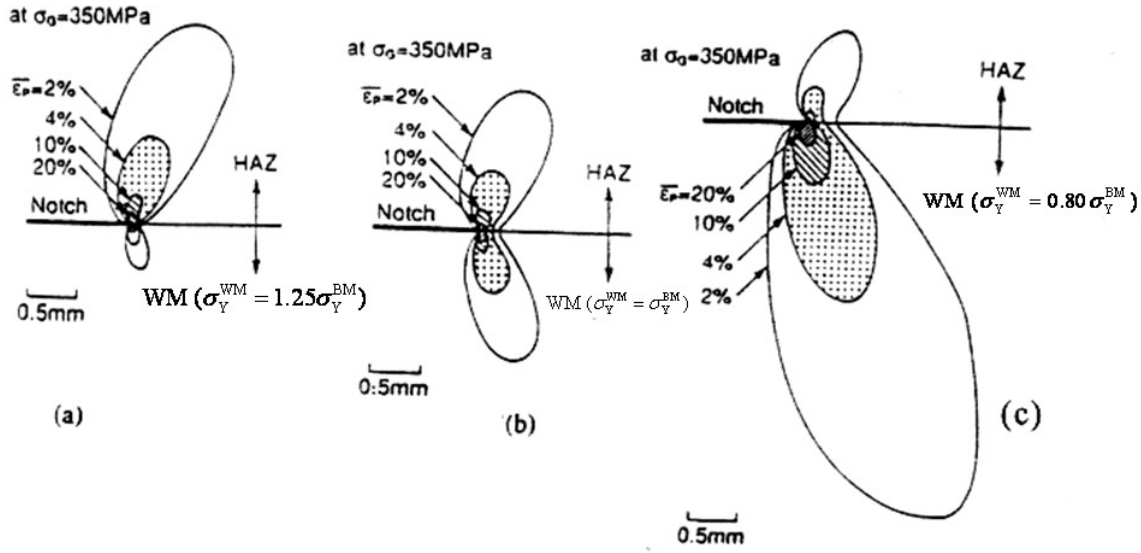

Figure 3.35 *Distribution of equivalent plastic strain around the crack tip for HAZ notched weld joint [53].*

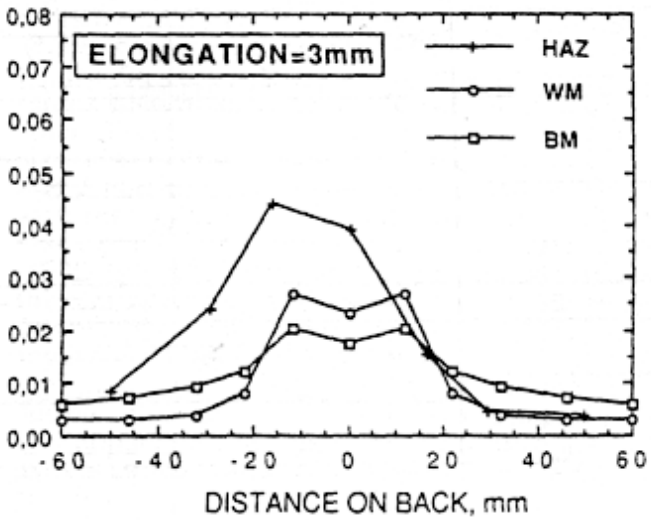

Figure 3.36 *Variation of plastic strains across the weld [54].*

Chapter 4

Structural Integrity Assessment Using Local Approach

4.1 Introduction

The assessment of the mechanical integrity of any flawed mechanical structure requires the development of approaches which can deal not only with simple situations, such as small-scale yielding (SSY) under pure mode I isothermal loading, but also with much more complex situations, including large-scale plasticity, mixed-mode cracking, and non-isothermal loading. Two types of approaches have been developed for this purpose. The first approach, referred to as the "global" approach, is essentially based on the extensive development over the past few decades of linear elastic fracture mechanics (LEFM) and elastic-plastic fracture mechanics (EPFM). In this approach, it is assumed that the fracture resistance can be measured in terms of a single parameter, such as K_{Ic}, J_{Ic}, or crack-tip opening displacement (CTOD). Rules uniquely based on the mechanical conditions of test specimens have been established for "valid" fracture toughness measurements, without paying attention to the failure micro-mechanisms. The standardization of fracture toughness testing continues to undergo rapid development. This approach is extremely useful and absolutely necessary, but it has also a number of serious limitations, in particular when large-scale conditions are prevailing or when dealing with non-isothermal conditions. Another limitation is the size effect which is usually observed when steels are tested in the brittle domain and in the ductile-to-brittle transition regime. It is now well established that fracture toughness is dependent on specimen thickness even when LEFM conditions are prevailing. The specimen size requirements, in particular the crack length and the ligament size which must be fulfilled in an EPFM test in order to measure "valid" fracture toughness, J_{Ic}, is still more problematic. This raises the important problem related to the transferability of laboratory

test results to large components. Subsequently, another approach to the problem has been developed. This is the so called "local" approach to fracture in which the modeling of fracture toughness is based on local fracture criteria established from tests carried out on volume elements, in particular notched specimens [56-58].

In this chapter, literature review has been presented about local approaches and their importance in structural integrity assessment.

4.2 Importance of local approach

Micromechanical or local approach to the assessment of fracture of various materials has been developed during past two decades. Despite some unsolved problems in prediction of the occurrence of various forms of fracture, local approach has become an often-used tool. It combines a detailed experimental analysis of the considered materials and their specific damage mechanisms at the mesoscale, a realistic modeling of these mechanisms and the implementation of these models into numerical simulation of damage and fracture of the structural components under investigation.

Standard recommended parameters of elastic-plastic fracture mechanics, like COD and *J*-integral, cannot reliably describe and predict the behavior of the materials affected by external loading under different operational conditions. Therefore, as convenient one, a local approach was introduced and has been simultaneously developed in theoretical, experimental and numerical sense. This approach describes the process of fracture in a way close to the actual phenomena in a material. It is based on a large number of models of microscopic damages, as an effort to explain and predict macroscopic failure. At the same time, it is necessary to define as accurately as possible the stress/strain fields and values of the variables describing material damage [59].

The advantage of a micro-mechanical damage approach, compared with conventional fracture mechanics, is that the approach parameters are only material not geometry-dependent. It also includes the effect of large-scale deformation and plastic straining on material failure. A disadvantage is that it is computationally expensive, so it is important to develop efficient procedures.

4.3 Fracture mechanisms in metals

There are three common fracture mechanisms in metals and alloys:

(a) Cleavage fracture.

(b) Intergranular fracture.

(c) Ductile fracture.

The main difference between cleavage and ductile fracture is the amount of plastic deformation that the material undergoes before the fracture occurs. Ductile fracture demonstrates large amount of plastic deformation, while cleavage demonstrates little plastic deformation before the fracture.

4.3.1 Cleavage Fracture

Cleavage fracture is the rapid propagation of crack along a particular crystallographic plane, and most likely occurs when plastic flow is restricted. Several cleavage cracks tend to converge in a single crack (*river patterns*), because multi cracks consume more energy for propagation than a single crack, Figure 4.1. The cleavage involves breaking bonds, so the local stress must be sufficient to overcome the cohesive strength of material. The cohesive strength is at least 50 times higher than the maximum stress achieved ahead of the crack tip. Since even the macroscopic crack does not provide the enough stress concentration that exceeds the bond strength, there must be a local discontinuity ahead of crack tip that is sufficient to exceed the bond strength. This discontinuity is micro crack intersecting slip planes by means of dislocation interaction or micro crack formed at inclusion and second phase particles. The micro crack can be treated as a Griffith crack, which propagates if the stress ahead of macroscopic crack is sufficient, Figure 4.2. The fracture stress is given by [43]:

$$\sigma_f = \left(\frac{\pi E \gamma_P}{(1-\nu) C_0} \right)^{1/2} \tag{4.1}$$

where γ_P is the plastic work required to create a unit area of fracture surface in ferrite, and C_0 is the particle diameter.

Once cleavage initiates, the crack may either propagate in unstable manner or arrest. The initiation is governed by the local stress at the critical particle. The propagation is controlled by the global driving force and the orientation of the neighboring grains. However, micro cracks must remain sharp to exceed the cohesive strength of the material.

The crack may arrest due to the subsequent deformation and dislocation motion in the matrix, causing the crack to blunt. The fracture toughness of the material can change the fracture mechanisms over the temperature range. So, one can expect the same material to fail by cleavage at low temperatures and by micro voids coalescence at high temperatures, Figure 4.3.

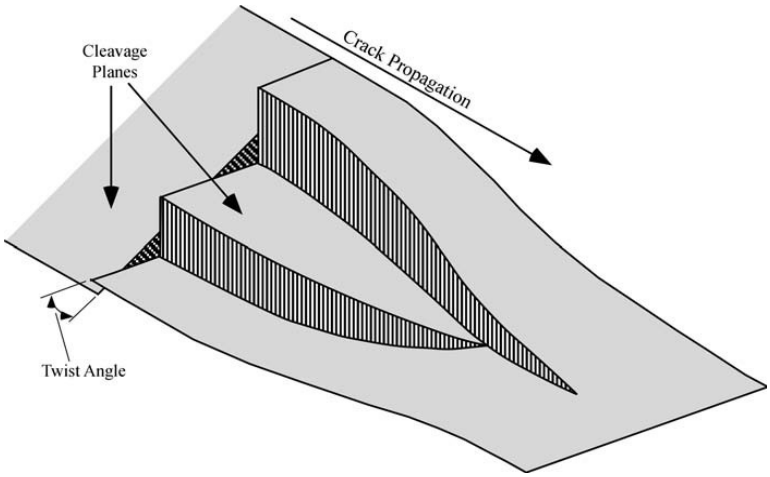

Figure 4.1 *Formation of river patterns, as a result of a cleavage crack crossing a twist boundary between grains [43].*

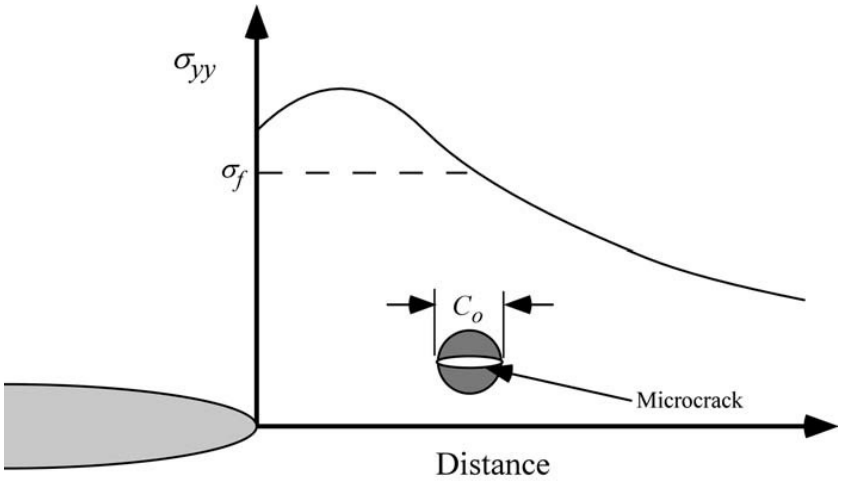

Figure 4.2 *Initiation of cleavage at a micro crack that forms in a second phase particle a head of a macroscopic crack [43].*

4.3.2 Intergranular fracture

Under special circumstances, cracks can form and propagate along grain boundaries, Figure 4.4. There are a variety of situations that can lead to cracking on grain boundaries. Brittle phases can be deposited on grain boundaries like tempered martensite and thin layers of impurity atoms (e.g. phosphorous and sulphur). Hydrogen embrittlement can

degrade the toughness, atomic hydrogen bonds with metal atoms and reduce the cohesive strength at grain boundaries.

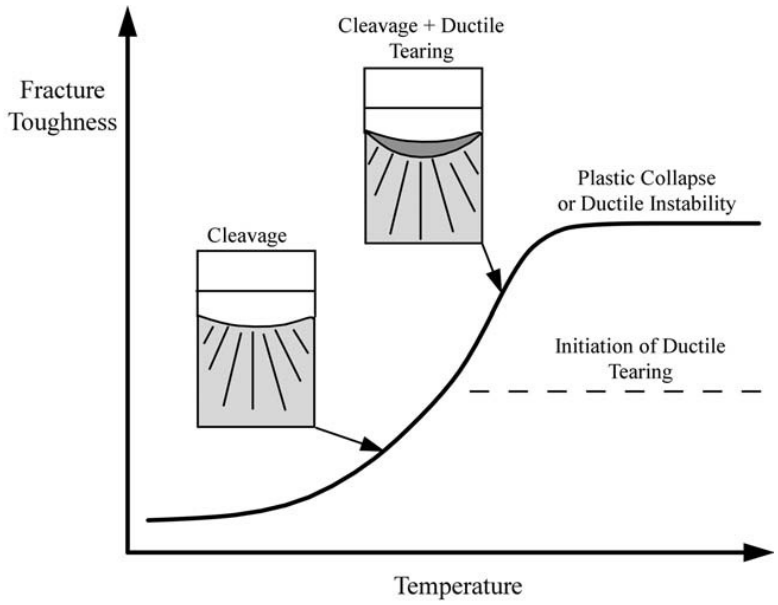

Figure 4.3 *The ductile brittle transition in ferritic steel [43].*

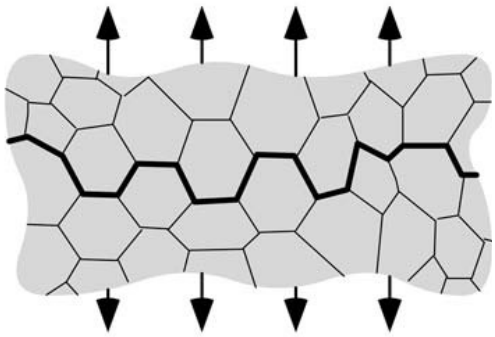

Figure 4.4 *Intergranular fracture [43].*

4.3.3 Ductile fracture

Ductile failure in metals is most often related to large deformation, i.e. large plastic strains preceding the failure instant. Another important characteristic of ductile fracture is that it occurs by a slow tearing of the metal with the expenditure of considerable energy. Ductile fracture of round bars in tension is usually preceded by a localized reduction in diameter, which is commonly called necking. Very ductile polycrystalline materials, i.e. gold and lead, can practically be drawn to a line or a point before rupture. In Figure 4.5(a) the stages in the development of a ductile cup-and-cone fracture are schematically illustrated.

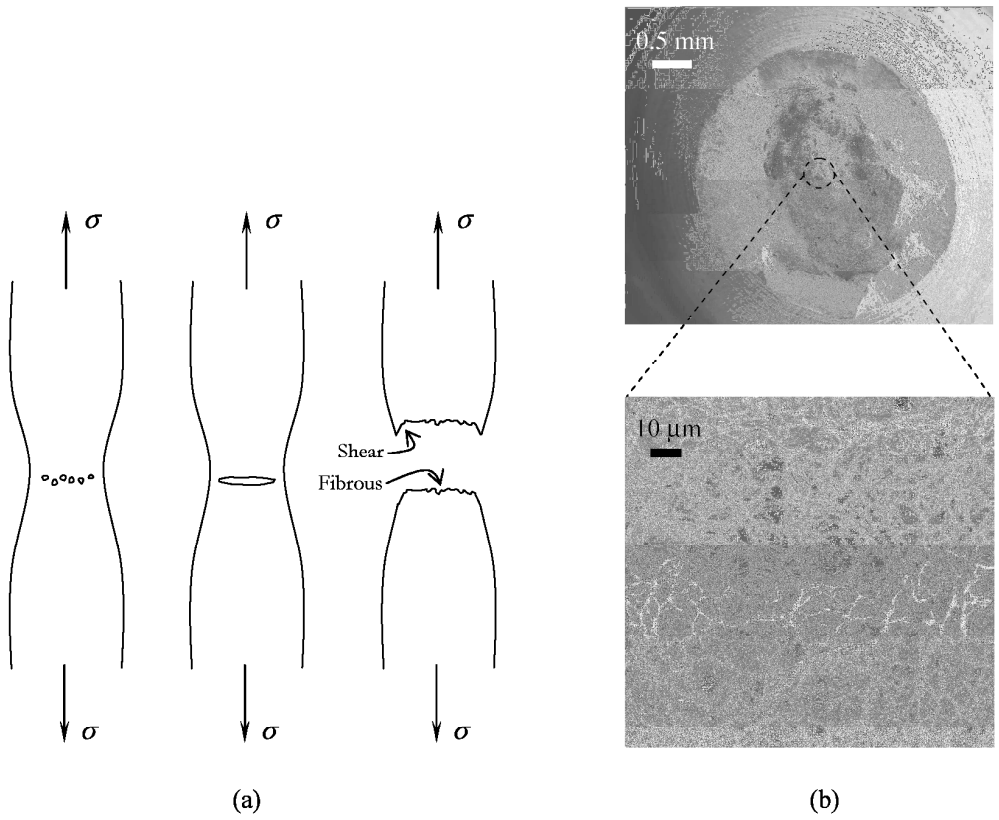

***Figure 4.5**: (a) stages in the ductile tensile failure process pertaining to nucleation, growth and coalescence of voids to form the macroscopic crack and (b) a typical fractured cross-section and a close up from the centre of the specimen [60].*

Necking begins at the point of plastic instability where the increase in strength due to strain hardening of the material fails to compensate for the decrease in cross-sectional area, which occurs at the maximum load. The formation of a neck introduces a triaxial state of stress in the neck region, with a hydrostatic stress component largest in the center of the neck. Many small cavities form in this region and under continued straining these cavities grow and coalesce into a central crack. This crack grows in a direction perpendicular to the axis of the specimen until it approaches the surface of the specimen. It then propagates along localized shear bands at about 45º to form the cone feature of the fracture. Voids are nucleated in these bands and form so called void sheets. Hence, ductile failure is essentially the process of nucleation, growth and coalescence of voids, where coalescence is the final stage of the rupture process. Here we distinguish between two modes of coalescence, one is internal necking down of the ligaments between the voids that have grown significantly, which leads to the formation of a fracture surface often referred to as dimple rupture, the other is internal shearing of the ligaments between the voids, i.e. in a shear band, and is often referred to as shear dimple rupture. A typical

dimple rupture fracture surface is shown in Figure 4.5(b), which corresponds to a close up at the centre of a fractured cross-section of a round bar in tension. The enlarged and coalesced voids that formed the macroscopic crack are visible, where some of the voids have grown to a diameter of about 20μm [60].

Ductile fracture can be classified into three stages [61]: void nucleation, void growth and void coalescence (Figure 4.6). For most engineering alloys, void can be nucleated from large inclusions and second phase particles by particle fracture or interfacial decohesion [62]. Once a void has been nucleated, it will grow under plastic deformation and hydrostatic stress. Eventually the voids will connect and ductile fracture by void coalescence will appear. The ductile fracture process due to the presence of voids can be separated into two phases, the homogenous deformation with void nucleation and growth, and the localized deformation due to void coalescence.

(a) Void nucleation

A void forms around a second-phase particle or inclusion when sufficient stress is applied to break the interfacial bonds between the particle and the matrix. A number of models for estimating void nucleation stress have been published, some of which are based on continuum theory [63,64] while others incorporate dislocation-particle interactions [62].

The most widely used continuum model for void nucleation is due to Argon et al. [63]. It has considered that decohesion stress is defined as a critical combination of mean stress and the effective (von Mises) stress:

$$\sigma_c = \sigma_e + \sigma_m \tag{4.2}$$

where σ_e is the effective stress, given by:

$$\sigma_e = \frac{1}{\sqrt{2}}\left[(\sigma_1 - \sigma_2)^2 + (\sigma_1 - \sigma_3)^2 + (\sigma_3 - \sigma_2)^2\right]^{1/2} \tag{4.3}$$

σ_m is the mean stress, defined as:

$$\sigma_{\mathrm{m}} = \frac{\sigma_1 + \sigma_2 + \sigma_3}{3} \tag{4.4}$$

and σ_1, σ_2, and σ_3 are the principle normal stresses.

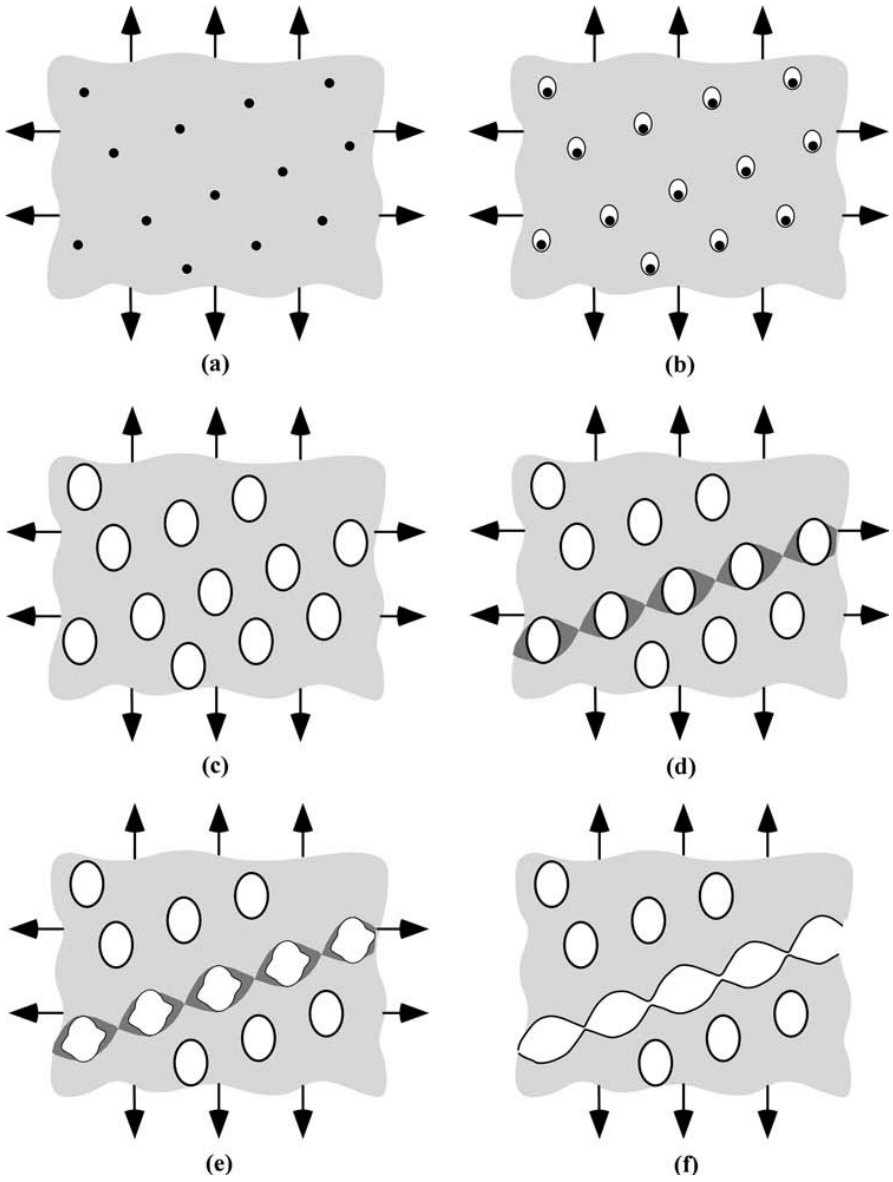

Figure 4.6 *Void nucleation, growth, and coalescence in ductile metals: (a) inclusions in a ductile matrix, (b) void nucleation, (c) void growth, (d) strain localization between voids, (e) necking between voids, and (f) voids coalescence and fracture [43].*

Good and Brown [62] have developed a dislocation model for void nucleation at submicron particles. They estimated that dislocations near the particles elevate the stress at the interface by the following amount:

$$\Delta\sigma_d = 5.4\alpha\mu\sqrt{\frac{\varepsilon_1 b}{r}} \tag{4.5}$$

where

α constant that ranges from 0.14 to 0.33.

μ shear modulus.

ε_1 maximum remote normal strain.

b magnitude of Burger's vector.

r particle radius.

The total maximum interface stress is equal to the maximum principle stress plus $\Delta\sigma_d$. void nucleation occurs when the sum of these stresses reaches a critical value:

$$\sigma_c = \Delta\sigma_d + \sigma_1 \tag{4.6}$$

(b) Void growth and coalescence

Once voids form, further plastic strain and hydrostatic stress cause the voids to grow and eventually coalesce. Figure 4.7 and Figure 4.8 are scanning electron microscope (SEM) fractographs that show dimpled fracture surfaces that are typical of microvoid coalescence. Figure 4.8 shows an inclusion that nucleated a void.

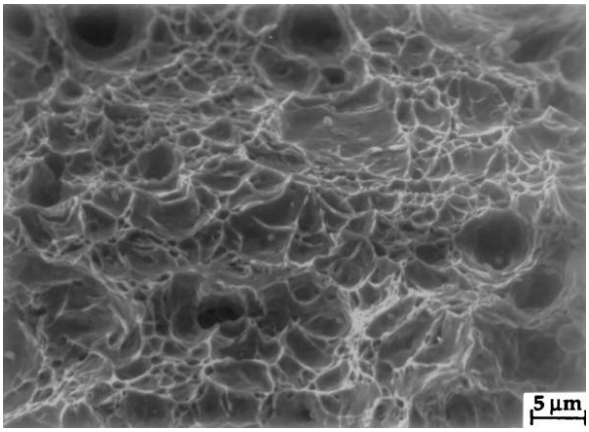

Figure 4.7 *Scanning electron microscope (SEM) fractograph which shows ductile fracture in a low carbon steel [43].*

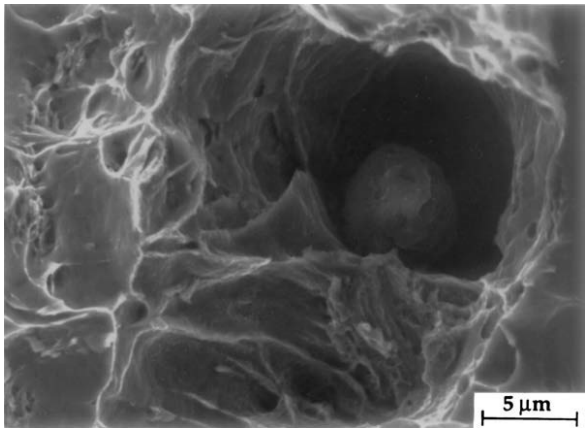

Figure 4.8 *High magnification fractograph of the steel ductile fracture surface. Note the spherical inclusion which nucleated a microvoid [43].*

4.4 Micromechanical-local approach to fracture

Micromechanical models have been used for structural integrity assessment such as; prediction of fracture initiation and crack growth propagation. They have recently been much improved. One of the problems still under consideration is defining the procedure for determination of numerous parameters present in the models. The other one is lack of physical significance of some parameters. Figure 4.9 shows basic steps in micro-mechanical approach to ductile fracture and cleavage.

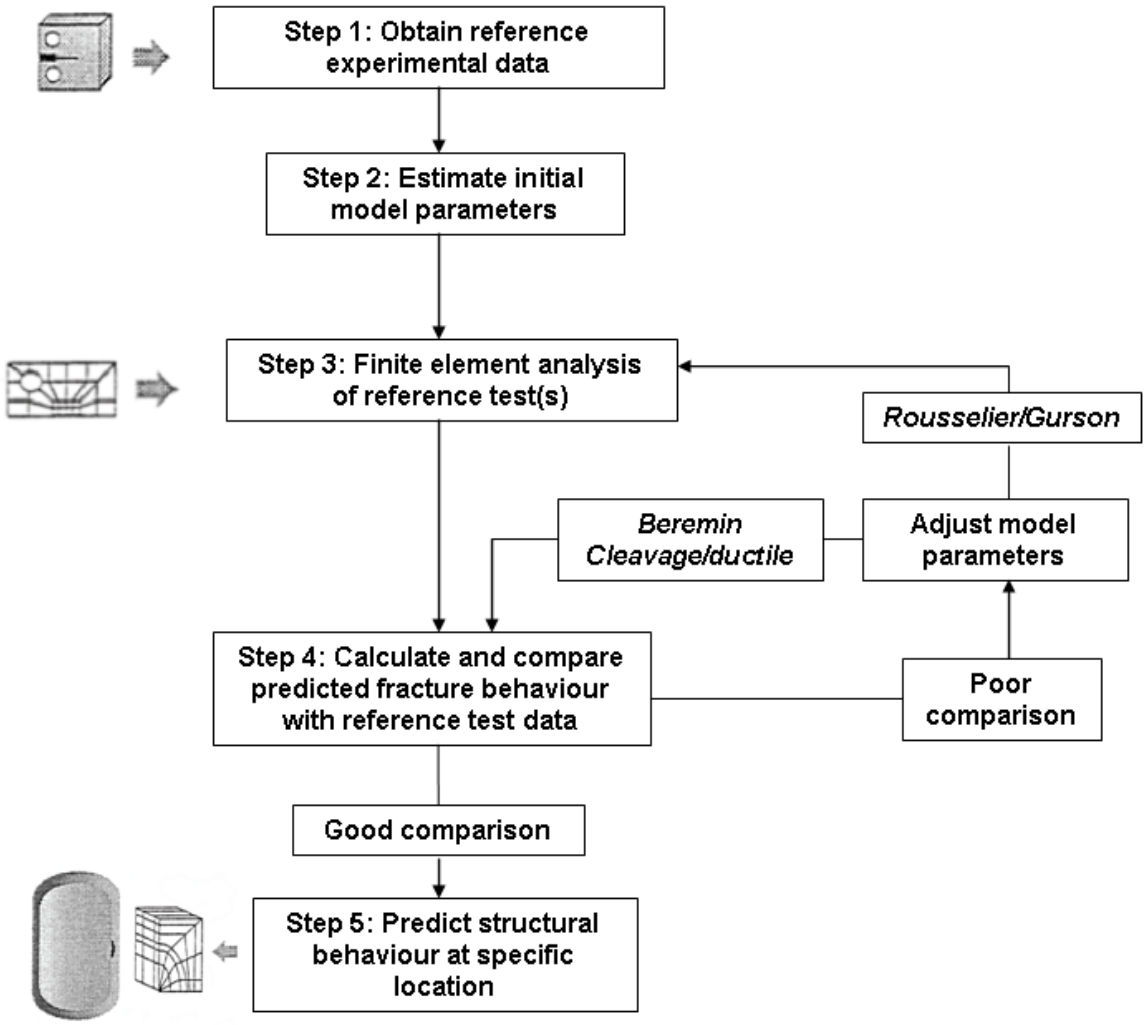

Figure 4.9 *Basic steps in micromechanical approach to fracture [59].*

Application of micromechanical models should enable so-called *transferability* of model parameters to different geometries (Figure 4.10). Their application should not include requirements related to test geometries, as the model parameters should depend solely on material.

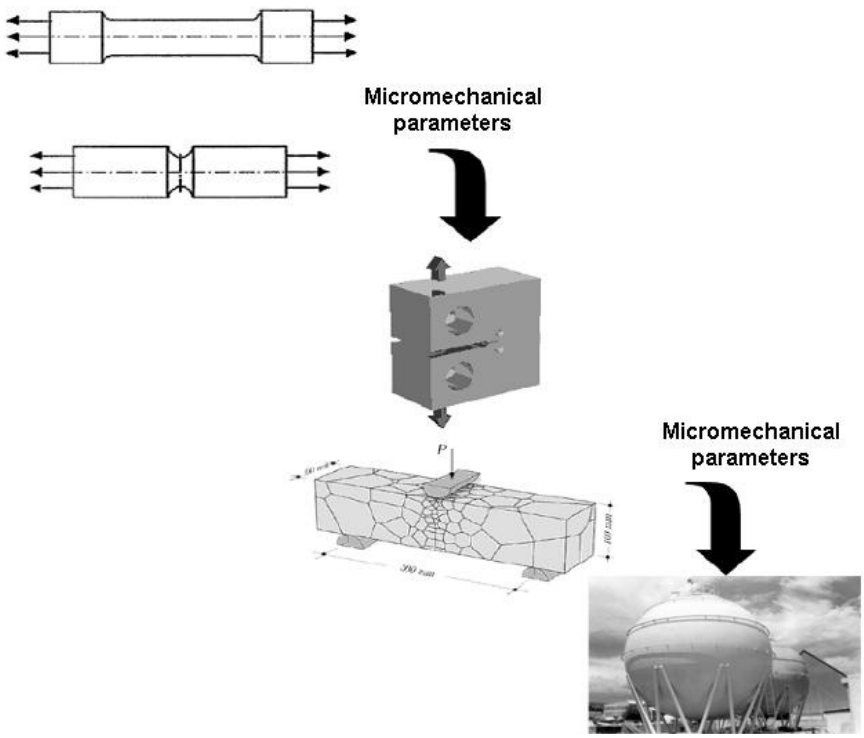

Figure 4.10 *Transferability of damage parameters.*

Some of the first micromechanical procedures [17,18,26,65-75] included investigations on round tensile specimens and notched tensile specimens with various values of notch radius to consider effect of stress triaxiality. The most recent methods and approaches are focused to some of the problems, including void coalescence criterion, more detailed microstructural analysis, influence of various quantities (size, shape and distribution of voids) [69,70]. These micromechanical models have been successfully applied to several classes of problems, including pressure vessels [71-73], pipelines, inhomogeneous materials, and welded joints [18,74,75]. One of the most recent models is CGM (Complete Gurson Model) [17,26]. It is developed by incorporating the Thomason's limit load criterion [76] into the Gurson-Tvergaard-Needleman (GTN) model, which developed by Gurson [77] and modified by Tvergaard and Needleman [3].

There are a number of mathematical models for void growth and coalescence. The two most widely referenced models were published by Rice and Tracey [78] and Gurson [79].

4.5 Micromechanical models for ductile fracture prediction

Ductile fracture process of most metals and alloys includes void nucleation, growth and coalescence. Void nucleation takes place around the non-metallic inclusions and

second-phase particles. Most of the proposed models state that void nucleates when so-called critical stress within inclusion or at inclusion-matrix interface has been reached [59]. In materials of distinct ductile behavior, fracture occurs after all three phases (Figure 4.11). These materials exhibit strain hardening during the loading, but they also exhibit softening due to the presence of voids. However, it is not possible to set clear boundaries between brittle and ductile materials, as the same materials can behave as brittle or ductile, depending on several factors such as; temperature, loading rate, geometry, size, strength. The influence of temperature on material fracture behavior can be seen in Figure 4.12 with commonly used micromechanical models for cleavage and ductile fracture predictions.

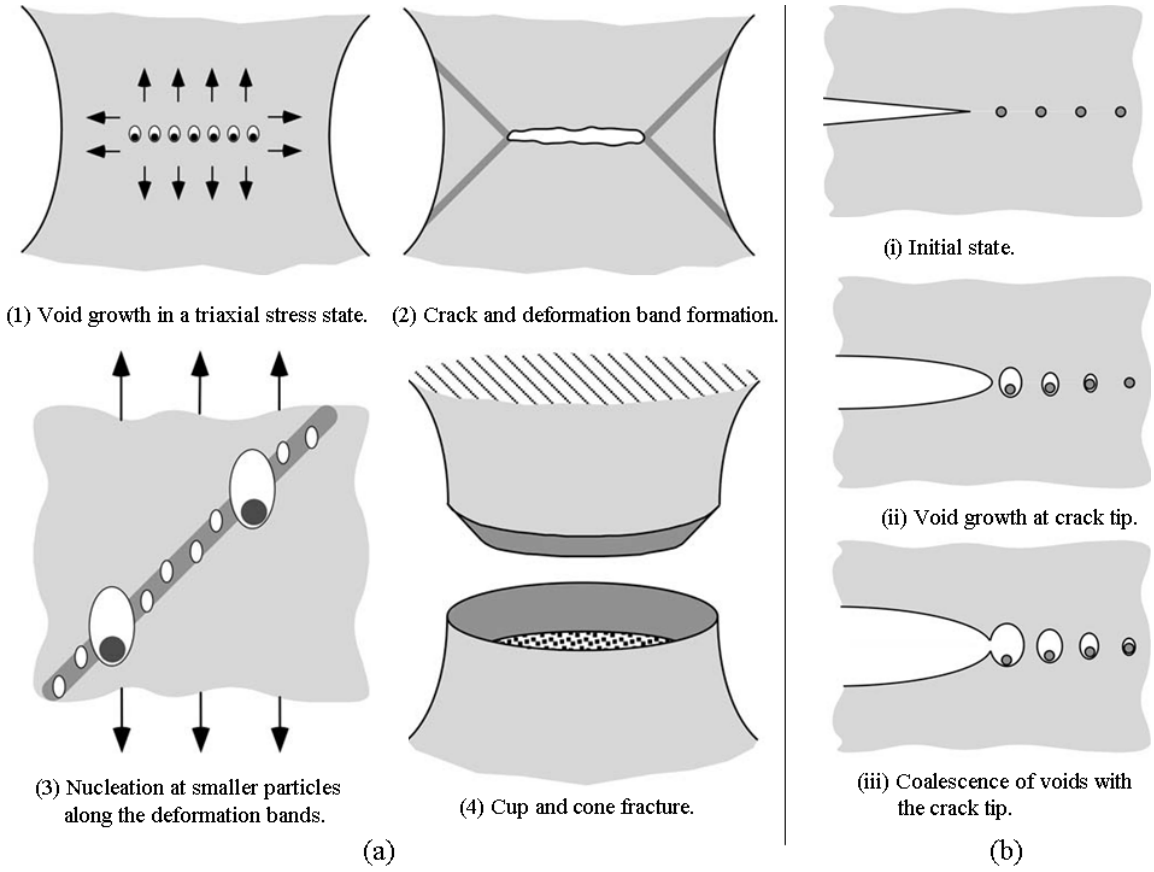

Figure 4.11 *Process of ductile fracture in geometry: (a) without a crack and (b) with initial crack [43].*

Micromechanical models can be classified into two groups: uncoupled and coupled models. According to the uncoupled model, void presence does not significantly alter material behavior; hence the damage parameter is not incorporated into the constitutive equation. Therefore, von Mises criterion is the most frequently used as the yield criterion.

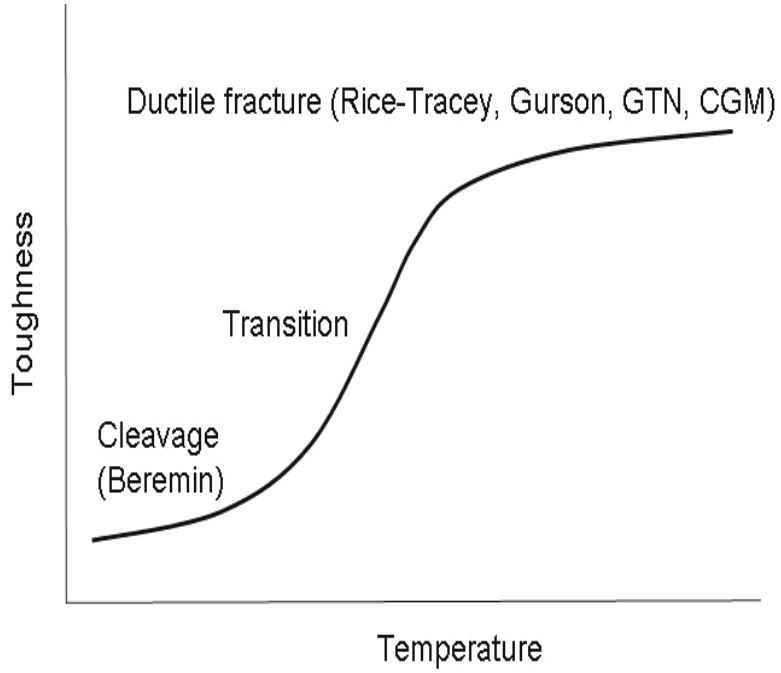

Figure 4.12 *Commonly used micromechanical models for cleavage and ductile fracture prediction [59].*

Research efforts have recently been directed toward so-called coupled models of damage, with damage parameter "built into" the numerical procedure and estimated during the finite elements (FE) analysis.

One of the most widely known micro-mechanical models for ductile fracture is Gurson model [77], which describes the progressive degradation of material stress capacity. In this model, which is a modification of the von Mises one, an elastic-plastic matrix material is considered and a new internal variable, the void volume fraction, f, is introduced. Although the original Gurson model was later modified by many authors, particularly by Tvergaard and Needlman [3,78,80]. One of these models has been developed by Tvergaard and Needlman [3], based on constitutive equations suggested by Gurson [77]. Main variable is void volume fraction, which is directly incorporated into the flow criterion. This model commonly is called Gurson-Tvergaard-needleman model (GTN), which can describe both damage development at microscopic level and plastic strain, as a global, macro-parameter of material behavior. The GTN model has been later developed by combining it and the coalescence criterion proposed by Thomason, and it has been shown to give accurate predictions for any level of stress triaxiality, for both strain non-hardening and strain hardening materials.

4.5.1 Micromechanical uncoupled models

One of the uncoupled models is Rice-Tracey model, which improved by Beremin [78], void growth is strongly dependent on stress-field multiaxiality. Similar applies to the uncoupled models of Huang [81] and Chaouadi et al. [82] as well. In these models, damages are calculated by post processing routines, based on the stress and strain fields determined experimentally and using FE analysis. Rice and Tracey considered growth of isolated void in remote uniform von Mises plastic field (Figure 4.13). The void is subject to remote stresses σ_1, σ_2, σ_3, and remote normal strains ε_1, ε_2, ε_3 .The model does not take account of interactions between voids, nor does it predict ultimate failure. A separate failure criterion must be applied to characterize microvoid coalescence. Using the Rice-Tracey model [78] and taking into account material hardening proposed by Beremin, void growth ratio (R/R_0) can be written as [83]:

$$\ln\left(\frac{R}{R_0}\right) = \int \alpha \exp\left(\beta \frac{\sigma_m}{\sigma_{eq}}\right) d\varepsilon_{eq}^{p} \tag{4.7}$$

where R stands for the actual mean void radius, R_0 is its initial value; σ_m / σ_{eq} represents stress state triaxiality, σ_m is mean stress, σ_{eq} is von Mises equivalent stress, and $d\varepsilon_{eq}^{p}$ is the equivalent plastic strain increment. Values of parameters α and β for Rice-Tracey model and two other models are given in Table (4.1).

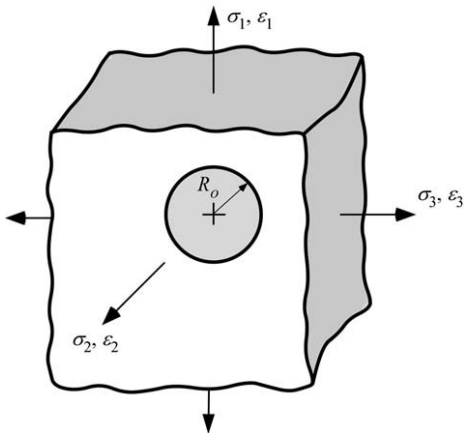

Figure 4.13 *Spherical void in a solid, subject to a triaxial stress state [43].*

Table 4.1 *Parameters α and β for various models [59].*

Model	α	β
Rice and Tracey	0.283	1.5
Hill	0.183	1.5
Huang, Marini et al.	0.427	1.5

According to the model, void presence does not significantly alter the behavior of the material [84], so that the damage parameter is not represented in the yield criterion.

In the Rice-Tracey model, significant influence of stress triaxiality on damage parameter and ductile fracture initiation can be seen from Equation (4.7). The increase of stress triaxiality (σ_m / σ_{eq}) directly causes the increase of void growth ratio R/R_0.

The model of Rice-Tracey has been modified by Huang [81], who introduced $\sigma_m / \sigma_{eq} = 1$ as the limit value for high stress triaxiality and separating the expressions defining the void growth for the two cases:

$$\ln\left(\frac{R}{R_0}\right) = 0.427 \int_0^{\varepsilon_{eq}^p} \left(\frac{\sigma_m}{\sigma_{eq}}\right)^{1/4} \exp\left(\frac{3\sigma_m}{2\sigma_{eq}}\right) d\varepsilon_{eq}^p \quad \text{for} \quad \sigma_m / \sigma_{eq} \le 1 \tag{4.8}$$

$$\ln\left(\frac{R}{R_0}\right) = 0.427 \int_0^{\varepsilon_{eq}^p} \exp\left(\frac{3\sigma_m}{2\sigma_{eq}}\right) d\varepsilon_{eq}^p \quad \text{for} \quad \sigma_m / \sigma_{eq} > 1 \tag{4.9}$$

Claouadi et al. [85] proposed another damage parameter for development of ductile fracture in the material-*damage work*, which is the work due to the plastic deformation, taking into account the change of volume at the local level around the void. The new parameter can be expressed as:

$$W_d = \int_0^{\varepsilon_{eq}^p} \left(\sigma_{eq} d\varepsilon_{eq}^p + 3\sigma_m \frac{dR}{R}\right) \tag{4.10}$$

One of the problems in application of the uncoupled approach is the treatment of the final stage of damage until the final failure. Beremin research group proposed a rather simple way to define the failure criterion, by integrating Equation (4.7) from zero to the experimentally determined strain at fracture ε_f [86]:

$$\ln\left(\frac{R}{R_0}\right)_c = 0.283 \int_0^{\varepsilon_f} \exp\left(\frac{3\sigma_m}{2\sigma_{eq}}\right) d\varepsilon_{eq}^p \tag{4.11}$$

where $(R/R_0)_c$ is the critical void growth ratio. Similar procedure can also be applied to the expressions of Huang and Chaouadi.

To apply Equation (4.11), it should be chosen the critical location(s) in the structure, e.g. crack tip, stress concentrators or regions with high stress triaxiality. But this change is not

significant, which was a conclusion of the round robin project dedicated to local approach to fracture. According to Chaouadi et al. [85], parameter W_{dc} (critical damage work) obtained using the parameters W_{dc} and $(R/R_0)_c$ do not differ significantly, because the damage work concept is derived on the basis of the model of Rice and Tracey.

The advantages of the uncoupled approach are required simple numerical procedure and possibility to use the results of a finite element analysis for many post-processing routines. However, significant disadvantages of this approach are modeling of the final stage of ductile fracture-void coalescence and nucleation of so-called secondary voids during the increase of the external loading [86].

4.5.2 Micromechanical coupled models

In the past two decades, more and more attention has been paid to and research efforts directed to the so-called coupled models of damage, where the damage parameter has been "built into" numerical procedure and is estimated by processing of FE elasto-plastic evaluation. The coupled approaches to material damage, ductile fracture initiation and propagation consider material as a porous medium, where the influence of nucleated voids on the stress-strain state and plastic flow cannot be avoided. The existence of voids in the plastically deforming metallic matrix is quantified through a scalar quantity-void volume fraction or porosity f:

$$f = \frac{V_{\text{voids}}}{V} \tag{4.12}$$

where V_{voids} is volume of all voids in the analyzed material volume V [86].

Based on the work of McClintock [79] and Rice and Tracey [78], Gurson [77] derived several models of void-containing unit cells, obtaining the yield criterion of a porous material that become the basis for many often-used models of coupled approach:

$$\phi = \frac{3S_{ij}S_{ij}}{2\sigma_Y^{\,2}} + 2f\cosh\left(\frac{3\sigma_m}{2\sigma_Y}\right) - \left(1+f^2\right) = 0 \tag{4.13}$$

where S_{ij} stands for the deviatoric components of the stress tensor, σ_m is the mean stress, σ_Y is the yield stress of the matrix material, and f is the void volume fraction. The behavior of material in this equation is assumed to be isotropic. The parameter f is

directly incorporated into Equation (4.13), which can calculate f during the processing procedure.

4.5.2.1 The Gurson-Tvergaard-Needleman model (GTN)

Based on the work of Rice and Tracey [78] and McClintok [79], Gurson further studied the plastic flow of a void containing material. In the model by Gurson the softening effect due to the presence of voids was reflected in a yielding function. By idealizing the true void distribution into a unit cell containing one spherical void and carrying out the rigid-plastic upper bound analysis. Thomason [87] and Tvergaard [80] have shown that Gurson yield criterion can capture the influence of the voids on the material damage during the early stage of ductile fracture (growth of voids), but the results deviate from the experimental ones with the increase of the external loading. Tvergaard [80] modified the original Gurson model to improve the material behavior assessment in the final stage of fracture. He has introduced two parameters of the constitutive model, $q_1 \geq 1$ and $q_2 \geq 1$, into the parts containing the void volume fraction, f, and mean stress, σ_m. Also the current yield stress of the material matrix σ has been introduced instead of yield stress σ_Y, to take the material hardening into account. The yield function of GTN model is:

$$\phi = \frac{3S_{ij}S_{ij}}{2\sigma^2} + 2q_1 f^* \cosh\left(\frac{3q_2\sigma_m}{2\sigma}\right) - \left[1 + q_3 f^{*2}\right] = 0 \tag{4.14}$$

where S_{ij} is the stress deviator; σ denotes the current yield stress of the material matrix; σ_m is the mean stress; q_1 and q_2 are the constitutive parameters; $q_3 = (q_1)^2$ and f^* is the so-called damage function proposed by Tvergaard and Needleman [3]:

$$f^* = \begin{cases} f & \text{for} \quad f \leq f_c \\ f_c + K(f - f_c) & \text{for} \quad f > f_c \end{cases} \tag{4.15}$$

where f_c is the critical void volume fraction corresponding to the occurrence of void coalescence; and the parameter K is the accelerating factor which defines the slope of sudden drop of force on the force - diameter reduction diagram:

$$K = \frac{f_u^* - f_c}{f_F - f_c} \tag{4.16}$$

where f_F is the void volume fraction at final fracture, $f_u^* = 1/q_1$ is the value of damage function at the moment of fracture.

The average void volume fraction of a material during a plastic strain increment will change, due partly to the growth of existing voids and partly to the nucleation of new voids. In the application of the Gurson model, a "homogenization" process is used. During a load increment, the increase of volume fraction from existing voids and newly nucleated voids are added together and homogenized as "one" void for the next load increment. The increase in the void volume fraction *f* during an increment of deformation can be expressed as:

$$\dot{f} = \dot{f}_{\text{growth}} + \dot{f}_{\text{nucleation}} \tag{4.17}$$

(a) Void growth

The void volume fraction due to growth can be estimated by:

$$\dot{f}_{\text{growth}} = (1-f)\dot{\varepsilon}_{ii}^{p} \tag{4.18}$$

where $\dot{\varepsilon}_{ii}^{P}$ is plastic part of the strain rate tensor.

For a given stress triaxiality, void growth with fixed q_1, q_2 is directly liked to the plastic strain and independent of material hardening exponent. Figure 4.14 shows the FE results of a plain strain cell model with fixed horizontal/vertical stress ratio 0.3 for different hardening materials. Low hardening results in higher void growth than high hardening.
In many practical applications of the Gurson model, the strain hardening effect on void growth can be neglected by choosing a fixed pair of constitutive parameters (q_1, q_2) [88].

(b) Modeling of void nucleation

Void growth may be treated independently of material (hardening); however, void nucleation is a highly material- dependent process. Void nucleation belongs to material intrinsic properties and governs material failure behavior. In general, it depends on particle strength, size and shape, and the hardening exponent of the matrix material. Void nucleation can be stress controlled or strain controlled. In the literature, strain controlled nucleation has been preferred, because it is easier to handle in the finite element implementation. The plastic-strain controlled mechanism can be employed to model void nucleation at small particles (less than 1 μm in size), which can be assumed to be

uniformly distributed in the matrix [76]. Thus, void nucleation in the model was considered to depend exclusively on the equivalent plastic strain in the matrix, $\dot{\varepsilon}_{eq}^{P}$:

$$\dot{f}_{\text{nucleation}} = A\dot{\varepsilon}_{eq}^{P} \tag{4.19}$$

The void nucleation intensity, A, is a function of the equivalent plastic strain, ε_{eq}^{p}, in the matrix material, and was assumed to follow a normal distribution as suggested by Chu and Needleman [89]:

$$A = \frac{f_N}{S_N\sqrt{2\pi}}\exp\left[-\frac{1}{2}\left(\frac{\varepsilon_{eq}^{p}-\varepsilon_N}{S_N}\right)^2\right] \tag{4.20}$$

where f_N is the void volume fraction of secondary-void forming particles, ε_N is the mean strain for void nucleation (the strain for which 50% particles are broken or separated from the matrix) and S_N is the corresponding standard deviation. Changing the standard deviation causes the change of the interval width corresponding to the nucleation of most voids.

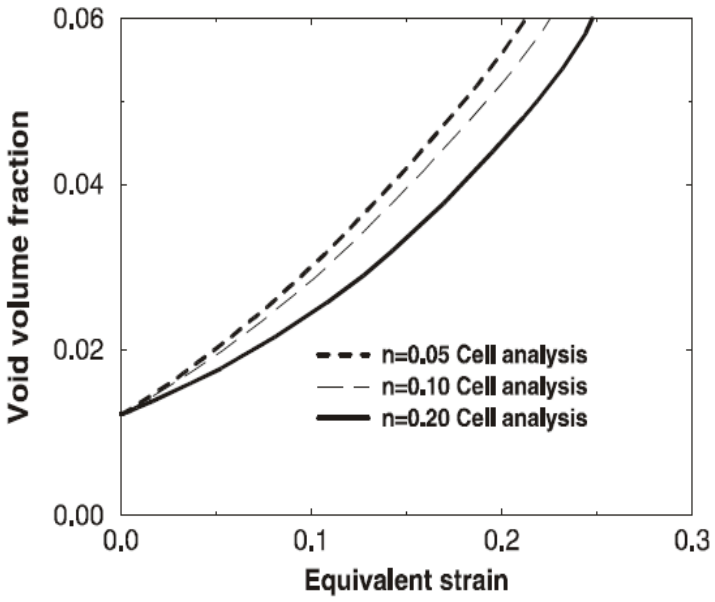

Figure 4.14 *The effect of hardening on void growth, where n is the material hardening exponent [88].*

There are three possible nucleation laws (Figure 4.15, where S stands for a stress or strain quantity); the first one is a cluster nucleation model. Cluster of voids will nucleate when some critical condition has been reached. For this model, it is usually assumed that

the voids will be nucleated in the beginning of plastic deformation. The parameter for this model is the initial void volume fraction f_0. The second model is called a continuous nucleation model. Gurland et al. [90] found that for some materials the number of voids increases with increasing plastic strain. There is also only one parameter in this nucleation model, $A_0 = \dot{f} / \dot{\varepsilon}_{eq}^{P}$. The third model is a statistical treatment of the first model, which indicates that most of the voids will be nucleated around the critical quantity S_c. Chu and Needleman have proposed the Equation (4.20) for strain controlled nucleation intensity A [88].

An important advantage of the Gurson model is that hydrostatic stress component influences the plastic flow of the material. This influence can be seen as deformation softening during the loading. Graphical interpretation of flow surface according to the Gurson and von Mises criteria with various values of porosity is shown in Figure 4.16.

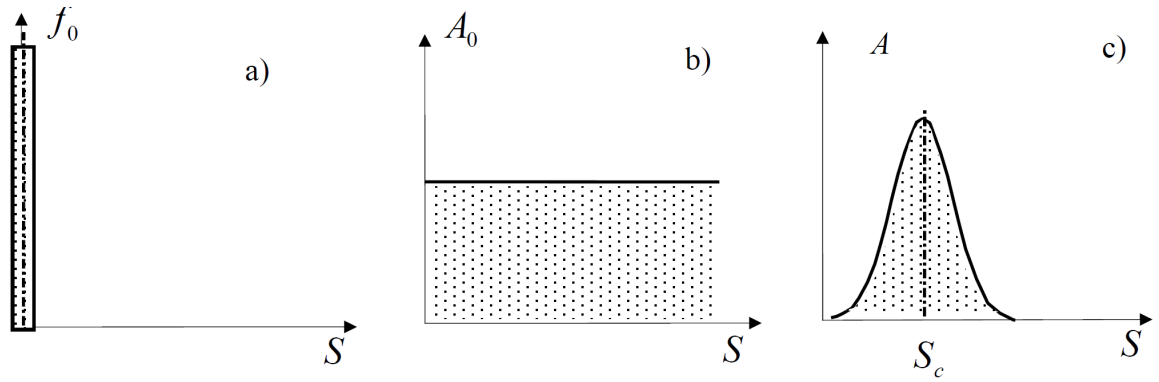

Figure 4.15 *Three void nucleation models: (a) cluster nucleation, (b) continuous nucleation and (c) statistical nucleation model [88].*

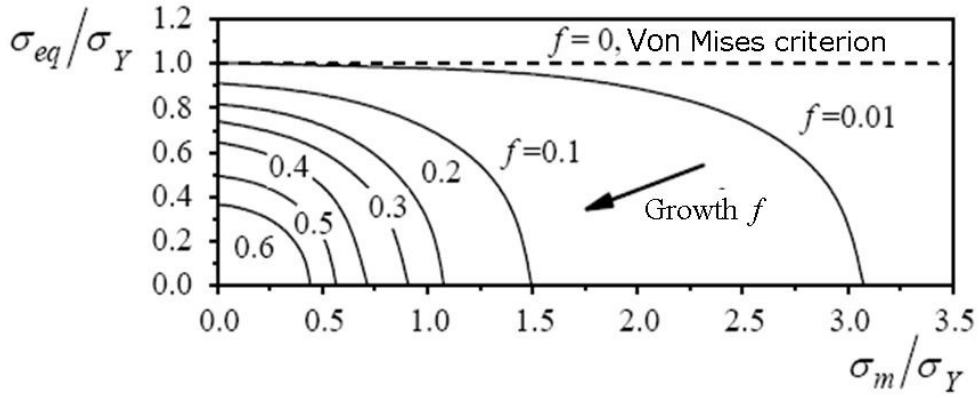

Figure 4.16 *Flow surfaces for Gurson and von Mises model [91].*

(c) GTN model parameters

To apply GTN model, nine parameters are necessary. They can be classified into two principle families [92]:

1. The "constitutive parameters": q_1, q_2 and q_3.
2. The "material parameters".

The material parameters are classified in two parts. Firstly "the initial material and nucleation parameters", which are determined as the initial void volume fraction f_0 and the void nucleation parameters f_N, ε_N and S_N. Secondly, "the critical and final failure parameters", the critical and final void volume fraction f_c and f_F.

In order to determine some parameters, a combination of numerical results and experimental data is necessary. Globally, there is no unique method to determine these parameters, which are not easy to define. Bensedddiq et al. [92] analyzed the large data available in the literature in order to examine the validity of the choices of these parameters. The following points can be summarized from the literature analysis:

(i) Determination of constitutive parameters: q_1, q_2 and q_3

Tvergaard et al. [3] has suggested fixing the q_1 and q_2 values at $q_1 = 1.5$ and $q_2 = 1$ in order to describe material ductile fracture. However, Gao et al. [93] showed the influence of yield stress and hardening exponent on q_1 and q_2 parameters in the range of stress triaxiality (2-3.3) with $\sigma_Y / E = 0.001 - 0.004$ (Table 4.2). Faleskog [94] indicates also that the two parameters depend on the material hardening exponent and material strength. Table 4.2 shows that the value of the constitutive parameter q_1 varies for many materials. However, this parameter is often fixed to 1.5 and $q_2 = 1$.

Table 4.2 *Optimal values for micro-mechanics parameters (q_1, q_2) [92].*

Hardening exponent	$\sigma_Y / E = 0.001$		$\sigma_Y / E = 0.002$		$\sigma_Y / E = 0.004$	
n	q_1	q_2	q_1	q_2	q_1	q_2
5	1.96	0.78	1.87	0.8	1.71	0.84
6.7	1.78	0.83	1.68	0.86	1.49	0.9
10	1.58	0.9	1.46	0.93	1.29	0.98

Dutta et al. [95] proposed another approach- dependence of q_2 on the distance of the point from the crack tip, r:

$$q_2 = 1 + q_{2a} e^{-(r/l_c)/q_{2b}} \tag{4.21}$$

where q_{2a} and q_{2b} are two new constants, defining the variation of q_2 in the vicinity of the crack tip [86].

(ii) Material parameters: f_0, f_c, f_F, f_N, ε_N, S_N and λ

Generally, the initial void volume fraction f_0 and volume fraction of void nucleating particle f_N are evaluated by microstructure observation of undamaged materials. In the initial stage of ductile fracture of steel, the voids nucleate mostly around the non-metallic inclusions. Therefore, the initial porosity f_0 is often assumed to be equal to the void volume fraction of non-metallic inclusions f_v, which can be determined by quantitative micro-structural analysis or evaluated from the chemical composition using Franklin's formula [96] based on; for most ductile steels, Manganese sulfides (MnS) and other oxide inclusions are the main particles involved in the ductile fracture process [97]. The volume fraction of MnS and Al_2O_3, f_v, can be estimated by formula:

$$f_v = 0.054\left(\%\mathrm{S} - \frac{0.001}{\%\mathrm{Mn}}\right) + 0.005\%\mathrm{O} \tag{4.22}$$

where %S , %Mn, and %O are the weight-% of sulfur, manganese, and oxides, respectively.

Rakin et al. [69] determined initial void volume fraction f_0 by microstructure examination using two measurement fields of tested material (Figure 4.17). One can clearly see a group of sulphides and one large oxide in the measurement fields, which show also spots of probable void nucleation, growth and coalescence, were marked by arrows.

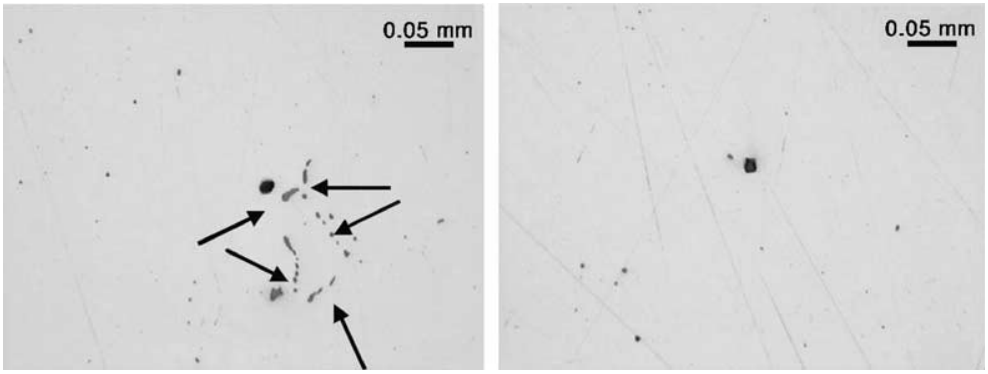

Figure 4.17 *Two optical micrographs of non-metallic inclusions [69].*

Volume fraction of sulphides and oxides in tested steel has been determined on base of equality with surface fraction:

$$V_v = A_A = \frac{A_i}{A_T} \tag{4.23}$$

where V_V and A_A are the volume and surface fraction of detected sulphides and oxides, respectively, A_i is the area of the detected inclusions and A_T is the measurement field area. f_0 is determined as a mean value of surface fraction of non-metallic inclusions for all used measurement fields:

$$f_0 = \overline{V}_V = \frac{\sum V_{Vi}}{n} \tag{4.24}$$

where n is a number of measurement fields [69].

Volume fraction of void nucleating particles f_N can be also determined by the lever rule, which is used for determination of volume fraction of iron carbides in steel. The lever rule is used to determine these particles content in a two-phase Fe-Fe_3C microstructure according to known chemical composition [59]:

$$\text{weight } \%\text{cem.} = \frac{\%C - 0.025}{6.67 - 0.025}.100\% \tag{4.25}$$

where %C is carbon content in used steel, 6.67 weight % of carbon is part in Fe_3C compound and 0.025 weight % is a carbon content in ferrite. The calculated value from Equation (4.25) is used as f_N in Chu-Needleman formulation.

According to the analysis which done by Beseddiq et al. [92] on the various results in the literature, the values of the nucleation parameters f_N, ε_N and S_N can be fixed arbitrarily. The values $\varepsilon_N = 0.3$ and $S_N = 0.1$ have been used in several studies, and they are determined by fitting.

The critical void volume fraction f_c was supposed to be a material constant and can be determined by fitting the numerical calculations with experimental results [98]. It is also assumed to be criterion for void coalescence appearance and independent of the initial value of the void volume fraction f_0, i.e. it does not matter whether it nucleates from large or small inclusions. Later on, with the advances of the study by Koplik and Needlman [99], Tvergaard commented that the critical void volume fraction should

depend on the initial void volume fraction, i.e. it should depend on the material. koplik and Needlman have also investigated the dependence of f_c on stress triaxiality and observed that the dependence can be neglected when the initial void volume fraction is very small, on the other hand, if the initial void volume fraction is large (>1%), the f_c at high stress triaxiality is significantly lower than that at low stress triaxiality. Tvergaard and Needleman [3] suggested that the value of f_c can be taken as constant $f_c = 0.15$ when the value of f_0 is small. Determination of the critical void volume fraction f_c is very important for application of Equation (4.15) and Equation (4.16). Different techniques are proposed in [72,98,100,101] for determining its value.

The original Gurson model itself can not predict the void coalescence, once the void coalescence has been determined to occur according to a criterion, the void coalescence process can be simulated by Equation (4.15) and Equation (4.16). The first part of Equation (4.15) can be applied before void coalescence, while the second one can be applied after the void coalescence has started to take the sudden loss of load carrying capacity into account (Figure 4.18).

The void volume fraction at final failure f_F is considered a parameter that may be determined from micro-structural observation of the fracture surfaces, but is a very difficult procedure. The studies show that f_F affects the post-initiation load diameter-reduction curve and that the smaller the f_F the faster load decreases [92]. Recently, Zhang et al. [26] have shown, using the unit cell model, that f_F depends on f_0, and can approximately be calculated as:

$$f_F = 0.15 + 2f_0 \tag{4.26}$$

This signifies that f_F can be fixed to a first approximation at 0.15 for low f_0 values. This parameter f_F can take values between 0.15 and 0.44 as used in many investigations [102-104]. The void volume fraction at final failure f_F is also influenced by stress triaxiality *T*. Figure 4.19 shows the influence of stress triaxiality on void volume fraction at final failure with two different initial void volume fractions f_0 [88].

According to numerous researchers [69,100,105], the mean free path λ between the non-metallic inclusions was used to define FE size in numerical analysis. In order to determine mean free path between non-metallic inclusions according to [106], in each

measurement field five horizontal measuring lines are drawn. Then the value of N_L is determined, representing the number of interception of oxides or sulphides per measurement line unit [69]:

$$N_L = \frac{N_i}{L_T} \tag{4.27}$$

where N_i is the number of inclusions interceptions and L_T is the true length of scan lines (number of scan lines multiplied by length of scan lines divided by the applied magnification).

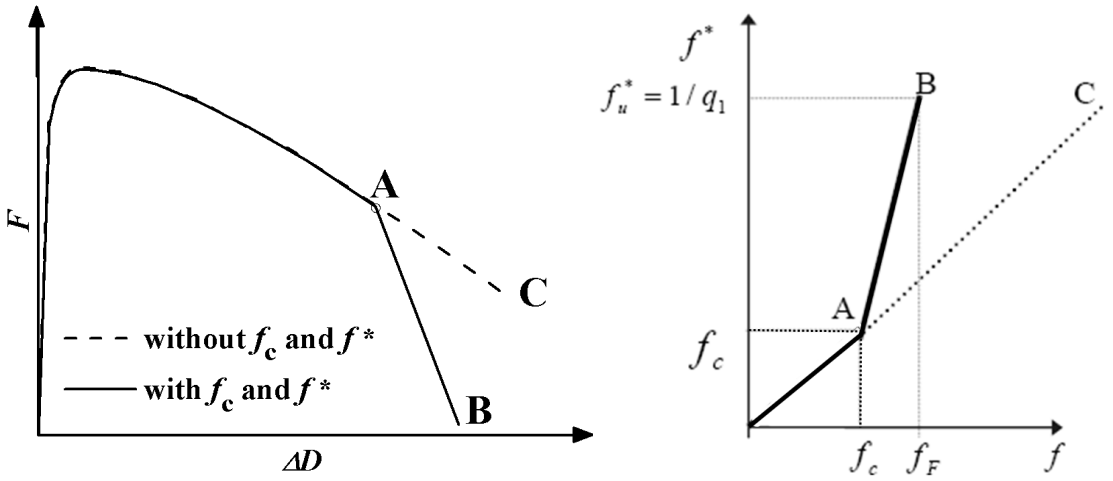

Figure 4.18 *Schematic plot of Equation (4.15) and Equation (4.16)- response of a material point in FE analysis with (line AB) and without (Line AC) Equation (4.15) and Equation (4.16) [88].*

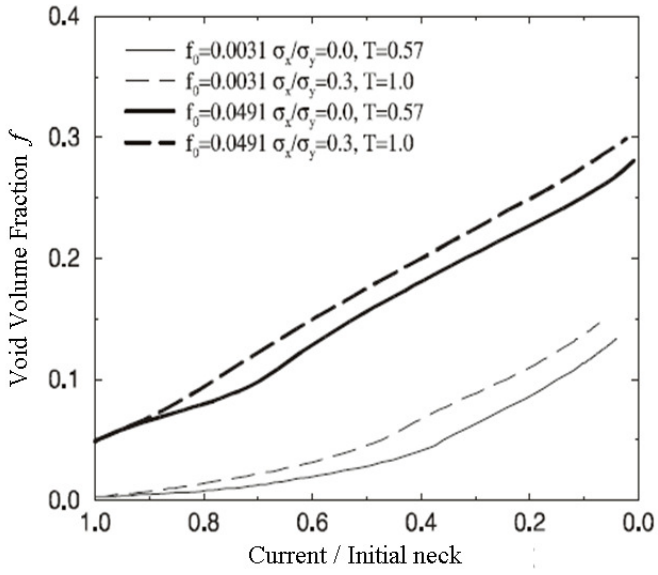

Figure 4.19 *Results of void volume fraction versus neck development from 2D plane strain cell model FEM analyses. In the legend, T is the stress triaxiality [88].*

The mean free path λ, as the mean edge-to-edge distance between inclusions, is determined as follows:

$$\lambda = \frac{1 - A_A}{N_L} \tag{4.28}$$

where, A_A is the area fraction of inclusions.

The inclusions should be located in each of the measurement fields as a condition for application of the presented procedure. The average of mean free path $\bar{\lambda}$ is determined on basis of calculated values of λ in all measurement fields:

$$\bar{\lambda} = \frac{\sum \lambda_i}{n} \tag{4.29}$$

where n is a number of measurement fields.

4.5.2.2 Complete Gurson model (CGM)

The GTN model describes the material as a continuum weakened by the presence of voids. Such representation corresponds to so-called homogenous deformation mode. The damage function (Equation (4.15)) proposed by Tvergaard and Needleman [3] can be used to model the loss of load-carrying capacity of the material, but it cannot be directly liked with the actual processes during the last stage of ductile fracture. Thomason [76] proposed a more realistic failure criterion, which is based on the analysis of deformation in the interviod ligaments-localized deformation mode [86]. Thomason found that the localized deformation mode by interviod matrix necking can be described by a plastic limit load model. It is important to note that the plastic limit load of a void-containing cell is not fixed but is strongly dependent on the void/matrix geometry. For a material without void, the plastic limit load is infinite. At the starting of plastic deformation of a void containing material, the void dimension is very small and the corresponding plastic limit load is very large. The homogenous deformation mode thus prevails. When a void starts to grow, the plastic limit load decreases, which indicates that the possibility of plastic localization increases. The homogenous deformation mode will be terminated once the localized mode of deformation becomes possible. The localized deformation mode is characterized by the maximum principal stress, $\sigma_1^{\text{Localized}}$, which represents the micro-capacity of a voided material to resist the localized deformation, and the homogenous

deformation mode is represented by the applied maximum principal stress, $\sigma_1^{\text{Homogenous}}$, at the current yield surface. The condition for void coalescence by internal necking of the interviod matrix can be written:

$$\sigma_1^{\text{Homogenous}} = \sigma_1^{\text{Localized}} \tag{4.30}$$

The competition of two deformation modes in the Thomason theory can be shown in Figure 4.20.

Zhang et al. [26] made a significant modification of the GTN model- they applied Thomason's void coalescence criterion based on the plastic limit load model (with the assumption that all the voids remain spherical during the increase of the external loading), thus introducing the so-called *Complete Gurson Model* (CGM).

According to GTN model, the critical void volume fraction f_c is a material constant, while in the complete Gurson Model, f_c is not a material constant, but the material response to coalescence. Zhang et al. shows that f_c decreases when the stress triaxiality ratio T increases (Figure 4.21). However, other authors note that f_c can be taken as constant only for small f_0 values as it can also be seen in the Figure 4.21. Zhang et al. has shown also that, f_c is a strong function of the initial void volume fraction f_0.

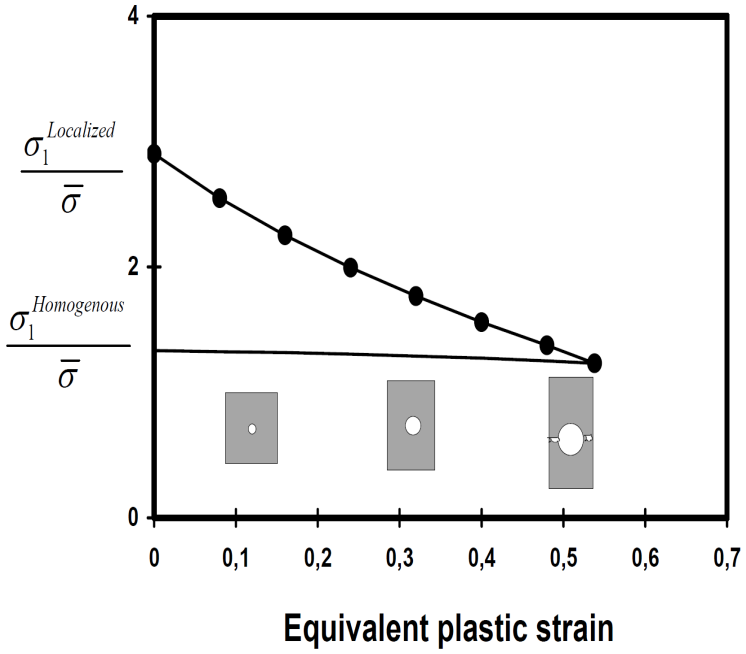

Figure 4.20 *The competition of the two deformation modes in the Thomason theory, here $\bar{\sigma}$ is the yield stress of the matrix material [88].*

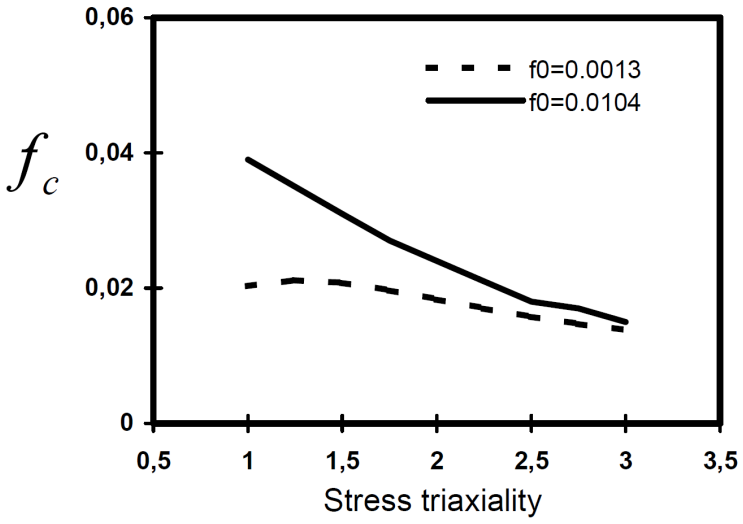

Figure 4.21 *Critical void volume fractions versus stress triaxiality [26].*

In the complete Gurson model [26], the plastic limit load criterion by Thomason for coalescence for general 3D problems at a specific material point can be written as follows:

$$\frac{\sigma_1}{\bar{\sigma}} < \left[\alpha_{\text{coalescence}} \left(\frac{1}{r_{\text{voids}}} - 1 \right)^2 + \frac{\beta_{\text{coalescence}}}{r_{\text{voids}}} \right] \left(1 - \pi r_{\text{voids}}^2 \right) \quad \text{no coalescence occurs} \qquad (4.31a)$$

$$\frac{\sigma_1}{\bar{\sigma}} = \left[\alpha_{\text{coalescence}} \left(\frac{1}{r_{\text{voids}}} - 1 \right)^2 + \frac{\beta_{\text{coalescence}}}{r_{\text{voids}}} \right] \left(1 - \pi r_{\text{voids}}^2 \right) \quad \text{coalescence occurs} \qquad (4.31b)$$

where the first term is related to the homogeneous deformation state, and the second one to the plastic limit load needed for coalescence. In the previous expression, σ_1 is the current maximum principle stress, $\alpha_{\text{coalescence}} = 0.1$, $\beta_{\text{coalescence}} = 1.2$, $\bar{\sigma}$ is the flow stress of the matrix material and r_{voids} is the void space ratio, which is given by:

$$r_{\text{voids}} = \sqrt[3]{\left(\frac{3f}{4\pi} \right) e^{\varepsilon_1 + \varepsilon_2 + \varepsilon_3}} \Bigg/ \left(\frac{\sqrt{e^{\varepsilon_2 + \varepsilon_3}}}{2} \right) \qquad (4.32)$$

where f is the actual void volume fraction and $\varepsilon_1, \varepsilon_2$ and ε_3, the principle strains.

The complete Gurson model has been verified by Zhang et al. [26] for non-hardening materials ($\alpha_{\text{coalescence}} = 0.1$). in addition, Pardoen and Hutchinson [107] have shown that in the case of a Ramberg-Osgood material with a strain hardening exponent n, and considering that voids remain always spherical, better predictions are obtained with:

$$\alpha_{coalescence} = 0.12 + \frac{1.68}{n}, \qquad \beta_{\text{coalscence}} = 1.2 \tag{4.33}$$

The complete Gurson model has been implemented into the ABAQUS using the algorithms developed by Zhang via the material user subroutine UMAT [26].

Micromechanical models for ductile fracture prediction are being improved through many on-going investigations. One the aims is application of local approach to ductile and cleavage fracture in structural integrity assessment.

Chapter 5

Computational Fracture Mechanics

5.1 Introduction

The Finite Element Method (FEM) has been one of the most powerful numerical tools for the solution of the crack problem in fracture mechanics, since relatively few practical problems have closed form solutions. The finite element method is firmly established as a standard procedure for the solution of practical fracture problems. Various conventional engineering procedure and micromechanical models for determination fracture parameters such as; *J*-integral and stress intensity factor *K*, have been implemented into FE commercial codes such as ABAQUS. Using FEM with experimental data, ductile fracture initiation and crack propagation can be predicted micromechanically. The physical process of ductile fracture, which includes void nucleation, growth and coalescence, has been simulated by damage models. These damage models such as; Gurson-Tvergaard-Needleman (GTN) and complete Gurson model (CGM), are implemented in FE codes for determining fracture mechanics parameters. In finite element method, the structure of interest is divided into discrete shapes called finite elements. The finite elements are connected at node points, where continuity of the displacement field is enforced.

In this chapter, literature review has been presented about using finite element methods in fracture mechanics.

5.2 Linear-elastic finite element method

The use of finite element in prediction of fracture parameters such as; *J*-integral and stress intensity factor *K* require two important considerations:

(a) Modeling of crack tip singularity.

(b) Interpretation of finite element results.

5.2.1 Modeling of crack tip singularity

In order to represent stress and strain field singularities accurately, extremely fine mesh subdivisions is required in the vicinity of the crack tip. However, for the efficient numerical solution of fracture problems, it is advantageous to develop special crack tip elements, which directly model the $1/\sqrt{r}$ elastic strain field singularity. Certain element / node configuration produces such strain singularities. In other words, forcing the elements at the crack tip to exhibit a $1/\sqrt{r}$ strain singularity can improve accuracy and reduces the need for a high degree of mesh refinement at the crack tip. The moving of the mid-side nodes to the ¼ points in quadric isoparametric elements can produce the desired singularity. The strain matrix for a two-dimensional element can be written in the following form:

$$\varepsilon = [J]^{-1}[B^*]\begin{Bmatrix} u_i \\ v_i \end{Bmatrix} \tag{5.1}$$

$$[B^*] = \begin{bmatrix} \frac{\partial N_i}{\partial \xi} & 0 \\ 0 & \frac{\partial N_i}{\partial \eta} \\ \frac{\partial N_i}{\partial \eta} & \frac{\partial N_i}{\partial \xi} \end{bmatrix} \tag{5.2}$$

where ξ and η are the parametric coordinates of a point in the element. Since the nodal displacement $\{u_i, v_i\}$ are bounded, the strain matrix can only be singular if either $[B^*]$ or $[J]^{-1}$ is singular. In general, the shape function for an eight-noded quadratic element is quadratic, Equation (5.3). Thus all (N_i, $\frac{\partial N_i}{\partial \xi}$ or $\frac{\partial N_i}{\partial \eta}$) are non-singular, and $[J]$ must be the cause of singularity. A strain singularity can arise if the determinant of the Jacobian matrix vanishes at the crack tip, Equation (5.4).

$$\begin{aligned} N_i = &\left[(1+\xi\xi_i)\cdot(1+\eta\eta_i) - (1-\xi^2)\cdot(1+\eta\eta_i) - (1-\eta^2)\cdot(1+\xi\xi_i)\right]\frac{\xi_i^2\,\eta_i^2}{4} + \\ &+ (1-\xi^2)\cdot(1+\eta\eta_i)\cdot(1-\xi_i^2)\frac{\eta_i^2}{2} + (1-\eta^2)\cdot(1+\xi\xi_i)\cdot(1-\eta_i^2)\frac{\xi_i^2}{2} \end{aligned} \tag{5.3}$$

$$\det|J| = \frac{\partial(x,y)}{\partial(\xi,\eta)} = 0 \tag{5.4}$$

Let us consider a triangular element by collapsing nodes 1, 7, 8 from eight-noded quadratic element into one point and moving nodes 2 and 6 to the quarter points, Figure (5.1). Along the axis η= 0 the shape functions are:

$$N_1 = N_3 = N_5 = N_7 = -\frac{1}{4}(1-\xi^2) \tag{5.5}$$

$$N_2 = N_6 = \frac{1}{2}(1-\xi^2) \tag{5.6}$$

$$N_4 = N_8 = \frac{1}{2}(1-\xi) \tag{5.7}$$

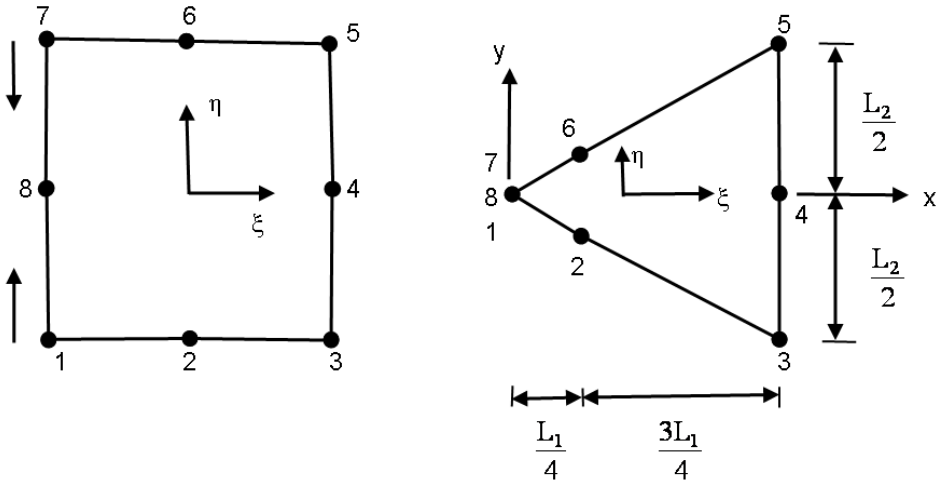

Figure 5.1 *Triangular element with mid side nodes at the quarter points [108].*

Locating the origin at node 1 as shown in Figure (5.1), we will get:

$$x_1 = x_7 = x_8 = 0 \tag{5.8}$$

$$x_2 = x_6 = \frac{L_1}{4} \tag{5.9}$$

$$x_3 = x_4 = x_5 = L_1 \tag{5.10}$$

The relation between x and η is given by:

$$x = \frac{L_1}{4}(1+\xi)^2 \tag{5.11}$$

$$\xi = -1 + 2\sqrt{\frac{x}{L_1}} \tag{5.12}$$

The displacement distribution along the x-axis is given by the Equation (5.5), Equation (5.6), and Equation (5.7):

$$u = -\frac{1}{4}(1-\xi^2)\cdot(u_1+u_3+u_5+u_7)+\frac{1}{2}(1-\xi^2)\cdot(u_4+u_8) \tag{5.13}$$

Solving for strain in x direction leads to the following equation:

$$\varepsilon_x = \frac{\partial u}{\partial x} = \frac{\partial \xi}{\partial x}\frac{\partial u}{\partial \xi} \tag{5.14}$$

$$\varepsilon_x = \frac{1}{L_1}(2u_1+u_3+u_5-2u_2-2u_6)-\frac{1}{2\sqrt{L_1 x}}(3u_1+u_3+u_4+u_5-2u_2-2u_6) \tag{5.15}$$

It is clear now that the strain component ε_x exhibits $1/\sqrt{r}$ singularity.

5.2.2 Interpretation of finite element results

The extrapolation procedures relate the analytical solution for the near crack tip stress and displacement fields to the values obtained from the finite element analysis, to provide the crack tip stress intensity factors. For linear elastic problem, the most often used methods for stress intensity factor evaluation are the following:

1. Strain energy release rate.
2. *J*–integral method.

5.2.3 *J*-integral method

As mentioned in the previous chapters, Rice [109] showed that, Figure 5.2:

$$J = \int_{\Gamma} W dy - T_i \frac{\partial u_i}{\partial x} ds \tag{5.16}$$

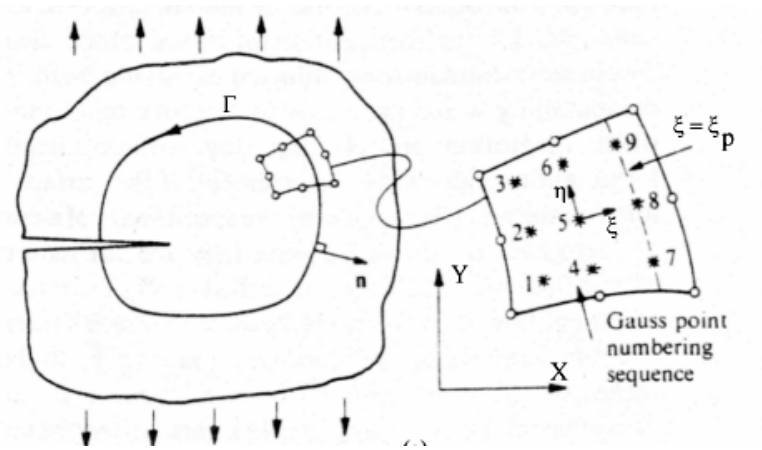

Figure 5.2 *Contour path for J-integral evaluation [108].*

For a closed path not containing the crack tip, $J = 0$. The J–integral can be directly related to the stress intensity factor:

$$K_I = \left(\frac{8\mu J}{1+\kappa} \right)^{1/2} \tag{5.17}$$

where μ is the shear modulus and κ is a parameter that allows consideration of plane stress and plane strain cases:

$$\kappa = \frac{3-\nu}{1+\nu} \qquad \text{(For plane stress)} \tag{5.18a}$$

$$\kappa = 3-4\nu \qquad \text{(For plane strain)} \tag{5.18b}$$

The path integration can be carried out element-by-element.

To find the stress intensity factor by the J–integral approach described previously, numerical integration techniques must be employed. Since the integral is path independent, the path can be always assumed with the line $\xi = \xi_p = constant$, as shown in Figure (5.2). The first requirement is to define the unit normal vector n to this line at any point. The vectors $\boldsymbol{A}$ and $\boldsymbol{B}$ which are respectively directed along the lines $\xi = constant$ and $\eta = constant$ are given by:

$$\mathbf{A}^T = \left[\frac{\partial x}{\partial \eta} \quad \frac{\partial y}{\partial \eta} \quad 0 \right], \quad \mathbf{B}^T = \left[\frac{\partial x}{\partial \xi} \quad \frac{\partial y}{\partial \xi} \quad 0 \right] \tag{5.19}$$

The vector $\boldsymbol{C}$ which is normal to the plane of the element is defined by the vector product of $\boldsymbol{A}$ and $\boldsymbol{B}$:

$$\mathbf{C}^T = \left[0 \quad 0 \quad \left(\frac{\partial x}{\partial \eta}\frac{\partial y}{\partial \xi} - \frac{\partial y}{\partial \eta}\frac{\partial x}{\partial \xi} \right) \right] \tag{5.20}$$

The vector ***D*** normal to the line $\xi = \xi_p$ is defined by:

$$\mathbf{D} = \mathbf{C} \times \mathbf{A} = \begin{Bmatrix} \dfrac{\partial y}{\partial \eta}\left(\dfrac{\partial y}{\partial \eta}\dfrac{\partial x}{\partial \xi} - \dfrac{\partial x}{\partial \eta}\dfrac{\partial y}{\partial \xi} \right) \\ \dfrac{\partial x}{\partial \eta}\left(\dfrac{\partial x}{\partial \eta}\dfrac{\partial y}{\partial \xi} - \dfrac{\partial y}{\partial \eta}\dfrac{\partial x}{\partial \xi} \right) \\ 0 \end{Bmatrix} = \begin{Bmatrix} D_1 \\ D_2 \\ 0 \end{Bmatrix} \tag{5.21}$$

Finally the unit normal is given as:

$$n^T = \begin{bmatrix} n_1 & n_2 & 0 \end{bmatrix} = \begin{bmatrix} \dfrac{D_1}{N} & \dfrac{D_2}{N} & 0 \end{bmatrix}; \; N = \sqrt{D_1^2 + D_2^2} \tag{5.22}$$

The elemental arc length along the line $\xi = \xi_p$ is given by:

$$ds = \sqrt{dx^2 + dy^2} = \sqrt{\left(\frac{\partial x}{\partial \eta} \right)^2 + \left(\frac{\partial y}{\partial \eta} \right)^2}\, d\eta \tag{5.23}$$

$$dy = \frac{\partial y}{\partial \eta} \partial \eta \tag{5.24a}$$

$$dx = \frac{\partial x}{\partial \eta} \partial \eta \tag{5.24b}$$

For plane problems, the strain energy density is:

$$W = \frac{1}{2}\left[\sigma_{xx}\varepsilon_{xx} + 2\sigma_{xy}\varepsilon_{xy} + \sigma_{yy}\varepsilon_{yy} \right] \tag{5.25}$$

Also the traction vector is:

$$\tau_i = \begin{Bmatrix} \sigma_{xx}n_1 + \sigma_{xy}n_2 \\ \sigma_{xy}n_1 + \sigma_{yy}n_2 \\ 0 \end{Bmatrix} \tag{5.26}$$

so, that

$$\tau_i \frac{\partial u_i}{\partial x} = \left(\sigma_{xx} n_1 + \sigma_{xy} n_2\right)\frac{\partial u}{\partial x} + \left(\sigma_{xy} n_1 + \sigma_{yy} n_2\right)\frac{\partial v}{\partial x} \tag{5.27}$$

Finally, one gets the expression for *J*-integral along $\xi = \xi_p$ of an element:

$$\begin{aligned} J_e = \int_{-1}^{1} \Bigg\{ & \frac{1}{2}\left[\sigma_{xx}\frac{\partial u}{\partial x} + \sigma_{xy}\left(\frac{\partial u}{\partial y} + \frac{\partial v}{\partial x}\right) + \sigma_{yy}\frac{\partial v}{\partial y}\right]\frac{\partial y}{\partial \eta} - \\ & - \left[\left(\sigma_{xx} n_1 + \sigma_{xy} n_2\right)\frac{\partial u}{\partial x} + \left(\sigma_{xy} n_1 + \sigma_{yy} n_2\right)\frac{\partial v}{\partial x}\right]\sqrt{\left(\frac{\partial x}{\partial \eta}\right)^2 + \left(\frac{\partial y}{\partial \eta}\right)^2} \Bigg\} d\eta \end{aligned} \tag{5.28}$$

For any other path similar expressions can be derived.

5.3 Elastic-plastic finite element method

For elastic–plastic solution, a non-linear finite element should be applied, where a set of linear equations is used to predict the response of a non-linear solution. Non-linear stress strain relationship is a common cause of non-linear structural behavior. A series of successive linear approximation with correction are needed to solve non-linear problem.

One approach to non-linear solution is to separate the load into a series of increments. At each completion of load increment, the stiffness matrix is adjusted to reflect non-linear changes in structural stiffness matrix. Unfortunately, a pure incremental approach accumulates the errors within each load increment, causing the final results to be out of equilibrium, Figure 5.3(a). Newton-Raphson equilibrium iterations overcome this difficulty: at the end of each load increment the solution is driven to equilibrium convergence within some tolerance limit. This iterative procedure continues until the solution converges, Figure 5.3(b).

In some non-linear analyses of physically unstable systems the slopes of the tangent stiffness matrix become zero or negative, causing convergence difficulties. The arc-length method forces the Newton-Raphson method to converge along an arc, thereby often preventing divergence to happen, Figure 5.4.

5.4 Elastic-plastic material deformation

When material deforms elastically, an explicit relation between stress and strain describes its behavior under the applied load. When higher load is applied, a yielding of

the material commences indicating the onset of plastic deformation and for any further increase in the applied load, post–yield behavior commences where the deformation is made up of elastic and plastic components, Figure 5.5.

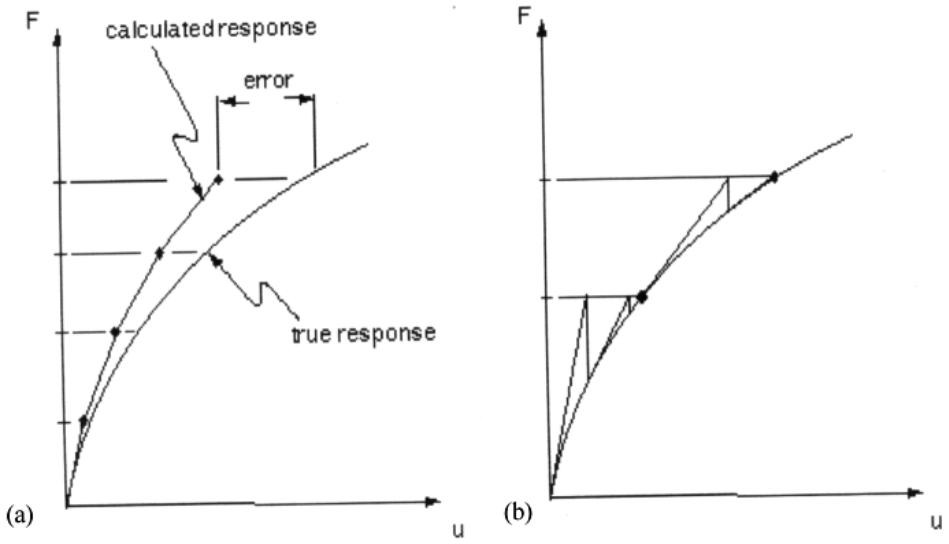

Figure 5.3 *Pure incremental approach vs. Newton-Raphson approach [110].*

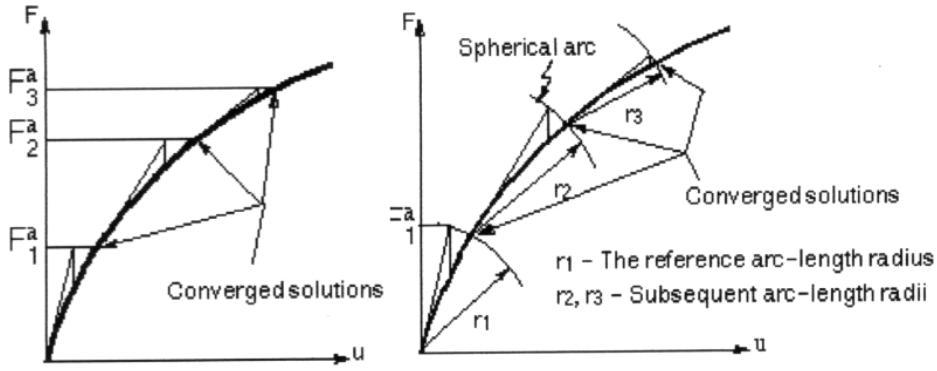

Figure 5.4 *Traditional Newton-Raphson method vs. arc-length method [110].*

5.4.1 Linear elastic deformation

Before the onset of plastic yielding the stress–strain relationship is given by linear elastic expression:

$$\sigma = D \cdot \varepsilon \tag{5.29}$$

where σ is stress, ε is strain and D is stress–strain constitutive matrix.

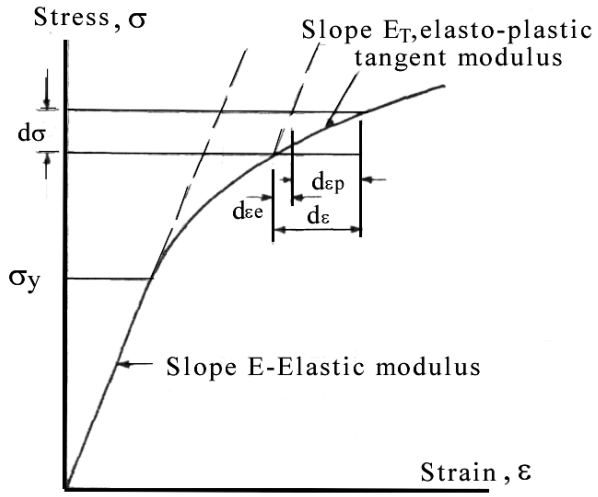

Figure 5.5 *Elastic-plastic strain hardening behavior for uniaxial case [108].*

5.4.2 The yielding criteria

The yielding criteria determine the stress level at which plastic deformation commences:

$$\sigma_1 - \sigma_2 = Y(\kappa) \qquad \text{(Tresca)} \tag{5.30}$$

$$\sqrt{\frac{1}{2}\left(\sigma_x^2 + \sigma_y^2 + \sigma_z^2\right) + \left(\tau_{xy}^2 + \tau_{yz}^2 + \tau_{xz}^2\right)} = k(\kappa) \qquad \text{(von Mises)} \tag{5.31}$$

where Y and k are the material stress and κ is the material hardening parameter and is given by:

$$\kappa = \int \sigma_{ij} \left(d\varepsilon_{ij}\right)_p \tag{5.32}$$

5.4.3 Elastic-plastic deformation

The changes of strain are assumed to be divisible into elastic and plastic components:

$$d\varepsilon_{ij} = \left(d\varepsilon_{ij}\right)_e + \left(d\varepsilon_{ij}\right)_p \tag{5.33}$$

The elastic strain component relationship is defined by Equation (5.29). The plastic strain component and stress relationship is given by:

$$\left(d\varepsilon_{ij}\right)_p = d\lambda \frac{\partial f}{\partial \sigma_{ij}} \tag{5.34}$$

where $d\lambda$ is proportionality constant called the plastic multiplier, and $\partial f / \partial \sigma_{ij}$ is a vector directed normal to the yield surface at the stress point under consideration.

5.5 Mesh design

The design of a finite element mesh is as much an art as it is a science. Modelling of crack by finite element mesh, in particular, require a certain amount of judgment on the part of the user, who should not lean completely on the automatic mesh generation capabilities of the commercial codes.

The common element types for crack problems are illustrated in Figure (5.6). The nine-node biquadrilateral Lagrangian element and the eight-node quadrilateral element are recommended for two-dimensional problems. The twenty-seven-node triquadrilateral Lagrangian element and the twenty-node quadratic element are recommended for three-dimensional problems.

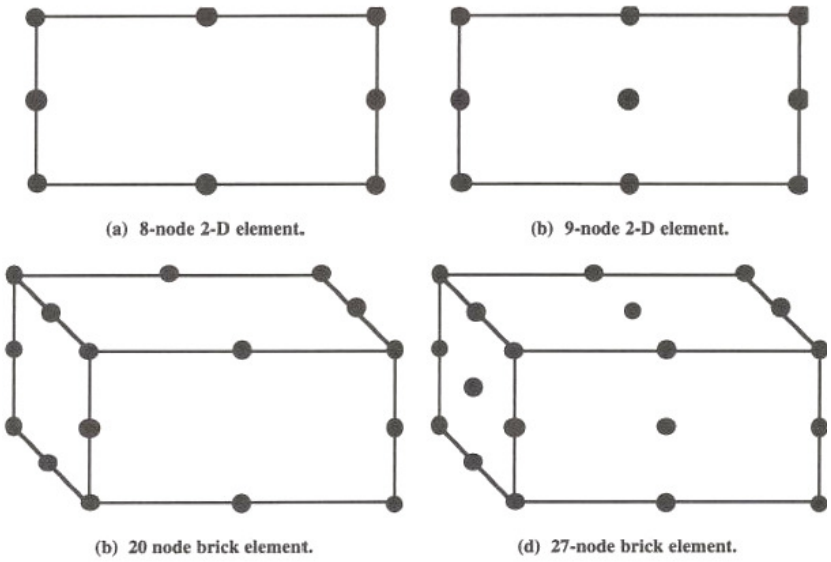

Figure 5.6 *Isoparametric elements for crack problem [111].*

Including the singularity in small-stain analysis (when geometry nonlinearities are ignored) often improves the accuracy of the *J*-integral, stress intensity factors, and the stress and strain calculations because the stresses and strains in the regions close to the crack tip are more accurate.

At the crack tip, four sided (eight-node) elements in two dimensions are often degenerated to triangles, Figure (5.7). Note that three nodes occupy the same point in

space. For the three dimension elements, the brick elements are degenerated to wedges Figure (5.8).

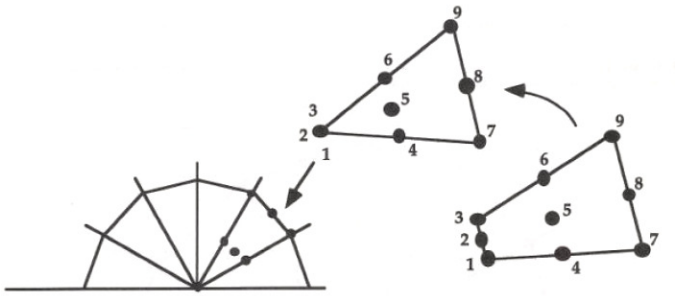

Figure 5.7 *Degeneration of the crack tip element [111].*

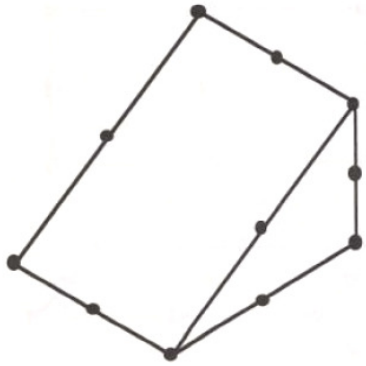

Figure 5.8 *Degeneration of the crack tip element [111].*

If r the distance from the crack tip, the strain singularity in small-strain analysis in elastic problems, the nodes at the crack tip should be tied, and the mid-side nodes moved to the ¼ points, Figure 5.9(a). Such a modification results in a $1/\sqrt{r}$ strain singularity in the element, which enhance numerical accuracy. In elastic–plastic problems, the plastic zone forms, so the strain singularity becomes of $1/r$ type. Figure 5.9(b) shows an element that provides the desired strain singularity under fully plastic conditions. The element has untied crack tip nodes and the location of mid-side nodes is unchanged. This element produces the $1/r$ strain singularity, which is appropriate for the actual crack tip strain field for fully plastic, non-hardening materials. This element also enables the crack tip blunting and computation of the crack tip opening displacement, Figures 5.10.

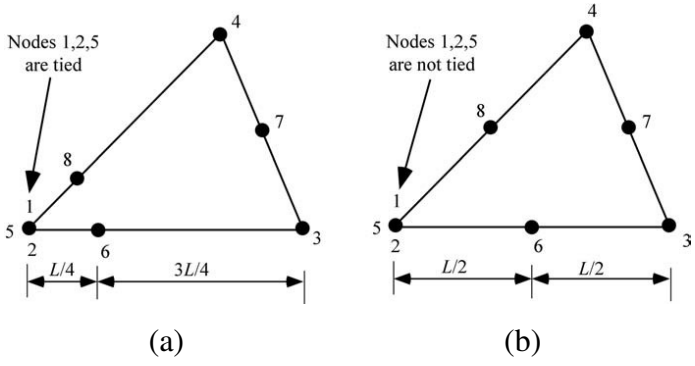

Figure 5.9 *Crack tip elements: (a) Elastic and (b) elastic-plastic [111].*

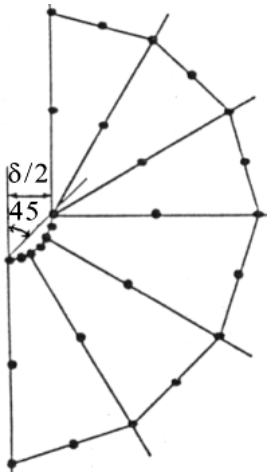

Figure 5.10 *Deformation of elastic-plastic crack tip element [111].*

For typical problems, the most efficient mesh design for the crack-tip regions has proven to be the "spider-web" configuration. This spider-web design facilitates a smooth transition from a fine mesh at the tip to a coarser mesh remote from the tip, e.g., Figure 5.11 shows a half-symmetric model of a two-dimensional simple cracked body. The spider-web meshing concept can be extended to three-dimensional problems, e. g., Figure 5.12 shows a quarter-symmetric model of a semielliptical surface crack in a plate.

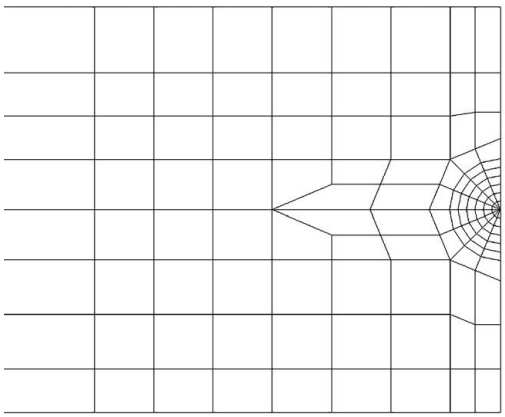

Figure 5.11 *Half-symmetric two-dimensional model of an edge-cracked plate [43].*

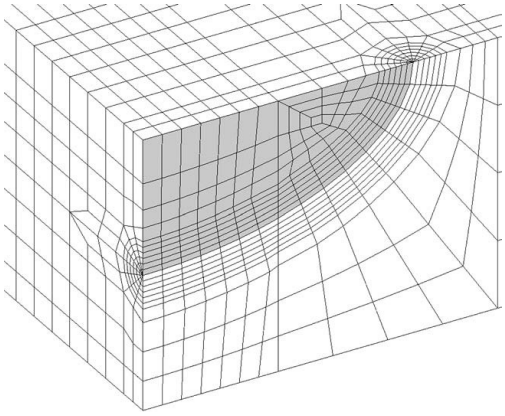

Figure 5.12 *Quarter-symmetric three-dimensional model of a semielliptical surface crack in a plate. The crack face is highlighted in grey [43].*

Another problem in finite element modeling is the point load, which is a kind of singularity by itself. The proper methods for applying the point load are illustrated in Figure 5.13.

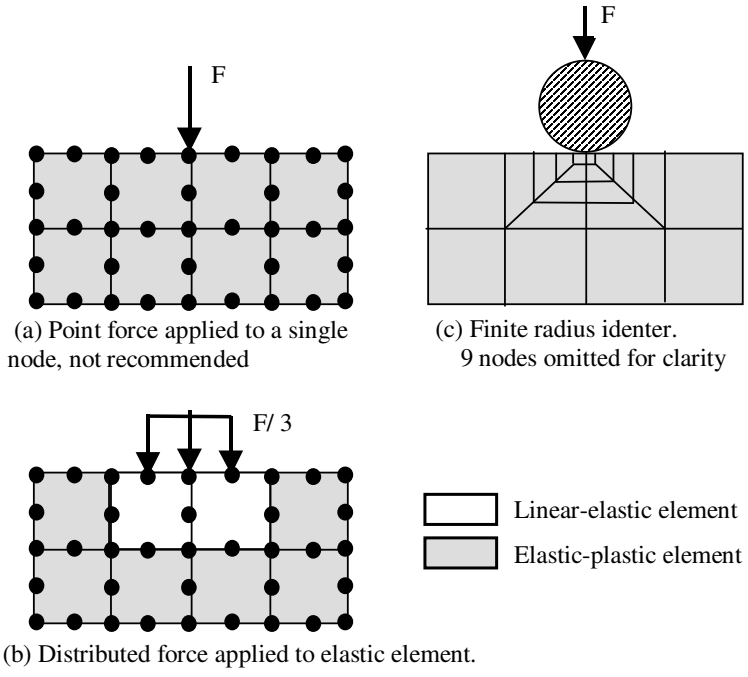

Figure 5.13 *Method of applying force to a boundary: (a) improper (b, c) proper methods [111].*

5.6 Numerical modeling of crack growth

Although most computational fracture mechanics analyses are performed on stationary cracks, there are instances where it is desirable to analyze crack growth. Crack growth in finite element model often required a special meshing strategy, and the analysis must include a criterion for crack advance. Crack growth requires a single mesh such as; cell mesh configuration, which enables to simulate it easily. Figure 5.14 shows an example of a cell mesh for semielliptical surface crack.

Generally there are four possible methods to simulate crack propagation in a cell mesh [112,113]:

(a) Element deleting from the model once a failure criterion is reached; e. g. ductile crack growth can be simulated in a cell mesh using the Gurson-Tvergaard plasticity model.

(b) Node releasing at specific load steps or according to a failure criterion.

(c) Element splitting.

(d) Stiffness decreasing.

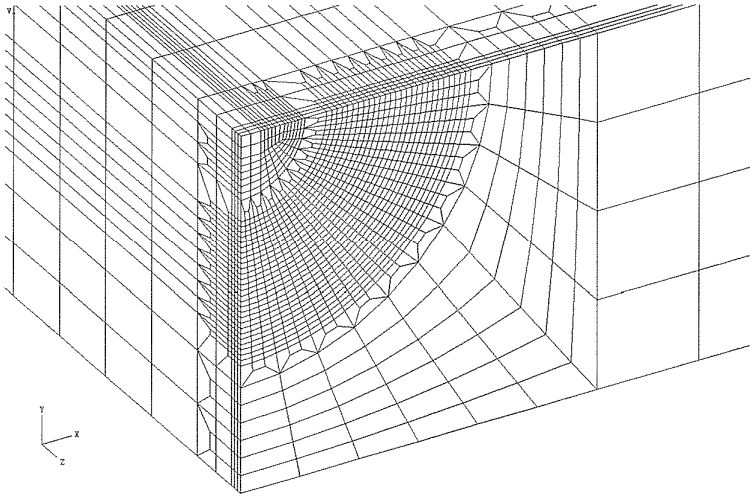

Figure 5.14 *Cell-type mesh for analysis of crack growth in a semielliptical surface crack in a flat plate [43].*

Irrespective of the numerical crack growth strategy, each increment of crack growth corresponds to the element size. For this reason the crack growth response in a finite element simulation is mesh dependent. In real materials, the crack growth response (e.g., the *J* resistance curve) depends on material length scales such as inclusion spacing (mean free path between non-metallic inclusions). A finite element continuum model does not

include microstructural features such as inclusions, so element size is the only available length scale to govern crack growth. Crack growth simulations usually need to be tuned to match experimental data. One of the key tuning parameters is the element size in the cell zone on the crack plane [43].

5.7 ESIS recommendation for use of FEM in fracture mechanics

1. For new problems, different mesh refinement is advisable including the known crack tip pattern (Figure 5.15).

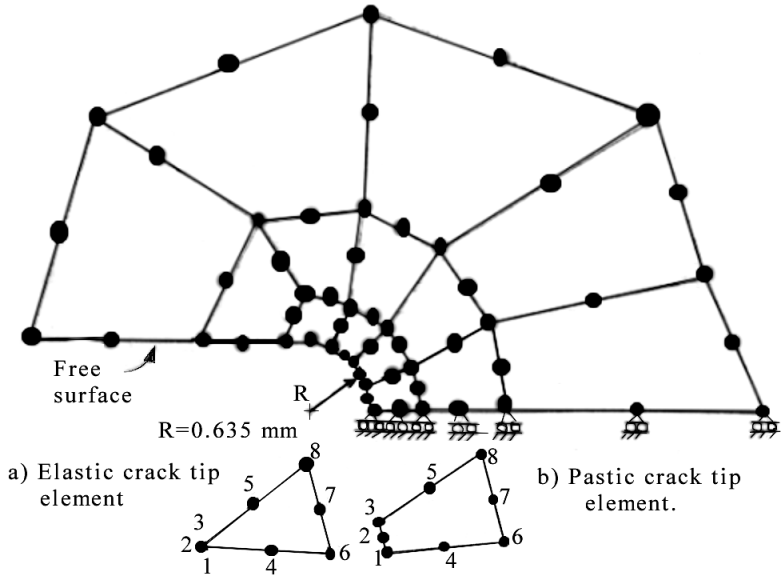

Figure 5.15 *Crack tip mesh pattern.*

2. Isoparametric elements with quadrilateral shape function (8-node for 2D, 20-node for 3D) are recommended.
3. The elements should be rectangular, skewed element should be avoided in region of high strain gradient.
4. In the region of transition, the sides of elements from small to larger should not be larger more than twice of smaller side.
5. For elastic analysis, collapsed isoparametric, triangle crack tip elements with one crack tip node and quarter–point mid-side nodes ($1/\sqrt{r}$ singularity), Figure 5.15(a).
6. For elastic–plastic analysis collapsed isoparametric triangle crack tip element with independent crack–tip nodes and mid-side nodes lying in the middle ($1/r$ singularity), Figure 5.15(b).

7. For non–linear analysis, limit the number of iteration to 10 for each load step to converge and avoid nodal point loads.
8. If large strains and large deformation are taken into account, true stress–strain curve should be used.

5.8 Damage modeling in finite element method

FE codes such as ABAQUS offer a general framework for material failure modeling that allows the combination of multiple failure mechanisms acting simultaneously on the same material. Material failure modeling can be applied to cracked or uncracked structures. Material failure refers to the complete loss of load-carrying capacity that results from progressive degradation of the material stiffness. The stiffness degradation process is modeled using damage mechanics. Figure 5.16 shows typical uniaxial stress-strain of a metal specimen as an example for using FEM in damage modeling. Figure 5.16 shows that the material response is initially linear elastic, a - b, followed by plastic yielding with strain hardening, b - c. Beyond point c there is a marked reduction of load-carrying capacity until rupture, c - d. The deformation during this last phase is localized in a neck region of the specimen. Point (c) identifies the material state at the onset of damage, which is referred to as the damage initiation criterion. Beyond this point, the stress-strain response c - d is governed by the evolution of the degradation of the stiffness in the region of strain localization. In the context of damage mechanics c - d can be viewed as the degraded response of the curve c - d′ that the material would have followed in the absence of damage [114].

Thus, in FE codes such as ABAQUS, the specification of a failure mechanism consists of four distinct parts as shown in Figure 5.16:

- The definition of the effective (or undamaged) material response (a - b - c- d′)
- A damage initiation criterion (point c),
- A damage evolution law (c - d), and
- A choice of element deletion whereby elements can be removed from the calculations once the material stiffness is fully degraded (point d).

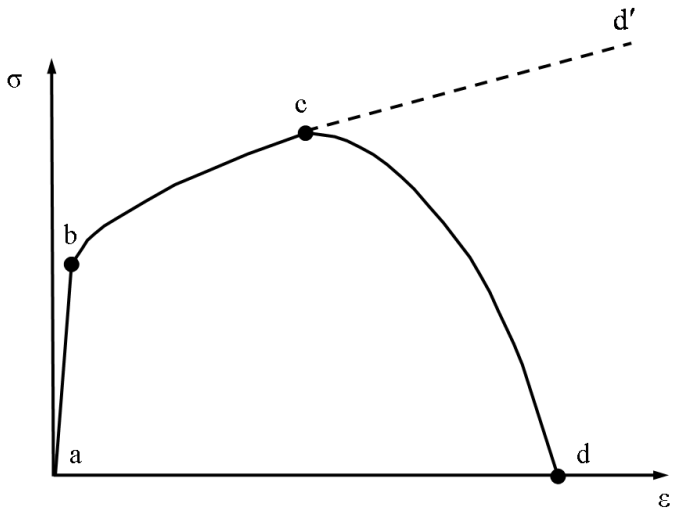

Figure 5.16 *Typical uniaxial stress-strain response of a metal specimen [114].*

In order to understand the ductile fracture behavior of structures, modeling of stable crack growth is required. Local approach can be used for crack growth modeling. In case of the some uncoupled micromechanical models, crack growth can be modeled using the node release technique, controlled by the critical value of damage parameter in the element ahead the crack tip. Similar procedure can be applied for the coupled models, using the critical value of appropriate damage parameter. Micromechanical coupled models offer another technique to simulate advance of crack. Advance of crack can be regarded as loss of material load-carrying capacity in the ligament ahead the crack tip. As the criterion for ductile fracture initiation is satisfied, the element ahead the current crack tip fails, according to the used micromechanical model [88].

Unlike the coupled micromechanical models, where the influence of the voids is defined through void volume fraction, there are techniques that include modeling of each void, using a very refined mesh around them. This approach is used by Tvegraad and Hutchinson [115] and Tvergaard [116], and the mesh in the part of the ligament in front of the crack tip is shown in Figure 5.17. This technique of crack growth modeling is very time-consuming, required computational resources and only a few numbers of voids can be analyzed. On the other hand, it is very useful for detailed analysis of the void size and distribution effects on the fracture process and material behavior [88].

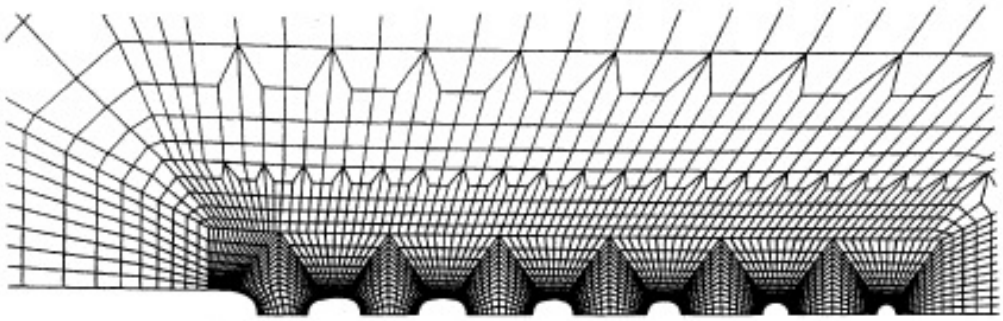

Figure 5.17 *Modeling of the voids in front of the crack tip [115].*

Chapter 6

Experimental Work of Weldments

6.1 Introduction

Welded structure must satisfy a certain level of safety and reliability in operation. Therefore, experimental study and interpretation of results are required especially for complex welded structures. Steel, NIOMOL 490K, which belongs to a group of micro-alloyed steels with molybdenum and minimum yield strength 490 MPa, is used for pressure vessels. Successful application of this steel depends on the degree of deterioration of the parent metal during welding. Practical application of welded structures made of steel, NIOMOL 490K, should be preceded by a detailed study of their mechanical properties to ensure a certain level of safety and reliability. Heat affected zone (HAZ) and weld metal (WM) are crucial regions for low toughness and higher transition temperature. These regions usually are the place of cracks especially in welded high strength steels. Therefore, study the effect of heterogeneity on crack initiation and propagation is required for their integrity assessment. Moreover, using standard fracture mechanics specimens such as single edge notched bending (SENB) with crack depth of $a/W = 0.5$ has a significantly higher geometry constraint than actual pressure vessel or pipeline with cracks, which therefore introduces a high degree of conservatism in engineering critical assessment of pressure vessels and pipelines. Thus, structural integrity of cracked pressure vessels and pipelines can be assessed by using specimens, which have a geometry constraint in front of the crack tip that is similar to the cracks in pressure vessels or pipes such as surface cracked tensile flat specimens.

The objective of experimental work was to determine mechanical properties of various zones of welded joint, especially heat - affected subzones (CGHAZ and FGHAZ), whose mechanical properties are difficultly determined by conventional methods. Moreover, the purpose of experimental work was to investigate the fracture behavior of

welded joints using micromechanical approaches, which need a combined experimental and numerical procedure. In addition, the objective of experimental research was to verify the investigations by numerical approaches.

6.2 Materials of welded joint regions

High strength low-alloyed (HSLA) steel, NIOMOL 490K has been used as base metal and consumable, VAC 60 Ni, as a filler metal. This kind of steel is used for steel structures such as pressure vessels. The chemical composition of base metal and consumable are listed in Table 6.1.

Table 6.1 *Chemical composition of base metal, NIOMOL 490K, and consumable in wt. %.*

Material	C	Si	Mn	P	S	Mo	Cr	Ni
NIOMOL 490K	0.123	0.33	0.56	0.003	0.002	0.34	0.57	0.13
VAC 60 Ni	0.096	0.58	1.24	0.013	0.160	0.02	0.07	0.03

6.3 Welding process and parameters

Shielded metal arc welding process (SMAW) was used with consumable; VAC 60Ni, wire diameter was 1.2 mm. Welding parameters (Table 6.2) were regulated to have good mechanical properties in welded joints. A mixture of shielding gases; 3.8% CO_2+93.7% Ar+2.5% O_2, was used in order to have a circular ferrite which raises toughness of welded joint. The amount of each gas in the mixture was chosen according to investigation in [117].

Table 6.2 *Welding parameters.*

Base material	Welding process	Electrode	Average voltage (V)	Average welding current (A)	Gas flow rate (l/min)	Electrode wire speed (cm/min)	Preheating temperature (ºC)	input energy (KJ/cm)
NIOMOL 490K	MIG	VAC 60 Ni	28	245	12	7	100	15-17

6.4 Welded joint and welding procedure

One plate, with dimensions (300×300×16 mm), was butt welded. The shape of welded joint was K, as shown in Figure 6.1 with plate geometry and cut specimens: single edge notched bend specimens with pre-cracks in HAZ and WM (SENB-HAZ and SENB-WM), specimen for quantitative microstructural analysis, uncracked tensile panel

(TP-uncracked), tensile panels with semi-elliptical surface cracks in HAZ and WM (TP-HAZ and TP-WM). The K shape of welded joint was selected for the research purpose to make easier positioning of a crack in HAZ. The number of passes was six, which were done in a specific order as shown in Figure 6.1(c) to avoid angular distortion in welded plate.

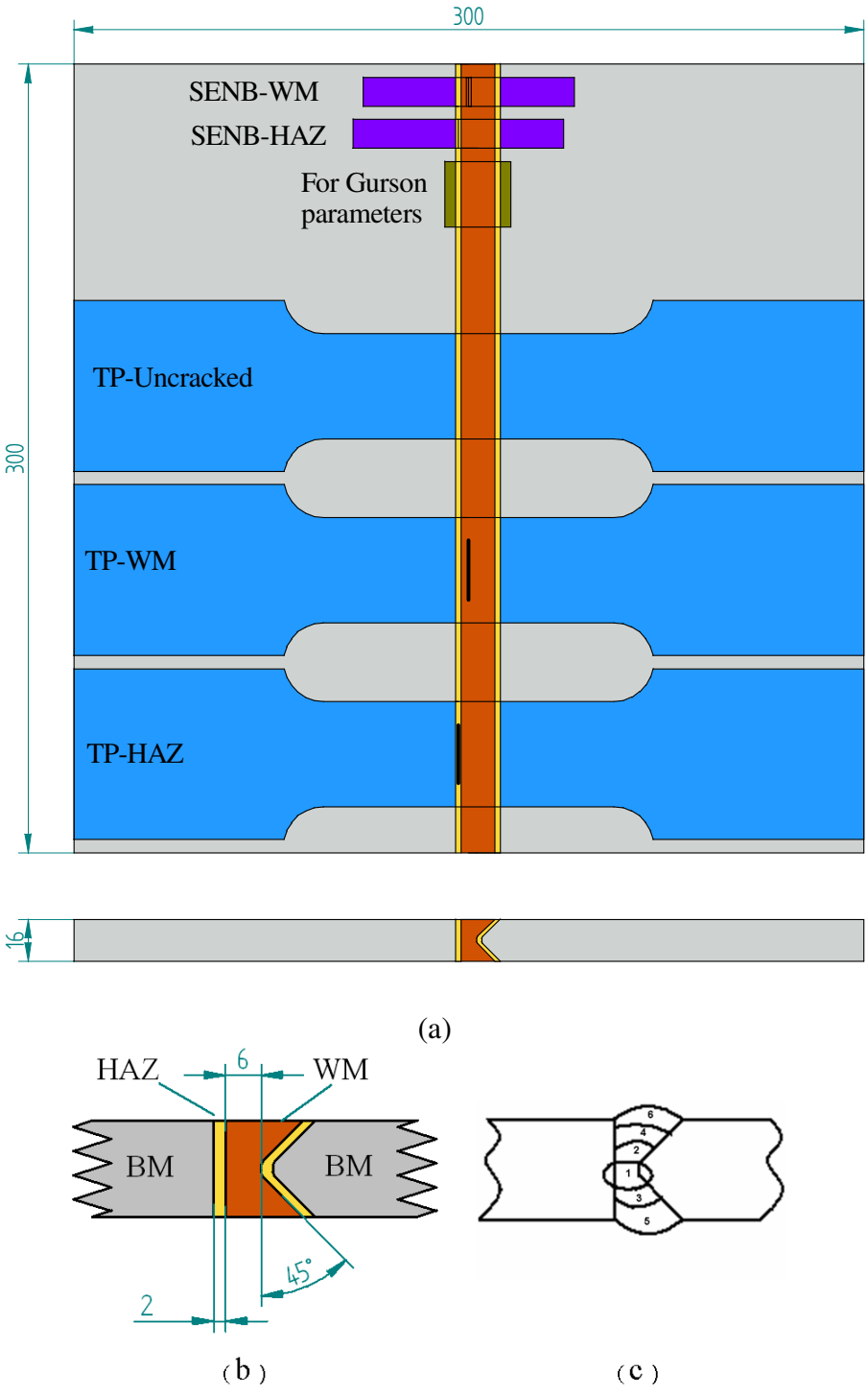

***Figure 6.1**: (a) geometry of welded plate with cut specimens, (b) detailed welded joint and (c) welding passes.*

6.5 Determination of micromechanical material parameters

Applying micromechanical approaches require determination of micromechanical parameters of used materials. Quantitative microstructural analysis was performed to estimate the micromechanical material parameters: volume fraction of non-metallic inclusions (f_v) and mean free path (λ) between the non-metallic inclusions for base metal (BM), heat affected zone (HAZ) and weld metal (WM) according to the explained procedure in chapter 4. In the initial stage of ductile fracture of steel, the voids nucleate mostly around non-metallic inclusions. Hence, the initial porosity (f_0) is here assumed to be equal to the volume fraction of non-metallic inclusions (f_v). Figure 6.2 shows two measurement fields for the heat affected zone and weld metal. Oxides and sulphides can be seen in the two measurement fields, which are marked by arrows.

Volume fraction of void nucleating particles (f_N), which represents the effect of secondary-voids on ductile fracture, was calculated from the content of carbon in tested materials using Equation (4.25). The f_N of HAZ and WM was calculated using the carbon content in BM and filler metal, respectively. The results of microstructural observations and calculated f_N for BM, HAZ and WM are given in Table 6.3.

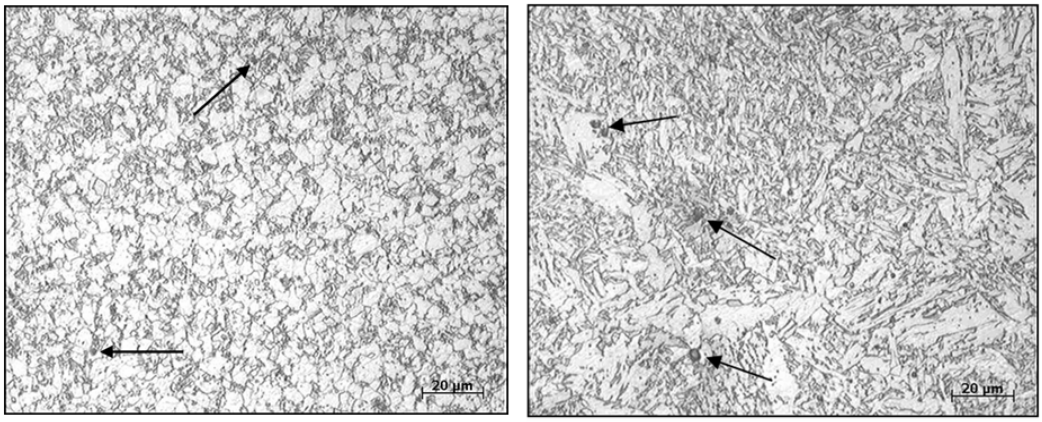

Figure 6.2 *Two optical micrographs of non-metallic inclusions in: (a) HAZ and (b) WM.*

Table 6.3 *Microstructural parameters of welded joint materials.*

Material	f_v	f_N	λ (µm)
BM (NIOMOL 490K)	0.0094	0.014748	578
HAZ	0.0086	0.014748	497
WM	0.0194	0.010685	202

6.6 Mechanical properties estimation for welded joint regions

Strength heterogeneity is pronounced in welded joints. Therefore, cracks usually initiate in welded joint regions such as; HAZ and WM. Structural integrity assessment of welded structures containing cracks requires elastic plastic mechanical properties of various welded joint materials. Precise estimation of mechanical properties for different welded joint regions is difficult due to metallurgical and strength heterogeneity especially for narrow heat affected subzones. Thus, comparison of experimental and numerical results provides approximate procedure to estimate mechanical properties of materials for various regions of welded joint.

The behavior of material properties of steel (stress-strain curve) are sometimes represented by bilinear relationship which can provide close approximation to real behavior. However, this relation could not provide accurate approximation for some ductile material properties beyond ultimate stress, which are required for application micromechanical models. In addition, mechanical properties of welded joint regions may be difficult to be determined in the direction of applied force, especially when the welded joint is subjected to transversally applied load. Therefore, attempts to estimate mechanical properties for various welded joint regions using combined experimental and numerical procedure are presented as alternative method to the conventional one. The power law relation, which has provided good approximation for stress-strain curves for investigated material, was used.

Smooth tensile plate (without cracks) was cut transversally from welded plate and tested at room temperature (Figure 6.3). Welded joint is divided into three zones: BM, HAZ and WM. The HAZ is divided into two subzones: coarse grain heat-affected zone CGHAZ and fine grain heat-affected zone FGHAZ. The specimen was pulled longitudinally, while force and remote displacement were monitored by testing machine (Figure 6.4). At the same time, longitudinal strains at different loads were measured for various regions of welded joints (WM, HAZ and BM) using ARAMIS strerometric measuring system (www.gom.com) [118] (Figure 6.3). Figure 6.5 shows ARAMIS measuring equipments with tested smooth tensile specimen.

The smooth tensile specimen (Figure 6.3) was numerically modeled using ABAQUS 6.7 with three-dimensional eight-node brick elements to simulate strains in various regions. Finer mesh has been used for the regions where the strains were measured. Due

to the symmetry about two planes: X-Y and X-Z, only one quarter of specimen was numerically modeled as shown in Figure 6.6 with boundary conditions and specimen geometry. One side of specimen was fixed, while prescribed displacement was applied to the other one representing applied load.

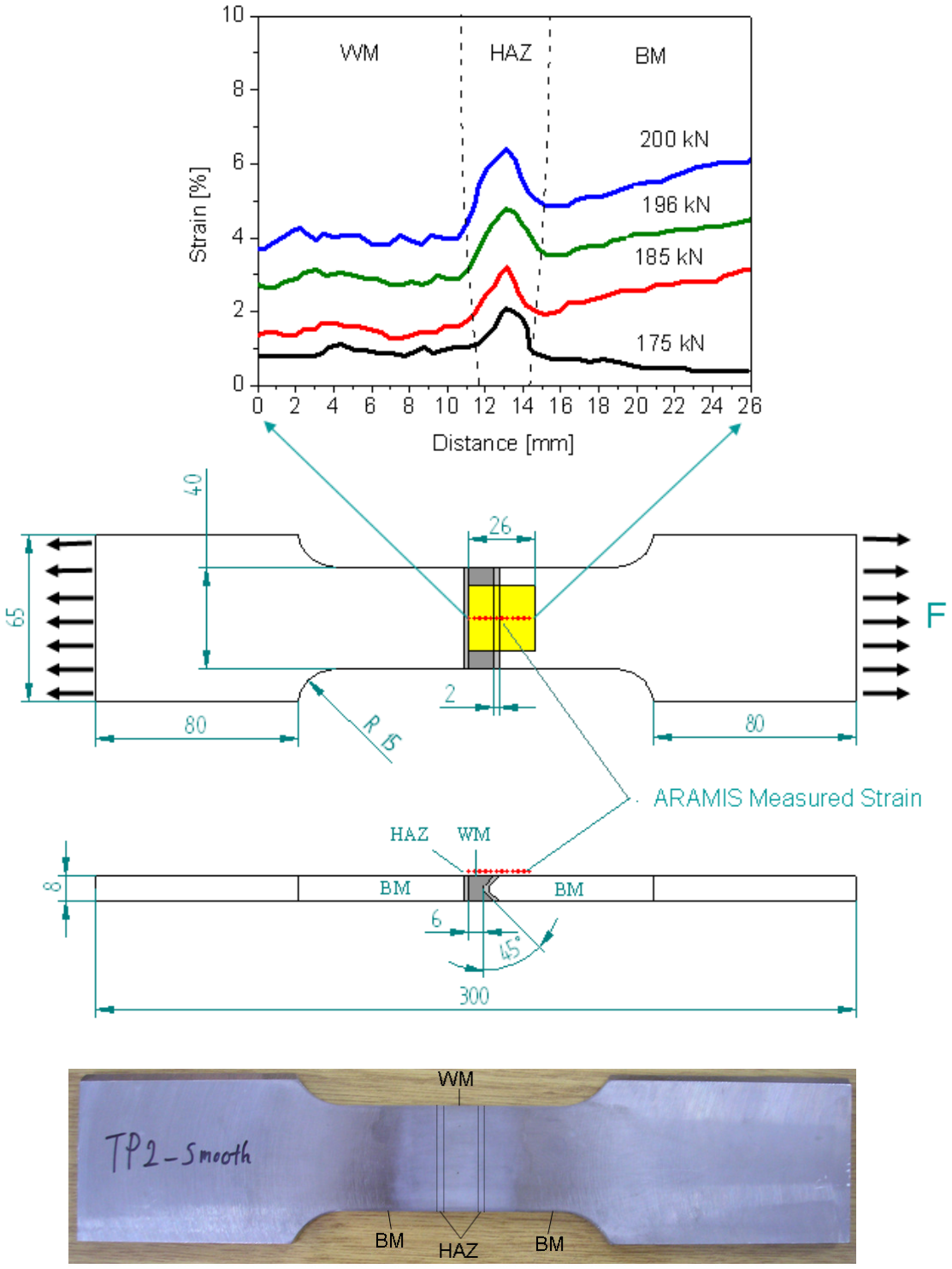

Figure 6.3 *Geometry of smooth tensile specimen with experimental ARAMIS measured strain at various loads.*

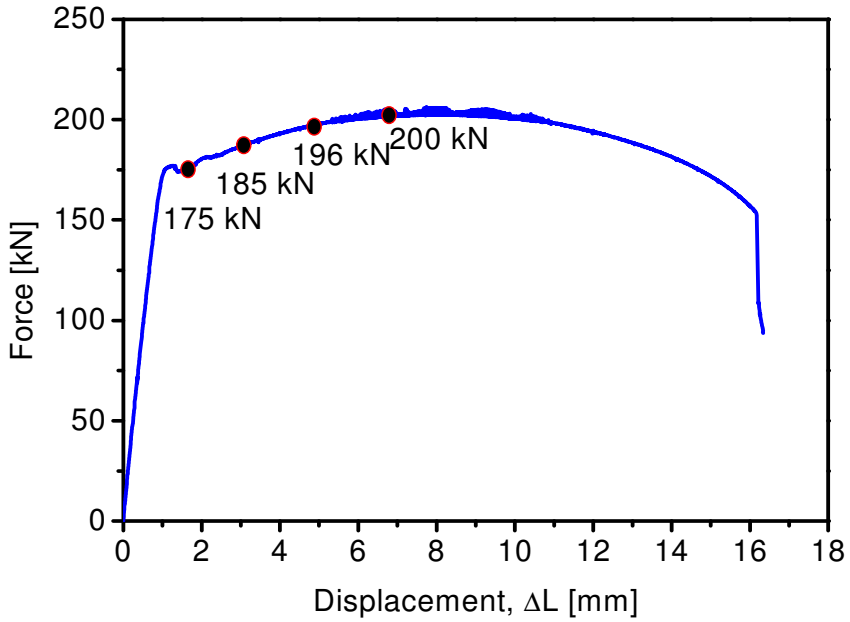

Figure 6.4 *Force (F) vs. remote displacement (ΔL) with load points, where local strains were measured.*

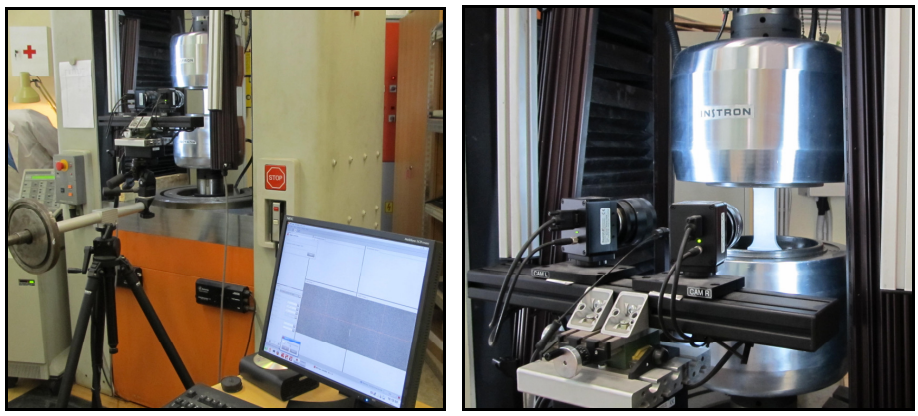

Figure 6.5 *ARAMIS measuring equipments and tested smooth tensile specimen.*

Engineering remote stress - true strain data for welded joint regions (BM, WM and HAZ) was obtained from ARAMIS measured strains (Figure 6.3) with corresponding applied force. Strains in each region at corresponding forces were calculated by averaging strains along measured line. Then, engineering remote stress was calculated at corresponding strain using initial cross section of tested specimen. The calculated engineering remote stress - true strain data is shown in Figure 6.7 for BM, HAZ and WM materials. The calculated engineering remote stress (σ) was converted up to the ultimate stress to true stress (σ_T) using expression:

$$\sigma_T = \sigma(1+\varepsilon) \tag{6.1}$$

where ε is average strain.

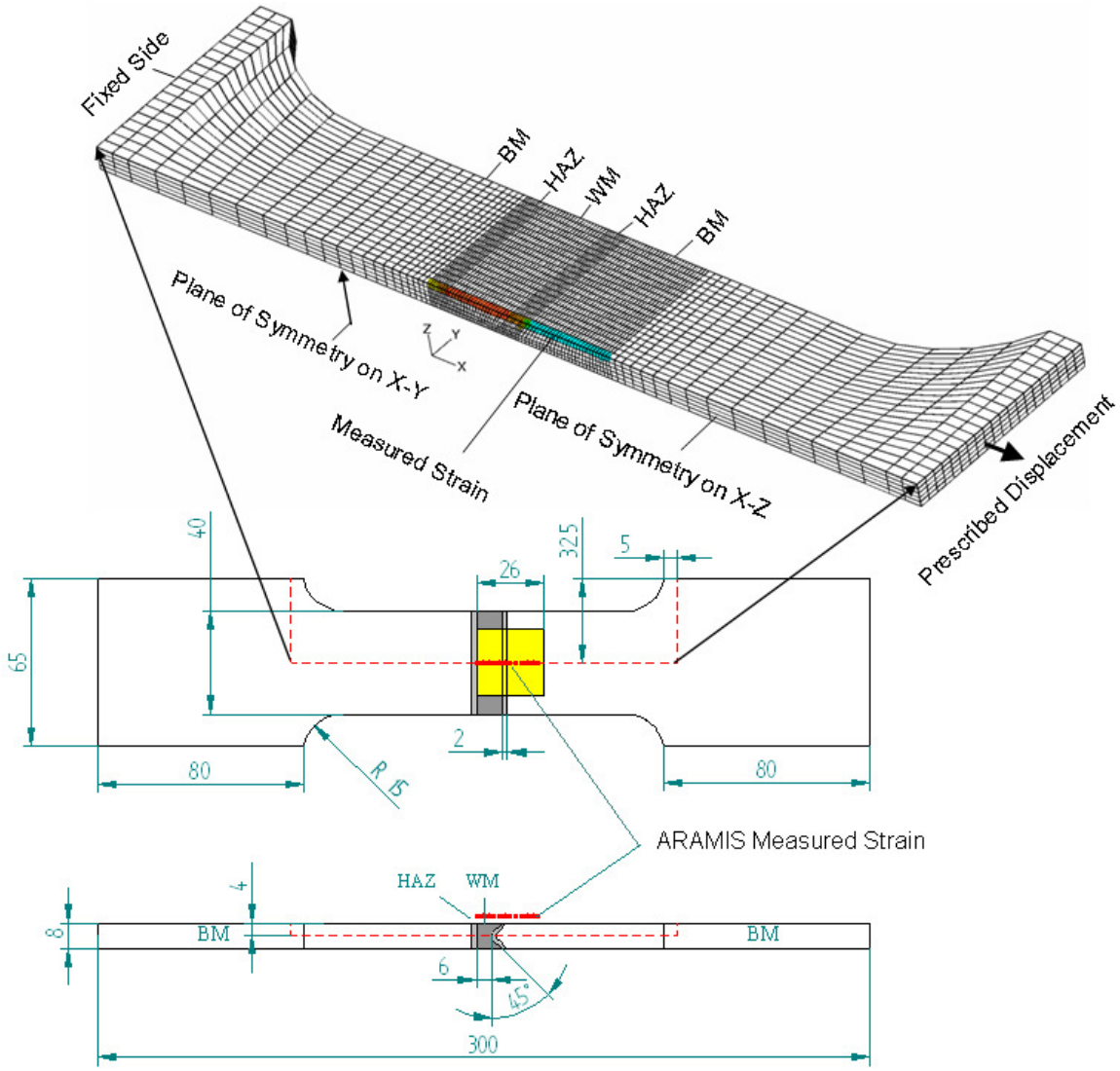

(a)

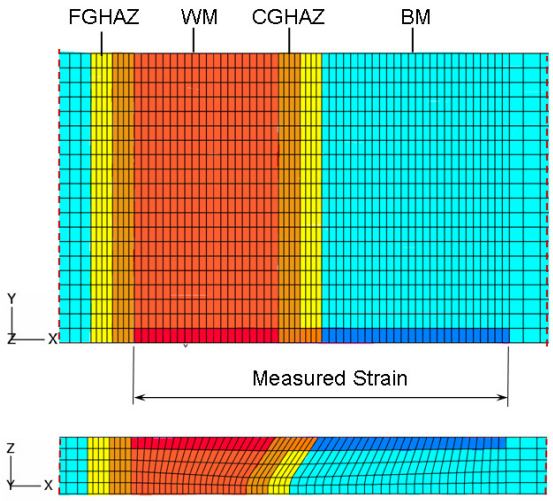

(b)

***Figure 6.6**: (a) Finite element mesh of quarter tensile specimen and (b) detailed mesh for the region of measured strains.*

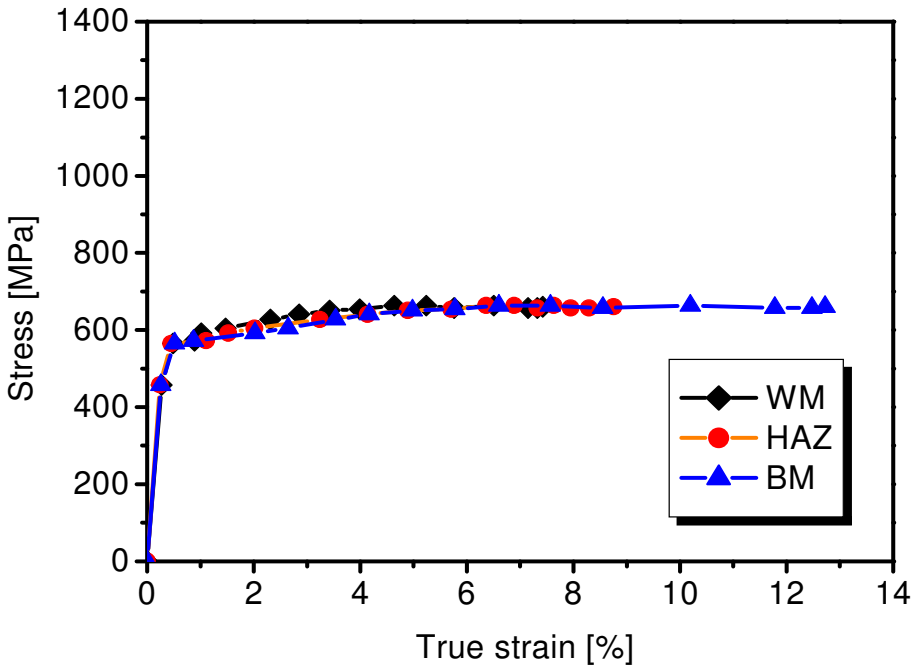

Figure 6.7 *Engineering remote stress vs. true strain data for materials of BM, HAZ and WM.*

True stress-strain behavior of materials was found to follow Hollomon power law up to maximum load according to expressions:

$$\varepsilon = \varepsilon_e + \varepsilon_{\mathrm{p}} \tag{6.2a}$$

$$\sigma = E\varepsilon_{\mathrm{e}} \quad \text{if} \quad \sigma \le \sigma_{\mathrm{YS}} \tag{6.2b}$$

$$\sigma = \mathrm{K}\varepsilon_{\mathrm{p}}^{\mathrm{n}} \quad \text{if} \quad \sigma > \sigma_{\mathrm{YS}} \tag{6.2c}$$

Where ε_{e} and ε_{p} are elastic and plastic strains, respectively, E is Young's modulus, σ_{YS} is yield strength, K is strength coefficient and n is material hardening exponent. The proper combination of mechanical properties (E, σ_{YS}) and Hollomon parameters (K and n) were determined by varying them up to obtaining good agreement between numerical and experimental results at different loads. About 25 iterations were performed to obtain the proper combination of elastic and plastic properties. The initial iteration values of E, σ_{YS}, K and n were estimated from the obtained experimental true stress - strain curves in Figure 6.8(a). The mechanical properties (E and σ_{YS}) and Hollomon parameters (K and n) are given in Table 6.4 for three iterations as example for performing iteration procedure. Experimental fracture stress and strain were used to estimate large strains beyond ultimate stress. Then, the whole data of true stress-strain curves have been

fitted by Harris model, which has given the closest fitting curves to data. The Harris model is given as follows:

$$y = \frac{1}{a + bx^c} \tag{6.3}$$

where a, b and c are parameters, which have been given in Table 6.5 for BM, CGHAZ, FGHAZ and WM and for three iterations in order to compare the results among iterations. The iteration 3 in Table 6.4 and Table 6.5 has given good matching between numerical and experimental results.

Figure 6.8-Figure 6.13 show comparison among numerical and experimental results: force (F) versus remote displacement (ΔL), distance versus strain at various loads (175 kN, 185 kN, 196 kN and 200 kN) for three iterations. Figure 6.14 shows comparison between tested specimen and numerical longitudinal strain distribution on 3 numerical models at the same overall elongation (ΔL = 16 mm). It is obvious that mechanical properties given in iteration 3 has presented good agreement among numerical and experimental results and necking has occurred at about the same place in both numerical model and tested specimen.

Table 6.4 *Mechanical properties of the materials for 3 numerical iterations.*

Material	Iteration	E (MPa)	σ_{YS} (MPa)	n	K (MPa)
WM	1	169320	459	0.1	944
	2	195000	550	0.08	971
	3	200000	530	0.21	1255
CGHAZ	1	190037	459	0.11	935
	2	200000	530	0.09	947
	3	203000	550	0.17	968
FGHAZ	1	190037	459	0.11	935
	2	200000	500	0.08	901
	3	195000	500	0.23	1217
BM	1	176972	459	0.11	929
	2	202000	540	0.1	940
	3	202900	520	0.22	1157

6.7 Micro-hardness measurements

Hardness testing was done according to standard EN 1043-1 and EN 1043-2. Vicker method was used to estimate hardness for different welded joint regions. The measurement was performed on WOLPERT - V-Testor 2 with load 100 N. The

magnification for measuring was 100x. These measurements are helpful to determine the local mismatch levels for various regions of weld metal and HAZ. Figure 6.15, Figure 6.16 have shown measuring machine, hardness measurements along three lines with macro structure and hardness profile of welded joint, respectively. The measured values of hardness are given in Table 6.6. Strength heterogeneity can be recognized by using empirical formula, which gives estimation of yield strength for different regions of welded joint [119]:

$$\sigma_{YS} = 3.15 \times HV - 168 \quad [\text{MPa}] \tag{6.4}$$

It can be seen that yield strength is proportional to the micro hardness, enabling simple evaluation of mismatching.

Table 6.5 *Harris model constants for true stress- true strain curves for 3 iterations.*

Material	Iteration	a	b	c
BM	1	0.07022	-0.06923	0.00242
	2	0.01353	-0.01246	0.00943
	3	0.02719	-0.00189	0.16269
CGHAZ	1	0.05325	-0.05228	0.00329
	2	0.01246	-0.0114	0.00952
	3	0.00217	-0.00119	0.25879
FGHAZ	1	0.05325	-0.05228	0.00329
	2	0.01369	-0.01258	0.00799
	3	0.00551	-0.00472	0.05847
WM	1	0.05175	-0.05079	0.00328
	2	0.01289	-0.01186	0.00756
	3	0.00438	-0.0036	0.06696

Table 6.6 *Hardness values on welded joint along three measuring lines.*

Line No.	Hardness HV10												
	BM			HAZ		WM			HAZ		BM		
1	209	202	204	202	215	208	196	201	217	196	212	208	200
2	214	214	210	216	220	195	210	206	215	203	205	215	202
3	203	198	213	197	226	212	208	210	207	202	218	202	216

6.8 Metallographic of microstructure in welded joint

Different regions of welded joint were polished and etched to study the microstructure of various zones of base metal, weld metal and HAZ. Figure 6.17 has

shown positions where the microstructures have been investigated and Figure 6.18 has shown the studied microstructures for different regions of welded joint.

The base metal, as shown in Figure 6.18(a), consists of fine grain ferrite-perlite structure. Figure 6.18(b) presents the heat-affected zone microstructure, which consists of incomplete normalized structure of ferrite-perlite. The microstructure of weld metal is shown in Figure 6.18(c), which consists of ferrite-perlite structure with different morphology of ferrite; acicular ferrite, a secondary ferrite phase and proeutectoid ferrite. Figure 6.18(d) shows the microstructure at fusion line (left part base metal and right part weld metal), which illustrates ferrite-perlite structure. Finally, Figure 6.18(e) presents the microstructure of base metal and HAZ that shows ferrite-perlite structure.

6.9 Fracture of weldments

In order to satisfy the basic requirements of each welded structure and analyze the transferability of numerical results and the validation of the ductile failure model implemented, it is necessary to study the real fracture behavior of different pre-cracked welded joints by means of experimental techniques. Thus, standard fracture mechanics specimens, single edge notched bend (SENB) specimens and tensile plates were transversally extracted from welded joints (Figure 6.1).

Fracture toughness and material resistance curves for steel NIOMOL 490K were obtained using SENB specimens at room temperature in accordance with the ASTM E1280-08 standard [120]. Welded SENB specimens and tensile plates were fatigue precracked in HAZ and WM to determine crack initiation and crack growth resistance curves.

6.9.1 Weldment preparation and precracking

Welded joint reinforcement was machined prior to the pre-cracking process, because of following:

- The reinforcement has irregular shape that make any numerical modeling complicated.
- The reinforcement produces stress concentration.
- It is easier to locate the crack position.
- To have straight HAZ in one side, where crack was placed.

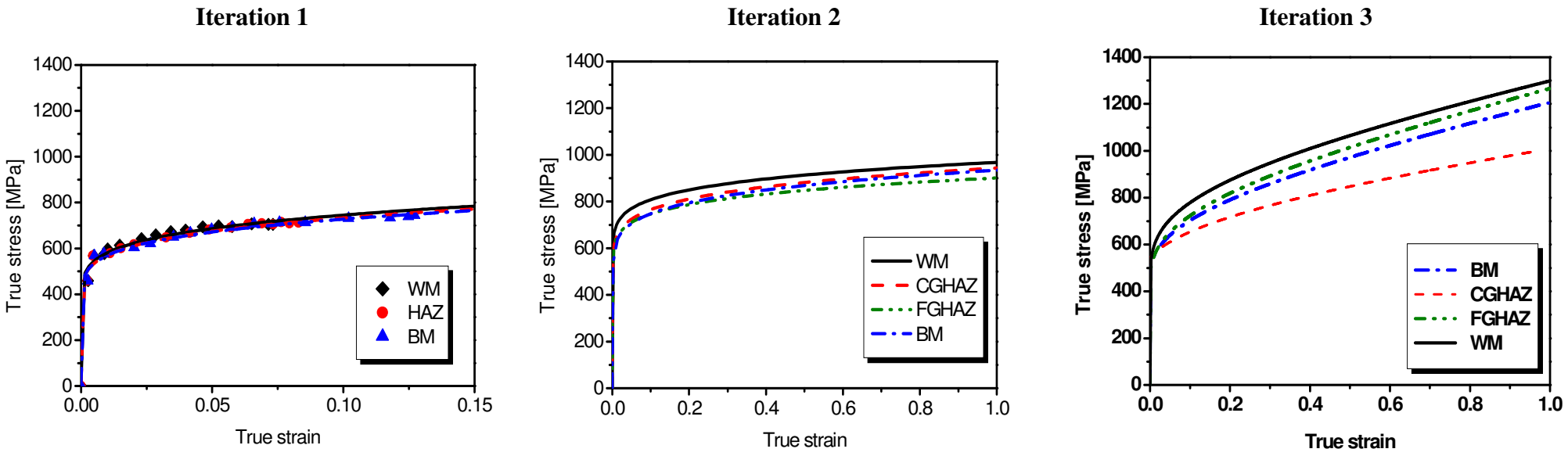

Figure 6.8 *Comparison among true stress vs. true strain curves of BM, CGHAZ, FGHAZ and WM for three iterations.*

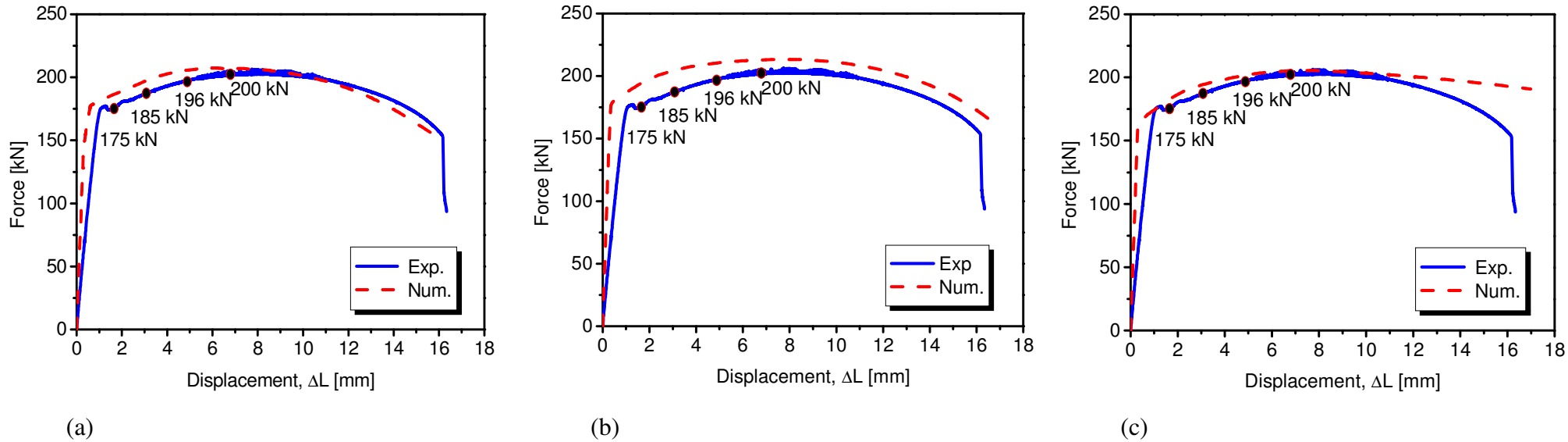

Figure 6.9 *Comparison among experimental and numerical force vs. remote displacement for three iterations.*

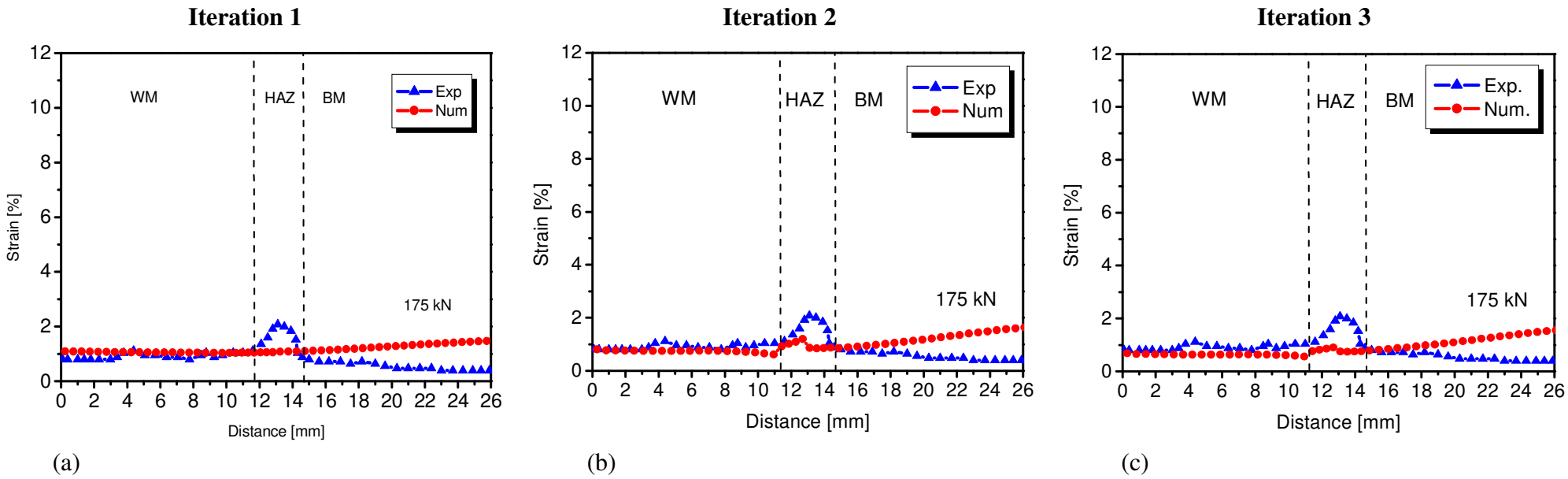

Figure 6.10 *Comparison among distance vs. strain distributions at load 175 kN for three iterations.*

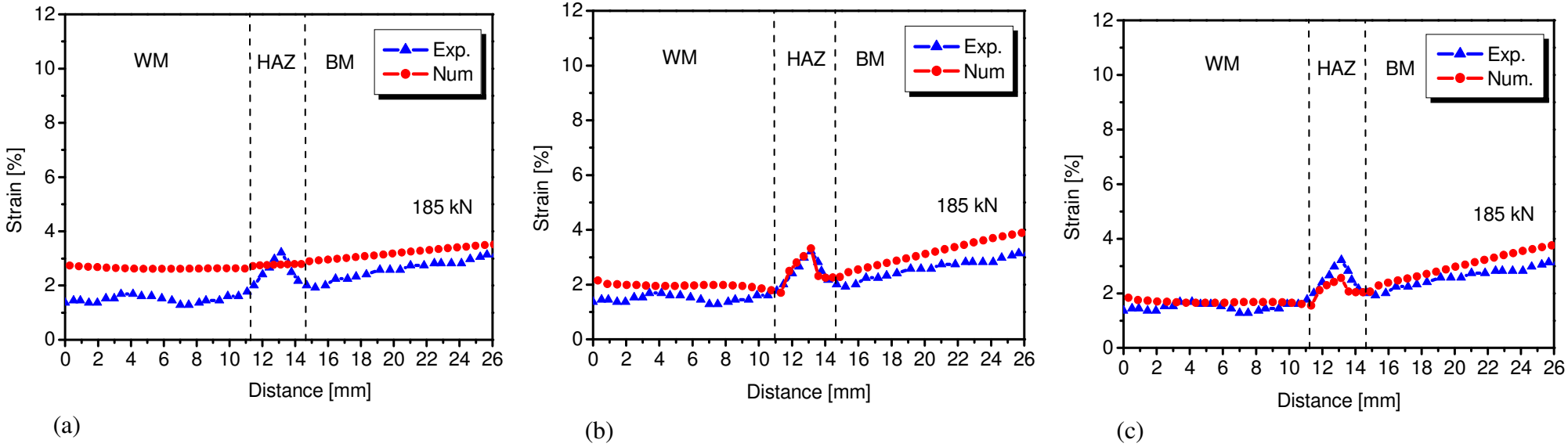

Figure 6.11 *Comparison among distance vs. strain distributions at load 185 kN for three iterations.*

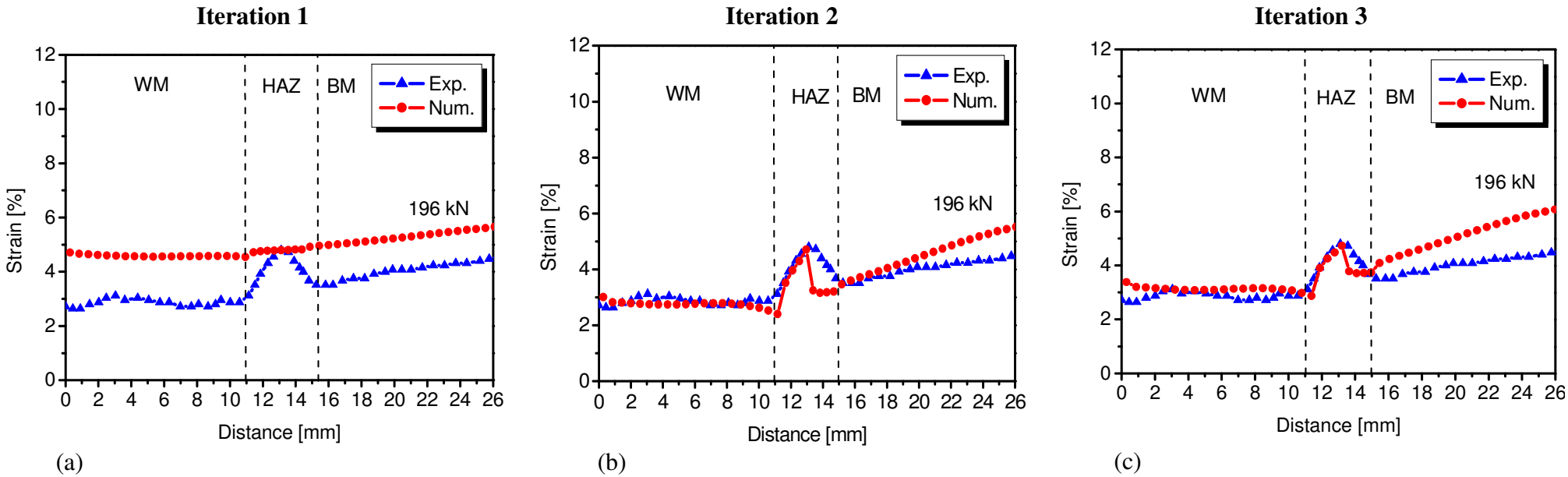

Figure 6.12 *Comparison among distance vs. strain distributions at load 196 kN for three iterations.*

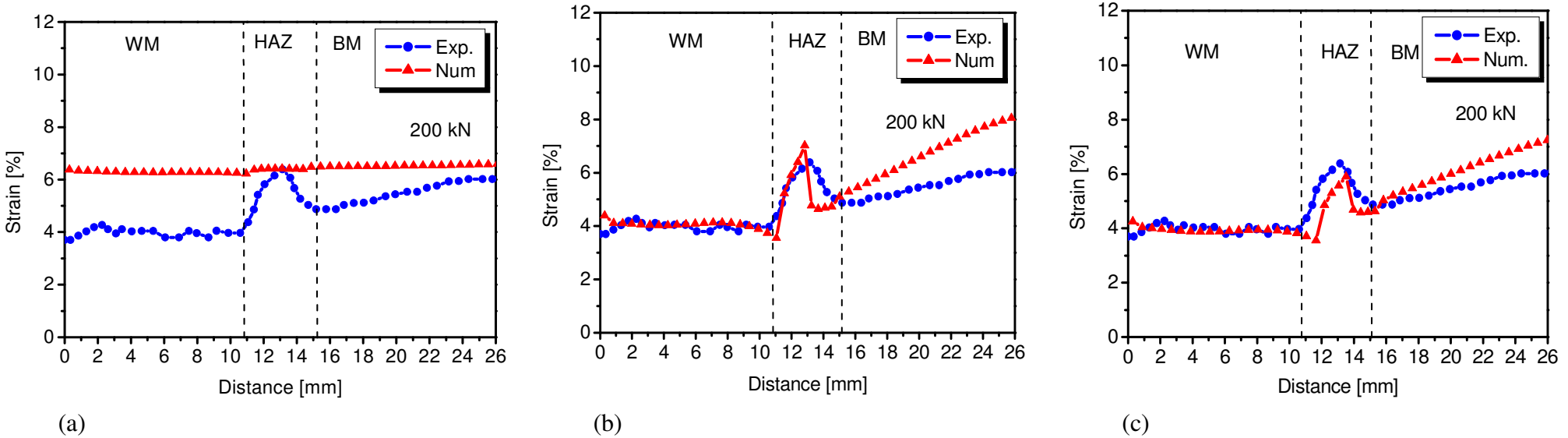

Figure 6.13 *Comparison among distance vs. strain distributions at load 200 kN for three iterations.*

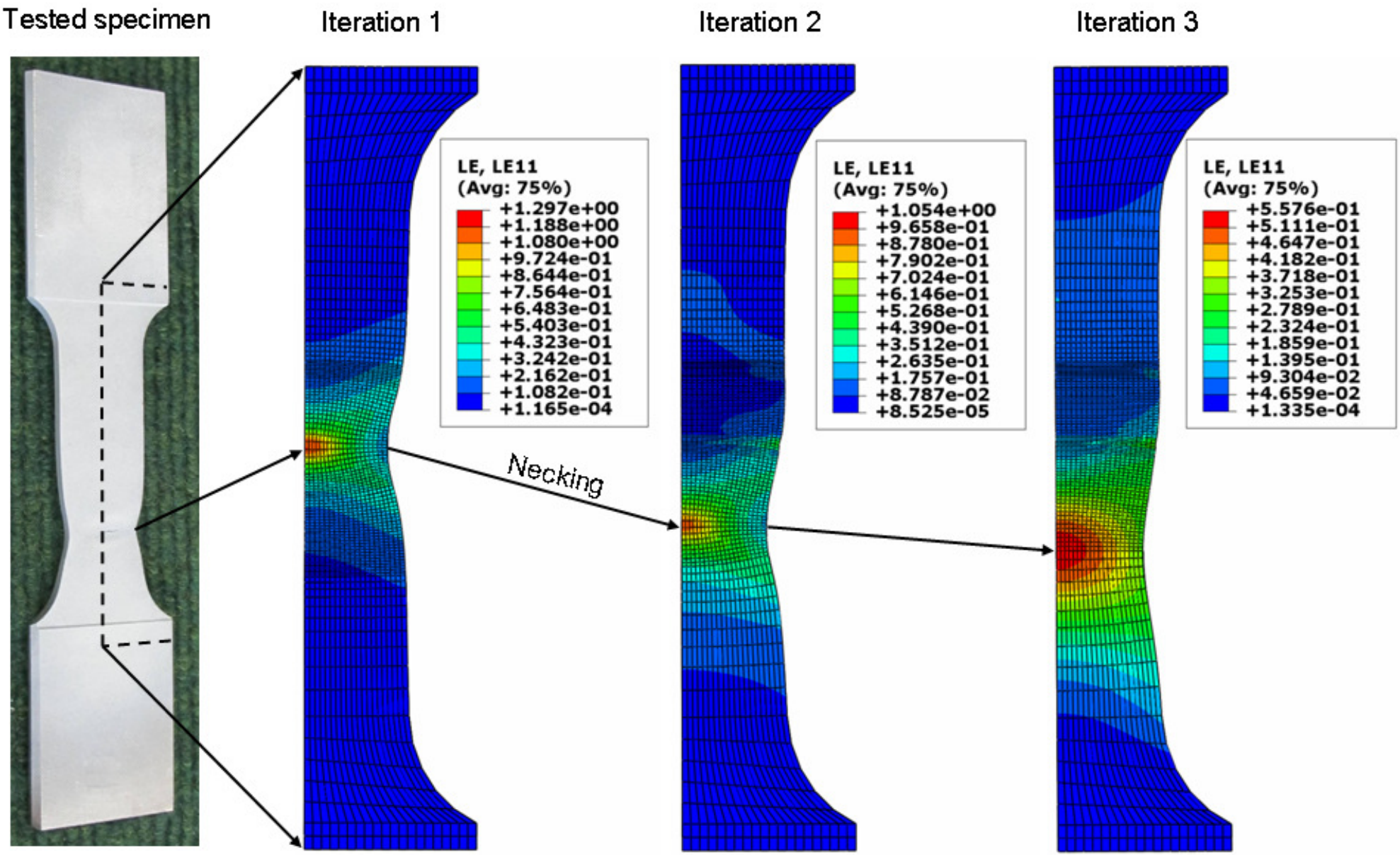

Figure 6.14 *Comparison between tested specimen and longitudinal true strain distribution in numerical models for 3 iterations at the same remote displacement (ΔL = 16 mm).*

Figure 6.15 *Hardness testing machine, WOLPERT - V-Testor 2.*

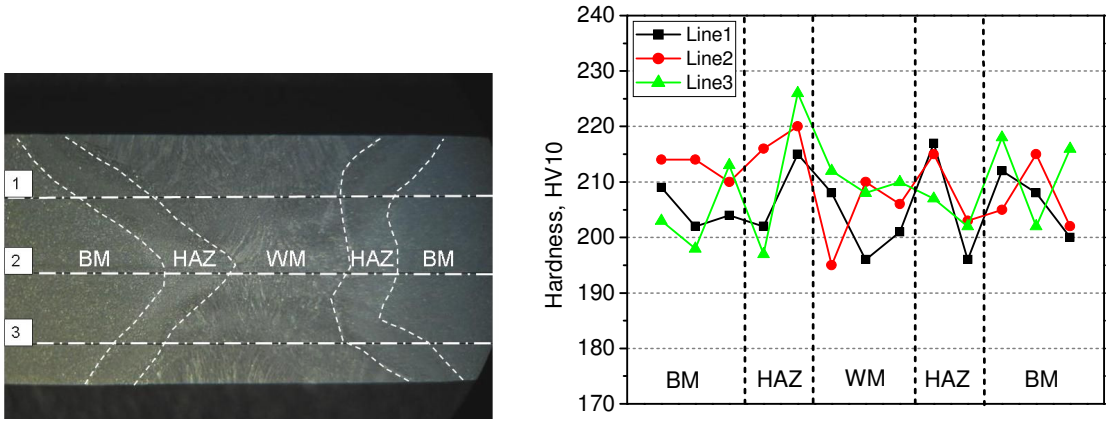

(a) (b)

Figure 6.16*: (a) hardness measurements on welded joint along three measuring lines, and (b) hardness profile.*

Crack position in weldment is important because the weldment has various toughness regions due to different metallurgical, mechanical strength and microstructure zones, as a result of welding dilution and thermal cycles. Two crack positions were considered, one in the center of weld metal (WM), and the other one in the heat-affected zone (HAZ).

6.9.2 Weldments fracture of SENB specimens

Fracture of cracked bodies cannot be assessed completely without carrying out any experimental works; *J-R* is a material property that should be determined from standard specimens. Thus, SENB standard specimen tests were carried out at room temperature for welded joints containing cracks in HAZ and WM. The scope of work was to investigate mechanical heterogeneity effect on crack initiation and *J-R* curves. Figure 6.19 and Figure 6.20 illustrate the geometries of SENB specimens with pre-cracks in WM and HAZ, respectively. Figure 6.21 and Figure 6.22 show the macrographs of welded joints containing pre-cracks in WM and HAZ, respectively.

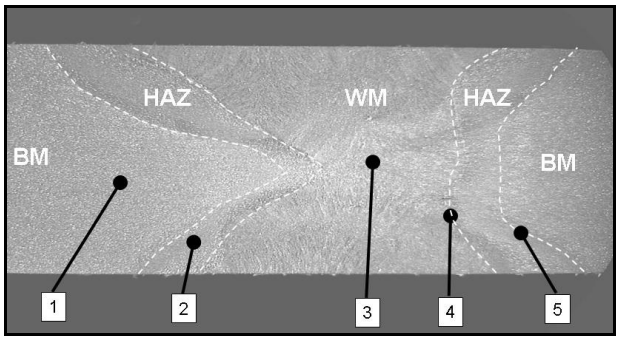

Figure 6.17 *Macrograph of welded joint with positions of studied microstructures.*

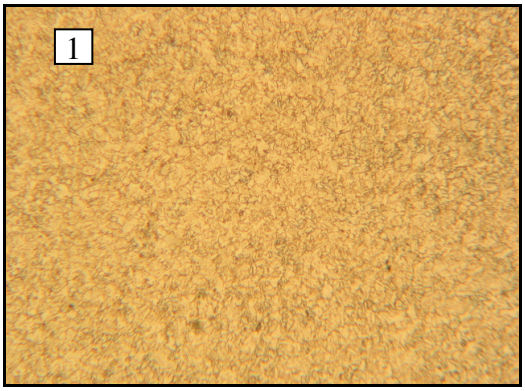

(a) Base metal (200x)

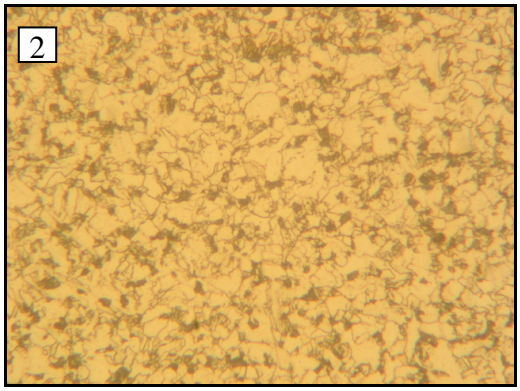

(b) HAZ (500x)

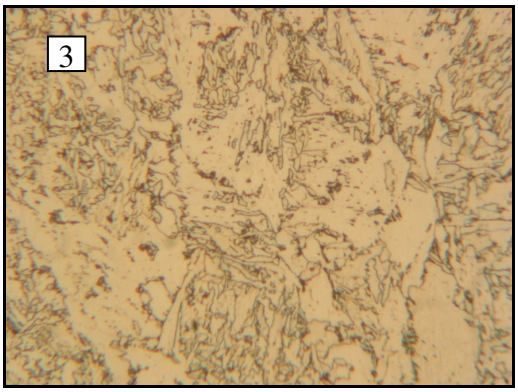

(c) Weld metal (320x)

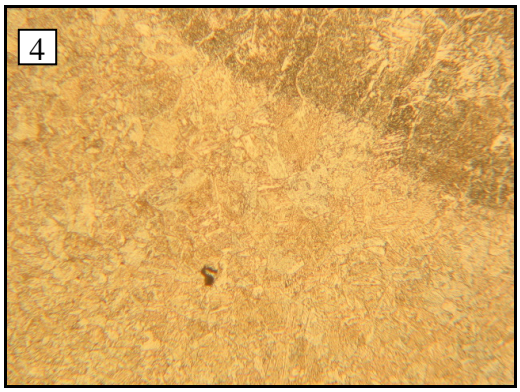

(d) Fusion line (100x)

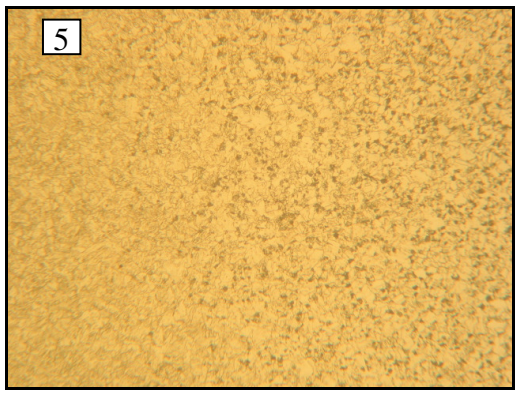

(e) HAZ-BM (200x)

Figure 6.18 *Studied microstructures for different regions of welded joint.*

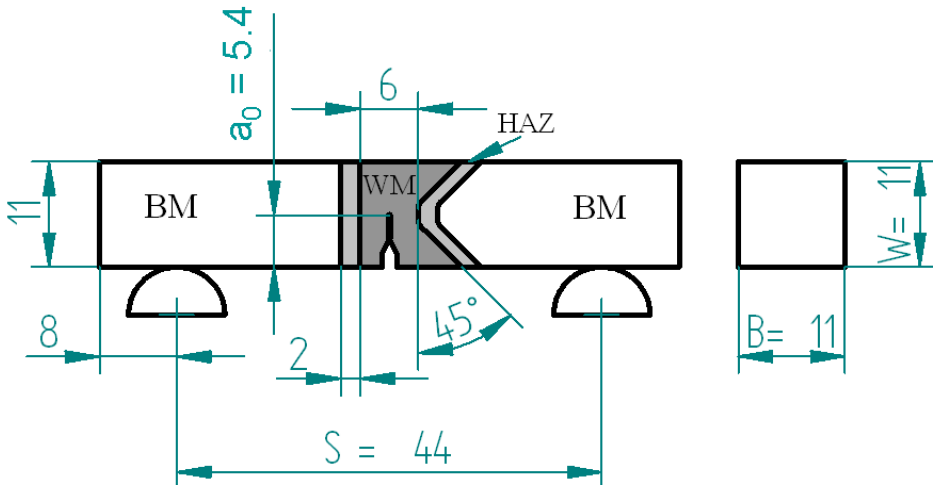

Figure 6.19 *Geometry of SENB specimen with a pre-crack in WM.*

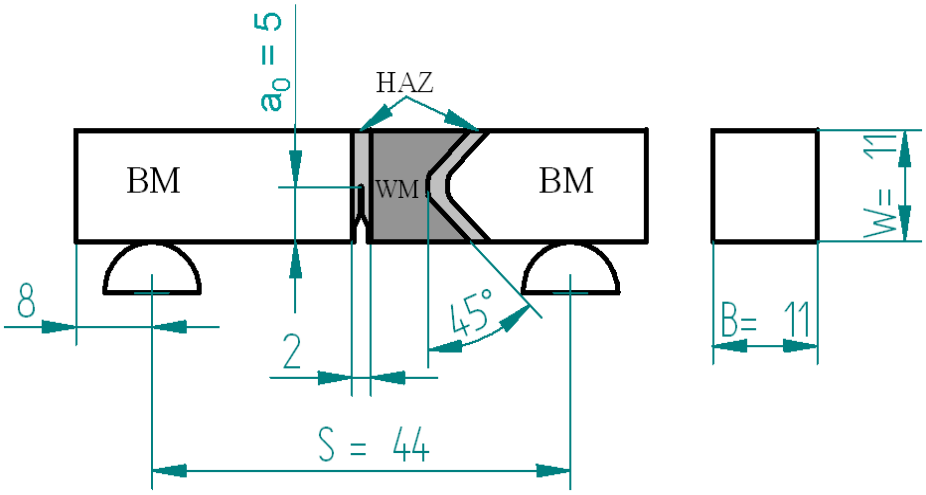

Figure 6.20 *Geometry of SENB specimen with a pre-crack in HAZ.*

(a) (b)

Figure 6.21*: (a) Macrograph of welded SENB specimen with a pre-crack in WM and (b) Detailed view of welded joint.*

The dimensions of tested SENB specimens were the same: W = 11 mm, B = 11 mm, $S = 4W$ = 44 mm. The specimens were fatigue precracked in accordance with [120]. The initial crack length to width ratio is $a_0 / W = 0.49$ and $a_0 / W = 0.45$ for SENB specimens

with pre-cracks in WM and HAZ, respectively. The single specimen method was used and the unloading compliance technique was applied for stable crack growth monitoring. Servo-hydraulic testing machine was used (Figure 6.23).

(a) (b)

***Figure 6.22**: (a) Macrograph of welded SENB specimen with a pre-crack in HAZ and (b) Detailed view of welded joint.*

Experiments were carried out at room temperature. Crack mouth opening displacement (CMOD) and applied force (F) were monitored for both SENB specimens (Figure 6.24 and Figure 6.25). The tests were terminated after the specimens had been failed in ductile manner. Fracture surfaces of both specimens were examined and measured after marked them by heat-tinting to determine the original crack length (a_0) and the amounts of stable crack extension (Δa) as shown in Figure 6.26 and Figure 6.27. The values of stable crack growth (Δa) are given in Table 6.7 for SENB specimens with pre-cracks in HAZ and WM.

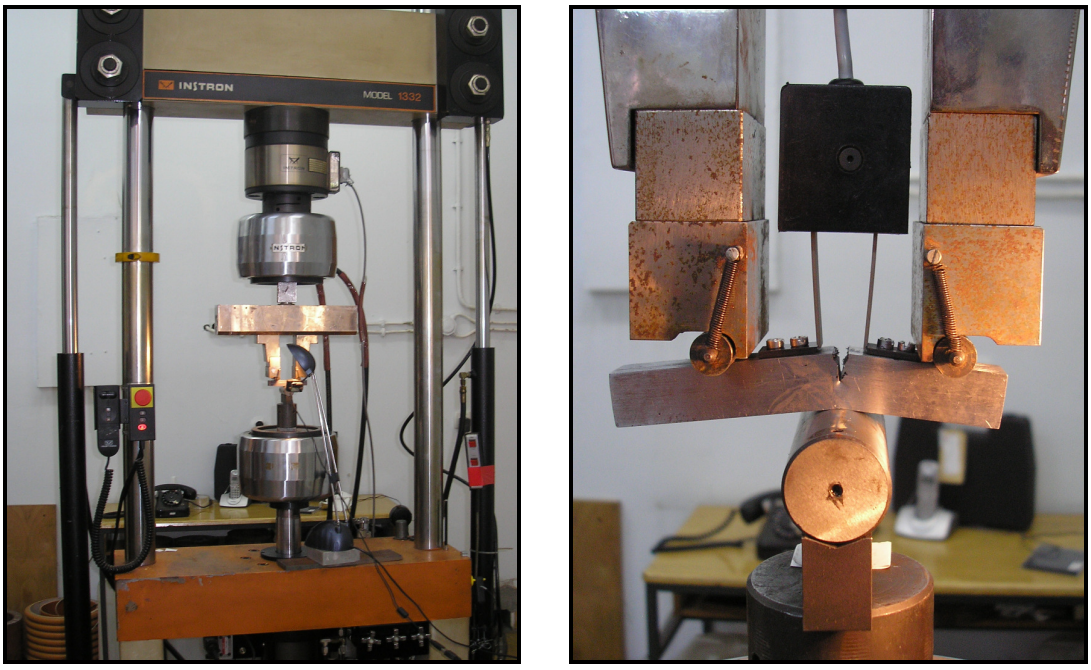

***Figure 6.23** Servo-hydraulic testing machine with tested specimen.*

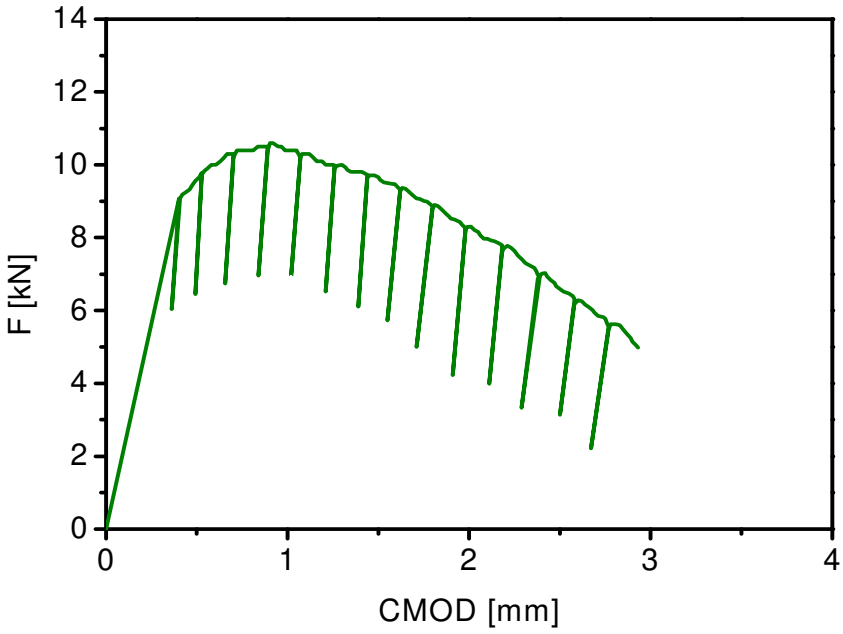

Figure 6.24 *Crack mouth opening displacement (CMOD) vs. force (F) for SENB specimen with a pre-crack in WM.*

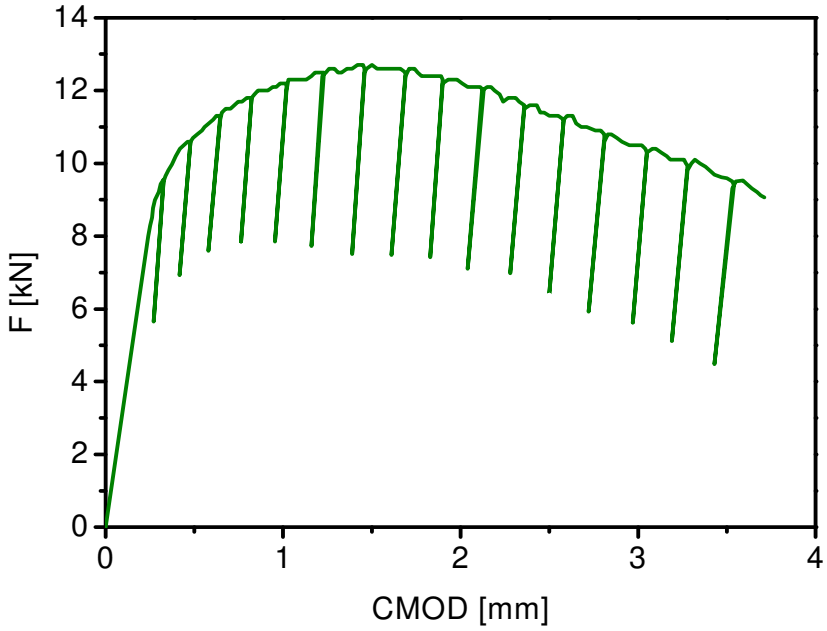

Figure 6.25 *Crack mouth opening displacement (CMOD) vs. force (F) for SENB specimen with a pre-crack in HAZ.*

Table 6.7 *Measured values of crack extension for SENB specimens with pre-cracks in HAZ and WM.*

Designation	Crack extension (Δa), (mm)					Average crack extension Δa_{avr}, (mm)
	Δa_1	Δa_2	Δa_3	Δa_4	Δa_5	
SENB-HAZ	1.04	1.07	1.11	1.09	1.03	1.068
SENB-WM	2.02	2.05	2.09	2.06	2.09	2.062

Figure 6.26 *Fracture surfaces of SENB specimen with a pre-crack in HAZ.*

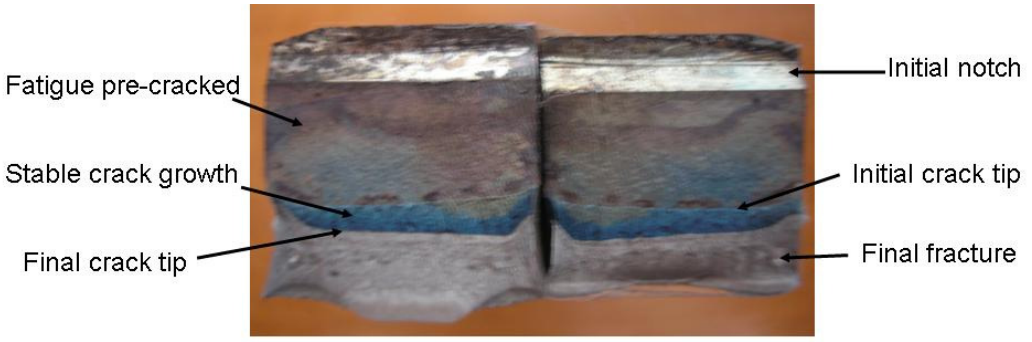

Figure 6.27 *Fracture surfaces of SENB specimen with a pre-crack in WM.*

Fracture toughness (K_{Ic}) is determined using J-integral critical value, a measure of fracture toughness (J_{Ic}) by tests according to the ASTM E1820-08 [120]:

$$K_{Ic} = \sqrt{\frac{J_{Ic}E}{1-v^2}} \tag{6.5}$$

where E is elasticity modulus and v is Poisson's ratio.

For determining the J-integral, a single specimen test method by successive partial unloading is applied. Obtained data of CMOD versus F was used to calculate crack extension and J-integral at unloading and reloading points (see Figure 6.24 and Figure 6.25). In a single specimen test, the specimen is unloaded in intervals to about 30% of actually attained force level, chosen by experience with material type. Based on change of compliance line slope (C) with crack extension, the crack length (a_i) is determined by expressions [120]:

$$\frac{a_i}{W} = [0.999748 - 3.9504u + 2.9821u^2 - 3.21408u^3 + 51.51564u^4 - 113.031u^5] \tag{6.6a}$$

where

$$u = \frac{1}{\left[\frac{B_e WEC_i}{S/4}\right]^{1/2} + 1} \tag{6.6b}$$

$C_i = (\Delta v_m/\Delta P)$ on an unloading/reloading sequence, P is applied load, v_m is crack opening displacement at notched edge, B_e is effective specimen thickness and S is specimen span. Based on calculated J-integral and crack growth (Δa), J-R curves have been obtained for specimens with pre-cracks in WM and HAZ (Figure 6.28 and Figure 6.29). Then, Fracture toughness (J_{Ic}) has been determined and used to calculate K_{Ic} by Equation (6.5). The values of fracture toughness J_{Ic} and corresponding calculated K_{Ic} are given in Table 6.8 for the HAZ and WM metals.

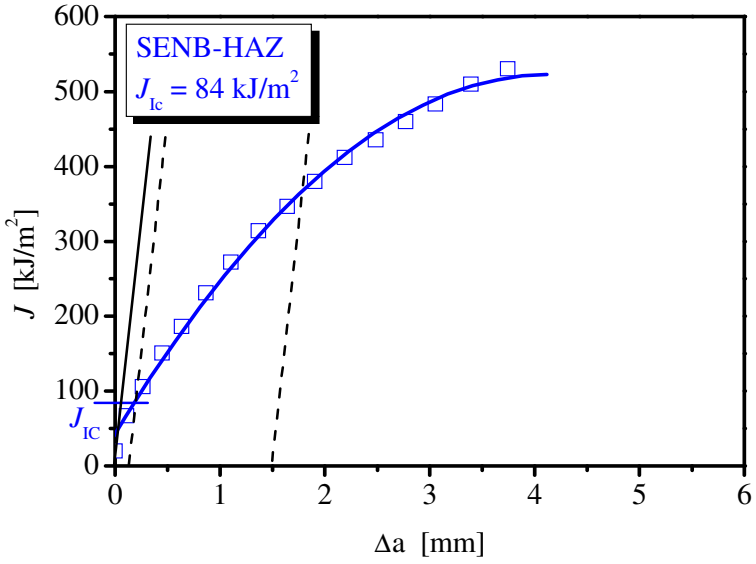

Figure 6.28 *J-R curve of the HAZ metal obtained from SENB specimen at room temperature.*

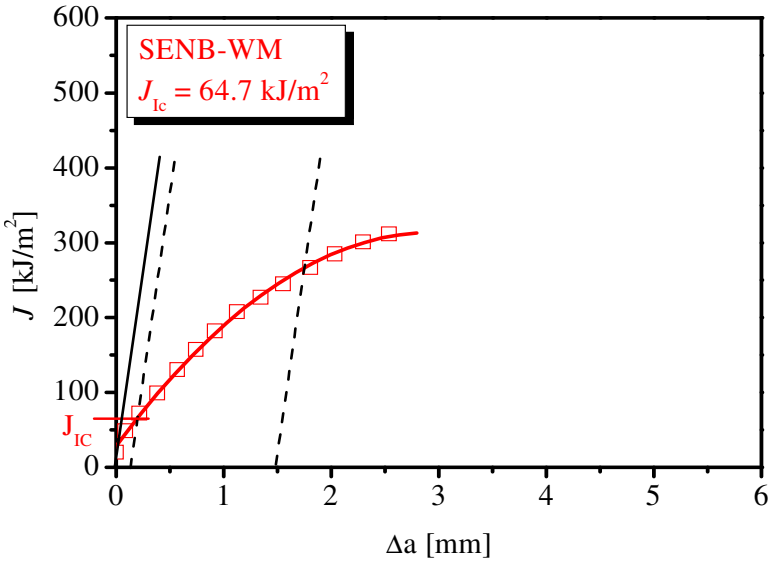

Figure 6.29 *J-R curve of the weld metal obtained from SENB specimen at room temperature.*

Table 6.8 *The values of fracture toughness (J_{Ic}) and corresponding K_{Ic}.*

Designation of specimen	Critical J-integral, J_{Ic} (kJ/m^2)	Critical stress intensity factor, K_{Ic} (MPa m$^{1/2}$)
SENB-HAZ	84	134.7
SENB-WM	64.7	119.2

6.9.3 Weldments fracture of tensile panels

Two tensile panels with semi-elliptical surface cracks in WM (TP-WM) and HAZ (TP-HAZ) were transversely cut and machined (Figure 6.1 and Figure 6.30). Semi-elliptical surface cracks (22.71 mm long, 5 mm deep and 22.14 mm long, 5 mm deep) in tensile panels were located in the weld metal and HAZ, respectively. Initial notches in both tensile panels were produced by electro-erosion technique. Afterwards, both panels were fatigue precracked in four-point bending (Figure 6.31). The geometry, specimen designations, crack length and depth for both specimens are summarized in Table 6.9.

Table 6.9 *Geometries of tensile panels with semi-elliptical surface cracks.*

Specimen designation	t (mm)	$2W$ (mm)	$2c$ (mm)	a_0 (mm)	a_0/t	a_0/c	c/W
TP-HAZ	10	40	22.14	5	0.5	0.45	0.55
TP-WM	10	40	22.71	5	0.5	0.44	0.57

Both specimens were tested at room temperature. During the experiment, the tensile panel was gripped rigidly at each end and pulled in tension until failure. The stereo-optical techniques of the ARAMIS [118] system were used to measure the crack mouth opening displacement (CMOD) and crack tip opening displacement (CTOD-δ_5), while servo hydraulic testing machine (Instron 1255) was used to monitor applied force (Figure 6.32). Figure 6.33-Figure 6.38 show experimentally obtained: CMOD versus applied (F), CTOD-δ_5 versus applied load (F) and CMOD versus CTOD-δ_5 for both tensile panels. The fracture surface of both tensile panels with semi elliptical surface crack can be seen in Figure 6.39 and Figure 6.40. It is obvious to see various surfaces on fracture surface: initial electron eroded notch, fatigue pre-crack, crack growth and final fracture. The region of stable crack growth on the fracture surface of tensile panel with pre-crack in WM is magnified to visualize the micromechanical damage effect (Figure 6.39). This fracture surface reveals typical ductile fracture features, showing dimples. This indicates that fracture is essentially governed by void growth and coalescence by internal necking.

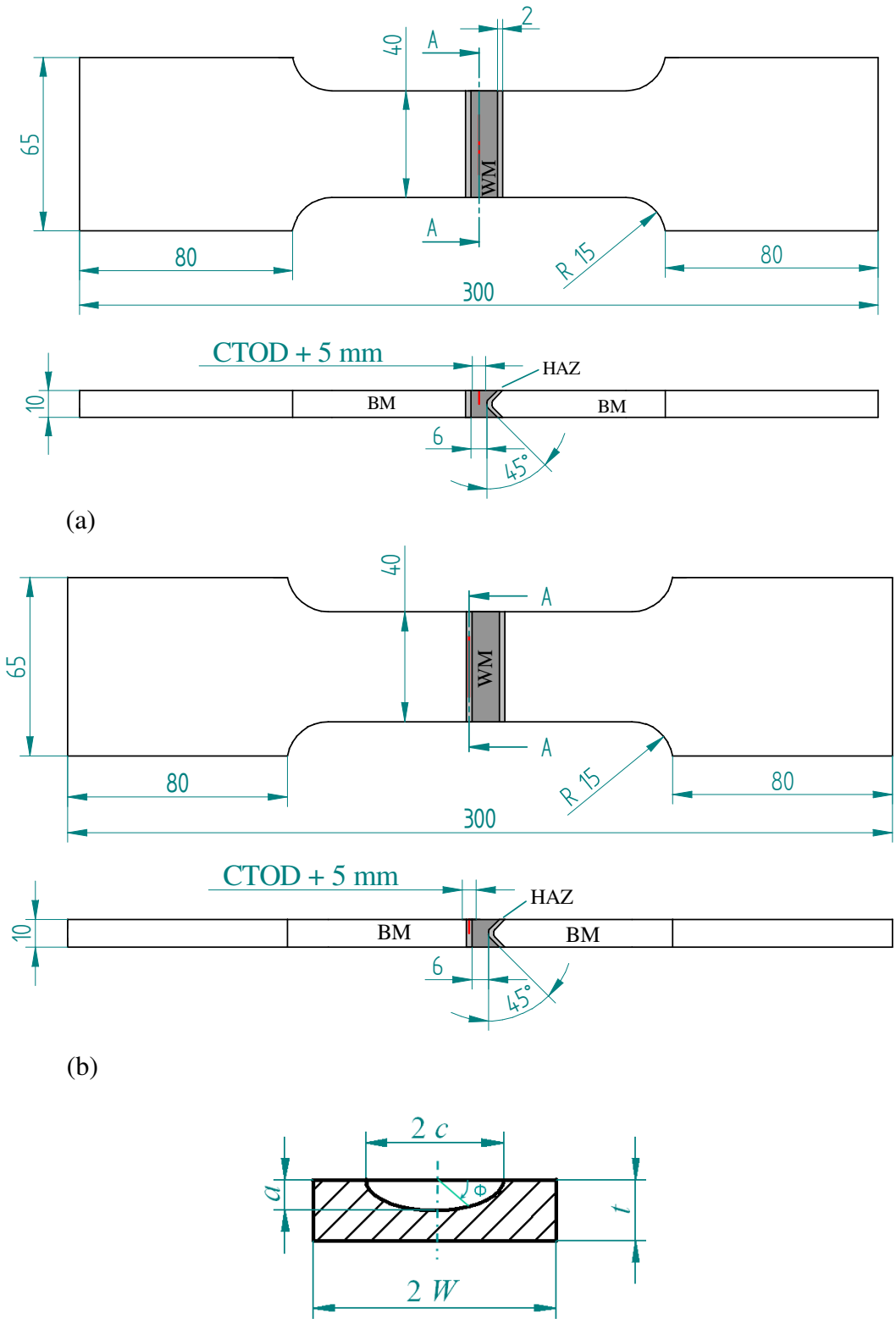

Figure 6.30 *Geometry of welded tensile specimens: (a) tensile panel with semi-elliptical surface crack in WM. (b) tensile panel with semi-elliptical surface crack in HAZ and (c) geometry of semi-elliptical crack.*

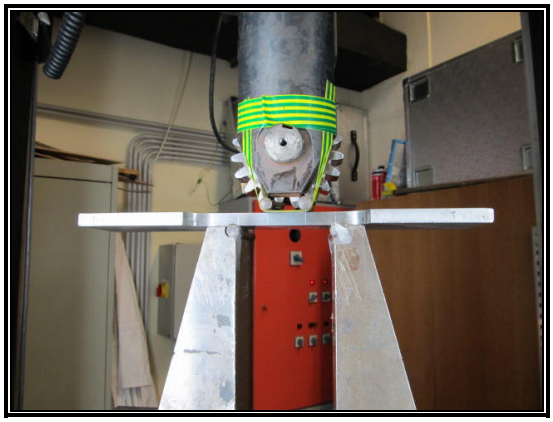

Figure 6.31 *Four-point bending fatigue precracking of tensile panel with a surface crack.*

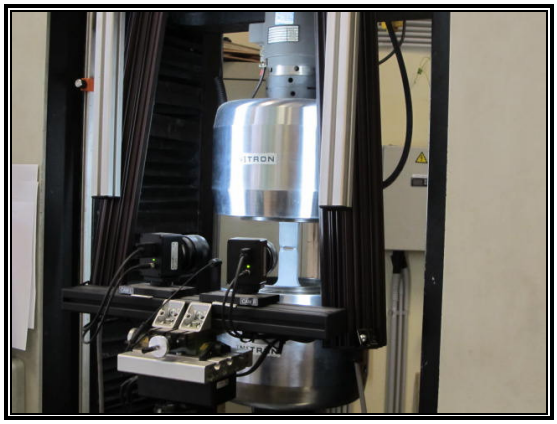

Figure 6.32 *Servo hydraulic testing machine with stereo-optical equipment of ARAMIS system.*

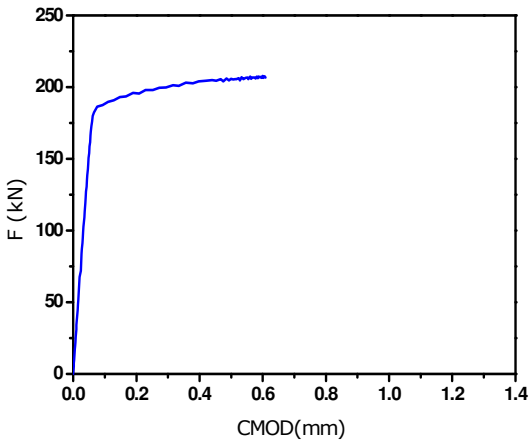

Figure 6.33 *Crack mouth opening displacement (CMOD) vs. force (F) for tensile panel with surface crack in WM.*

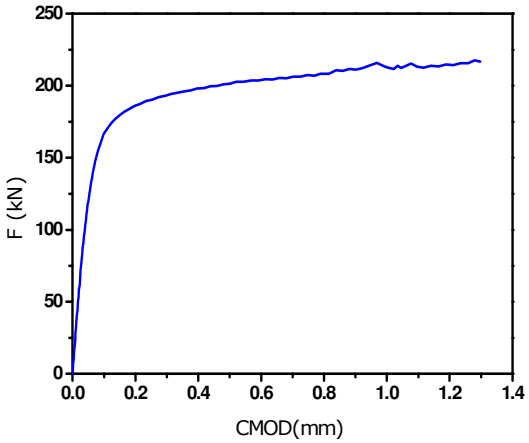

Figure 6.34 *Crack mouth opening displacement (CMOD) vs. force (F) for tensile panel with surface crack in HAZ.*

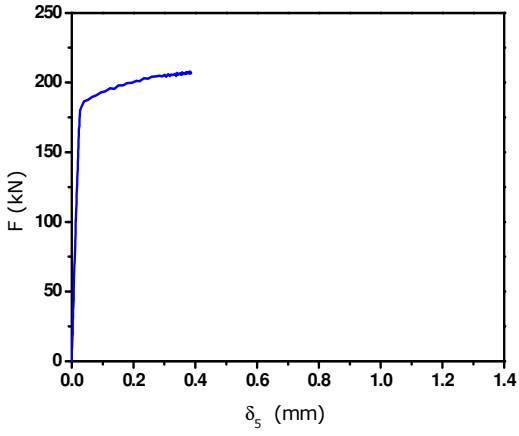

Figure 6.35 *Crack tip opening displacement (δ_5) vs. force (F) for tensile panel with surface crack in WM.*

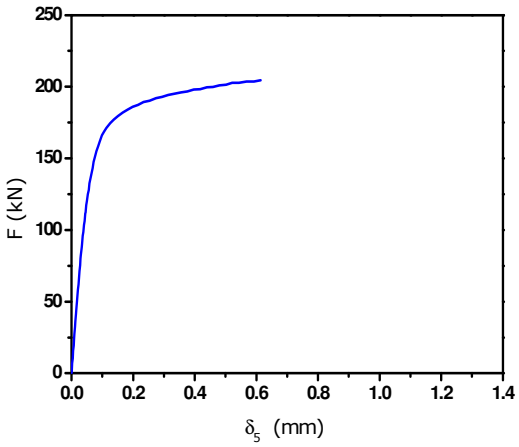

Figure 6.36 *Crack tip opening displacement (δ_5) vs. force (F) for tensile panel with surface crack in HAZ.*

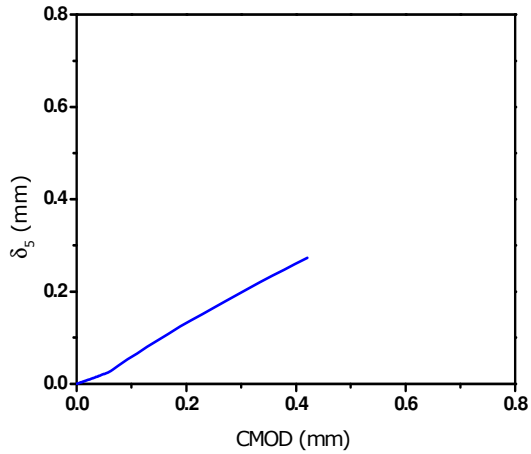

Figure 6.37 *Crack mouth opening displacement (CMOD) vs. crack tip opening displacement (δ_5)for tensile panel with surface crack in WM.*

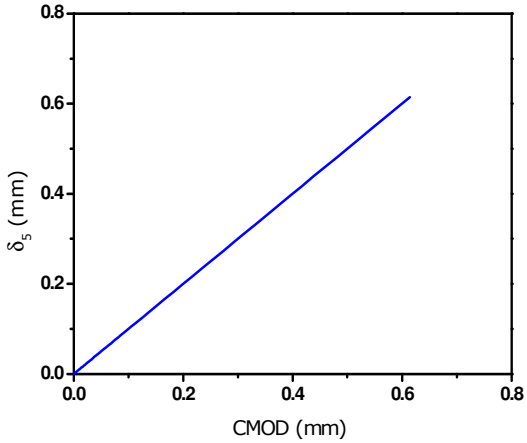

Figure 6.38 *Crack mouth opening displacement (CMOD) vs. crack tip opening displacement (δ_5) for tensile panel with surface crack in HAZ.*

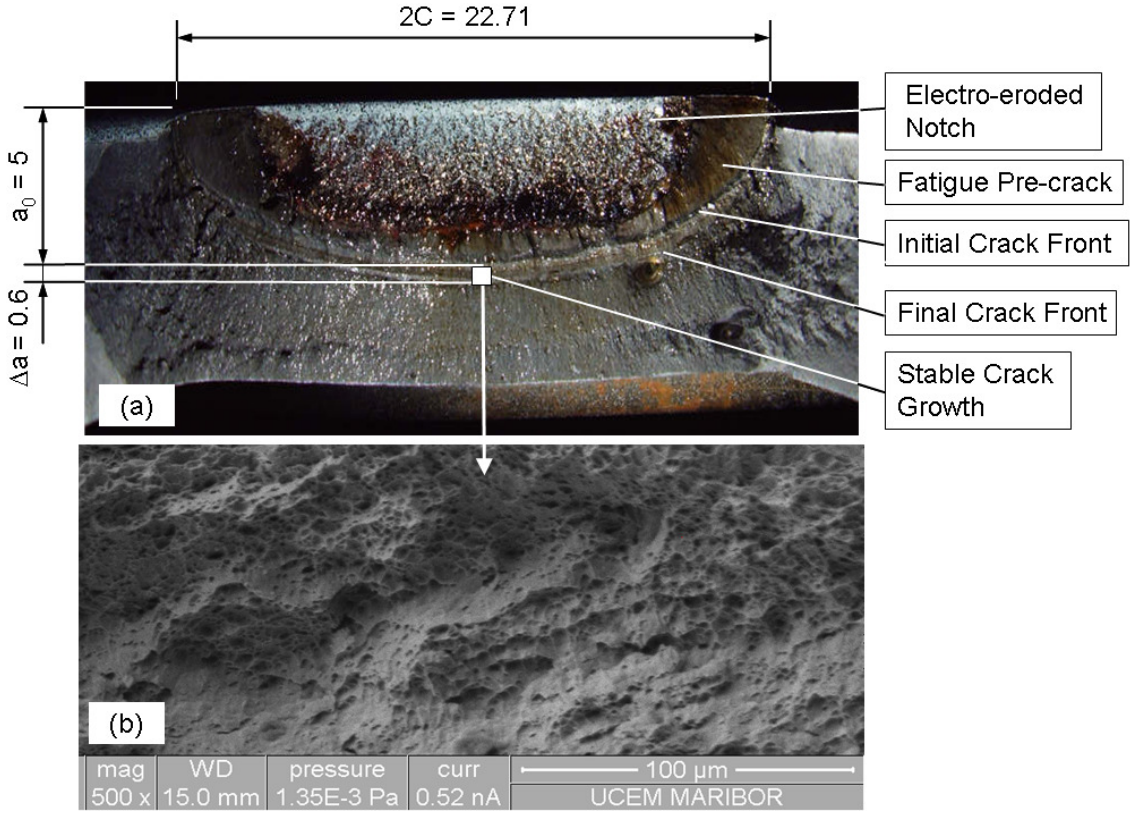

Figure 6.39: *(a) fracture surface of tensile panel with semi-elliptical surface crack in WM and (b) magnified region on stable crack growth surface.*

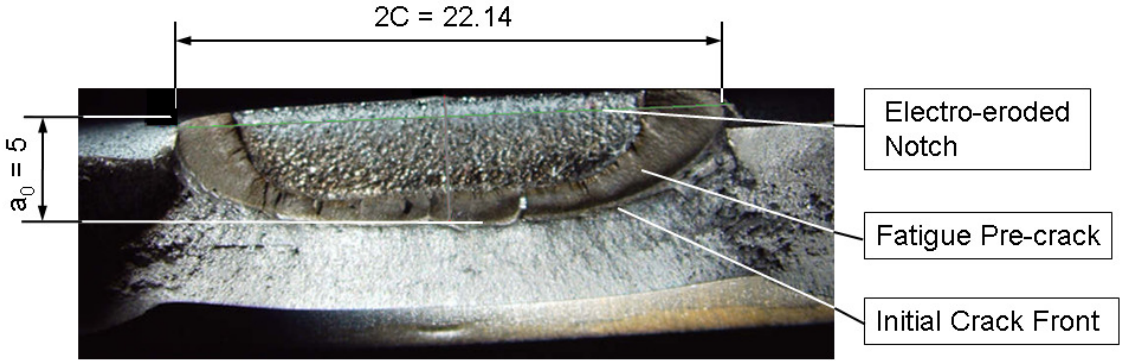

Figure 6.40 *Fracture surface of tensile panel with semi-elliptical surface crack in HAZ.*

6.9.3.1 Determination of J-integral at crack initiation

Based on results of tested tensile panels, *J*-integral at crack initiation (J_i) was determined using stretch zone width. Fracture surfaces of tensile panels with surface cracks in WM and FGHAZ were analyzed to determine a critical stretch zone width. The critical stretch zone width ($\Delta a_{SZW,i}$) on fracture surface was measured on photographs taken in scanning electron microscope (SEM) as shown in Figure 6.41 and Figure 6.42 . It was measured at 9 positions on each fracture surface. At least 5 measurements were taken at each position to calculate the local mean critical stretch zone width ($\overline{\Delta a}_{SZW,L}$) using formula [121]:

$$\overline{\Delta a}_{SZW,L} = \frac{1}{k}\sum_{i=1}^{k}\Delta a_{SZW,i} \qquad \text{for} \quad k \geq 5 \tag{6.7}$$

The average critical stretch zone width for the nine local measurements was calculated as follows:

$$\overline{\Delta a}_{SZW} = \frac{1}{9}\sum_{i=1}^{9}\Delta a_{SZW,i,i} \tag{6.8}$$

The average values of critical stretch zone width are given in Table 6.10 for tensile panels with a precrack in WM and FGHAZ.

Table 6.10 *The critical average values of SZW for tensile panels with precrack in WM and FGHAZ.*

Specimen designation	$\overline{\Delta a}_{SZW}$ (µm)
TP-WM	45.4
TP-FGHAZ	123.6

The *J*-integral at crack initiation (J_i) can be determined using critical stretch zone width [47,122,123].

The J_i has been determined using formula:

$$J_i = m\sigma_{YS}CTOD_i = m\sigma_{YS}\left(2\overline{\Delta}a_{SZW}\right) \tag{6.9}$$

where m is a coefficient, with the value between 1 and 2.6 [34], σ_{YS} is the yield stress of material which is given in Table 6.4. The coefficient m = 2.6 has been selected for calculation plane strain fracture mechanics. The calculated values of J_i for tensile panel with pre-cracks in WM and FGHAZ are given in Table 6.11.

Table 6.11 *The values of J-integral at crack initiation (J_i) for tensile panels.*

Designation of specimen	Critical *J*-integral, J_i (kJ/m^2)
TP-FGHAZ	321.4
TP-WM	125.1

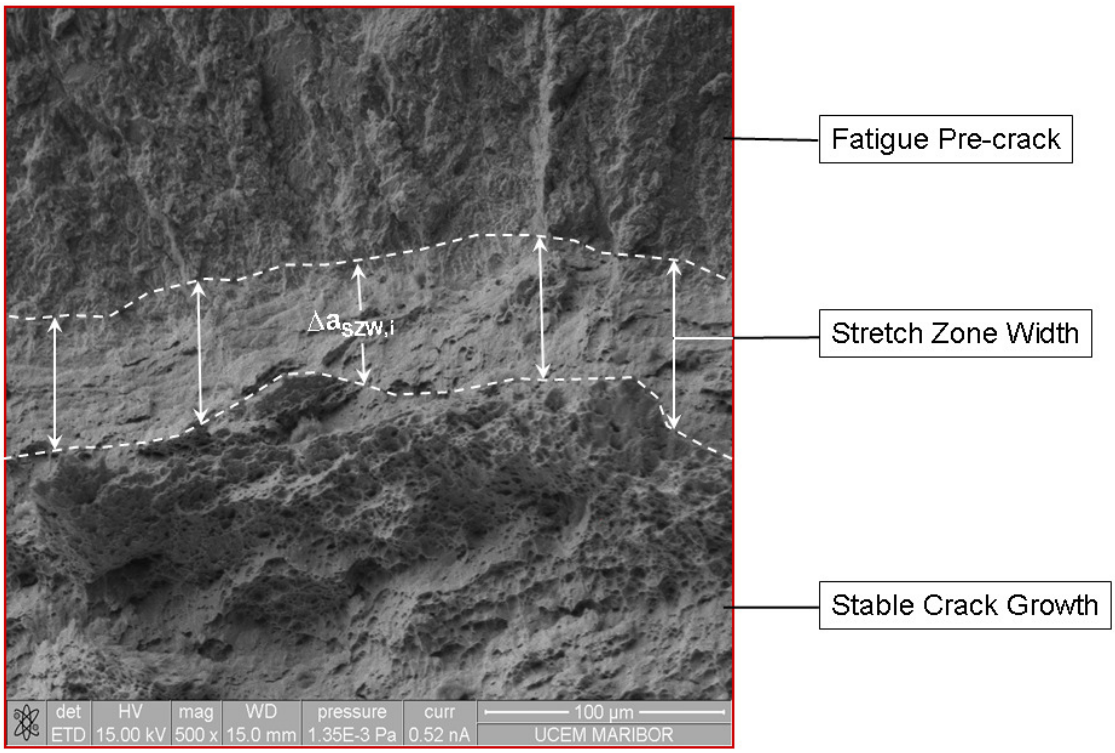

Figure 6.41 *Measurement of stretch zone width for tensile panels with semi elliptical surface pre-crack in WM.*

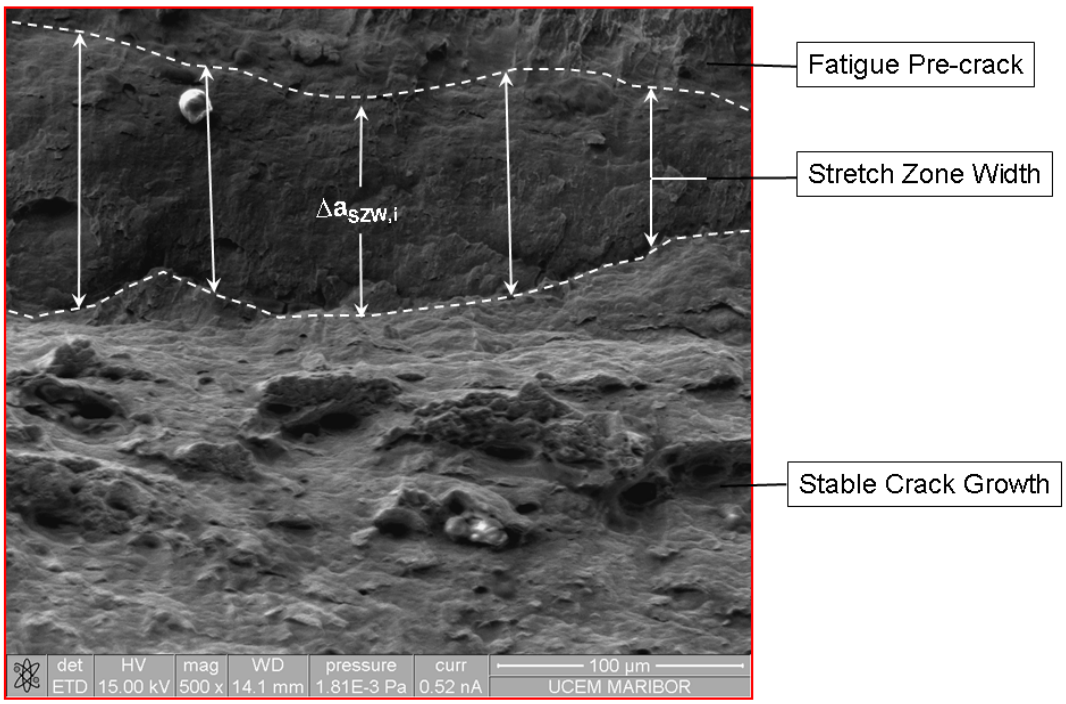

Figure 6.42 *Measurement of stretch zone width for tensile panels with semi elliptical surface pre-crack in HAZ.*

Chapter 7

Numerical Analysis of Local Damage in Weldments

7.1 Introduction

Numerical solution enables investigation of complex real problems, including detailed parametric analysis of any influencing factor. There are cases where experimental works and closed mathematical solutions are inadequate, e.g. due to high cost for large structures, problems in the existing hazard structures (radiation) and complexity of the problem.

Applications of micromechanical approaches usually require a combination of experimental and numerical work. Micromechanical models are directly implemented in numerical FE codes or through user subroutines to simulate local damage in investigated structures. Crack initiation and propagation can be numerically simulated by applying micromechanical models such as a complete Gurson model (CGM), which was used in this work.

In case the crack is located in the middle of the weld metal, not in the vicinity of the heat affected zone (HAZ), the joint can be analyzed as bimaterial. However, there are situations when it is also very important to understand the behavior of HAZ during the fracture process, bearing in mind that it is often susceptible to cracks and its toughness may influence the overall fracture behavior of a welded joint. Besides the cracks initiated in HAZ (e.g. around some initial defect), it is important to take into account the possibility that the fracture path can run through HAZ even if the crack was initiated in WM or BM. Therefore, there are many cases when a welded joint should not be considered as bimaterial.

In this work, the crack initiation and propagation has been analyzed in welded single edge notched bend SENB specimens and tensile panels with a pre-crack in WM or HAZ. The aim was to determine the effects of mechanical heterogeneity and constraints on ductile crack initiation and propagation in high strength steel weldments using the same and different specimen geometries and loading configurations. In addition, the scope of numerical analysis of local damage in weldments was also to analyze the transferability of material damage parameters among different welded specimens.

2D and 3D FE analyses were carried out for various welded specimens using ABAQUS. The effect of heterogeneity was numerically analyzed by considering welded specimens with pre-cracks in WM and HAZ. Moreover, constraint effect on fracture behavior was analyzed as well.

7.2 Numerical analysis of welded specimens fracture

For the determination of the value of stress and strain components and the value of damage parameter f at non-linear behavior of the materials exposed to external mechanical loading, the finite element method (FEM) program ABAQUS (www.simulia.com) was used, with CGM user subroutine, UMAT, developed by Zhang. Two SENB specimens and two tensile panels with pre-cracks in HAZ and WM have been modeled. Crack initiation and propagation have been modeled too.

It is well known that ductile tearing of metals occurs by the nucleation, growth and coalescence of microvoids with significant plastic deformation. Therefore, the zone of interest, containing the crack, is modeled by the CGM model and the rest of the model is characterized by elastic-plastic behavior without damage [97]. Based on this fact, ductile fracture was modeled in the current models by introducing a tearing zone surrounding the crack line, where material degradation and separation can occur. This tearing zone is embedded in a continuous elastic-plastic material where only plastic deformation occurs. Thus, tearing zone was considered in WM for the specimen with a pre-crack in WM and in HAZ for the specimen with a pre-crack in HAZ.

The welded joint is divided into four regions: BM, HAZ (CGHAZ and FGHAZ) and WM. Non-linear behavior of these regions materials was modeled by obtained true stress-strain curves using iteration 3, which is shown in Figure 6.8(c). The mechanical properties are given in Table 6.4, iteration 3. To simplify the finite element analysis, all

regions materials of welded joint were assumed to be isotropic. The incremental plasticity model provided by ABAQUS was used. The loading of all specimens was controlled by prescribed displacements.

In order to apply the CGM model to simulate the ductile tearing in SENB specimens and tensile panels with pre-cracks in WM and HAZ, various model parameters must be determined:

The first set of constitutive parameters is q_1 and q_2, which related to the hardening of the matrix material. In this study, q_1 and q_2 were 1.6 and 1.0, respectively, for specimens with a pre-crack in WM and 1.2 and 1.0, respectively, for specimens with a pre-crack in HAZ. The values of q_1 and q_2 were determined according to the study in [94]. The second set of parameters is void initiation and coalescence parameters: f_0, f_c and f_F. Initial void volume fraction f_0 are assumed to be equal to the volume fractions of non-metallic inclusions f_v, which are given in Table 6.3 for BM, HAZ and WM. The critical void volume fraction f_c is a crucial damage parameter in CGM model since it represents the end of stable void growth and the start of void coalescence. It is not a material constant according to CGM model, but it is calculated during the processing procedure, based on stress and strain fields. Void volume fraction at final fracture f_F is determined according to the relation $f_F = 0.15 + 2f_0$ [26]. The third set of parameters: ε_N, S_N, and f_N is related to secondary voids nucleation. The volume fraction of void nucleating particles f_N has been evaluated from Fe_3C content in materials using Equation 4.25. The nucleation parameters defined by Chu and Needleman, $\varepsilon_N = 0.3$ and $S_N = 0.1$, were considered for the analysis [95,102,124].

7.2.1 The 2D FE numerical analysis of SENB specimens

Two SENB specimens presented in chapter sixth were considered; one was precracked in WM and the other one in FGHAZ (Figure 7.1(a) and Figure 7.2(a)). They were analyzed as 2-D model under plane-strain conditions. Isoparametric quadrangular eight-node finite elements with 2×2 Gauss integration were used for simulating crack initiation, while four-node finite elements with full Gauss integration were used for simulating crack propagation. In front of the crack tip, squared finite elements (0.2×0.2 mm for specimen with a pre-crack in WM and 0.5×0.5 mm for specimen with a pre-crack in FGHAZ) were used. These sizes approximate the value of the mean free

path λ between non-metallic inclusions in tested materials (see Table 6.3). Figure 7.1 and Figure 7.2 show geometries and finite element meshes used to model the SENB specimens with pre-cracks in WM and FGHAZ, respectively. The geometries of specimens are given in Table 7.1 as well.

Table 7.1 *Geometry of SENB specimens.*

Specimen designation	B (mm)	W (mm)	a_0 (mm)	a_0/W
SENB-FGHAZ	11	11	5	0.45
SENB-WM	11	11	5.4	0.49

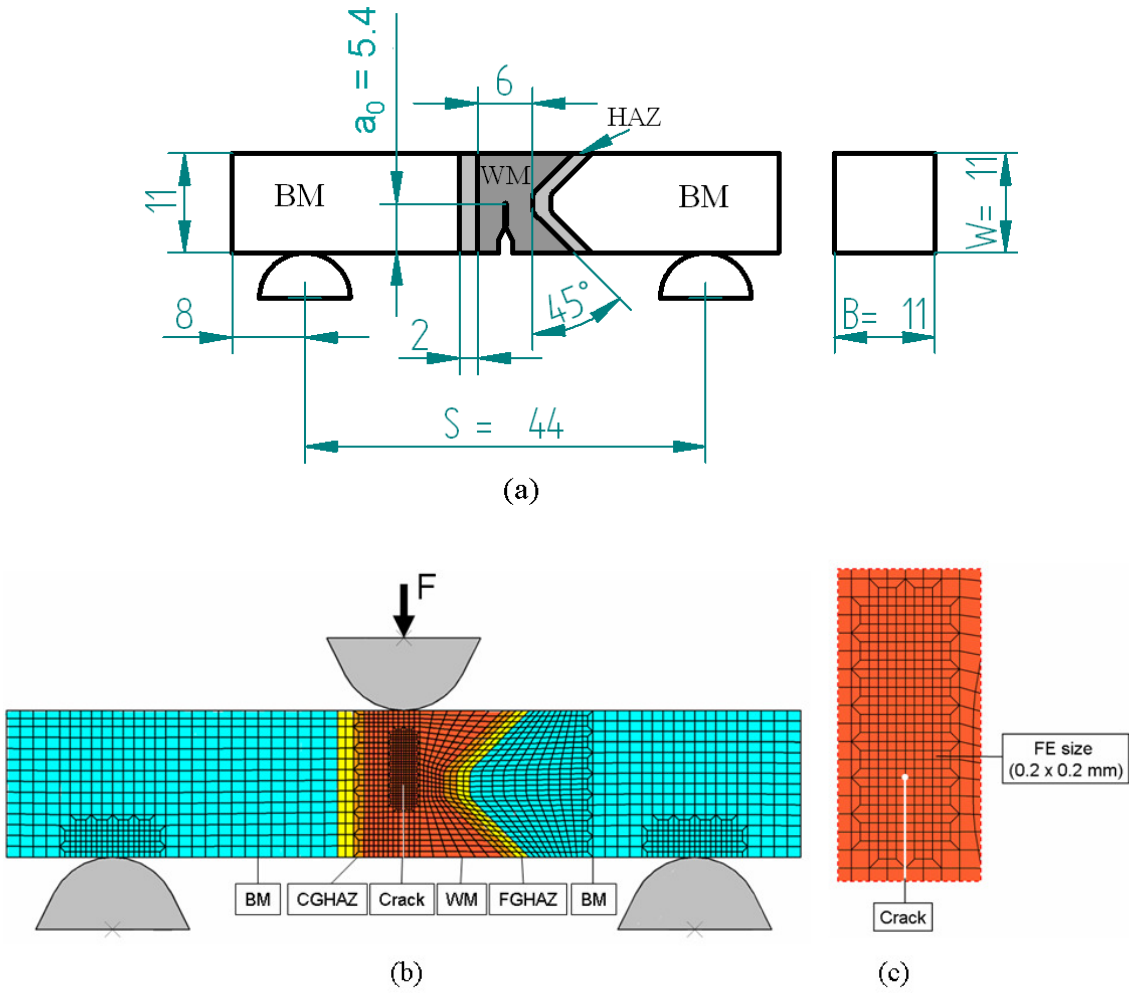

Figure 7.1*: (a) Geometry of SENB specimen with precrack in WM, (b) Finite element mesh and (c) Detailed crack-tip mesh.*

Heat affected zone (HAZ) is divided into two subzones; coarse grain heat affected zone CGHAZ and fine grain heat affected zone FGHAZ.

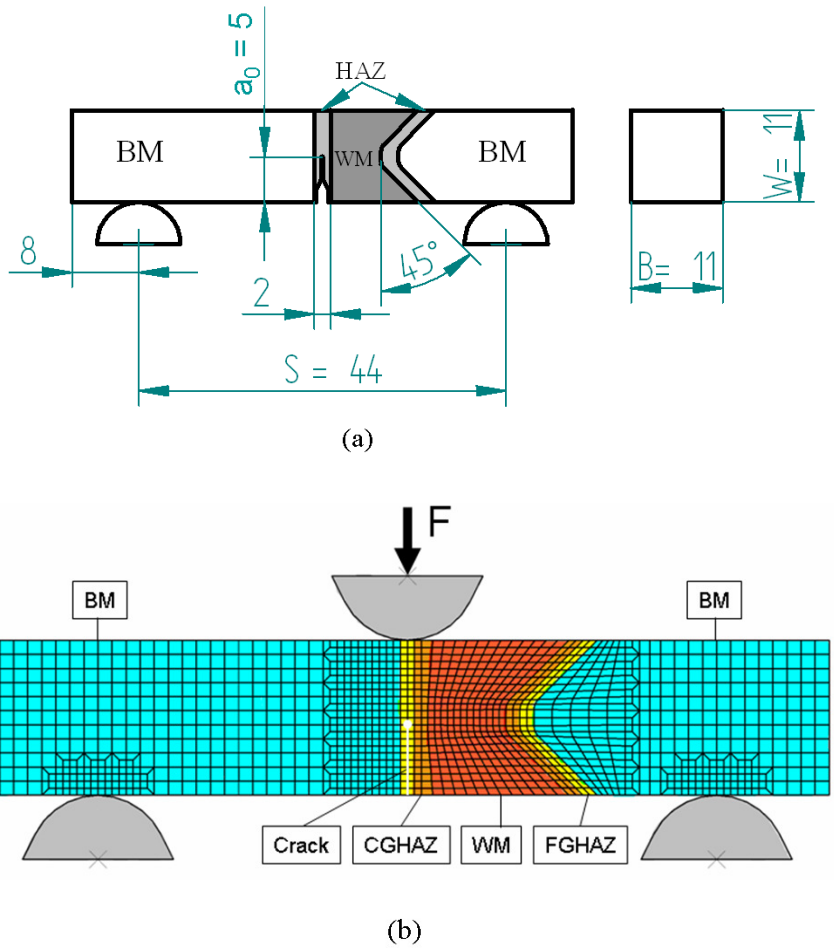

***Figure 7.2**: (a) Geometry of SENB specimen with a precrack in HAZ and (b) Finite element mesh.*

Obtained model parameters have been verified by comparing numerical results with experimental ones. Figure 7.3 and Figure 7.4 show a comparison between numerical (using the CGM model and von Mises) and experimental results of crack mouth opening displacement (CMOD) versus force (F) for SENB specimens with pre-cracks in WM and FGHAZ, respectively. Good agreement between numerical and experimental results has been achieved.

The effects of heterogeneity and constraint on ductile crack initiation and propagation have numerically been analyzed as follows:

7.2.1.1 Numerical modeling of crack initiation

Crack initiation can be predicted by using the CGM model according to failure criterion. Failure is defined by the instant when the first element in front of the crack tip

becomes damaged. The condition for the onset of the crack growth as determined by the J-integral, J_i, is most adequately defined by the micromechanical criterion [18]:

$$f \geq f_c \tag{7.1}$$

when the condition given by Equation (7.1) is satisfied, the onset of the crack growth occurs. The critical void volume fraction f_c in CGM model is determined by evaluating Equation (4.31(b)) at the end of every increment step. Once Equation (4.31(b)) is satisfied, void coalescence is started and the current void volume fraction is regarded as f_c for that integration Gauss point. To determine numerically crack initiation, the increase of void volume fraction f should be monitored at the nearest Gauss point to the crack tip. When current monitored f reaches f_c and Equation (7.1) is satisfied, crack initiation parameter is determined.

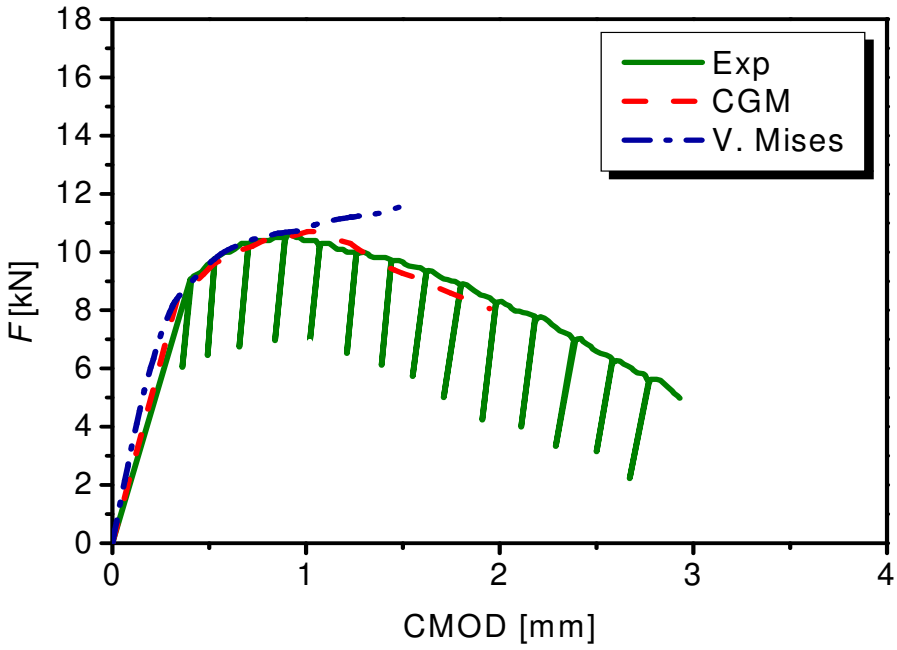

Figure 7.3 *Crack mouth opening displacement (CMOD) vs. force (F) for SENB specimen with a pre-rack in WM.*

Crack initiation values for SENB specimens with a pre-crack in WM and FGHAZ have been predicted using the CGM model. In Figure 7.5 the increase of the value of f is given as a function of the J-integral for SENB specimens with pre-cracks in WM and FGHAZ. Distributions of void volume fraction f at the onset of crack growth are shown in Figure 7.6 and Figure 7.7 for SENB specimens with pre-cracks in WM and FGHAZ, respectively. Equivalent von Mises stress distributions at the onset of crack growth are

shown in Figure 7.8 and Figure 7.9 for SENB specimens with pre-cracks in WM and FGHAZ, respectively. The *J*-integral for a stationary crack under loading is obtained by using the domain integral method. The values of the *J*-integral corresponding to the initiation (J_i) of crack growth are computed on the basis of the micromechanical parameters of the CGM model. The values of J_i are given in Table 7.2 with experimental values of fracture toughness ($J_{0.2/BL}$) obtained from SENB specimens with pre-cracks in WM and FGHAZ. It is important to know that the value of J_i can be determined experimentally by measuring the stretch zone width according to the ESIS P2-92 procedure [121], while $J_{0.2/BL}$ was determined without measuring the stretch zone width according to ASTM E1820-08. The value of $J_{0.2/BL}$ is greater than J_i for the majority of structural materials (see [121]). The values of plastic strain zone size in FGHAZ and WM were numerically determined at the onset of crack growth (Figure 7.10).

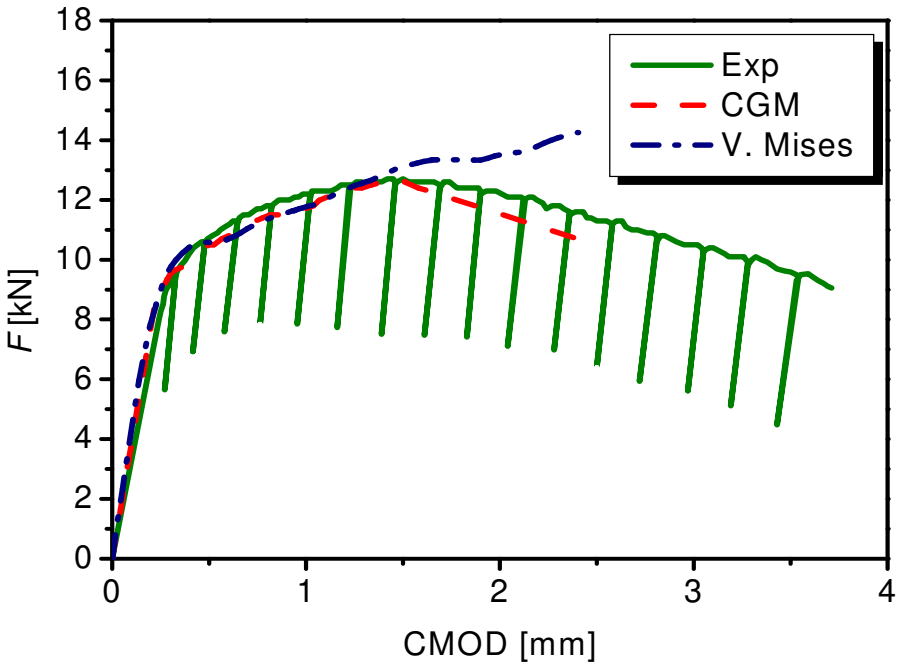

Figure 7.4 *Crack mouth opening displacement (CMOD) vs. force (F) for SENB specimen with a pre-crack in FGHAZ.*

Table 7.2 *Experimental $J_{0.2/BL}$ and numerical J_i values obtained from SENB specimens with a precrack in FGHAZ and WM.*

Specimen designation	$J_{0.2/BL}$ (kJ/m^2)	J_i (kJ/m^2)
SENB-FGHAZ	84	121
SENB-WM	64.7	57.6

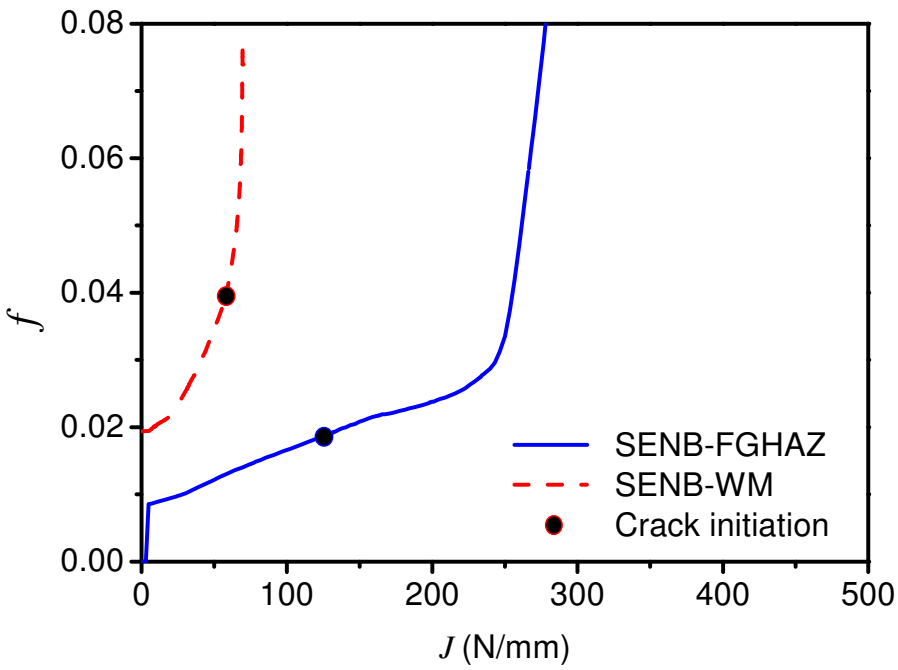

Figure 7.5 *Void volume fraction vs. J-integral for SENB specimens with pre-cracks in WM and FGHAZ.*

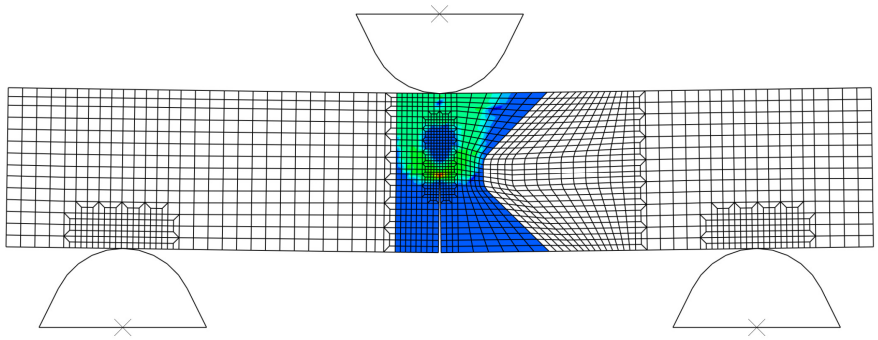

(a)

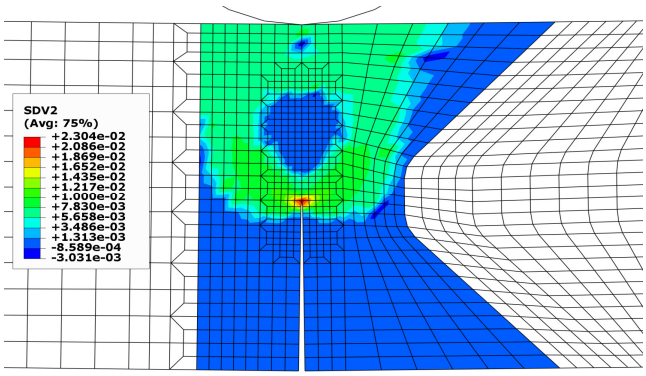

(b)

Figure 7.6*: (a) distribution of void volume fraction at the onset of crack growth for SENB specimen with a pre-crack in WM and (b) detailed view at crack tip.*

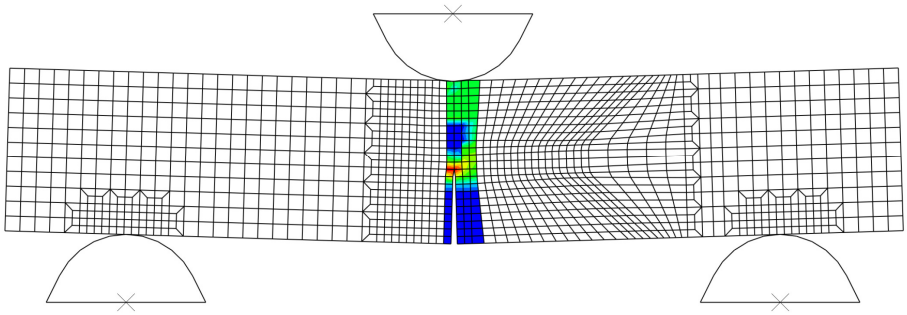

(a)

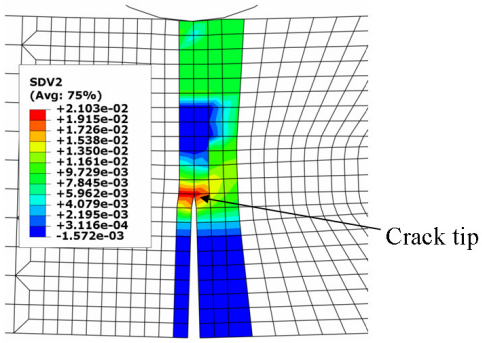

(b)

***Figure 7.7**: (a) distribution of void volume fraction at the onset of crack growth for SENB specimen with a pre-crack in FGHAZ and (b) detailed view at crack tip.*

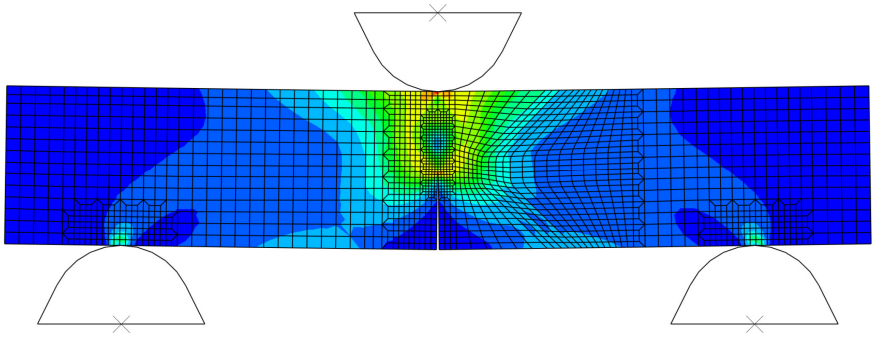

(a)

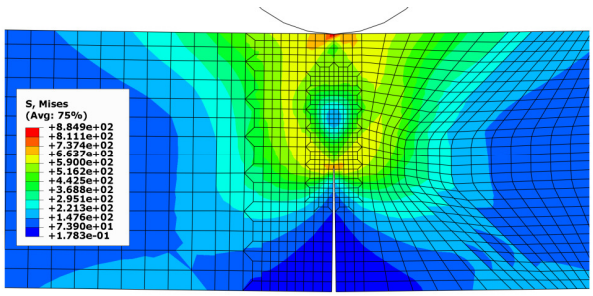

(b)

***Figure 7.8**: (a) distribution of equivalent von Mises stress at the onset of crack growth for SENB specimen with a pre-crack in WM and (b) detailed view at crack tip.*

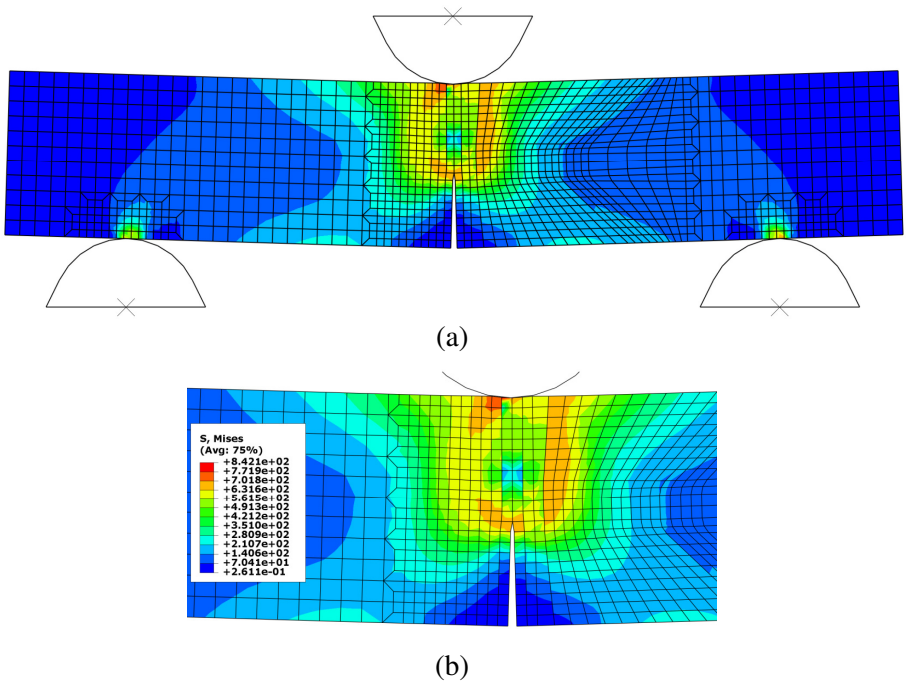

***Figure 7.9**: (a) distribution of equivalent von Mises stress at the onset of crack growth for SENB specimen with a pre-crack in FGHAZ and (b) detailed view at crack tip.*

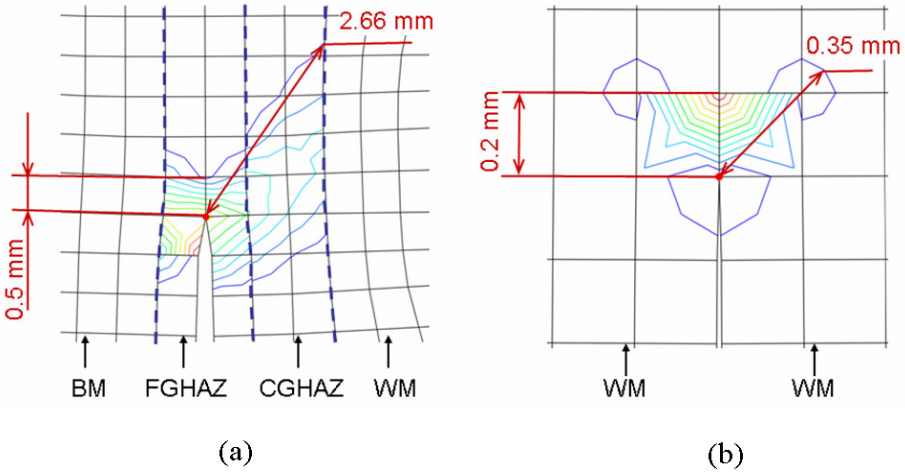

***Figure 7.10** Plastic strain zone size at the onset of crack growth for SENB specimens with a pre-crack in: (a) HAZ and (b) WM.*

7.2.1.2 Numerical modeling of crack propagation

Generally, there are four possible methods to simulate crack propagation in finite element analysis: element splitting, node releasing, element deleting and stiffness decreasing. The last technique has been used in this work.

The computational simulation within an element follows Equation 4.15 after it reaches the critical damage value f_c, and is forced to continue until the void volume fraction f^*, reaches its maximum value f_u^*. At this point in the simulation the element of

that material is fully failed according to Equation 4.14, leading to local stiffness reductions [97].

J-R curves have been obtained for weld and HAZ metals using specimens with a pre-crack in WM and HAZ. The FE meshes for both specimens are shown in Figure 7.1 and Figure 7.2. In the model of tearing zone, minimum two layers of elements with a highly refined mesh stretch out across the ligament ahead of the crack tip because of expected damage and crack propagation in this region. However, several researchers [112,125] have introduced a single layer of elements in front of the prospective crack plane to simulate the ductile tearing.

The crack growth (Δa) has been simulated by tracing the path of completely damaged elements, which appear completely in different color in Figure 7.11 and Figure 7.12. In other words, the crack growth has been estimated by multiplying the original length of an element (l_c) with the number of completely damaged elements. The element is assumed to be failed (completely lost load carrying capacity) when the void volume fraction at final failure f_F is reached according to the relation $f_F = 0.15 + f_0$. Then, the corresponding value of *J*-integral is obtained. The crack growth resistance curves were obtained and shown in Figure 7.13 and Figure 7.14 for materials of WM and HAZ.

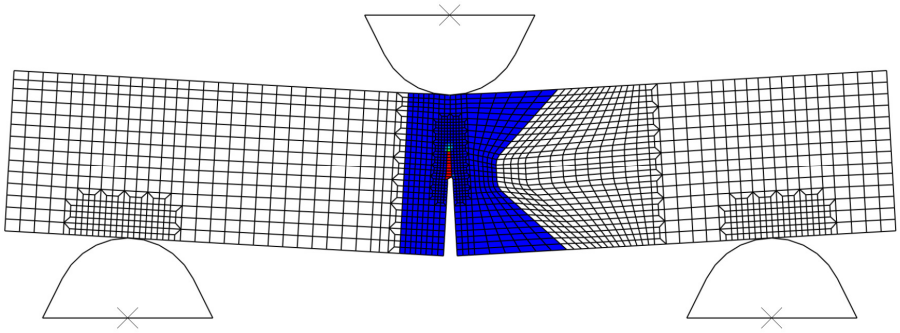

(a)

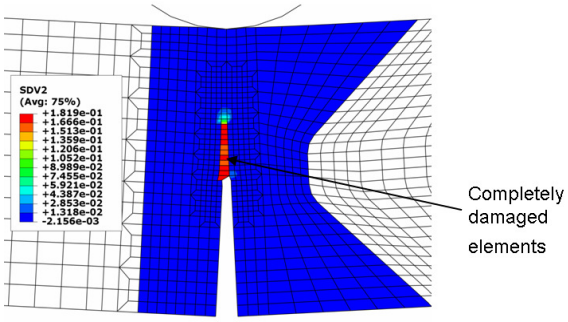

(b)

***Figure 7.11**: (a) distribution of void volume fraction for SENB specimen with a pre-crack in WM and (b) detailed view at crack tip.*

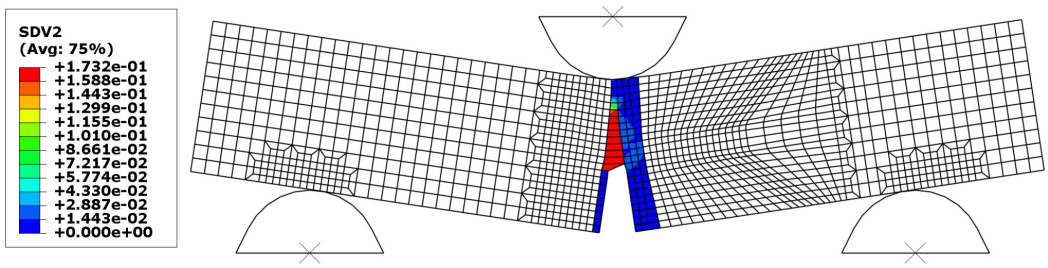

Figure 7.12 *Distribution of void volume fraction for SENB specimen with a pre-crack in FGHAZ.*

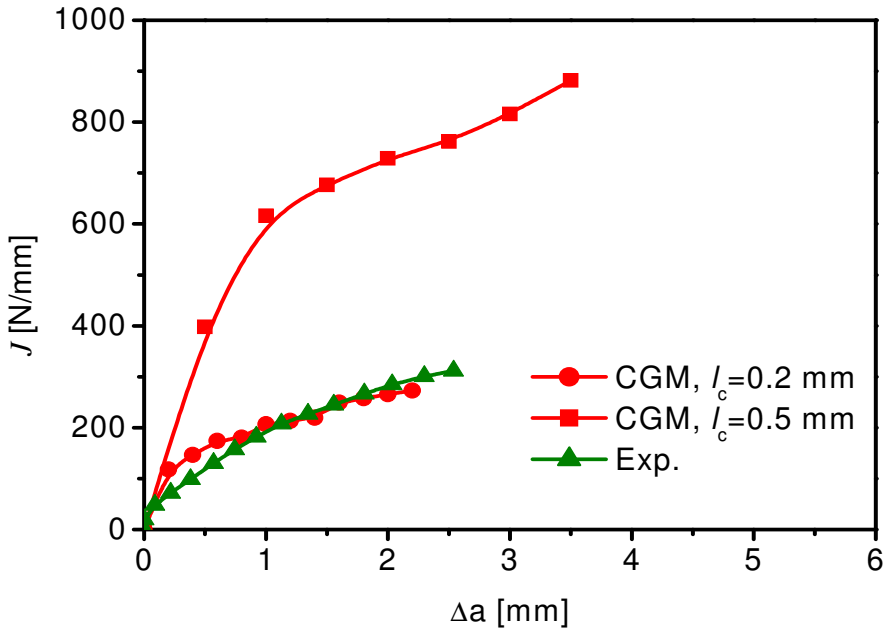

Figure 7.13 *Experimental and numerical J-R curves obtained from SENB specimen with a pre-crack in WM with the effect of mesh size l_c.*

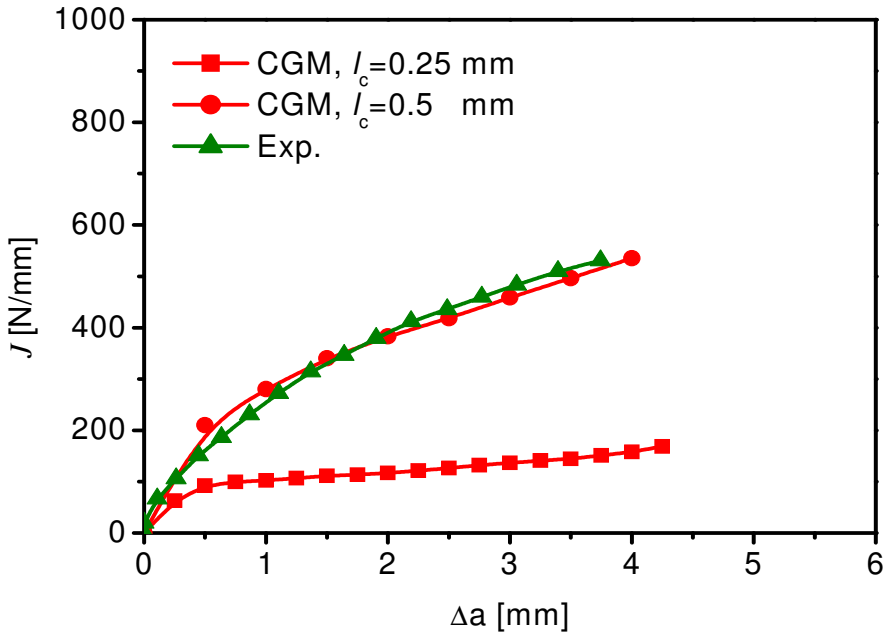

Figure 7.14 *Experimental and numerical J-R curves obtained from SENB specimen with a pre-crack in FGHAZ with the effect of mesh size l_c.*

7.2.2 The influence of FE size on crack initiation and propagation

Several researches analyzed the effect of finite element size on the prediction of crack initiation and crack resistance curves [17,18,26,100]. In this study, it is also found that the size of FE mesh significantly affects the material resistance curves and crack initiation values for specimens with pre-cracks in WM and HAZ. These results are in agreement with the literature results. For both materials, the initial FE size is set to the approximate value of the mean free path (λ) between non-metallic inclusions. In addition, one more mesh size was considered for each specimen; these sizes were chosen as follows: elements larger than λ for WM and elements smaller than λ for HAZ. In this way, two similar finite element sizes are used for each of the materials. Significant effect of FE mesh size on material resistance curves can be seen in Figure 7.13 and Figure 7.14. Moreover, the effect of FE mesh size on distribution of void volume fraction can be seen in Figure 7.15 at specific prescribed displacement (u_2), which represents applied force. The good agreement between experimental and numerical results is obtained for the size of the element approximating the mean free path between the non-metallic inclusions in analyzed materials, given in Table 6.3.

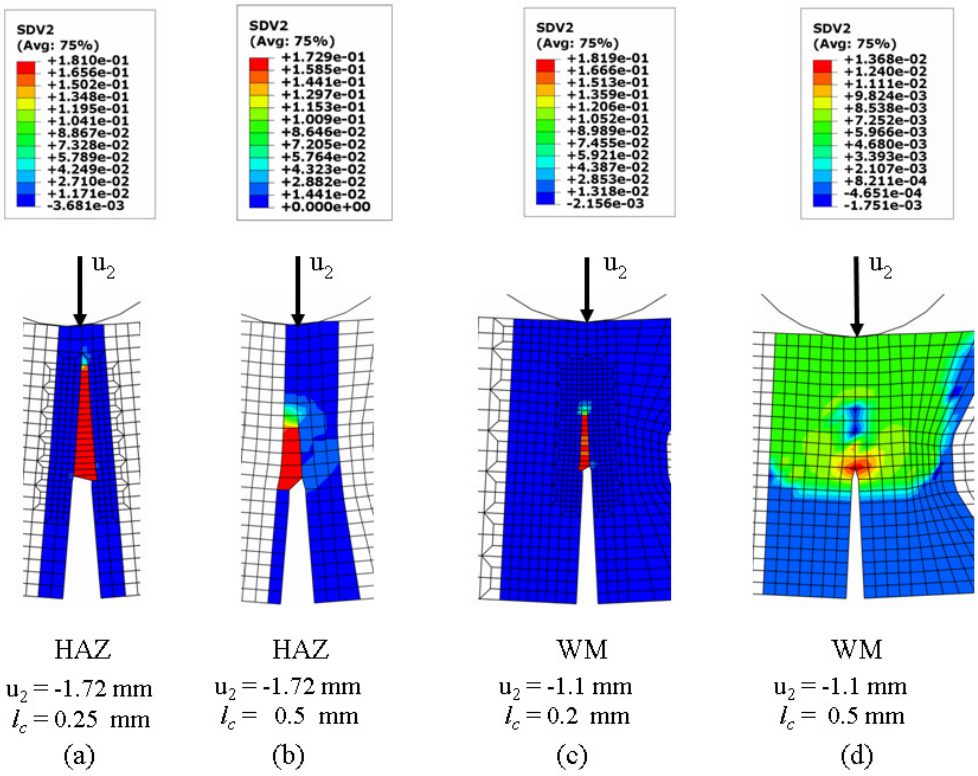

Figure 7.15 *The effect of mesh size (l_c) at crack tip on the distribution of void volume fraction at prescribed displacement (u_2) for SENB specimens with a pre-crack in: (a), (b) HAZ and (c), (d) WM.*

7.2.3 The 3D FE numerical analysis of tensile panels

In order to study fracture behavior of welded high strength steels, used for pressure vessel, tensile panels with semi-elliptical surface cracks in HAZ and WM were used. Three-dimensional finite damage models for welded tensile panels with surface crack were developed. Ductile crack growth initiation values and *J-R* curves have been predicted numerically. The effect of crack tip constraint, mechanical heterogeneity and loading condition on ductile crack initiation and propagation has been studied numerically as well. Finite element code ABAQUS with material user subroutine UMAT was used to model the tensile panels. The tensile panels given in Table 7.3 and shown in Figure 7.16 were modeled with three-dimensional eight-node bricks elements. Figure 7.17 and Figure 7.18 display a typical mesh employed to model the tensile panels with surface crack in WM and FGHAZ, respectively. The K groove of welded joint has been considered symmetric about crack plane to simplify the FE model. During numerical analysis of tensile panel with semi elliptical crack in WM, symmetrical conditions were applied to the boundary surfaces on the *X-Z* plane ($Y = 0$) and the *Y-Z* plane ($X = 0$) in the finite element model while only symmetrical one was applied to the boundary surface on the *X-Z* plane ($Y = 0$) of tensile panel with semi elliptical crack in FGHAZ. Due to these symmetries, only one quarter of the tensile panel with semi-elliptical surface crack in WM was modeled while half tensile panel with semi-elliptical surface crack in FGHAZ was modeled. A uniform prescribed displacement, which represents the force in the *X* direction, was applied to the remote end of the tensile panels (Figure 7.17 and Figure 7.18). The FE model left side movement of the tensile panel with semi-elliptical surface crack in FGHAZ has been restricted in X direction.

Table 7.3 *Geometries of tensile panels with semi-elliptical surface cracks in HAZ and WM.*

Specimen designation	t (mm)	$2W$ (mm)	$2c$ (mm)	a_0 (mm)	a_0/t	a_0/c	c/W
TP-FGHAZ	10	40	22.14	5	0.5	0.45	0.55
TP-WM	10	40	22.71	5	0.5	0.44	0.57

Several researchers [126-128] have modeled the entire specimen or structure using damage constitutive relations to study the ductile fracture of metals. However, from metallurgical observations of ductile tearing [129], it has been found that many metals

have a very narrow fracture process zone. That is, damage is restricted to a region around the prospective crack plane. Thus, 3D modelling the whole specimen or structure using a damage constitutive model is unnecessary and inefficient in terms of computational economy. Several researchers [112,125] have introduced a single layer of elements with a damage constitutive model, namely computational cells, in front of the crack front to simulate the ductile tearing. This procedure has been adopted herein.

In the model of the tearing zone, ahead the crack front, minimum two layers of elements with a highly refined mesh stretch out across the ligament, because of expected damage and crack propagation in this region. Coarse meshes are applied beyond this region where no significant material degradation is anticipated. In current models, it was assumed that the materials were isotropic in order to simplify the finite element analysis. Moreover, the materials of base metal, coarse grain-HAZ and fine grain-HAZ have been modeled by using conventional J_2 flow theory von Mises plasticity with large displacement analysis and the region of weld metal, where the crack is located, has been considered as tearing zone modeled by the CGM model. While, the materials of base metal, weld metal have been modeled by using conventional J_2 flow theory von Mises plasticity with large displacement analysis and the regions of CGHAZ and FGHAZ, where the position of the crack is located, have been considered as tearing zone modeled by the CGM model. The mesh size, l_c, was chosen to approximate the mean free path between non-metallic inclusions. A fixed mesh sizes l_c = 0.2 mm and l_c = 0.5 mm of elements were chosen on vertical planes on the crack front of; the tensile panel with semi-elliptical surface crack in WM and the tensile panel with semi-elliptical surface crack in FGHAZ, respectively, but along the crack front is about $5l_c$ because the variation of stress/strain in this direction is not significant (Figure 7.17 and Figure 7.18).

To analyze the transferability of micromechanical material parameters and the validation of the ductile failure model implemented, the numerical and experimental results have to be compared. Figure 7.19-Figure 7.24 show comparison between numerical (using the CGM model) and experimental results of: force (F) versus crack tip opening displacement (δ_5), force (F) versus crack mouth opening displacement (CMOD) and CMOD versus δ_5 for tensile panels with surface crack in WM and FGHAZ. In numerical calculations, loading forces were determined by summing all reaction forces on the remote surface of the finite element model.

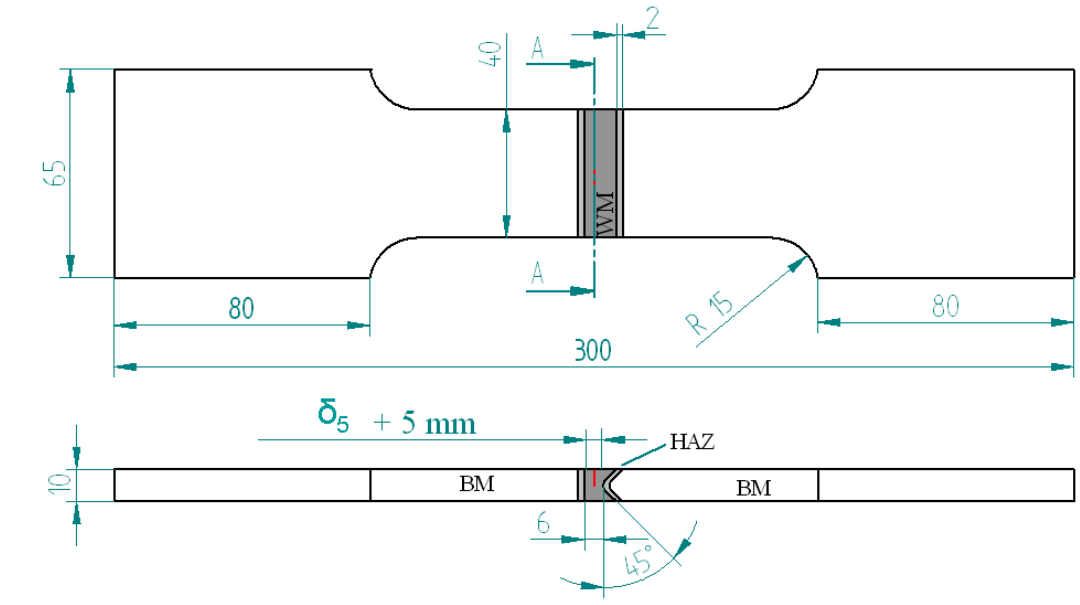

(a)

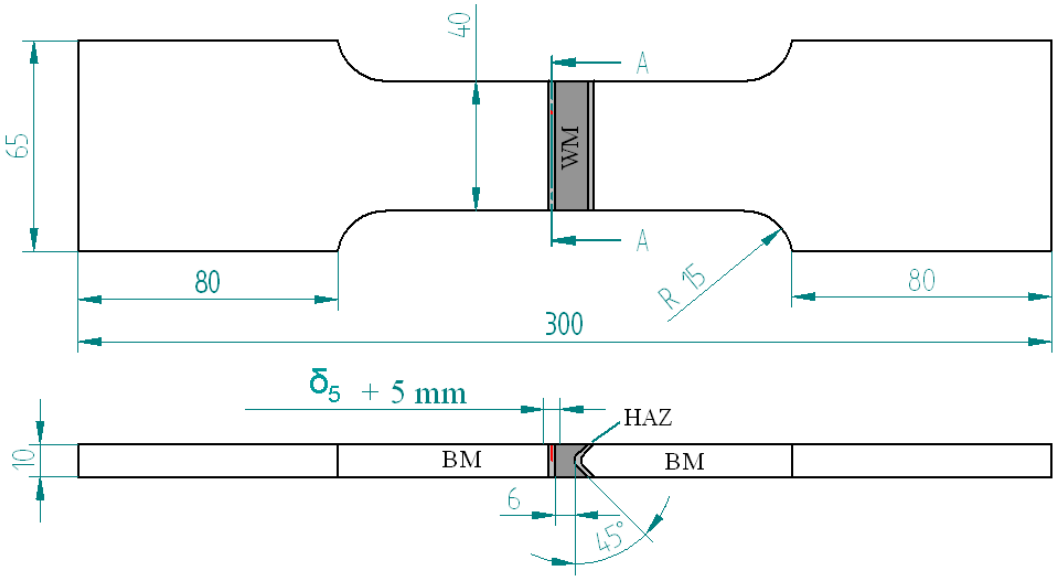

(b)

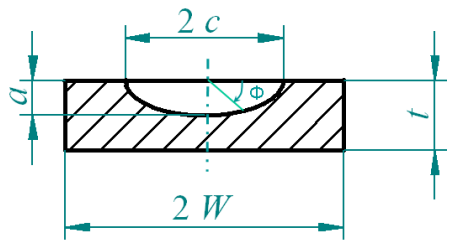

Section A-A

(c)

Figure 7.16 *Geometry of welded tensile specimens: (a) tensile panel with semi-elliptical surface crack in WM, (b) tensile panel with semi-elliptical surface crack in HAZ and (c) geometry of semi-elliptical crack.*

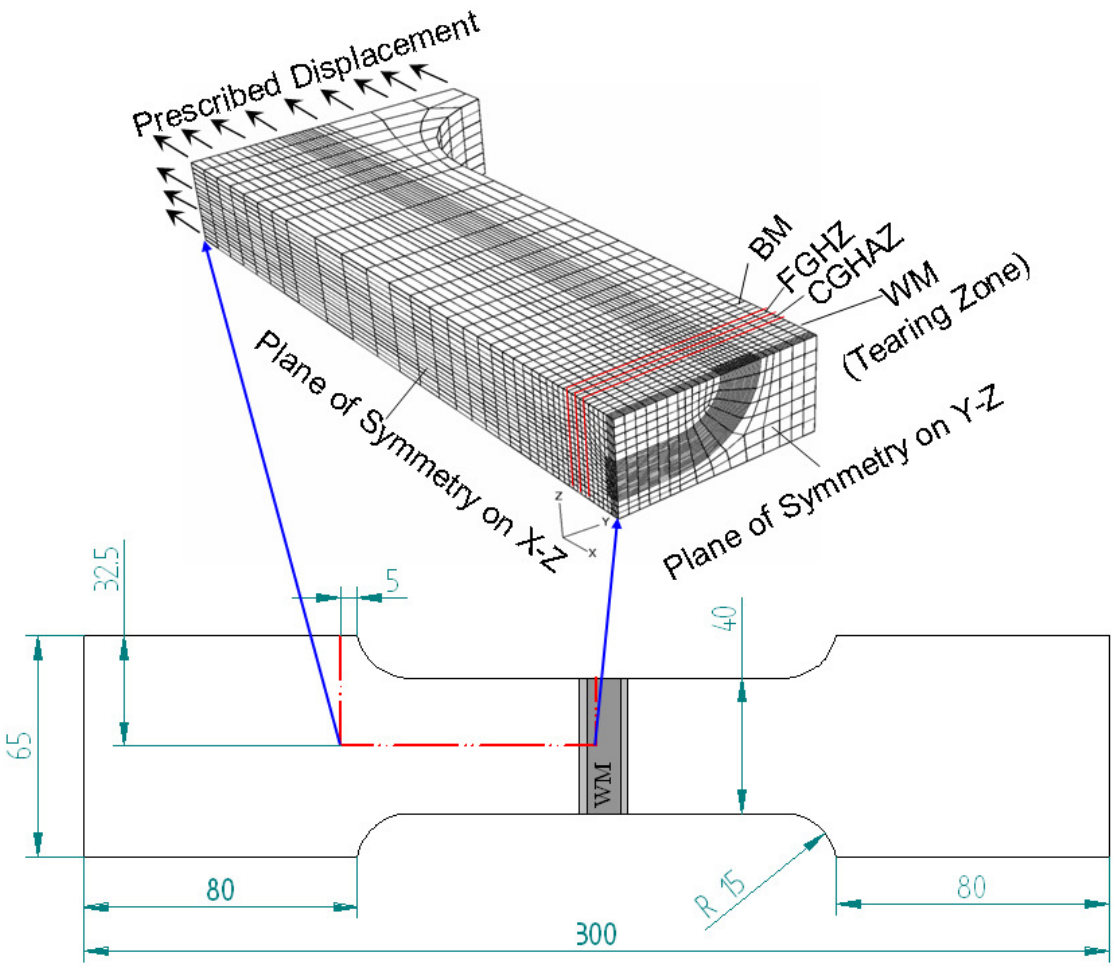

(a)

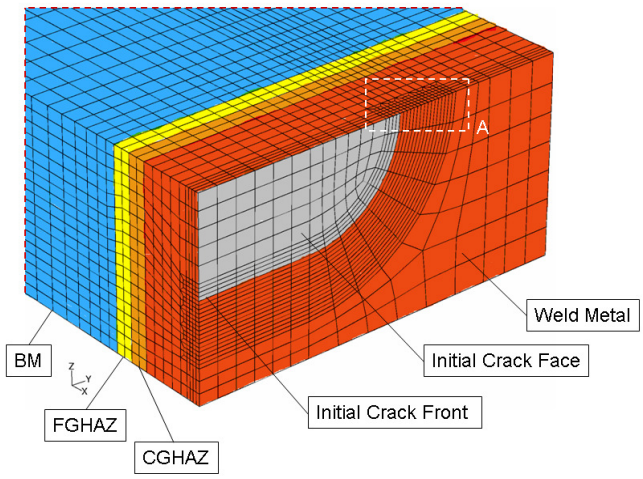

(b)

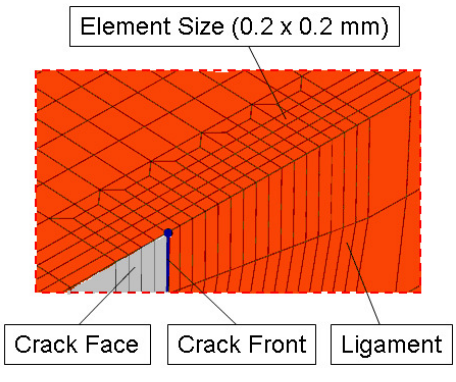

(c)

Figure 7.17 *Three-dimensional finite element model for tensile panel with surface crack in weld metal: (a) 3D finite element mesh for one quarter of specimen with boundary conditions, (b) Detailed mesh for the region near the crack front, and (C) Detail A for the mesh near the crack front.*

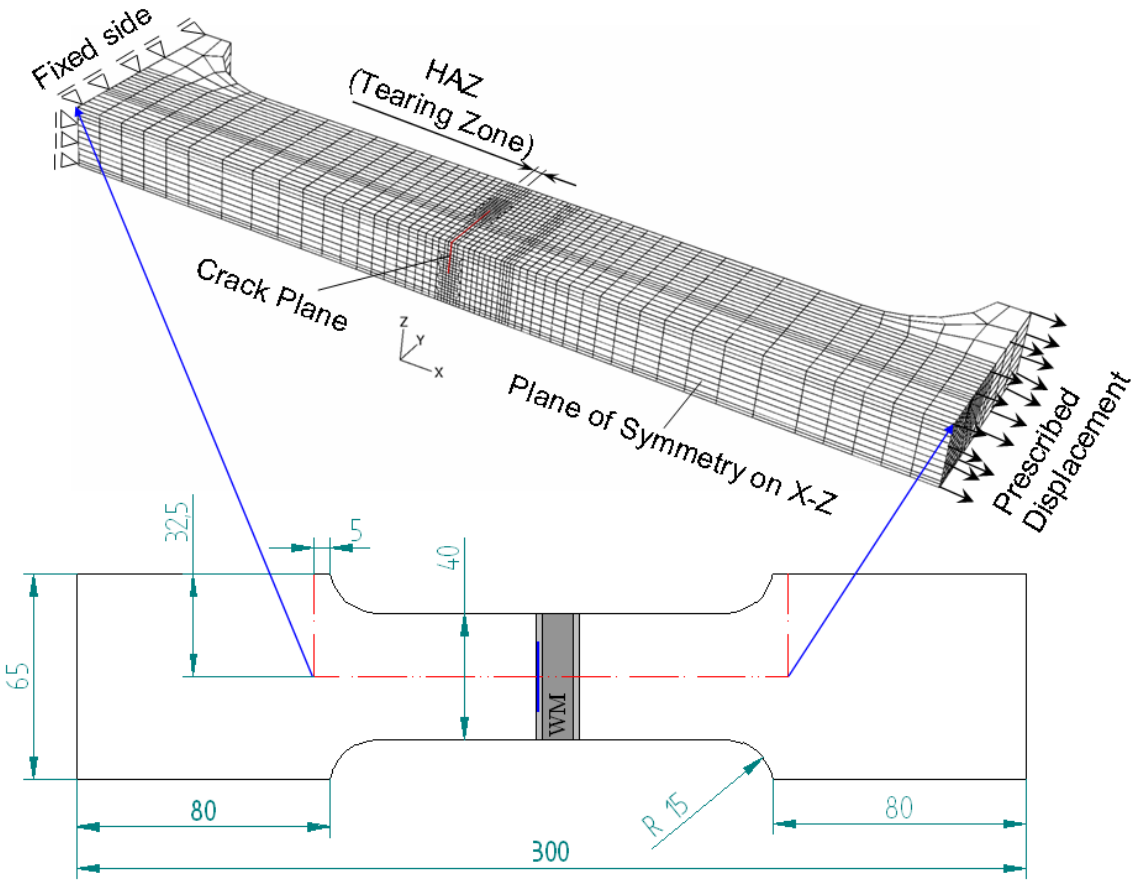

(a)

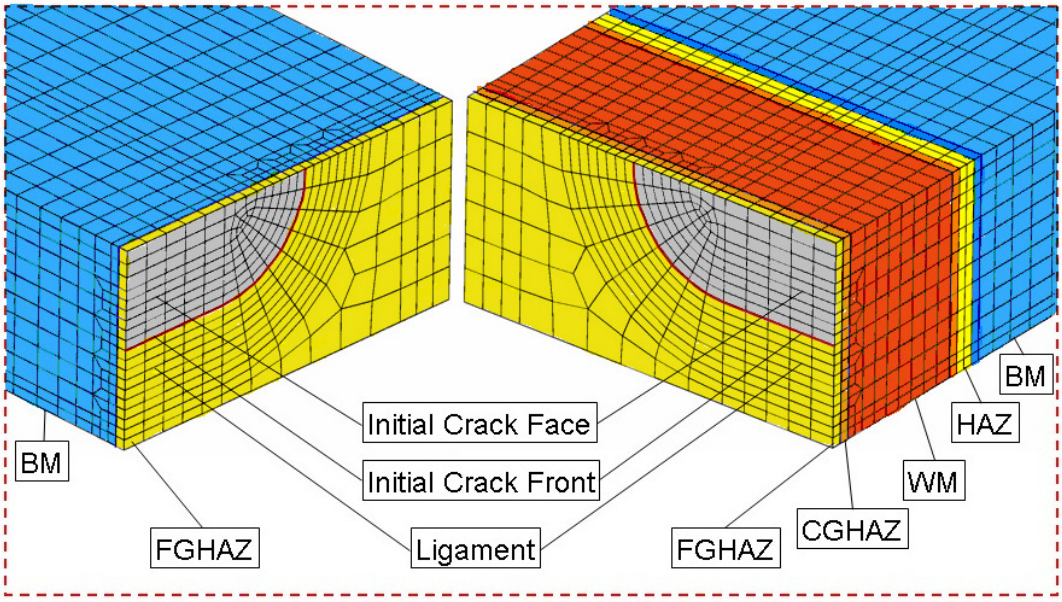

(b)

Figure 7.18 *Three-dimensional finite element model for tensile panel with surface crack in fine grain-HAZ: (a) 3D finite element mesh for half of specimen with boundary conditions, and (b) Detailed mesh for the region near the crack front.*

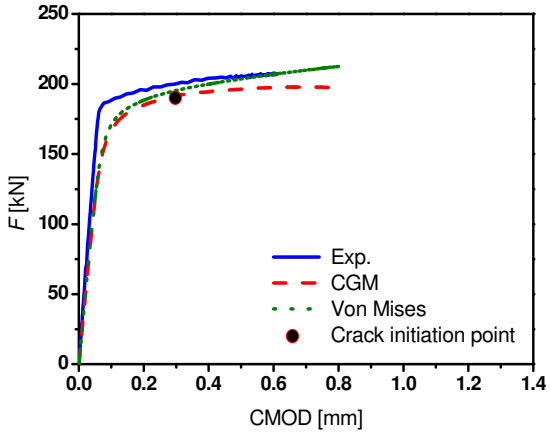

Figure 7.19 *Crack mouth opening displacement (CMOD) vs. force (F) for tensile panel with surface crack in WM.*

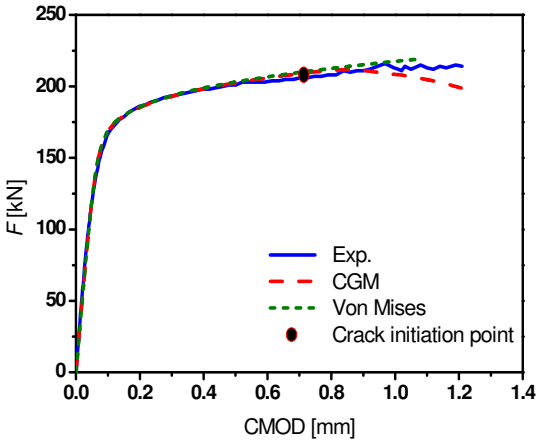

Figure 7.20 *Crack mouth opening displacement (CMOD) vs. force (F) for tensile panel with surface crack in FGHAZ.*

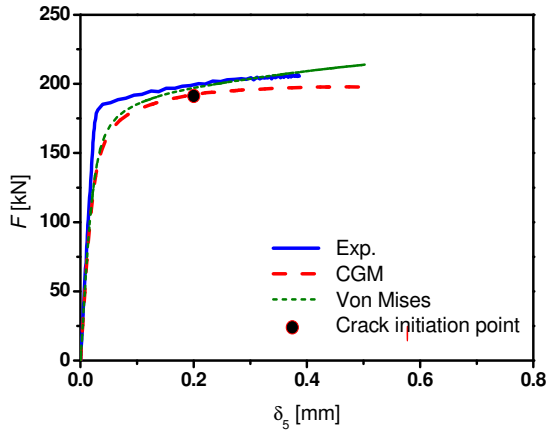

Figure 7.21 *Crack tip opening displacement (δ_5) vs. force (F) for tensile panel with surface crack in WM.*

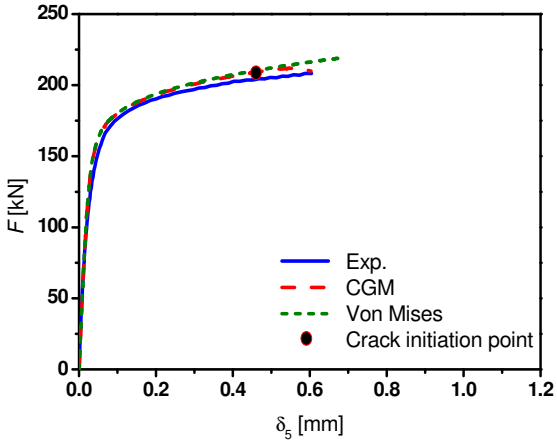

Figure 7.22 *Crack tip opening displacement (δ_5) vs. force (F) for tensile panel with surface crack in FGHAZ.*

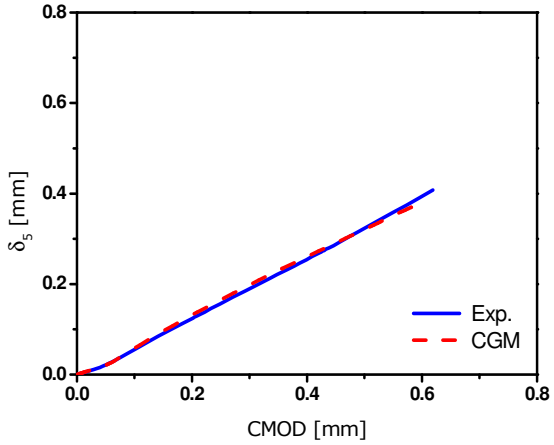

Figure 7.23 *Crack mouth opening displacement (CMOD) vs. Crack tip opening displacement (δ_5) for tensile panel with surface crack in WM.*

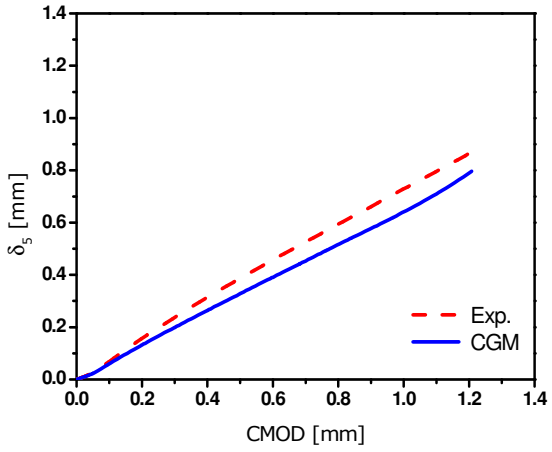

Figure 7.24 *Crack mouth opening displacement (CMOD) vs. Crack tip opening displacement (δ_5) for tensile panel with surface crack in FGHAZ.*

The ductile growth initiation and propagation for tensile panels have been modeled as follows:

7.2.3.1 Numerical modeling of crack initiation

Ductile crack growth initiation described here by J-integral at initiation (J_i) is modeled for tensile panels with surface cracks in FGHAZ and WM based on critical void volume fraction criterion (f_c) which represents the end of stable void growth and the start of void coalescence in the material. The same procedure used for prediction of crack growth initiation on SENB specimens was applied to the tensile panels. The values of J_i have numerically been estimated at the middle of the specimen thickness in front of crack line, where the highest value of void volume fraction occurs. The values of J_i for tensile panels with surface crack in WM (TP-WM) and FGHAZ (TP-FGHAZ) are given in Table 7.4 with values of J_i for SENB specimens for comparison purpose.

Table 7.4 *Experimental and numerical values of J-integral at the onset of crack growth obtained from SENB and tensile specimens.*

Specimen designation	$J_{0.2/BL}$ [N/mm]	J_i [N/mm]	
		Using SZW	CGM
SENB-WM	64.7	-	57.6
SENB-FGHAZ	84	-	121
TP-WM	-	125.1	114.7
TP-FGHAZ	-	321.4	346.2

Figure 7.25 and Figure 7.26 show the distribution of void volume fraction (f) at the instant of crack growth initiation for tensile panels with pre-cracks in WM and FGHAZ, respectively. Concentration of large values very close to the crack front is obvious. The location of crack initiation is also shown in this figure, which corresponds to the place of maximum stress triaxiality. It can be seen also in Figure 7.27-Figure 7.30 the effects of applied stresses and strains on the distribution of void volume fraction at crack growth initiation for both specimens with pre-cracks in WM and FGHAZ.

In Figure 7.31, the increase of the value of f is given as a function of the J-integral for tensile panels in comparison with results of SENB specimens with a pre-crack in WM and HAZ. As mentioned above for SENB specimens, the J-integral for a stationary crack under loading is obtained by using the domain integral method. It can be noticed in the Figure 7.31, the most rapid increase of the volume fraction of voids f was obtained for the specimens in the following order: SENB specimen with a pre-crack in WM, tensile

panel with a pre-crack in WM, SENB specimen with a pre-crack in FGHAZ and tensile panel with a pre-crack in FGHAZ.

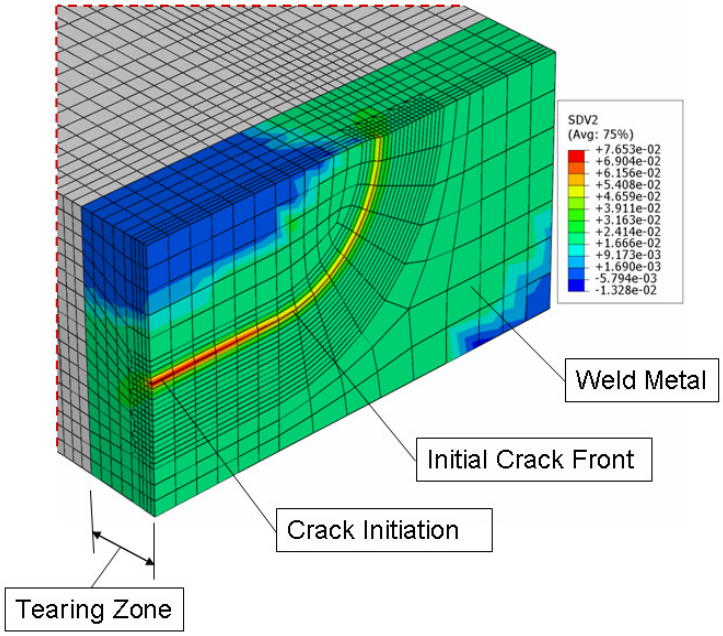

Figure 7.25 *Distribution of void volume fraction (f) in weld metal at the onset of crack growth.*

7.2.3.2 Numerical modeling of crack propagation

Crack growth in ductile materials is conventionally characterized by fracture resistance curves, obtained from the standard fracture tests. However, these standard fracture tests introduce a high degree of conservatism in engineering critical assessment of real structures such as pressure vessels. Therefore, using specimens such as cracked tensile panels may present better integrity assessment.

J-R curves for WM and HAZ materials have been numerically obtained using tensile panels with surface crack in WM and FGHAZ. The crack growth (Δa) was obtained by applying the same procedure used for SENB specimens. It has been simulated by tracing the path of completely damaged elements, which appear completely in different colors in this work (Figure 7.32 and Figure 7.33). The element is assumed to be failed (completely lost its load carrying capacity) when the void volume fraction at final failure (f_F) is reached according to the relation $f_F = 0.15 + f_0$. Then, the corresponding value of *J*-integral is obtained. The crack growth resistance curves are presented in Figure 7.34 for tested SENB specimens and tensile panels with pre-cracks in WM and HAZ at the deepest point of the crack front (Φ = 90º, Figure 7.16(c) and Figure 7.32), where the largest crack growth occurs.

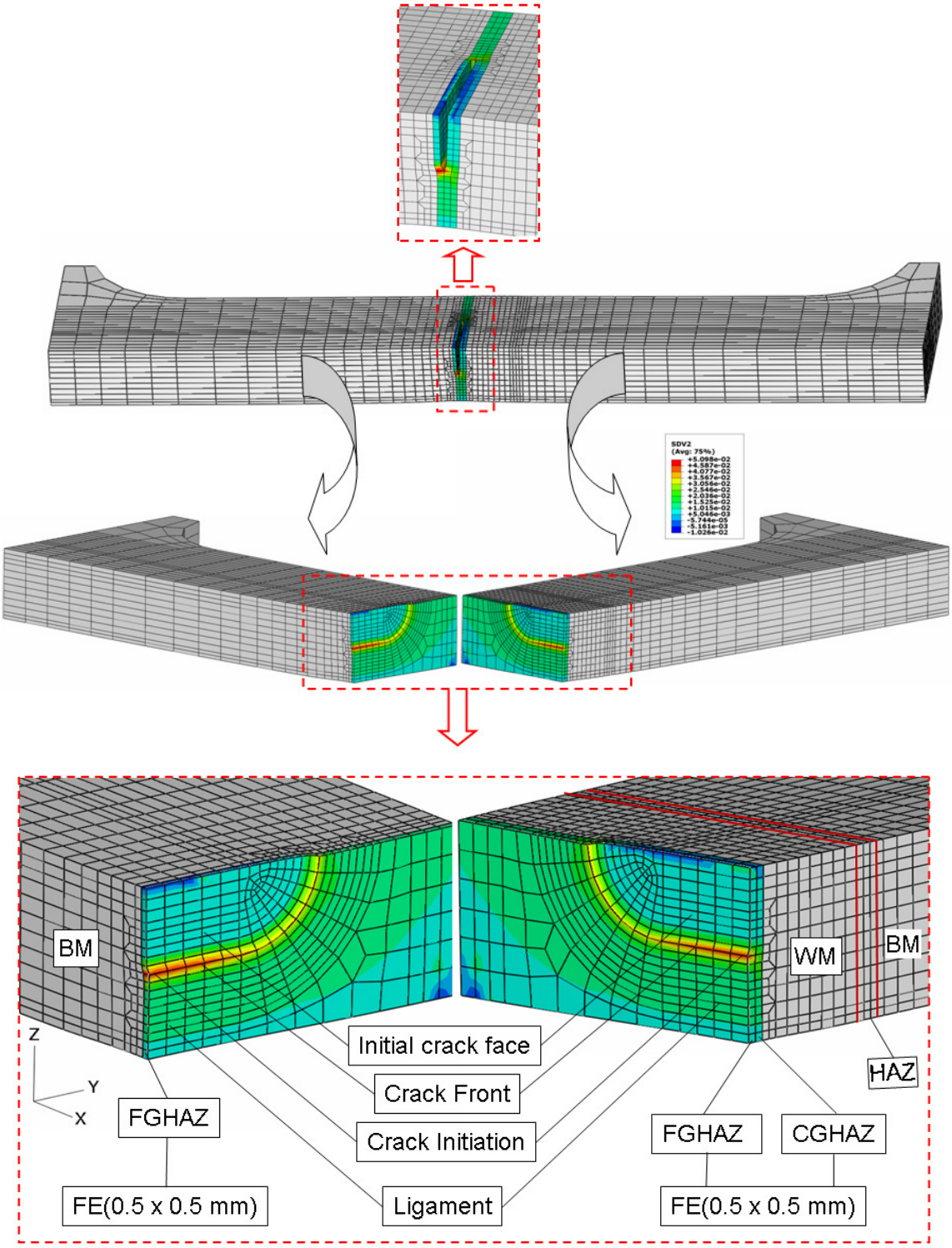

Figure 7.26 *Distribution of void volume fraction (f) in HAZ at the onset of crack growth.*

To analyze the validation of the ductile failure model implemented to tensile panels, the numerical and experimental results were compared. The tensile panel with surface crack in WM was just failed before ultimate applied load (Figure 7.19 and Figure 7.21). The tested specimen exhibits short stable crack growth. The experimental and numerical

(in terms of void volume fraction) fracture surfaces of tensile panel with surface crack in WM were compared (Figure 7.35). The comparison of experimental and numerical stable crack growth surfaces has shown that good agreement was obtained at the same value of CMOD. The stable crack growth value at final experimental value of CMOD ($CMOD_f$ = 0.6 mm) was compared with the same value of CMOD in FE model. It has been found that the stable crack growth on experimental fracture surface is about 0.6 mm, which can also be noticed on the numerical stable crack growth surface. At CMOD = 0.6 mm in numerical model, three elements, which their size are 0.2 mm, were completely failed at the deepest position of crack front (Figure 7.35).

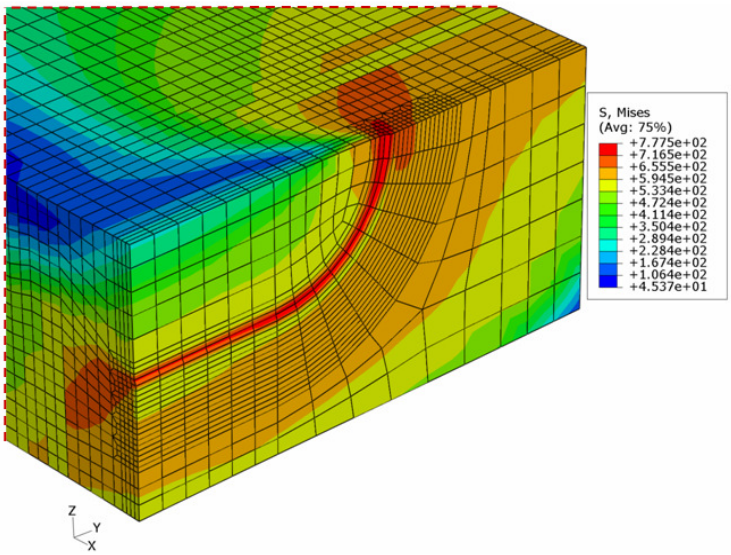

Figure 7.27 *Equivalent von Mises stress distribution at the onset of crack growth for tensile panel with semielliptical crack in WM.*

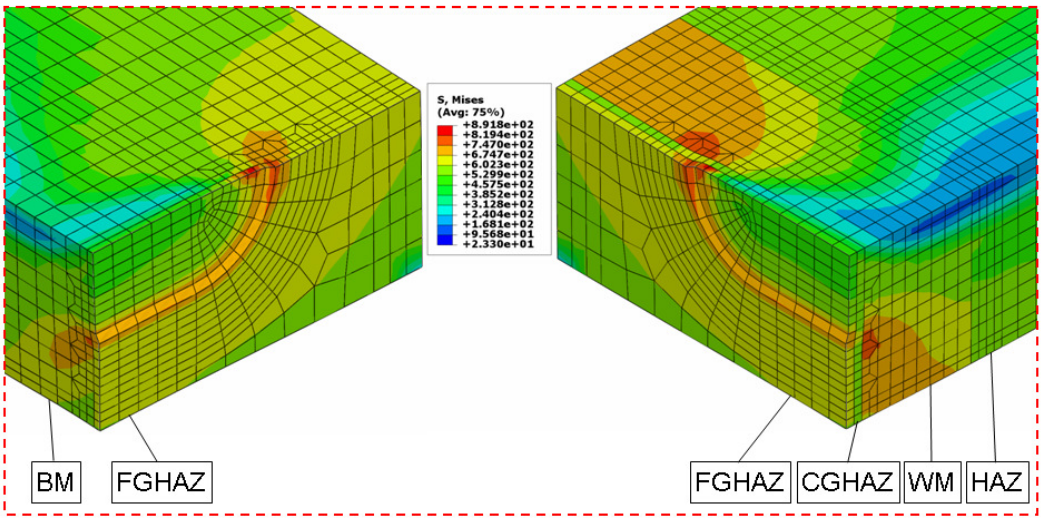

Figure 7.28 *Equivalent von Mises stress distribution at the onset of crack growth for tensile panel with semi elliptical crack in FGHAZ.*

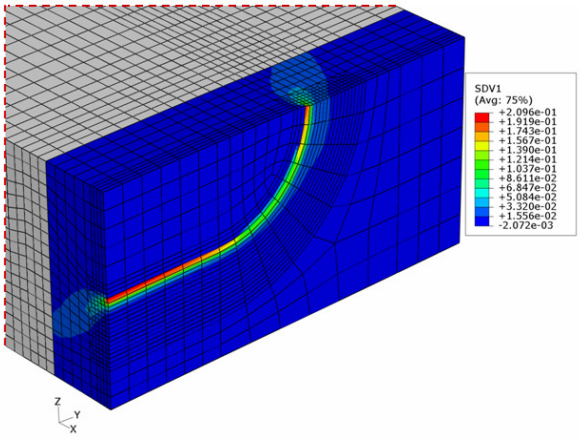

Figure 7.29 *Equivalent plastic strain distribution at the onset of crack growth for tensile panel with semi elliptical crack in WM.*

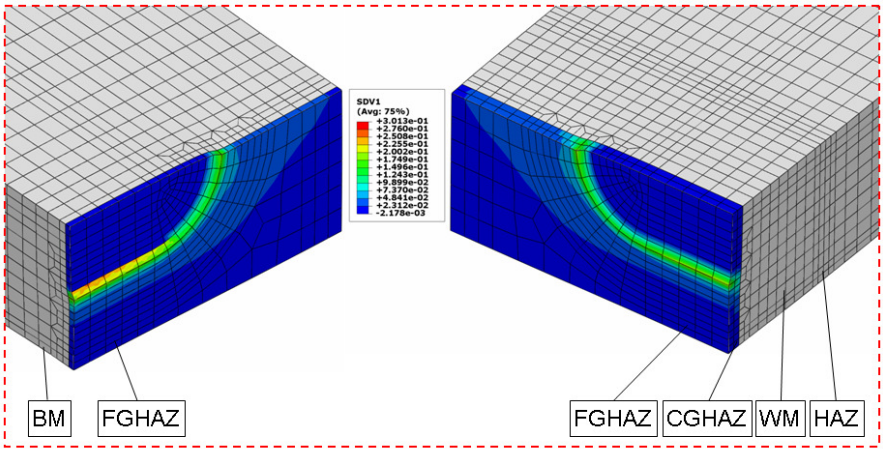

Figure 7.30 *Equivalent plastic strain distribution at the onset of crack growth for tensile panel with semi elliptical crack in FGHAZ.*

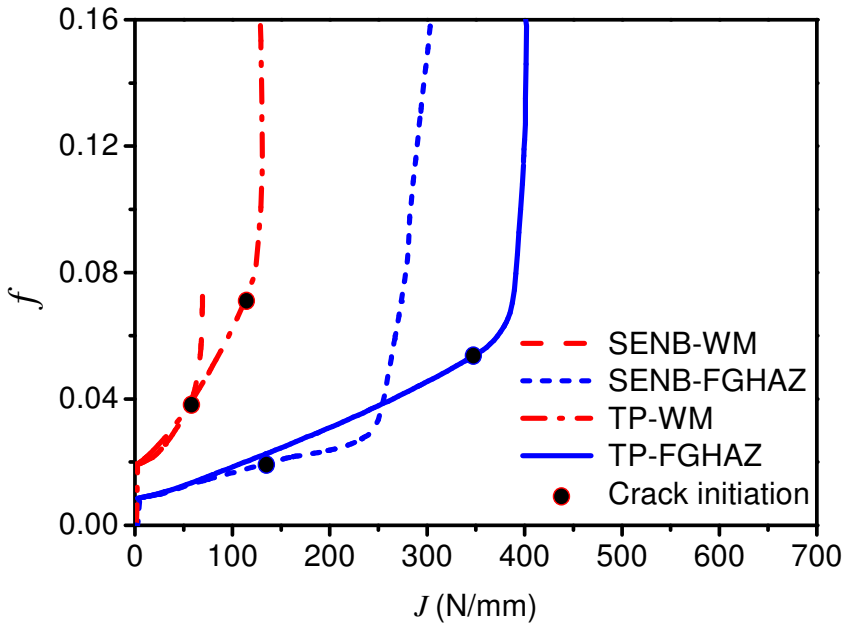

Figure 7.31 *Comparison of J-integral vs. void volume fraction (f) among tensile panels and SENB specimens with a pre-crack in HAZ and WM.*

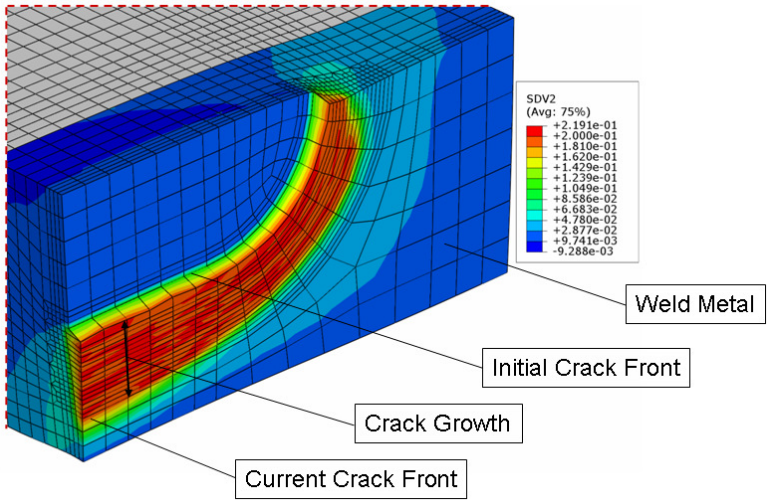

Figure 7.32 *Distribution of void volume fraction (red damaged elements represent crack growth path) for tensile panel with surface crack in WM.*

7.3 Constraint effect on crack initiation and propagation

The choice of specimens for structural integrity assessment in conventional fracture mechanics depends on constraint level - if the constraint level of the specimen matches the constraint level of the component, the results of specimen seem to be transferred to that of component within certain circumstances. Thus, micromechanical models do not depend on parameters which cannot be transferred directly from one geometry to another, but it depends on material parameters which are considered constant and can be transferred.

To understand fracture behavior of welded structures, constraint level has been analyzed on basis of stress triaxiality (σ_m / σ_{eq}), which is defined as the ratio of mean stress (σ_m) to the equivalent von Mises stress (σ_{eq}). Constraint effect has been studied on SENB specimens and tensile panels with pre-cracks in WM and HAZ. A comparison of stress triaxiality effect on ductile crack initiation can be seen in Figure 7.36 for all specimens. The stress triaxiality of tensile panel was determined in front of crack front, where the crack initiation occurs (Φ = 90º, see Figure 7.16, Figure 7.25 and Figure 7.26). The stress triaxiality along the crack front was also recorded at the onset of void coalescence (crack initiation) for tensile panels (Figure 7.37). The results in Figure 7.36 indicate that the specimen geometry with loading configuration (results of SENB-WM compared with TP-WM or SENB-FGHAZ compared with TP-FGHAZ) has the highest

influence on crack growth initiation and propagation, while mechanical heterogeneity has the least influence (see also Figure 7.31, Figure 7.34 and Table 7.4).

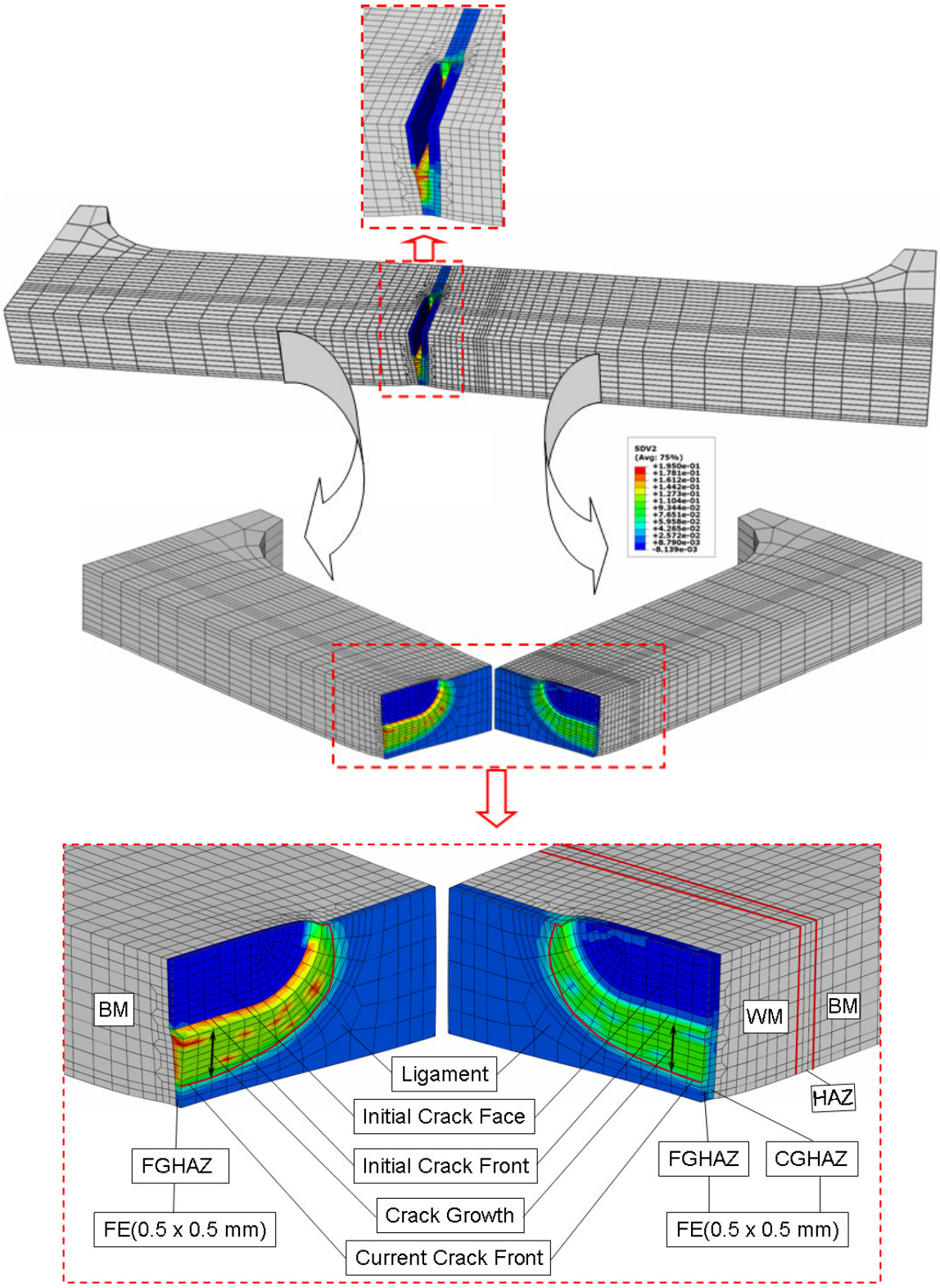

Figure 7.33 *Distribution of void volume fraction, which shows crack growth for tensile panel with surface crack in FGHAZ.*

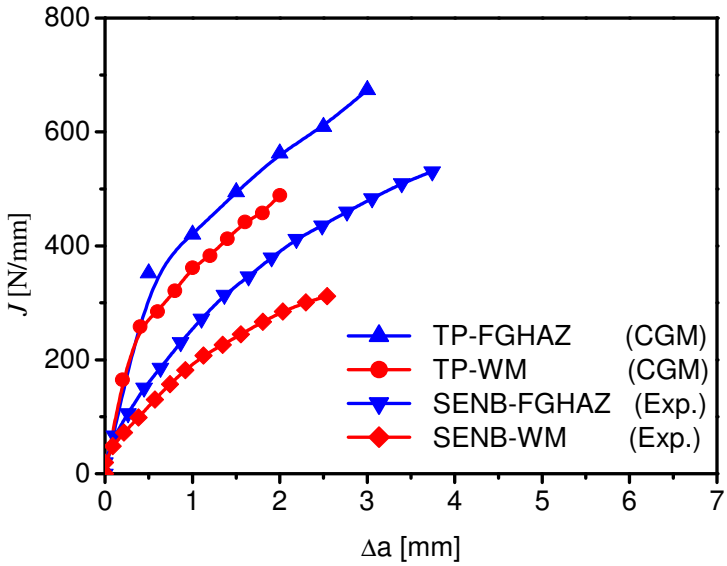

Figure 7.34 *Comparison among experimental J-R curves obtained from SENB specimens with pre-cracks in WM and HAZ and numerical J-R curves obtained from tensile panels with semielliptical surface cracks in WM and FGHAZ.*

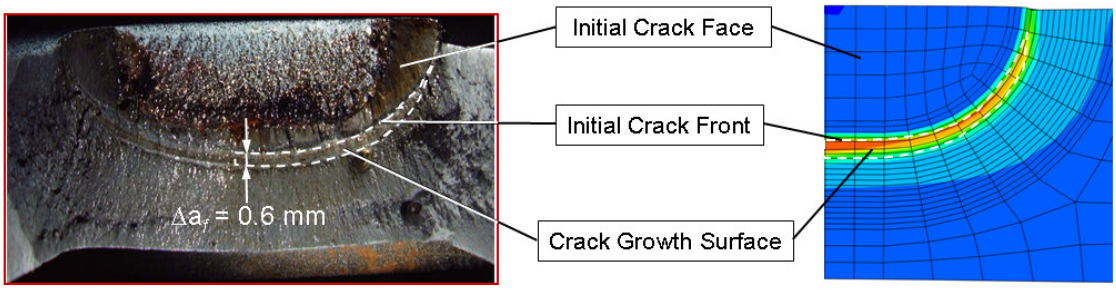

Figure 7.35 *Comparison between experimental and numerical fracture surfaces at the same value of CMOD (numerical fracture surface is represented by distribution of void volume fraction).*

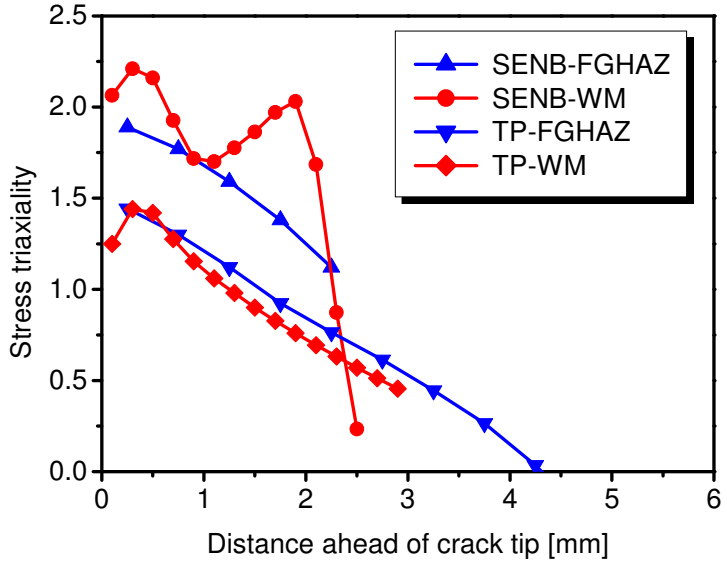

Figure 7.36 *The variation of stress triaxiality ahead of the initial crack tip for SENB specimens and tensile panels with pre-cracks in FGHAZ and WM at the moment of crack growth initiation.*

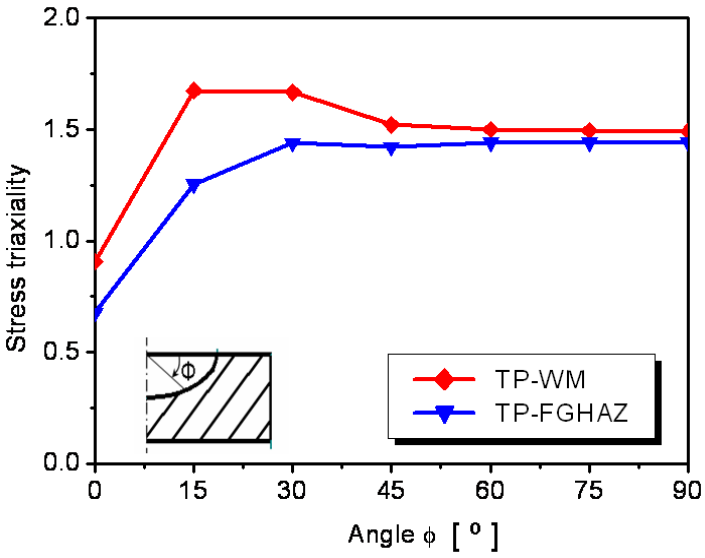

Figure 7.37 *Variations of stress triaxiality along the crack front at the onset of crack growth.*

The path of crack growth in tested specimens is also influenced by stress triaxiality as shown in Figure 7.38, which displays the result of tensile panel with a pre-crack in WM. The results exhibit highly non-uniform crack growth along the crack front due to the variation in stress triaxiality under even a pure tension load. For tensile panel, the crack grows the most at the deepest point of the crack front (Φ = 90º) and the least at the surface point (Φ = 0º). It is obvious also that the crack front remains semi-elliptic during crack growth.

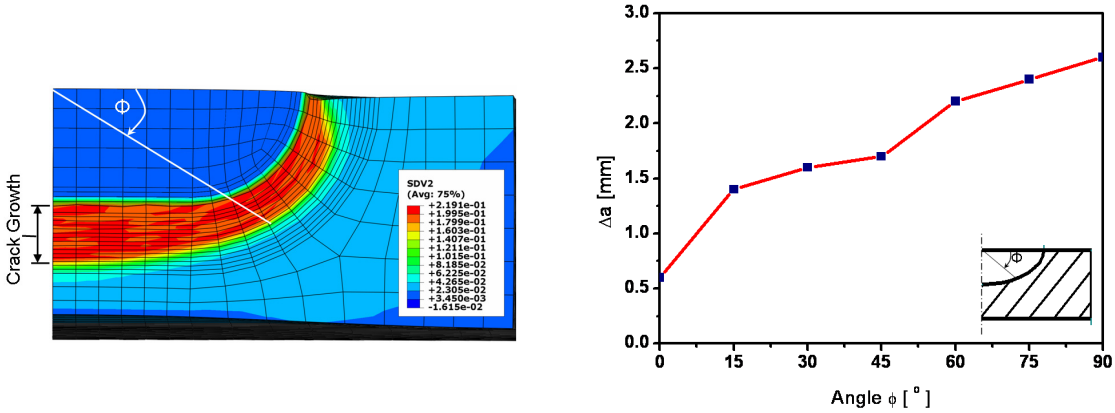

(a) (b)

Figure 7.38*: (a) numerical prediction of crack growth along the crack front for tensile panel with a pre-crack in WM, and (b) crack growth value along the crack front.*

In the complete Gurson model, the failure criterion, critical void volume fraction (f_c) is not a material constant. It depends on stress triaxiality. Figure 7.39 shows the variation of f_c at the crack tip along the crack growth path for SENB specimens and tensile panels. The variation of f_c for tensile panels was determined in front of the crack tip, where the

crack initiation occurs at Φ = 90°. The results show that the value of f_c varies significantly along the crack growth path especially in case of tensile panels and it is higher in comparison with values for SENB specimens. The effect of stress triaxiality on f_c along the path of the crack growth can also be seen in Figure 7.40 for SENB specimen with a pre-crack in WM.

The effect of constraint also on near tip stress distribution for growing cracks can be seen in Figure 7.41 for SENB specimens and tensile panels with pre-cracks in WM and FGHAZ. The opening stress (σ_{11}) for tensile panels was determined in front of the crack tip, where the crack initiation occurs at Φ = 90°. It has been used to give a picture of how constraint effects on fracture behavior of specimens. The results show that the highest required opening stress at the crack tip is obvious for specimens in the following order: SENB-FGHAZ, TP-FGHAZ, TP-WM and SENB-WM.

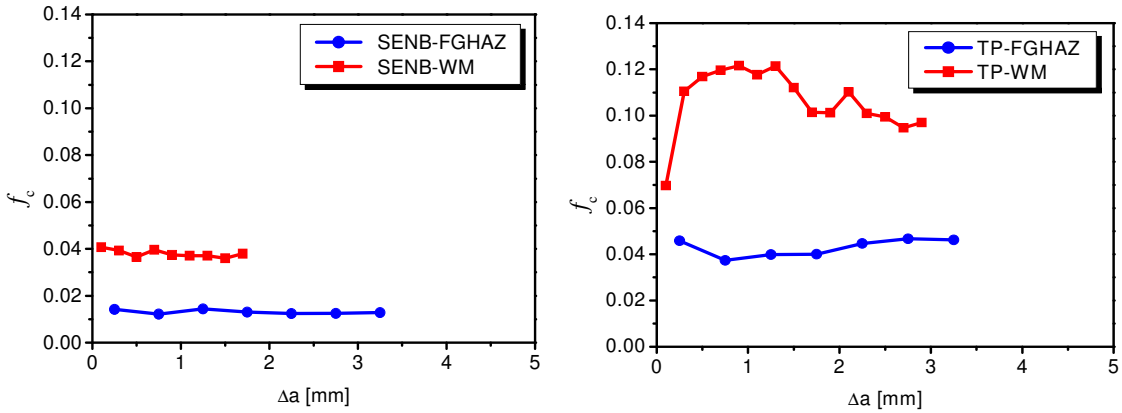

(a) (b)

Figure 7.39 *The variation of critical void volume fraction (f_c) at the crack tip along the crack growth path for: (a) SENB specimens, and (b) tensile panels.*

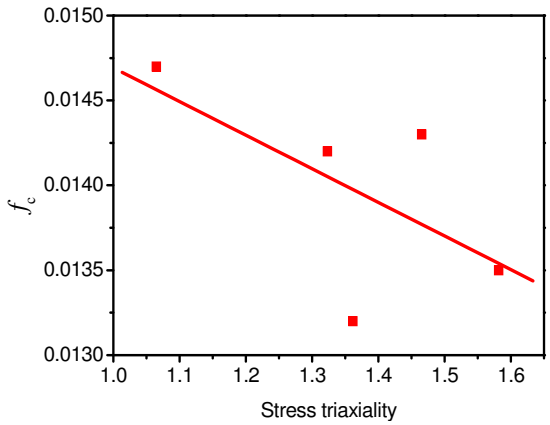

Figure 7.40 *Critical void volume fraction (f_c) vs. stress triaxiality at the crack tip along crack growth path for SENB specimen with a pre-crack in WM.*

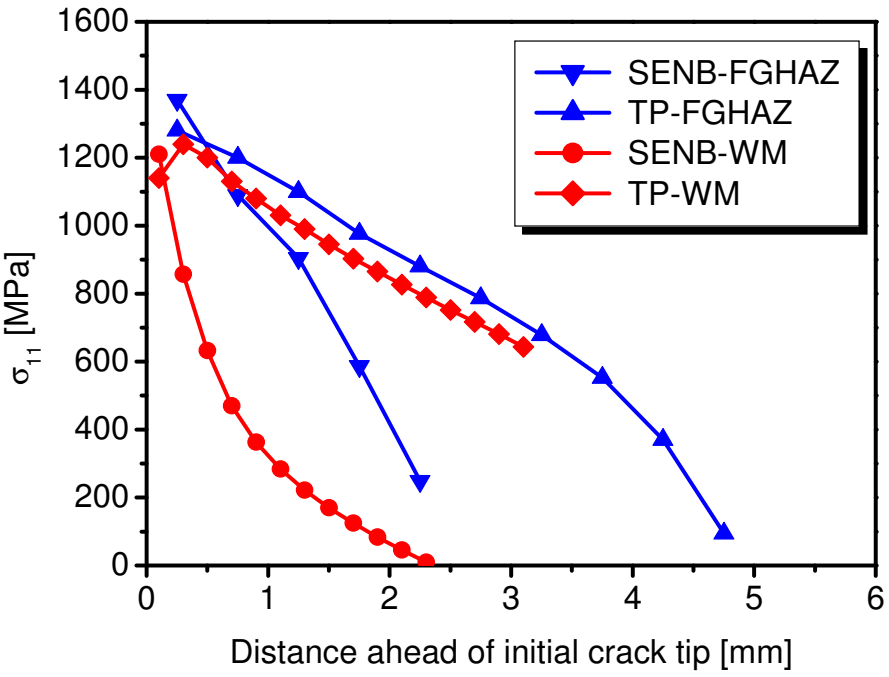

Figure 7.41 *The effect of constraint on opening stress (σ_{11}) ahead of the initial crack tip front at the onset of crack growth for SENB specimens and tensile panels with pre-cracks in WM and FGHAZ.*

Chapter 8

Discussion

8.1 Introduction

In this study, the ductile fracture behavior of welded joints made of High-strength low-alloyed steel was micromechanically analyzed using recently developed local approaches (The CGM model). The effect of mechanical heterogeneity and constraint on crack growth initiation and material resistance behavior have been studied using mechanical properties estimated for welded joint regions (BM, HAZ:CGHAZ and FGHAZ, and WM). The mechanical properties were estimated using experimental and numerical procedure done on butt welded smooth tensile panel.

Using micromechanical approaches usually requires combination experimental and numerical procedure. Therefore, the study was carried out using finite element and experimental analysis. Experimental analysis has been done using welded tensile panels and standard fracture mechanics SENB specimens with pre-cracks in WM and HAZ. The tensile panels with surface pre-cracks in WM and HAZ have been chosen to analyze the transferability of micromechanical damage parameters and to assess structural integrity of pressure vessels, which are made of NIOMOL 490K steel. Also, the 2D plane strain and 3D finite element models were carried out.

8.2 Characterization of mechanical properties

The occurrence of mechanical and metallurgical heterogeneity is inevitable for high strength steels and in particular their HAZ. Therefore, using standard methods to estimate mechanical properties for various regions of welded structure may be difficult or not accurate, especially for heat affected subzones. In other words, mechanical properties of welded joint regions may be difficult to be determined in the direction of applied force, especially when the welded joint is subjected transversally to applied load. Thus, attempts to estimate mechanical properties for various welded joint regions using combined

experimental and numerical procedure are presented as alternative method to the conventional one. The experimental-numerical procedure has been performed on smooth tensile panel. Experimental results have shown that the specimen failed in base metal and the welded joint exhibits slight strength overmatching (Figure 6.3, Figure 6.7 and Figure 6.8). It can also be noticed that the specimen have exhibited significant nonlinear behavior preceding final fracture, as expected, and confirm the ductility of materials (Figure 6.4). Moreover, the average strain in HAZ changes rapidly in comparison with that for BM and WM, due to probably the effect of heterogeneity, Figure 6.3.

Using obtained experimental data (stress and strain data) for estimation of mechanical properties have not given good matching between experimental and numerical results (Figure 6.8 (a)-Figure 6.13(a)). It has provided approximation for initial mechanical properties, which were used for first iteration in numerical modelling. Mechanical properties of iteration 3 have provided good matching between experimental and numerical strain results up to the ultimate load (Figure 6.8(c)-Figure 6.13(c)). However, iterations 1 and 2 have also presented close matching between experimental and numerical result of force versus remote displacement (Figure 6.9(a) and Figure 6.9(b)). This can be explained that the numerical load drop after ultimate load is due to only a geometry effect (reduction of specimen cross section) without including damage effect. Consequently, they do not simulate the real behavior of tested ductile steel. In other words, in Figure 6.9(c), the discrepancies between experimental and numerical results after ultimate load are due to the fact that load-carrying capability is lost due to a combination of large-scale yielding and material damage as a result of ductile behavior. This combined mechanism can only be taken into account using a suitable damage model. In addition to comparison experimental and numerical results, necking in both; specimen and FE model (Figure 6.14) occurred in the BM at about the same position using mechanical properties given in iteration 3, while it occurred in the WM using iteration 1.

Obtained true stress-strain curves have shown that weld metal has the highest strength and CGHAZ region has the lowest one (Figure 6.8(c)). According to obtained results, experimental and numerical procedure for determination of mechanical properties may be considered as alternative procedure to standard one, especially when the welded joint is subjected transversally to applied load in very narrow welded joint zones such as: heat affected subzones and weld metal.

Quantitative microstructural analysis was performed to estimate the micromechanical parameters: volume fraction (f_v) and mean free paths (λ) between the non-metallic inclusions for the zones of the welded joint. The results show that the volume fraction (f_v) of non-metallic inclusion for WM is larger than one for BM and HAZ (Table 6.3). Thus, it has more influence on fracture behavior of specimens with a pre-crack in WM than specimens with a pre-crack in BM and HAZ. Moreover, the f_v is about twice larger than the volume fraction of void nucleating particles (f_N) for WM and it is about half smaller than the volume fraction of void nucleating particles (f_N) for HAZ. Therefore, void nucleation has higher effect on acceleration of WM void growth at high plastic strains in comparison with its effect on HAZ materials. This parameter (f_N) is necessary in order to accurately model the load drop after maximum load.

Material hardness has a direct relation to its strength. Micro-hardness measurements were carried out to investigate strength heterogeneity and to determine welded joint regions. The results have indicated a global evenmatching and slightly local overmatching in CGHAZ as expected for welded joint, Figure 6.16.

8.3 Effect of heterogeneity on fracture behavior

The effect of heterogeneity on crack initiation and propagation has been studied using standard SENB specimens and tensile panels with pre-cracks in HAZ and WM. The results of force versus CMOD for SENB specimens with pre-crack in HAZ and WM (Figure 6.24 and Figure 6.25) have shown that both specimens have exhibited significant nonlinear behavior preceding unstable fracture, as expected, and confirm the ductility of materials, which is higher in the HAZ than WM. Nevertheless, the differences in the maximal resistance force arise from the welding mechanical heterogeneity. Moreover, the rate of load drop of the SENB specimen with a pre-crack in the WM is higher than the one of the SENB specimen with a pre-crack in the HAZ. It can be attributed to the effect of volume fraction of non-metallic inclusions, which is higher in WM than HAZ material. Similar heterogeneity effect on force versus CMOD and force versus CTOD-δ_5 (Figure 6.33-Figure 6.36) can be noticed on tensile panels with semi-elliptical surface pre-cracks in WM and HAZ. However, tensile panel with a pre-crack in WM failed closely to maximal load.

The magnified region on stable crack growth surface for tensile panel with a pre-crack in WM (Figure 6.39) reveals typical ductile fracture features, showing dimples. This indicates that fracture is essentially governed by void growth and coalescence by internal necking.

8.3.1 Heterogeneity effect on the initiation fracture toughness

The initiation toughness in terms of J integral has been determined for SENB specimens and tensile panels with pre-cracks in HAZ and WM. The results have displayed that the effect of heterogeneity can be noticed from the various obtained values of the J-integral corresponding to the initiation (J_i) of crack growth (Table 6.8 and Table 6.11). It can be seen that the value of initiation toughness for SENB specimen with a pre-crack in HAZ (Table 6.8) is higher than that for SENB specimen with a pre-crack in WM. It could be explained that the FGHAZ region, where probably the crack is, has higher toughness, slightly smaller crack depth, smaller defects and smaller volume fraction of non-metallic inclusions compared to WM region (Figure 6.19, Figure 6.20 and Table 6.3). The same behavior was obtained for tensile panels, too. It can be noticed also that the values of J_i for tensile panels with a pre-crack in HAZ and WM (Table 6.11) are about 3.5 and 2 times larger than that for SENB specimens with a pre-crack in HAZ and WM, respectively. That is to say that the differences among these values between different specimens with pre-cracks in the same material (HAZ or WM) are due to the effect of specimen and crack geometries with loading configuration. In addition, the difference between the values of J_i for SENB specimen and tensile panel with a pre-crack in HAZ is much larger than that for SENB specimen and tensile panel with a pre-crack in WM. This difference is mainly the result of the larger value of stretch zone width for tensile panel with a pre-crack in HAZ (Table 6.10).

In general, if the initiation toughness reflects the material properties in the vicinity of the crack tip, the initiation toughness should be affected only by the heterogeneity near the crack tip. Obtained different values of initiation toughness indicate that it is affected by mechanical heterogeneity. Therefore, it can be concluded that the plastic zones controls the initiation toughness. Plastic deformation occurs at the crack tip for most structural steels while crack initiating and this plastic zone size and the associated degree of deformation can reflect the initiation toughness. The better the toughness of the material is, the larger the plastic deformation region near the crack tip region, and the

stronger the effect of mechanical heterogeneity on the initiation toughness. If the toughness of the material is not so good, the plastic zone is smaller when the crack initiates (Figure 7.10). In this situation, the effect of mechanical heterogeneity of weldment will be smaller.

8.3.2 Heterogeneity effect on the crack growth resistance

It is well known that the crack can continually grow under the load increasing after crack initiation and the *J* value will increase also as the load increases, that is, so called crack growth resistance. The toughness of heat affected zone and weld metal was measured in terms of *J*-*R* curve in SENB specimens. Both specimens failed in ductile mode and results indicate that the weld metal has lower toughness compared to heat affected zone metal (Figure 6.28 and Figure 6.29). This difference is due to the effect of mechanical heterogeneity, slight difference in crack depth and volume fraction of non-metallic inclusions, which is larger in weld metal than heat affected zone. It can be noticed also that the tendency of mechanical heterogeneity effect is the same on both initiation toughness and crack growth resistance.

8.4 Numerical prediction of crack initiation and propagation

Numerical predictions of crack initiation and propagation using micromechanical approach require a combined numerical and experimental procedure. To analyze the transferability of the numerical results and the validation of the ductile failure model implemented, the numerical and experimental results have to be compared. In order to illustrate the advantages of used damage model, finite element predictions using large-deformation elastic-plastic deformation only, without the introduction of a damage mechanism, were also obtained for SENB specimen and tensile panel. It is obvious that good agreement between numerical (using CGM model) and experimental results of force versus CMOD and CTOD-δ_5 has been achieved (Figure 7.3, Figure 7.4 and Figure 7.19-Figure 7.22). The damage model (CGM) predicts the sharp load drop after maximum load, which represents the stage of ductile tearing, quite well, whereas the simulation without the damage model cannot predict this phenomenon. This sharp load drop after maximum load is due to the softening effect of void growth and coalescence, which is more pronounced for SENB specimen with a pre-crack in WM than that for SENB specimen with a pre-crack in HAZ. It can be seen also for tensile panel with a pre-crack

in WM that discrepancies between predictions with and without the damage model are evident before maximum load is achieved, which means that the softening effect is substantial even before maximum load (Figure 7.19 and Figure 7.21). However, this effect on tensile panel with a pre-crack in HAZ (Figure 7.20 and Figure 7.22) was negligible before maximum load compared with results of tensile panel with a pre-crack in WM due to the larger fraction of initial void volume fraction in WM. From these experiments and model predictions, load-carrying capability in tested specimens is lost due to a combination of large-scale yielding and material damage as a result of ductile tearing. This combined mechanism can only be taken into account using a suitable damage model as demonstrated in Figure 7.3, Figure 7.4 and Figure 7.19-Figure 7.22.

It is also interesting to notice in Figure 7.19 and Figure 7.21 that the load level at the onset of crack initiation is well below the maximum load for tensile panel with a pre-crack in WM. At this instant, the global load changes from linear to non-linear. This emphasizes that ductile NIOMOL 490K steel plate exhibits considerable residual strength even when containing cracks. For this steel, the maximum load in plate is often preceded by a large amount of slow, stable crack growth.

8.4.1 Prediction of crack initiation

As it was mentioned before that crack initiation value was predicted using CGM model according to failure criterion. As it can be seen in Table 7.4, the numerical value of J_i obtained using SENB specimen with a pre-crack in WM is higher than the fracture toughness value $J_{0.2/BL}$, which was experimentally determined. This behavior of WM is confirmed with that the value of $J_{0.2/BL}$ is greater than J_i for the majority of structural materials, while it is not in the case of HAZ. Furthermore, predicted crack initiation values are in good agreement with experimental ones for both SENB specimen and tensile panel with a pre-crack in WM, while they are in less agreement with experimental ones for both SENB specimen and tensile panel with a pre-crack in HAZ. It is likely that they are very sensitive to heterogeneity, which may be more pronounced in HAZ than WM. Thus, HAZ may require more material characterization and to be divided into more than two subzones with various mechanical properties.

The advantage of implemented damage model is that the crack initiation site in tensile panels can be determined (Figure 7.25 and Figure 7.26), which corresponds to the highest concentration of void volume fraction and maximum crack driving force.

Material damage (f) is influenced by the effects of heterogeneity and the geometries (specimen and crack) with loading configuration (Figure 7.31). The increase of the value of f is given as a function of the J-integral for SENB specimens and tensile panels with pre-cracks in WM and HAZ. It is obvious that the more rapid increase of the volume fraction of voids (f) at the onset of crack growth was obtained for the SENB specimen with a pre-crack in WM compared with that for the SENB specimen with a pre-crack in HAZ. The same behavior was obtained also for the tensile panel with a pre-crack in WM compared with the tensile panel with a pre-crack in HAZ. These behaviors are due to the effect of heterogeneity and various initial damage values of HAZ and WM. It can be noticed also that the more rapid increase of the volume fraction of voids (f) at the onset of crack growth was obtained for the SENB specimen with a pre-crack in WM compared with that for the tensile panel with a pre-crack in WM. This behavior is consequences of geometry with loading mode effect. It can also be seen that the effect of heterogeneity and geometry with loading configuration on damage are more pronounced for WM than HAZ due to the larger initial damage value in WM (Figure 7.31).

8.4.2 Prediction of crack propagation

The crack growth resistance curves have been obtained numerically for SENB specimens and tensile panels with pre-cracks in HAZ and WM (Figure 7.13 and Figure 7.14). The results show that good agreement has been obtained between experimental and numerical crack growth resistance curves for SENB specimens with pre-cracks in HAZ and WM, however there was large discrepancy between experimental and numerical crack initiation values obtained for SENB specimen with a pre-crack in HAZ (Figure 7.13, Figure 7.14 and Table 7.2). Furthermore, the results show that the resistance curves are different for various specimens and crack geometries with loading configuration (Figure 7.34). It is obvious that the resistance curve obtained using tensile panel with a pre-crack in WM has higher crack growth resistance compared with that for SENB specimen with a pre-crack in the same WM. This difference is due to the effect of specimen and crack geometries with loading configuration. The same behavior can be seen for the crack growth resistance curves obtained from SENB specimen and tensile panel with pre-cracks in HAZ. It is also interesting to note that the crack growth resistance curve obtained from tensile panel with a pr-crack in HAZ has higher resistance in comparison with that for tensile panel with a pre-crack in WM. The same behavior was

also observed for crack growth resistance curves obtained from SENB specimens with pre-cracks in HAZ and WM. This behavior is due to the effect of heterogeneity on crack growth resistance, which is lower than the effect of geometries with loading configuration. Therefore, using standard SENB specimen, which has a significantly higher geometry constraint than the actual structures such as pressure vessels, introduces a high degree of conservatism in engineering critical assessment. Moreover, it is difficult to know how conservative the results are, because the geometry constraint is highly material-dependent. It has been found in this study that the obtained crack growth resistance curve using tensile panel has more than 1.5 higher resistance than that obtained using SENB specimen with a pre-crack in the same material. Thus, using micromechanical approach to assess the structural integrity of weldments may be the solution for transferability problem, because it separates transferable parameters for ductile fracture from the parameters which describe geometry effect.

The experimental and numerical fracture surfaces have been compared. In Figure 7.35, the comparison of experimental and numerical stable crack growth surfaces for tensile panel with a pre-crack in WM has shown that good agreement was attained at the same value of CMOD.

8.5 The influence of FE size on crack initiation and propagation

The influence of FE size on crack initiation and propagation was studied. In this study, it is found that the size of FE mesh affects the material resistance curves and crack initiation values for SENB specimens with pre-cracks in HAZ and WM. These results are in agreement with the literature results. For both materials, the initial FE size is set to the approximate value of the mean free path (λ) between non-metallic inclusions. In addition, one more mesh size was considered for each SENB specimen; these sizes were chosen as follows: elements larger than λ for WM and elements smaller than λ for HAZ. In this way, two similar finite element sizes are used for each of the materials. Significant effect of FE mesh size on material resistance curves and crack growth can be seen in Figure 7.13-Figure 7.15; the good agreement is obtained for the size of the element approximating the mean free path (λ) between the non-metallic inclusions in analyzed materials (Table 6.3).

8.6 Constraint effect on crack initiation and propagation

Constraint level has been analyzed on basis of stress triaxiality, which plays a key role in used damage model. According to the Gurson model, local crack initiation and growth will be accelerated by higher values of stress triaxiality along with increased plastic deformation. Since this effect performs such an important role in the ductile fracture process, the stress triaxiality ahead and along initial crack front was determined at the onset of void coalescence (crack initiation) for all specimens. The results (Figure 7.36) indicate that the specimen and crack geometries with loading configuration (compare results of SENB-WM with TP-WM or SENB-FGHAZ with TP-FGHAZ) have the highest influence on crack growth initiation and propagation, while mechanical heterogeneity has the least one (compare results of SENB-FGHAZ with SENB-WM or TP-FGHAZ with TP-WM). It is obvious also that stress triaxiality for SENB specimen was higher than that for tensile panel. This behavior reflects the constraint level in the specimens, which was higher in SENB specimen than tensile panel. The results (Figure 7.37) indicate that stress triaxiality for both tensile panels was always higher at the deepest point of the crack front (Φ = 90°) than at the surface point (Φ = 0°) irrespective of crack configuration. However, the maximum value of stress triaxiality does not take place at the deepest point of the crack front for tensile panel with a pre-crack in WM. It occurs below the surface. The variation in stress triaxiality depends on the crack configuration. It is also obvious in Figure 7.37 that the stress triaxiality along the crack front for tensile panel with a pre-crack in WM is higher than that for tensile panel with a pre-crack in HAZ due to the effect of mechanical heterogeneity and volume fraction of non-metallic inclusions.

The path of crack growth in tensile panels is also influenced by stress triaxiality (Figure 7.38). For tensile panels, the results exhibit highly non-uniform crack growth along the crack front due to the strong variation in stress triaxiality under even a pure tension load (Figure 7.32, Figure 7.33 and Figure 7.38). It is obvious that the crack grows the most at the deepest point of the crack front (Φ = 90°) and the least at the surface point (Φ = 0°).

In the complete Gurson model, the failure criterion, critical void volume fraction (f_c) is also influenced by stress triaxiality, so it is not a material constant as demonstrated in Figure 7.39 and Figure 7.40. The results show that the value of f_c varies significantly

along the crack growth path, especially for tensile panels, which is higher in comparison with the values of SENB specimens. Moreover, it can be noticed that the effect of heterogeneity on the f_c values for SENB specimens (Figure 7.39 (a)) is lower than that for tensile panels (Figure 7.39(b)). It is also obvious that the highest value of f_c corresponds to the lowest value of stress triaxiality and vice versa (Figure 7.40).

Chapter 9

Conclusions and Recommendations

9.1 Conclusions

This study has demonstrated the experimental and numerical techniques that may be useful in the process of defect characterization in high strength steel weldment. Experimental work has been carried out on; smooth tensile panel, SENB specimens and tensile panels with pre-cracks in WM and HAZ to estimate; mechanical properties of various zones of weldment and to analyze the fracture behavior of NIOMOL 490K steel. Numerical analysis, detailed elastic-plastic finite element models with implemented damage model (2D, plane strain and 3D) have also been performed. A complete damage model CGM has been used to simulate the ductile tearing of NIOMOL 490K steel in SENB specimens and tensile panels with various crack geometries. The proposed model was also used to study the effects of mechanical heterogeneity and constraints on crack initiation and propagation. Moreover, a combined experimental and numerical procedure was developed to characterize mechanical properties of various zones of weldment. The transferability of micromechanical model parameters, which are only material not geometry dependent, are also analyzed. Based on this study, the following conclusions were drawn:

- A combined experimental and numerical procedure for mechanical properties characterization may be used as alternative procedure to the standard one, especially when welded joint is subjected transversally to applied load in weld metal and heat affected subzones, which have higher heterogeneity compared with base metal.
- HAZ has proved to be more resistant to crack initiation and growth than WM, which is not common for high strength low alloyed steels. This behavior was due to that the crack was probably located in FGHAZ.

- The CGM model was able to account for both material-softening behavior and to predict crack initiation and propagation.
- The model predictions are in good agreement with experimental data, especially results of specimens with a pre-crack in WM. Thus, HAZ may require more accurate material characterization and to be divided into more than two subzones with various mechanical properties.
- Micromechanical damage parameters, which are only material not geometry dependent, can be transferred from one geometry to another providing good matching between experimental and numerical results.
- The increase rate of damage growth ahead of the crack tip at the onset of crack growth is smaller in the HAZ than the WM. This difference can be attributed to much higher initial void volume fraction of the latter, as well as to slightly longer crack in this zone.
- For NIOMOL 490K steel, void nucleation and growth has an insignificant effect on overall mechanical behavior of the material; material-softening behavior is extremely weak until void coalescence (crack initiation) occurs.
- Crack resistance curves (*J-R* curves) and crack initiation values were successfully predicted using the CGM and obtained true stress-strain curves of the welded joint zones.
- For the tensile panels with surface cracks, cracks initiated at a load level well below maximum. That is, maximum load in tensile panel was most often preceded by large amounts of slow, stable crack growth.
- The resistance to crack initiation and growth is greatly affected by the heterogeneity of the weldment. The heterogeneity of the examined joints cannot be adequately represented by the often used ratio of the yield strengths, because hardening behavior and microstructure also influence the fracture behavior.
- The effect of mechanical heterogeneity on crack initiation and propagation is lower than the effect of specimen and crack geometries with loading configuration. Therefore, using standard SENB specimens, which have a significantly higher geometry constraint than the actual structures such as pressure vessels, introduces a high degree of conservatism in engineering critical assessment.

- The obtained crack growth resistance curve using tensile panel has more than 1.5 higher resistances than that obtained using SENB specimen with a pre-crack in the same material. Thus, using micromechanical approach to assess the structural integrity of weldments may be the solution for transferability problem, because it separates transferable parameters for ductile fracture from the parameters which describe geometry effect.
- NIOMOL 490K steel exhibits considerable strength even when containing cracks.
- The ductile tearing process in high strength steel cannot be accurately simulated without considering damage evolution and the used model was able to account for the effects of both large plastic deformation and material damage due to ductile tearing.
- The size of FE mesh greatly affects the material resistance curves and crack initiation values.
- Local crack initiation and growth are accelerated by higher values of stress triaxiality along with increased plastic deformation. Therefore, the path of crack growth is influenced by stress triaxiality.
- In the damage model, the critical void volume fraction (f_c), which determines the onset of void coalescence, is not a material constant and varies with stress triaxiality.
- Prediction of crack growth path using micromechanical approach may help in applications of leak before break (LBB) concept.

9.2 Recommendations for future work

Although prediction of weldment fracture behavior has successfully been done using CGM model and estimated mechanical properties, which were obtained using the experimental and numerical procedure, improvements are still necessary and can be made in the following directions.

- More experimental and numerical analysis is needed to study real behavior of pressure vessels made of NIOMOL 490K steel and to verify the transferability of micromechanical material parameters to real structures.
- More material characterization using experimental and numerical procedure is needed, especially for very narrow sub zones of HAZ. Furthermore, for smooth

tensile panel, the comparison of experimental and numerical results with implemented damage model beyond maximum load is required to verify the numerical results.

- Experimental work is needed to determine crack growth resistance curves for tensile panels and then to verify the numerical results.
- More micromechanical fracture analysis is required to study the fracture behavior of structures with a pre-crack in CGHAZ, which probably has the worst toughness.

References

[1] Satoh K, Toyoda M. Joint strength of heavy plates with lower strength weld metal. Welding Journal Research Supplement 1975:311-319.

[2] Rouselier G. Ductile fracture models and their potential in local approach of fracture. Nucl Eng Des 1987;105:97-111.

[3] Tvergaard V, Needleman A. Analysis of cup-cone fracture in a round tensile bar. Acta Metallurgica 1984; 32(1): 157-169.

[4] Tvergaard V, Needleman A. Effects of non-local damage in porous plastic solids. International Journal of Solids and Structures 1995; 32:1063-1077.

[5] Schwalbe KH, Ainsworth RA, Eripret C, Franco C, Gilles P, Koçak M, et al. Common views on the effects of yield strength mis-match on testing and structural assessment. In: Mis-matching of Interfaces and Welds, GKSS Research Centre, Geesthacht 1997; 99-132.

[6] Koçak M, editor. Weld mis-match effect. International Institute of Welding (IIW), IIW Document 1998;X:1419-1498.

[7] Clausmeyer H, Kussmaul K, Roos E. Influence of stress state on the failure behavior of cracked components made of steel. ASTM Appl Mech Rev 1991;44:77-92.

[8] Hackett EM, Schwalbe K-H, Dodds RH, editors. Constraint effects in fracture. ASTM STP 1171, ASTM, Philadelphia, 1993.

[9] Kirk M, Bakker A, editors. Constraint effects in fracture – theory and applications, vol. 2. ASTM STP 1244, ASTM, Philadelphia 1995.

[10] Ravi S, Balasubramanian V, Babu S, Nemat Nasser S. Assessment of some factors influencing the fatigue life of strength mis-matched HSLA steel weldments. Mater Des 2004;25:125-135.

[11] Kozak D, Gubeljak N, Konjatic´ P, Sertic´ J. Yield load solutions of heterogeneous welded joints. Int J Pres Ves Pip 2009;86:807-812.

[12] Zhang ZL, Hauge M, Thaulow C. Two-parameter characterization of near-tip stress fields for a bi-material elastic-plastic interface crack. Int J Fract 1996;79:65-83.

[13] Burstow MC, Howard IC, Ainswort RA. The influence of constraint on crack tip stress fields in strength mismatched welded joints. J Mech Phys Solids 1998;46:845-872.

[14] Betegon C, Penuelas I. A constraint based parameter for quantifying the crack tip stress fields in welded joints. Eng Fract Mech 2006;73:1865-1877.

[15] O'Dowd NP, Shih CF. Family of crack-tip fields characterized by a triaxiality parameter III. Structure of field. J Mech Phys Solids 1991;39:989-1015.

[16] Schmitt W, Kienzler R. The J-integral concept for elastic-plastic material behavior. Eng Fract Mech 1989;32:409-418.

[17] Penuelas I, Betegon C, Rodriguez C. A ductile failure model applied to the determination of the fracture toughness of welded joints. Numerical simulation and experimental validation. Eng Fract Mech 2006;73:2756-2773.

[18] Rakin M, Gubeljak N, Dobrojevic M, Sedmak A. Modeling of ductile fracture initiation in strength mismatched welded joint. Eng Fract Mech 2008;75:3499-3510.

[19] Chhibber R, Biswas P, Arora N, Gupta SR, Dutta BK. Micromechanical modeling of weldments using GTN model. Int J Fract 2011;167:71-82.

[20] Wang T, Yang JG, Liu XS, Dong ZB, Fang HY. Stress intensity factor expression for centre-cracked butt joint considering the effect of joint shape. Mater Des 2012;35:72-79.

[21] Moltubakk T, Thaulow C, Zhang ZL. Application of local approach to inhomogeneous welds. Influence of crack position and strength mismatch. Eng Fract Mech 1999;62:445–462.

[22] Gubeljak N. Fracture behavior of specimens with surface notch tip in the heat affected zone (HAZ) of strength mis-matched welded joints. Int J Fract 1999;100:155-167.

[23] Rak I, Treiber A. Fracture behavior of welded joints fabricated in HSLA steels of different strength level. Eng Fract Mech 1999;64:401-415.

[24] Wilsius J, Imad A, Nait Abdelaziz M, Mesmacque G, Eripret C. Void growth and damage models for predicting ductile fracture in welds. Fatigue Fract Eng Mater Struct 2006;23:105-112.

[25] Toyoda M, Minami F, Ruggieri C, Thaulow C, Hauge M. Strength mis-match effect on fracture behavior of HAZ. In: Mis-matching of Interfaces and Welds, GKSS Research Centre, Geesthacht 1997: 75-98.

[26] Zhang ZL, Thaulow C, Odgard J. A complete Gurson model approach for ductile fracture. Eng Fract Mech 2000; 67: 155-168.

[27] Satoh K, Toyoda M. Fracture toughness evaluation of welds with mechanical heterogeneity. Transactions of Japan Welding Society 1982;13(1).

[28] Easterling K. Introduction to the physical metallurgy of welding. Butterworths Monographs in Materials, London, 1983.

[29] Rozenthal D. The theory of moving sources of heat and its application to metal treatment. Transactions ASME 1946;68:pp. 849.

[30] Inagaki M, Sekiguchi H. Continuous cooling transformation diagram of steels for welding and their applications. Transactions of Japan Institute of Metals, No.2, 1960, pp. 40.

[31] Sedmak S. The application of fracture mechanics to life estimation of power plant components. Proceedings of the 5th international fracture mechanics summer school, Belgrade, 1990.

[32] Toyoda M. Crack tip opening displacement (CTOD) testing method for heat affected zone (HAZ) toughness of steel welds with particular reference to local inhomogeneity. Fracture Mechanics: 24th Volume, ASTM-STP 1207, ASTM Publication 1994:291 -307.

[33] Schwalbe KH, Kim YJ, Hao S, Cornec A, Koçak M. EFAM ETMMM 96: The ETM method for assessing the significance of crack-like defects in joints with mechanical heterogeneity (strength mismatch), GKSS research centre Geesthacht, GKSS Report 97/E/9, 1997.

[34] Sedmak A, Sedmak S, Milović Lj. Pressure equipment integrity assessment by elastic-plastic fracture mechanics methods. Monograph; Society for structural integrity and life (DIVK), Belgrade, 2011.

[35] Kocak M, Dneys R. CTOD and wide plate testing of welds with particular emphasis on mis-matched welded joints. ECF 10-Structural Integrity: Experiments -Models -Applications, ESIS Publication, 1994: 97 -120.

[36] Schwalbe KH, Hao S, Cornec A, Kocak M. Status of the engineering treatment model for mis-matched welds (ETM –MM) Handbook. Proceeding the Second

Symposium on Mis-Matching of Welds, Edited by Schwalbe K. and Kocak M., GKSS, FRG, 1997: 675-690.

[37] Zhang J, Shi Y. The effect of welding mechanical heterogeneity on fracture toughness feature of base metal. Int J Press & piping 1997;72:199-202.

[38] Zhang J, Shi Y, Murakawa H. The study on ductile fracture of the over-matched weldment with mechanical heterogeneity. Int J Press & piping 1998;75:773-776.

[39] Brocks W, Yuant H. Numerical studies on stable crack growth. Proceedings of the European Symposium on EPFM: Element of Defected Assessment, ESIS/ECF Pub. 9, 1991: 19 -33.

[40] Rice JR. A path independent integral and the approximate analysis of strain concentration by notches and cracks. Journal of applied mechanics 1968;35:379-386.

[41] Dodds RH, Read DT. Experimental and analytical estimates of the *J*-integral for tensile panels containing short center cracks. Int J of Fracture 1985;28:39-54.

[42] Ganti S, Parks DM, McClintock. Analysis of strength mis-matched interface cracks in SSY. Proceeding the Second Symposium on Mis-Matching of Welds, Edited by Schwalbe K, Kocak M, GKSS, FRG, 1997: 3-16.

[43] Anderson TL. Fracture mechanics: fundamental and application. CRC Press, 3rd edition, 2005.

[44] GKSS:1991. Displacement gauge system for applications in fracture mechanics. Patent Publication, Geesthacht, 1991.

[45] Schwalbe KH. Introduction of δ_5 as an operational definition of the CTOD and its practical use. In:ASTM STP 1256, eds. Reuter W, Underwood J, Newmann JC, American Society for Testing and Materials, West Conshohocken, 1995b:763-778.

[46] Schwalbe KH, Newman JC, Jr., Shannon JL, Jr. Fracture mechanics testing on specimens with low constraint-standardization activities within ISO and ASTM. Eng Fract Mech 2005;72:557-576.

[47] Saxena S, Ramakrishnan N, Chouhan S. Numerical determination of stretch zone width (SZW) using tensile test data. Fatigue & Fracture of Engineering Materials & Structures 2011;34:205-214.

[48] Kannienen MF, Popelar C H. Advanced fracture mechanics. Oxford Press Inc., 1985.

[49] Agatonovic P, Henriksen TK. Development of residual strength elasto-plastic fracture mechanics. Proc. Conference on spacecraft structure, material and mechanical testing, ESA SP-386, June 1996:389-398.

[50] Ainsworth RA, Schwalbe KH. Comprehensive structural integrity. Volume 7: Practical failure assessment methods, 2003.

[51] Eripert C, Hornet P. Fracture toughness testing procedures for strength mis-matched structures. Proceeding the second symposium on mis-matching of welds, Edited by Schwalbe K, Kocak M. GKSS, FRG, 1997:17-34.

[52] Sedmak S, Petrovski B, Sedmak A. The Resistance to crack growth of different regions of weldments in a real structure. Int J Pres Ves & Piping 1992;52:313-335.

[53] Toyoda M, Minami F, Ruggieri C, Thaulow C, Hange M. Fracture property of HAZ-notched weld joint with mechanical mis-matching. Part I, Mis-matching of welds, ESIS 17, Mechanic Engineering Publication, London, 1994:399-415.

[54] Petrovski B, Kocak M, Sedmak S. Fracture behavior of undermatched weld joint with short surface crack. Proc. 10th international conference on offshore mechanics and arctic engineering, 1991:101-107.

[55] Kocak M, Yao S, Chen L, Schwalbe KH. Evaluation of HAZ toughness by CTOD and tensile panels. Proceedings of the European symposium on EPFM: Element of defected assessment, ESIS/ECF Pub. 9, 1991:845-859.

[56] Pineau A. Review of fracture micromechanisms and a local approach to predicting crack resistance in low strength steels. In: Advances in Fracture Research, ICF5, ed. Francois D, Pergamon, Oxford, UK, 1982:553-577.

[57] Beremin FM. A local criterion for cleavage fracture of a nuclear pressure vessel steel. Metall. Trans. A, 1983; 14:2277-2287.

[58] Pineau A, Joly P. Local versus global approaches to elastic-plastic fracture mechanics. In: Applications to ferritic steels and a cast duplex stainless steel in 'defect assessment in components-fundamentals and applications,' ESIS/EGF9. eds. J. G. Blauel and K. H. Schwalbe, Mechanical Engineering Publications, London, 1991:381-414.

[59] Rakin, M, Sedmak, A. Micromechanical analysis in structural integrity assessment. In: Monograph of the 9th International Fracture Mechanics Summer School (IFMASS 9), Faculty of Mechanical Engineering, Society for Structural Integrity and life, Faculty of Technology and Metallurgy, GOSA, Belgrade, 2008:85-104.

[60] Barsoum I. The effect of stress state in ductile failure. PhD dissertation, Royal Institute of Technology, Stockholm, Sweden, 2008.

[61] Wilsforf HGF. The ductile fracture of metals: A Microstructural viewpoint. Material Science and Engineering, 1983; 59:1-19.

[62] Goods SH, Brown LM. The nucleation of cavities by plastic deformation. Acta Metallurgic, 1979;27:1-15.

[63] Argon AS, Im J, Safoglu R. Cavity formation from inclusions in ductile fracture, Metallurgical Transactions, 1975;6A:825-837.

[64] Beremin FM. Cavity formation from inclusions in ductile fracture of a 508 steel. Metallurgical Transactions, 1981;12A:723-731.

[65] Mudry F, Di Fant M. A round robin on the measurement of local criteria, Rapport Abrege N_RE 93.319, IRSID, St. Germain, 1993.

[66] Brocks W. Numerical round robin on micromechanical models-results, IWM-Bericht T8/95, Fraunhofer Institut fuer Werkstoffmechanik (IWM), Freiburg, 1995.

[67] Zrilic M. The application of local approach to residual life assessment of equipment components at elevated temperatures, PhD. Thesis, Faculty of Technology and Metallurgy, Belgrade University, Serbia, 2004.

[68] Rakin M. Application of the local approach in Analysis of fracture of steel, M.Sc. Thesis, Faculty of Technology and Metallurgy, Belgrade University, Serbia, 1996.

[69] Rakin M, Cvijovic Z, Gubeljak N, Sedmak A. The influence of microstructure on the ductile fracture initiation in low-alloyed steel, materials science forum, 2004; 453,454: 175-180.

[70] Needleman A, Tvergaard V. Numerical modeling of the ductile-brittle transition, International Journal of Fracture, 2000;101:73-97.

[71] Rakin M, Cvijovic Z, Grabulov V, Zrilic M, Sedmak A. Determination of micromechanical ductile fracture parameters of pressure vessel steel, proceeding of the 7th European Conference on Advanced Materials and processes-Euromat, Published on CD, Rimini, 2001.

[72] Rakin M, Sedmak A, Cvijovic Z, Zrilic M, Sedmak S. Micromechanical coupled study of crack growth initiation criterion in pressure vessel steel. Strength of Materials, 2004;36:33-36.

[73] Zrilic M, Rakin M, Sedmak A, Aleksic R, Cvijovic Z, Arsic M. Ductile fracture prediction of steam pipeline steel. Materials Science Forum, 2006;518:537-542.

[74] Younise B, Rakin M, Medjo B, Sedmak A. Local approach for prediction of ductile fracture initiation in welded specimens, In: Proceedings of Tima 10, The 4th International Conference, Timisoara, Romania; 2010:228-233.

[75] Younise B, Rakin M, Gubeljak N, Medjo B, Sedmak A. Numerical simulation for studying constraint effect on ductile fracture initiation using complete Gurson model, FME Transactions Journal, 2010; 38:197-202.

[76] Thomason PF. Ductile fracture of metals. Pergamon Press, Oxford, 1990.

[77] Gurson AL. Continuum theory of ductile rupture by void nucleation and growth: Part I-yield criteria and flow rules for porous ductile media. Journal of Engineering Materials and Technology, 1977;99:2-15.

[78] Rice JR, Tracey DM. On the ductile enlargement of voids in triaxial stress field. J. Mech. Phys. solids, 1969;17:201-217.

[79] McClintock FA. A criterion for ductile fracture by the growth of holes. J. Appl. Mech, 1969;35:363-371.

[80] Tvergaard V. Influence of voids on shear bands instabilities under plane strain conditions. Int J Fract 1981;17:389-407.

[81] Haung Y. Accurate dilatation rates for spherical voids in triaxial stress fields. Trans ASME, 1991;58:1084-1086.

[82] Chaouadi R, De Meester P, Vandermeulen W. Damage work as ductile criterion. International Journal of Fracture, 1994;66:155-164.

[83] Rakin M, Cvijovic Z, Grabulov V, Putic S, Sedmak A. Prediction of ductile fracture initiation using micromechanical analysis, Engineering Fracture Mechanics, 2004;71:813-827.

[84] Bauvineau L, Burlet H, Eripret C, Pineau A. Modelling ductile stable growth in a C-Mn steel with local approaches. In: Pineau A, Rousselier G, editors. Proceedings of the Euromech-Mecamat Conference on Local Approach to Fracture 86-96. Fontainebleau- France, 1996, pp. 22.

[85] Chaouadi R, De , Meester P, Scibetta M. Micromechanically modeling of ductile fracture toughness of reactor pressure vessel steels. In: Proceedings of the 1st European Mechanics of Materials Conference on Local Approach to Fracture, EUROMECH-MECAMAT96,Fontainebleau , 1996:126-138.

[86] Rakin M, Medjo B. Micromechanical constitutive equations for ductile fracture prediction. In: Monograph of the 10th International Fracture Mechanics summer

School (IFMASS 10), Faculty of Mechanical Engineering, Society for Structural Integrity and life, Faculty of Technology and Metallurgy, GOSA, Belgrade, 2009:69-86.

[87] Thomason PF. Three-dimensional models for the plastic limit-loads at incipient failure of the intervoid matrix in ductile porous solids. Acta Metallurgica, 1985;33(6):1079-1085.

[88] Zhang ZL. Nonlinear fracture and damage mechanics: A complete Gurson model. WIT Press Southampton, UK, 2001.

[89] Chu C, Needlman A. Void nucleation effects in biaxially stretched sheets. ASME, Journal of Engineering Materials and Technology, 1980;102:249-256.

[90] Gurland J. Observation on the fracture of cementie particles in a spheroidized 1.05 C steel deformed at room temperature. Acta Metallurgica, 1972;20:735-741.

[91] Rakin M. Monograph of local approach to fracture of metallic materials. RIC Graphic Engineering, Faculty of Technology and Metallurgy, Belgrade University, Belgrade, 2009.

[92] Benseddiq N. A local fracture analysis using a local damage model. International Journal of Pressure Vessels and Piping, 2008;85:219-227.

[93] Gao X, Faleskog J, Shih CF, Dodds RH. Ductile tearing in part-through cracks: experiments and cell-model predictions. Engineering Fracture Mechanics, 1998;59: 761-777.

[94] Faleskog J, Gao X, Shih CF. Cell model for nonlinear fracture analysis-I. Micromechanics calibration. Int J Fract, 1998;89:365-373.

[95] Dutta BK, Guin S, Sahu MK, Samal MK. A phenomenological form of the q_2 parameter in the Gurson model. International Journal of Pressure Vessels and Piping, 2008;85:199-210.

[96] Franklin AG. Comparison between a quantitative microscope and chemical methods for assessment of non-metallic inclusions. Journal of the Iron and Steel institute, 1969;207:181-186.

[97] Chen Y, Lambert S. Analysis of ductile tearing of pipeline-steel in single edge notch tension specimens. International Journal of Fracture, 2003;124:179-199.

[98] Sun DZ, Kienzler R, Voss B, Schmitt W. Application of micro-mechanical models to the prediction of ductile fracture. Fracture Mechanics, 22nd Symposium (Volume

II), ASTM STP 1131, eds S. N. Atluri, et al, American Society for Testing and Materials, Philadelphia, 1992:368-378.

[99] Koplik J, Needlman A. Void growth and coalescence in porous plastic solids. International Journal of Solids and Structures, 1988;24:835-853.

[100] Bernaur G, Brocks W. Numerical round robin on micro-mechanical models-Results. ESIS TC8, GKSS Research Center, Geesthacht, 2000.

[101] Steglich D, Brocks, W. Micro-mechanical modeling of damage and fracture of ductile metals. Fatigue and Fracture of Engineering Materials and Structures, 1998;21:1175-1188.

[102] Betegon C, Rodriguez C, Belzunce FJ. Analysis and modelisation of short crack growth by ductile fracture micromechanisms. Fatigue Fract Eng Mater Struct, 1997;20:633-644.

[103] Ghosal AK, Narasimhan R. Numerical simulations of hole growth and ductile fracture initiation under mixed-mode loading. Int J Fract, 1996;77:281-304.

[104] Xia L, Cheng L. Transition from ductile tearing to cleavage fracture: a cell-model approach. Int J Fract, 1997;87(3):289-306.

[105] Sun DZ, Siegele D, Voss B, Schmitt W. Application of local damage models to the numerical analysis of ductile rupture. fatigue Fract Engng Mater Struct, 1989;12:201-212.

[106] Standard practice for determining inclusion content of steel and other metals by automatic image analysis. ASTM Standard E1245-89. American Society for Testing and Materials, Philadelphia; 1989.

[107] Pardoen T, Hutchinson JW. An extended model for void growth and coalescence. J Mech Phys Solids, 2000;48:2467-2512.

[108] Owen DJ, Fawkes AJ. Engineering fracture mechanics; numerical methods and applications. Pineridge Press LTD., Swansea - UK, 1982.

[109] Rice J R, Tracey DM. Numerical and computer methods in structural mechanics. Fenves S. J, Academic Press, New York, 1968;b:585-623.

[110] ANSYS/Mechanical 5.4, Manual Guide, 1997.

[111] Anderson TL. Fracture mechanics: fundamental and application. CRC Press, 2nd edition, 1994.

[112] Ruggieri C, Panontin TL, Dodds RH. Numerical modeling of ductile crack growth in 3-D using computational cell elements. International Journal of Fracture, 1996;82:67-95.

[113] Gullerud A, Dodds RH. Simulation of ductile crack growth using computational cells: Numerical Aspects, Engineering Fracture Mechanics, 2000;66:65-92.

[114] ABAQUS version 6.7, Theory Manual,2003.

[115] Tvergaard V, Hutchinson JW. Two mechanisms of ductile fracture: void by void growth versus multiple void interaction. International Journal of Solids and Structures, 2002;39:3581-3597.

[116] Tvergaard V. Discrete modeling of ductile crack growth by void growth to coalescence. International Journal of Fracture, 2007;148:1-12.

[117] Prokic-Cvetkovic R, Popovic O, Sedmak A, Bukvic A, Milosevic M, Jovicic R. The influence of welding process on mechanical properties and microstructures of micro-alloyed steel weldments. The 4th International conference, Proceedings, Timisoara, Romania, 2010:218-221.

[118] ARAMIS V6, GOM mbH. Braunschweig, Germany; 2007.

[119] Gubeljak N. The effect of strength mismatch on welded joint fracture behavior. Ph.D. Dissertation, Faculty of Mechanical Engineering-University of Maribor, Maribor-Slovenia, March 1998.

[120] ASTM E1820-08. Standard test method for measurement of fracture toughness. Book of ASTM standards, 2008, Vol. 03-01.

[121] ESIS P2-92. Procedure for determining the fracture behavior of materials. European Structural Integrity Society: ESIS Publication; 1992.

[122] Ramakrishnan N, Rama Rao P. An FEM study on crack tip blunting in ductile fracture initiation. CMC-Tech Science Press, 2005;3:163-176.

[123] Kobayashi H, Hirano K, Nakamura H, Nakazawa H. A fractographic study on evaluation of fracture toughness. Proceedings of the 4th Int. conf. fract, 1977.

[124] Chu C, Needlman A. Void nucleation effects in biaxiality stretched sheets. ASME, J Eng Mater Technol 1980;102:249-256.

[125] Gao X, Faleskog J, Shih F. Cell model for nonlinear fracture analysis-II. Fracture-process calibration and verification. Int J Fract 1998;89:375-389.

[126] Pardeon T, Doghri I, Delannay F. Experimental and numerical comparison of void growth models and void coalescence criteria for the prediction of ductile fracture in copper bars. Acta Mater,1998;46:541-552.

[127] Baaser H, Gross D. Crack analysis in ductile cylindrical shells using Gurson's model. International Journal of solids and structures, 2000;37:7093-7104.

[128] Besson J, Steglich D, Brocks W. Modeling of crack growth in round bars and plane strain specimens. International Journal of solids and structures, 2001;38:8259-8284.

[129] Van Stone R, Cox T, Low J, Psioda J. Microstructural aspects of fracture by dimpled rupture. International Metals Reviews, 1985;30:157-179.

Biography of the Author

Bashir S. Younise was born on 6th July 1969 in Libya, Libyan nationality. He finished his secondary school in Al-Khom, Libya in 1987. In 1993, he received his B.Sc. degree from Tripoli University, department of Mechanical Engineering, branch of Production Engineering. In 2006, Bashir received M.Sc. degree with distinction grade from Budapest University of Technology and Economics, Faculty of Mechanical Engineering, department of Material Engineering. Since October 2008, He has been Ph.D. candidate at the University of Belgrade, Faculty of Mechanical Engineering.

In the period 1994-1996, he worked as a lecturer at the Technical Institute in Al-Khoms, Libya, and from 1997 to 2003 he worked as an assistant at the University of Al-Mergib, department of Mechanical Engineering in Al-Khoms, Libya. Bashir also worked as a part-time at Libyan Executive Railways Board. From 2007 up to July 2008, he worked as lecturer at the University of Al-Mergib, department of Mechanical Engineering in Al-Khoms, Libya. He taught some subjects such as: theory of machines, industrial management, engineering drawing and production engineering. He engaged in his Ph.D. research and worked under supervision of Professor Aleksandar Sedmak in the field of material sciences, fracture of metals. His master's thesis was also related to the same field and it was entitled "determination of reference temperature for ferritic steels".

So far, Bashir has published 5 papers in domestic and international scientific journals with impact factor and participated in 4 conferences.

Прилог 1.

Изјава о ауторству

Потписани-а Башир С. Иоунисе

број уписа Д 26/08

Изјављујем

да је докторска дисертација под насловом

МИКРОМЕХАНИЧКА АНАЛИЗА ЛОМА ЗАВАРЕНИХ СПОЈЕВА ЧЕЛИКА ПОВИШЕНЕ ЧВРСТОЋЕ

- резултат сопственог истраживачког рада,
- да предложена дисертација у целини ни у деловима није била предложена за добијање било које дипломе према студијским програмима других високошколских установа,
- да су резултати коректно наведени и
- да нисам кршио/ла ауторска права и користио интелектуалну својину других лица.

Потпис докторанда

У Београду, 17.06.2013

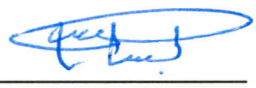

Прилог 2.

Изјава о истоветности штампане и електронске верзије докторског рада

Име и презиме аутора Башир С. Иоунисе

Број уписа Д 26/08

Студијски програм _____

Наслов рада МИКРОМЕХАНИЧКА АНАЛИЗА ЛОМА ЗАВАРЕНИХ СПОЈЕВА ЧЕЛИКА ПОВИШЕНЕ ЧВРСТОЋЕ

Ментор Проф. др Александар Седмак

Потписани Башир С. Иоунисе

изјављујем да је штампана верзија мог докторског рада истоветна електронској верзији коју сам предао/ла за објављивање на порталу **Дигиталног репозиторијума Универзитета у Београду.**

Дозвољавам да се објаве моји лични подаци везани за добијање академског звања доктора наука, као што су име и презиме, година и место рођења и датум одбране рада.

Ови лични подаци могу се објавити на мрежним страницама дигиталне библиотеке, у електронском каталогу и у публикацијама Универзитета у Београду.

Потпис докторанда

У Београду, 17.06.2013

_____

Прилог 3.

Изјава о коришћењу

Овлашћујем Универзитетску библиотеку „Светозар Марковић“ да у Дигитални репозиторијум Универзитета у Београду унесе моју докторску дисертацију под насловом:

МИКРОМЕХАНИЧКА АНАЛИЗА ЛОМА ЗАВАРЕНИХ СПОЈЕВА ЧЕЛИКА ПОВИШЕНЕ ЧВРСТОЋЕ

која је моје ауторско дело.

Дисертацију са свим прилозима предао/ла сам у електронском формату погодном за трајно архивирање.

Моју докторску дисертацију похрањену у Дигитални репозиторијум Универзитета у Београду могу да користе сви који поштују одредбе садржане у одабраном типу лиценце Креативне заједнице (Creative Commons) за коју сам се одлучио/ла.

1. Ауторство

2. Ауторство - некомерцијално

3. Ауторство – некомерцијално – без прераде

4. Ауторство – некомерцијално – делити под истим условима

5. Ауторство – без прераде

6. Ауторство – делити под истим условима

(Молимо да заокружите само једну од шест понуђених лиценци, кратак опис лиценци дат је на полеђини листа).

Потпис докторанда

У Београду, 17.06.2013

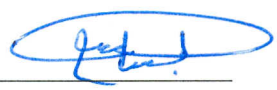

1. Ауторство - Дозвољавате умножавање, дистрибуцију и јавно саопштавање дела, и прераде, ако се наведе име аутора на начин одређен од стране аутора или даваоца лиценце, чак и у комерцијалне сврхе. Ово је најслободнија од свих лиценци.

2. Ауторство – некомерцијално. Дозвољавате умножавање, дистрибуцију и јавно саопштавање дела, и прераде, ако се наведе име аутора на начин одређен од стране аутора или даваоца лиценце. Ова лиценца не дозвољава комерцијалну употребу дела.

3. Ауторство - некомерцијално – без прераде. Дозвољавате умножавање, дистрибуцију и јавно саопштавање дела, без промена, преобликовања или употребе дела у свом делу, ако се наведе име аутора на начин одређен од стране аутора или даваоца лиценце. Ова лиценца не дозвољава комерцијалну употребу дела. У односу на све остале лиценце, овом лиценцом се ограничава највећи обим права коришћења дела.

4. Ауторство - некомерцијално – делити под истим условима. Дозвољавате умножавање, дистрибуцију и јавно саопштавање дела, и прераде, ако се наведе име аутора на начин одређен од стране аутора или даваоца лиценце и ако се прерада дистрибуира под истом или сличном лиценцом. Ова лиценца не дозвољава комерцијалну употребу дела и прерада.

5. Ауторство – без прераде. Дозвољавате умножавање, дистрибуцију и јавно саопштавање дела, без промена, преобликовања или употребе дела у свом делу, ако се наведе име аутора на начин одређен од стране аутора или даваоца лиценце. Ова лиценца дозвољава комерцијалну употребу дела.

6. Ауторство - делити под истим условима. Дозвољавате умножавање, дистрибуцију и јавно саопштавање дела, и прераде, ако се наведе име аутора на начин одређен од стране аутора или даваоца лиценце и ако се прерада дистрибуира под истом или сличном лиценцом. Ова лиценца дозвољава комерцијалну употребу дела и прерада. Слична је софтверским лиценцама, односно лиценцама отвореног кода.